

FUNDAMENTAL KINETICS AND INNOVATIVE APPLICATIONS OF
NONEQUILIBRIUM ATOMIC VIBRATION IN THERMAL ENERGY
TRANSPORT AND CONVERSION

by

Seungha Shin

A dissertation submitted in partial fulfillment
of the requirements for the degree of
Doctor of Philosophy
(Mechanical Engineering)
in the University of Michigan
2013

Doctoral Committee:

Professor Massoud Kaviany, Chair
Assistant Professor Barry Dov Duniety
Assistant Professor Pramod Sangi Reddy
Professor Ctirad Uher

© Seungha Shin 2013
All Rights Reserved

Acknowledgements

Since starting my Ph.D. studies in Ann Arbor, I have been fortunate to meet many outstanding researchers, labmates, and friends. I have learned a lot from them and had wonderful moments with them, and without their help and inputs, it would have been impossible to complete this work.

I would like to especially thank Professor Massoud Kaviani, my advisor, for being a constant source of motivation and valuable discussions which lead to novel ideas. He also encouraged me to raise fundamental questions, and provided me with much insight and advice about academe as well as life in general. It is my great fortune to join his group and be his student, and I admire his patience, enthusiasm, and willingness to discuss anything. I am thankful to Professors Barry Dunietz, Pramod Sangi Reddy, and Ctirad Uher, my Ph.D. committee members for their support during the dissertation process. I am also grateful to Doctor Nikolai Sergueev for useful discussion on the Green function code. Professors Tomas Palacios (MIT) and Jamie Phillips provided many insightful comments and suggestions on phonon conversion applications, and I thank them. I express my gratitude to our group alumni, Professors Xiulin Ruan (Purdue University) and Alan McGaughey (Carnegie Mellon University)

for their comments on my work and responses to my questions. Professors Pramod Sangi Reddy, Duncan Steel, Vanessa Sih, and Donald Siegel taught me courses that were very helpful in learning about quantum mechanics, condensed matter physics, and atomistic computer modeling. The Mechanical Engineering and Center for Solar and Thermal Energy Conversion staff, Laura Vespaziani, Kelly Chantelois, Barbara Behm, and Brenda Vyletel, all have been of tremendous help to me. I would like to extend my thanks to all my former and current labmates, Baoling Huang, Gi-Suk Hwang, Jedo Kim, Hyoungchul Kim, Corey Melnick, and Taehwa Lee for their guidance and extensive discussions related to research and everyday life. Their camaraderie has made it easier for me to go through these past challenging five years.

Finally, special thanks go to my wife Jae Min Sim and my daughter Grace Heeju Shin, for they are my source of strength and comfort. Also, I greatly appreciate my parents and parents-in-law for their unconditional love and support across the long distance and throughout these years.

This work has been supported by the National Science Foundation (Thermal Transport Processes, Grant No. CTS-0966229), Department of Energy (Center for Solar and Thermal Energy Conversion at University of Michigan, Award No. DESC0000957), Rackham Graduate School Pre-doctoral Fellowship, and Mechanical Engineering Fellowship

Table of Contents

| | |
|---|----------|
| Acknowledgements | ii |
| List of Figures | xi |
| List of Tables | xxxix |
| List of Appendices | xxxix |
| Nomenclature | xxxix |
| Abbreviations | xxxix |
| Abstract | xli |
| Chapter | 1 |
| 1 Introduction: Harvesting Nonequilibrium Atomic Motions | 1 |
| 1.1 Fundamentals of energy transport and conversion | 1 |
| 1.2 Nonequilibrium atomic motions | 3 |
| 1.2.1 Nonequilibrium phonons | 5 |
| 1.2.2 Nonequilibrium molecular-gas vibration | 8 |

| | | |
|----------|---|-----------|
| 1.3 | Properties of principal carriers and interaction kinetics | 10 |
| 1.3.1 | Determining properties from atomic structure | 11 |
| 1.3.2 | Interaction kinetics | 12 |
| 1.4 | Atomistic computer simulations | 16 |
| 1.4.1 | <i>Ab initio</i> calculations | 16 |
| 1.4.2 | Molecular dynamics simulations | 17 |
| 1.4.3 | Mesoscale simulations: Monte Carlo method | 20 |
| 1.5 | Statements of objective and scope of thesis | 21 |
| 2 | Heterobarrier for Hot-Phonon Absorption by Conduction Electron | 24 |
| 2.1 | Heterobarrier for hot-phonon energy conversion | 24 |
| 2.1.1 | GaAs/Al _x Ga _{1-x} As barrier system | 25 |
| 2.1.2 | Hot-phonon absorption barrier (HPAB) structure | 26 |
| 2.2 | Interaction kinetics in HPAB | 28 |
| 2.2.1 | Electron-phonon interaction rate | 28 |
| 2.2.2 | Phonon-phonon interaction rate | 31 |
| 2.3 | Monte-Carlo simulation | 31 |
| 2.3.1 | Electron scattering and transport in simulation | 32 |
| 2.3.2 | Simulation of phonon population and transport | 34 |
| 2.3.3 | Simulation of barrier transition | 35 |
| 2.3.4 | Analysis of simulation results | 36 |
| 2.4 | Results and discussions | 37 |
| 2.4.1 | Electron transport | 37 |

| | | |
|----------|---|-----------|
| 2.4.2 | Phonon population and absorption distribution | 40 |
| 2.4.3 | Energy conversion efficiency | 41 |
| 2.4.4 | Operational Regime | 43 |
| 2.5 | Summary | 45 |
| 3 | Phonon-Electron Energy Conversion Entropy and Efficiency | 46 |
| 3.1 | Introduction | 46 |
| 3.2 | Entropy analyses | 47 |
| 3.2.1 | Statistical entropy | 47 |
| 3.2.2 | Interactions between phonon subsystems | 49 |
| 3.2.3 | Electron-phonon interactions | 51 |
| 3.2.4 | Steady electrical current | 53 |
| | 3.2.4.1 Electron drift | 53 |
| | 3.2.4.2 Electrochemical potential | 54 |
| 3.3 | Entropy in energy conversion systems | 59 |
| 3.3.1 | Hot phonon relaxation by e - p and p - p interactions | 60 |
| | 3.3.1.1 Distributions and interaction kinetics | 60 |
| | 3.3.1.2 System evolution during relaxation | 62 |
| 3.3.2 | Barrier transition conversion | 66 |
| | 3.3.2.1 Analysis scheme | 66 |
| | 3.3.2.2 Barrier transition | 68 |
| | 3.3.2.3 Maximum potential gain and efficiency | 71 |
| 3.4 | Summary | 75 |

| | | |
|----------|---|-----------|
| 4 | Interfacial Atomic Restructuring and Phonon Conductance | 76 |
| 4.1 | Interfacial thermal transport | 76 |
| 4.1.1 | Treating interfacial phonon transport | 77 |
| 4.1.2 | Electronic thermal transport | 78 |
| 4.2 | Nonequilibrium molecular dynamics (NEMD) | 80 |
| 4.2.1 | Interatomic potentials | 80 |
| 4.2.2 | NEMD simulation scheme and equations | 82 |
| 4.2.3 | Heat flow and phonon properties | 83 |
| 4.3 | Results and analysis | 84 |
| 4.3.1 | Atomic structure | 84 |
| 4.3.2 | Thermal conductivity | 86 |
| 4.3.3 | Decomposition of interfacial resistance | 90 |
| 4.3.4 | Analysis of interfacial resistance | 91 |
| 4.3.4.1 | Phonon spectrum in interfacial region | 91 |
| 4.3.4.2 | Interfacial-region resistance | 92 |
| 4.3.4.3 | Boundary resistance | 93 |
| 4.4 | Summary | 95 |
| 5 | Low Dimensionality Effect: Passivated-Graphene Interflake Junction Electron and Phonon Conductance | 98 |
| 5.1 | Introduction | 99 |
| 5.1.1 | Graphene composite and edge passivation | 99 |
| 5.1.2 | Thermal transport bottleneck in Graphene composite | 99 |

| | | |
|----------|---|------------|
| 5.1.3 | Treatments of nanoscale thermal transport | 100 |
| 5.2 | Phonon thermal transport | 101 |
| 5.2.1 | Nonequilibrium Green function (NEGF) formalism | 101 |
| 5.2.2 | Transmission at interfaces | 104 |
| 5.2.2.1 | Lattice dynamics and dispersion | 104 |
| 5.2.2.2 | NEGF transmission | 105 |
| 5.2.2.3 | Polarization | 108 |
| 5.2.3 | Semi-classical Transmission | 110 |
| 5.2.4 | Phonon conductance | 112 |
| 5.3 | Electronic thermal transport | 115 |
| 5.4 | Prediction of composite effective conductivity | 117 |
| 5.5 | Summary | 119 |
| 6 | Selecting Molecular Vibrations for Molecular-Gas Laser Cooling | 120 |
| 6.1 | Introduction | 120 |
| 6.1.1 | Prior studies on gas laser cooling | 121 |
| 6.2 | Model for molecular-gas laser cooling system | 121 |
| 6.2.1 | Vibrational states in molecular gas | 121 |
| 6.2.2 | System description and cooling mechanism | 123 |
| 6.3 | Analysis | 125 |
| 6.3.1 | Population distribution | 125 |
| 6.3.2 | Transition Kinetics | 126 |
| 6.3.3 | Re-absorption | 130 |

| | | |
|----------|--|------------|
| 6.3.4 | Temperature Distribution | 131 |
| 6.3.5 | Dimensionless analysis | 134 |
| 6.4 | Results and Discussion | 135 |
| 6.4.1 | Laser irradiation wavelength | 135 |
| 6.4.2 | Gas condition: T , p , and x_{Xe} | 136 |
| 6.4.3 | Geometrical condition: reabsorption effects | 138 |
| 6.5 | Summary | 139 |
| 7 | Summary and Future Work | 141 |
| 7.1 | Contributions | 141 |
| 7.2 | Recommendation for further studies | 145 |
| 7.2.1 | Further studies of hot-phonon energy conversion | 145 |
| 7.2.1.1 | Phonon energy conversion in high electron mobility transistor | 146 |
| 7.2.1.2 | Other applications of hot-phonon absorption barrier system | 148 |
| 7.2.1.3 | Advance simulations | 149 |
| 7.2.2 | Further studies of thermal interfacial and junction transports . | 153 |
| 7.2.3 | Experimental studies | 155 |
| 7.3 | Outlook | 155 |
| | Appendix | 157 |
| A | Monte Carlo Method for Carrier Transport | 157 |

| | | |
|----------|--|------------|
| A.1 | Introduction | 157 |
| A.2 | Electron transport | 158 |
| A.3 | Simulation of phonon, fluid particle, and photon transport | 161 |
| B | Molecular Dynamics for Molecular Junction | 164 |
| | Bibliography | 169 |

List of Figures

- 1.1 Occupancy deviation from equilibrium distribution (f_p^o) in nonequilibrium phonon state. One optical mode with $E_{p,O}$ is overpopulated by $f'_{p,O}$ ($= f_{p,O} - f_{p,O}^o$). Nonequilibrium mode temperature $T_{p,O}$ (only for this mode) can be defined as temperature where the occupancy corresponds to nonequilibrium occupancy ($f_{p,O}$). 3
- 1.2 Nonequilibrium in phonon transport (GaAs phonon distribution). With temperature distribution in a system (by nonequilibrium temperature setting), phonon distribution is deviated from the equilibrium. This nonequilibrium causes phonon transport for a larger entropy state (finally equilibrium), and the phonon flux (\mathbf{q}_p) increases with the nonequilibrium (f'_p). D_p is the phonon density of states, and dn_p/dE_p is phonon distribution showing phonon population per unit energy. 5

| | | |
|-----|---|----|
| 1.3 | Hot phonon emission from various sources. Optical phonons are emitted while electric potential, photon, energetic ion, molecular vibration, and magnetic energy are relaxed. With some sources phonons are directly emitted, and with others electron/spin system is first excited and then phonons are emitted during the electron/spin relaxation. | 7 |
| 1.4 | Energy relaxation process from chemical reaction (methane catalytic combustion [102]). High-energy vibrational modes are first excited and thermalized to low-energy and large-entropy modes. By extracting energy before thermalization, higher energy conversion efficiency can be achieved. | 9 |
| 1.5 | Framework for the calculation of material properties in solid. Various carrier properties can be calculated from the carrier dispersion, interaction kinetics and distribution functions. | 10 |
| 1.6 | Phonon interactions during energy conversion and transport processes. (a) Phonon are emitted when high energy states in other principal particles are relaxed, and (b) they are absorbed to excite other energy states. (c) Through the three-phonon interactions [69], phonon modes can be up- and downconverted. (d) Phonons are propagated with their speed depending on mode and wavevector, and scattered by boundaries and impurities. | 13 |

| | | |
|-----|--|----|
| 1.7 | Electron energy conversion and transport. (a) Electron state can be excited by photon and phonon absorption, and chemisorbed particle relaxation. (b) During their relaxation and recombination, electrons can emit phonons or photons, or excite other electrons. (c) Electron density distribution and electric field cause electron transport, and the electrons can be also scattered by boundaries and impurities as phonons. | 14 |
| 1.8 | Various interaction times in GaAs system. | 15 |
| 1.9 | Schematics of NEMD simulation for phonon conductivity k_p with gallium nitride GaN structure. Thermal conductivity k_p is obtained by the ensemble average calculation of heat current (with a given ΔT) or temperature profile (with a given \mathbf{q}). | 19 |
| 2.1 | Ideal band discontinuity of GaAs/ $\text{Al}_x\text{Ga}_{1-x}\text{As}$. Because of the bandgap difference, the interface has a band edge discontinuity in the conduction ΔE_c and valence bands ΔE_v depending on x_{Al} . Because of the charge redistribution, the bands will be bent as the red dash-dot lines. | 26 |

| | | |
|-----|--|----|
| 2.2 | Spatial distributions of Al content, electric field and potential, and phonon temperatures in the hot-phonon absorbing barrier structure. x_{Al} abruptly increases, creating the potential barrier (with height φ_b) in the conduction band edge, while the grading maintains the current. Phonon absorption populates electrons with higher energy than barrier height ($E_e > \varphi_b$) before or after the barrier transition, and this energy is converted to electric potential. The population of optical phonons quickly decreases at the barriers and recovers by upconversion. | 27 |
| 2.3 | Variations of the electron interaction rates in the lowest conduction band, as a function of electron energy (E_e) for $T_p = 300$ K. Insets show the band structure and various interaction mechanisms (left) and the interaction rates for low- E_e Γ -valley electrons (right). Polar optical phonon scattering is dominant at low E_e , and intervalley scattering rates increase with E_e | 29 |
| 2.4 | Average polar optical phonon absorption (+)/emission (−) rates as functions of T_e and $T_{p,\text{LO}}$. The phonon absorption or emission rate becomes faster as nonequilibrium between electron and phonon increases. | 30 |
| 2.5 | Various electron scattering mechanisms. The mechanisms in bold red are included in the Monte-Carlo simulation for this study. | 32 |

| | | |
|-----|---|----|
| 2.6 | Variation of the electron drift velocity ($u_{e,d}$) with respect to electric field (e_e). The drift velocity from the MC simulations (black squares) are in good agreement with experiments (crosses and circles from Ref. [147] and triangles from Ref. [72]). Since the electron mobility μ_e is given as $u_{e,d}/e_e$, μ_e also agrees well with experiments. | 33 |
| 2.7 | (a) Wavevector (κ) space for barrier (φ_b) transition [182]. Region 1 describes the range of momentum vector for electron barrier transition, when the lateral momentum (in x and y direction) is conserved, and region 2 shows the nonconserving lateral momentum scheme. When the lateral momentum is conserved, lower transition efficiency (smaller volume) is expected. (b) The sawtooth interface model and the electron trajectory near the barrier [11]. The electrons can be directed normal to interface through multiple reflections, then more electrons can be transmitted. | 35 |
| 2.8 | Variations of drift velocity ($u_{e,d}$, left) and current density (j_e with doping density $n_d = 10^{16} \text{ cm}^{-3}$, right) with respect to the number of barriers (N_b) for different temperatures (T_e , $T_{p,A}$ and $T_{p,LO}$. Constant temperatures are used in the simulation). High $T_{p,LO}$ reduces the current loss under the same $e_{e,HPAB}$, and as hot phonon system is relaxed (T_e and $T_{p,A} = 300 \text{ K}$, $T_{p,LO} = 325 \text{ K} \Rightarrow T_e, T_{p,A}$ and $T_{p,LO} = 304 \text{ K}$), less potential gain or electrical power is expected without current loss. ($\Delta\varphi_g = 20.03 \text{ meV} \Rightarrow 19.57 \text{ meV}$). | 37 |

| | | |
|------|---|----|
| 2.9 | Sampled particle number density, drift velocity ($u_{e,d}$), and particle-energy distributions over the simulation cell. Electrons are accumulated behind barriers and low-energy electrons are highly populated near barriers. | 38 |
| 2.10 | Distributions of phonon temperatures ($T_{p,A}$ and $T_{p,LO}$) and phonon energy absorption rate (\dot{s}_{p-e}). Large phonon absorption occurs around the barriers because of the large population of low-energy electrons, and this leads to the extended nonequilibrium between phonon modes. The total phonon absorption rate in HPAB (\dot{S}_{p-e}/A) is proportional to the number of barriers, as in the inset (top right). | 40 |
| 2.11 | Energy (electric potential p and thermal energy q) flow in HPAB. Red arrows show phonon flows and blue and light blue arrows show electronic thermal and potential flow. Absorbed phonon energy (q_p) is used to increase electric potential (p_e). | 42 |
| 2.12 | Variations of the HPAB efficiency (η_{HPAB}) with respect to the drift velocity ($u_{e,d}$). η_{HPAB} first increases with $u_{e,d}$ due to increase in the electrical power gain ($p_g = \Delta\varphi_g j_e$) and then decreases because of smaller $\Delta\varphi_g$. The maximum efficiency $\eta_{\text{HPAB,max}}$ is 18.8% for $u_{e,d} = 6.2 \times 10^4$ m/s and $\varphi_b = 30$ meV. | 43 |

| | | |
|------|--|----|
| 2.13 | HPAB operational regime and variations of phonon energy absorption rate \dot{S}_{p-e}/A with respect to n_e , for $\Delta\varphi_g = 0.02, 0.1, \text{ and } 0.2$ eV, and $u_{e,d} < 10^4$ m/s. Inset shows variations of η_{HPAB} with respect to n_e and j_e . \dot{S}_{p-e}/A (for $\Delta\varphi_g$ and j_e corresponding to $\eta_{\text{HPAB,max}}$) increases with n_e | 44 |
| 3.1 | (a) Electron acceleration by an electric field. Electron distribution is shifted, but electrons with higher energy (larger distance from the origin) have the favorable condition for phonon emission, whereas the low-energy electrons are absorption favorable. (b) Electron distribution with a drift velocity $\mathbf{u}_{e,d}$. Due to the phonon scattering (absorption and emission), the electron distribution has a finite bias in κ -space showing the electron drift velocity. | 53 |
| 3.2 | Energy (\mathbf{j}_E) and entropy flux (\mathbf{j}_S) in a steady electrical current. With constant temperatures (i.e., constant electron and phonon occupancies), the electrochemical potential is converted to phonon energy, and this results in the entropy production. | 59 |
| 3.3 | Phonon density of states (D_p) in GaAs [55]. D_p in the left y -axis shows the density of state per unit volume and unit energy ($\text{eV}^{-1}\text{m}^{-3}$), and the right one represents D_p per a primitive cell and unit energy (eV^{-1}). Since GaAs has 6 modes in a primitive cell, $\int_0^\infty D_p dE_p = 6$, and in this analysis, phonons with energy less than $E_{p,\text{LO},m}$ are regarded as other phonon modes (p,A) when $\int_0^{E_{p,\text{LO},m}} D_p dE_p = 5$ ($E_{p,\text{LO},m} = 32.7$ meV). | 60 |

- 3.4 Electron density of states (D_e), equilibrium electron occupancy (f_e^o) and population distribution (dn_e/dE_e) with a parabolic band approximation in GaAs. Using D_e and f_e^o , the equilibrium electron population distribution is found. Since the occupancy is a function of the Fermi energy and temperature, the population distribution also varies with E_F and T_e 61
- 3.5 (a) Variations of the number density ($n_{e,OB}$) and fraction ($n_{e,OB}^o$) of electrons with $E_e > E_{p,LO}$ with respect to time. This number density is maximized near 1 ps since hot phonon relaxation begins. (b) Time evolution of the temperatures. For nonequilibrium electrons, temperatures at which equilibrium distribution has the same fraction ($n_{e,OB}^o$), density ($n_{e,OB}$), and total energy (E_e), are used. T_e first increases and then decreases, whereas $T_{p,LO}$ decreases and $T_{p,A}$ increases monotonically. 64
- 3.6 (a) Electron (e , blue) and phonon (p , red) distributions at 1 ps since the hot phonon relaxation begins. [Initial e (cyan) and p (magenta) distributions are also presented. Initially T_e and $T_p = 300$ K, and $T_{p,LO} = 600$ K]. (b) Entropy (S) evolution of hot phonon relaxation process ($S_{p,o}$ is initial phonon entropy). Total entropy S increases with time. 65

3.7 Energy and entropy flux in a barrier structure under a steady state.

The barrier is located just before the right boundary, and the effective barrier height is defined as the increase in the conduction band edges, ($\varphi_{b,e} = \varphi_b - \varphi_d$). Phonon temperature is fixed as $T_{p,LO}$, and the injected electron distribution ($dn_{e,L}/dE_e$) is equilibrium while the exiting distribution ($dn_{e,R}/dE_e$) is not. With electrochemical potential gain ($\Delta\varphi_e = E_{F,R} - E_{F,L}$), the system produces entropy, conserving electron number and energy. 66

3.8 (a) Momentum change by barrier transition. With the lateral momentum conservation, electrons lose their momentum by κ_b in z direction.

Smaller electron number density after transition leads to a larger drift velocity. (b) Phonon absorption for constant electrical current. With a short distance (Δz) from equilibrium and sufficient phonon absorption, equilibrium distribution before the barrier can be approximated despite faster depletion of high energy electrons. (c) Fraction of transmitted electron population at energy level $E_{e,\kappa}$ ($E_{e,\kappa,1} < E_{e,\kappa} < E_{e,\kappa,2}$). The fraction is the ratio of volume of spherical shell with dark red and volume with dark and light red. 68

| | | |
|------|---|----|
| 3.9 | <p>Electron population distributions at the left and right boundaries ($dn_{e,L}/dE_e$ and $dn_{e,R}/dE_e$) and variation of barrier transmission with respect to electron kinetic energy ($E_{e,\kappa}$). Electrons at the left boundary are equilibrium with $T_{e,L} = 300$ K and $n_{e,L} = 10^{16}$ cm⁻³, and the effective barrier height $\varphi_{b,e} = 20$ meV. As the energy increases, larger number of electrons can have momentum over κ_b, and this results in higher transmission.</p> | 70 |
| 3.10 | <p>Variations of energy conversion efficiency ($\eta_{p\rightarrow e}$) and the net entropy flux (Δj_S) with respect to the potential gain ($\Delta\varphi_e$). Δj_S represents the entropy production rate per unit area in the 1-D transport system. As $\Delta\varphi_e$ increases, $\eta_{p\rightarrow e}$ increases and the entropy production rate decreases. The maximum efficiency $\eta_{p\rightarrow e,\max}$ and potential gain ($\Delta\varphi_{e,\max}$) are found when $\Delta j_S = 0$.</p> | 71 |
| 3.11 | <p>Variations of the maximum potential gain ($\Delta\varphi_{e,\max}$) and the maximum energy conversion efficiency ($\eta_{p\rightarrow e,\max}$) with respect to the potential barrier height ($\varphi_{b,e}$). $\Delta\varphi_{e,\max}$ increases with $\varphi_{b,e}$ while $\eta_{p\rightarrow e,\max}$ has the maximum with $\varphi_{b,e} = 25$ meV.</p> | 72 |

| | | |
|------|--|----|
| 3.12 | Effects of the LO phonon temperature ($T_{p,LO}$) on (a) the maximum potential gain ($\Delta\varphi_{e,max}$) and (b) the maximum conversion efficiency ($\eta_{p\rightarrow e,max}$). High phonon temperature leads to large $\Delta\varphi_{e,max}$ and high $\eta_{p\rightarrow e,max}$. The efficiency from the MC simulations (in Chapter 2) is lower than this theoretical upper limit $\eta_{p\rightarrow e,max}$. With an overpopulated LO phonons ($T_{p,LO} > T_{p,A}$), the inclusion of the p - p interactions reduces $\eta_{p\rightarrow e,max}$ and $\Delta\varphi_{e,max}$ | 74 |
| 4.1 | NEMD simulation scheme and the initial structure. In and Si have initially face-centered cubic (FCC) and diamond cubic (or zinc-blende) structures, respectively. The simulated structure is periodic in the x and y directions, and different temperatures are prescribed on both sides through the Langevin thermostats. | 82 |
| 4.2 | (a) Interfacial Si and In atomic structures without interactions (initial equilibrium condition), and (b) with interactions and restructuring obtained from the MD simulations at 300 K. The bulk resistances ($AR_{p,Si}$ and $AR_{p,In}$) and the total interfacial resistance ($AR_{p,Si/In}$) [decomposed into the boundary ($AR_{p,b,Si/In}$) and two interfacial-region resistances ($AR_{p,r,Si}$ and $AR_{p,r,In}$)] are shown through the thermal circuit diagram. | 85 |
| 4.3 | Structure factor, $S(\mathbf{k})$ in (a) Si and (b) In layers at 300 K. $S(\mathbf{k})$ decreases around the Si/In boundary, showing non-crystalline by restructuring. Softer In has longer restructuring layers than Si. | 86 |

| | | |
|-----|--|----|
| 4.4 | Temperature distribution with heat flowing along direction z (cold thermostat at 100 and hot at 300 K). | 87 |
| 4.5 | Size dependence of Si phonon conductivity, $k_{p,\text{Si}}$. Inverse conductivity is proportional to inverse simulation cell size [150]. Using this relation and extrapolation, the bulk thermal conductivity can be obtained. | 88 |
| 4.6 | Variation of In phonon conductivity ($k_{p,\text{In}}$) with respect to temperature (T). Conductivity decreases with T . The phonon conductivity of solid In agrees well with the Slack relation, and the kinetic theory with the Kittel model for the mean free path works well in liquid. | 89 |
| 4.7 | MD phonon density of states of Si and In, in the bulk and the interfacial regions [within $0.5r_{c,\text{Si-In}}$ from the nominal interface]. Due to the interpenetration of force fields and atomic restructuring, D_p is distorted in the interfacial region. The blue shaded region represents shared phonon states between Si and In in the interfacial region. The interfacial D_{ps} (solid lines) have more shared phonon states participating in the boundary transport, compare to the bulk D_{ps} (dashed lines). | 91 |
| 4.8 | Comparison of the variations of the NEMD Si/In thermal boundary resistance as a function of temperature, with the DMM theory. The liquid NEMD simulation results have larger scatter due to the local temperature fluctuations. The scatter increases with increase in temperature (larger kinetic energy) and with smaller heat flux (lower thermal conductivity). | 92 |

| | | |
|------|--|-----|
| 4.9 | Comparison of the variations of the NEMD thermal interfacial-region resistances (in In and Si) as a function of temperature, with the approximate relation $\delta_{r,i}/k_{p,r,i}$ | 94 |
| 4.10 | Overall thermal circuit diagram. (a) All the resistances in the Si/In contact are described, and the main transport channels are shown with thicker lines. (b) This work mainly considers phonon resistances, and the decomposition of interfacial resistance (into $AR_{p,b}$ and $AR_{p,r}$) is suggested. (c) The interfacial region has a lower thermal conductivity ($k_{p,r}$) due to the atomic restructuring. | 95 |
| 5.1 | The edge-passivated graphene-flake junction used for the thermal transport calculations. The entire domain is divided into a central and two semi-infinite regions, and the central region is divided into a scattering and two electrode regions. The temperatures T_L and T_R are prescribed. d is the interatomic distance, and a and b is the width and height of the periodic bulk cell. | 101 |
| 5.2 | NEGF calculation processes for the carrier transmission at interfaces. The self energies and Green functions are calculated with the dynamical (Hessian) matrices from the DFT calculation. Using the Caroli formula with the Green functions, the transmission at interfaces can be found. | 102 |

| | | |
|-----|---|-----|
| 5.3 | The phonon dispersion from Γ to M for the bulk graphene. The solid line is from the DFT dynamical matrix calculations. The red solid circles are from the neutron scattering data and the blue open circles are from the electron energy loss spectroscopy (EELS) data [128]. | 105 |
| 5.4 | The variations of the phonon transmission with the transport direction ($\kappa_y^* = 0$) with respect to the phonon energy, for the bulk graphene and the passivated junctions. The transmissions for the passivated junctions are largely suppressed, while the O-H junction has the largest transmission. | 106 |
| 5.5 | Phonon transmissions as functions of the component κ_y^* in the wavevector space and the phonon energy for (a) bulk graphene, (b) O-H, (c) O-O and (d) H-H junctions. The transmissions are symmetric and larger near the transport direction ($\kappa_y^* = 0$). | 107 |
| 5.6 | Variations of the phonon density of states and transmissions (at $\kappa_y^* = 0$) with respect to the phonon energy for (a) the longitudinal (L), (b) transverse (T), and (c) out-of-plane (Z) directions, for the O-H passivated junction. Due to the interaction with the junction atoms and the atomic restructuring, D_p is distorted in the interfacial regions. The iso-surface of the charge density ($\rho_e^* = 0.02$), the charge (q_e^*) associated with each atom, and the difference from the valence charges (δ) are shown in (d). Note that τ_p is the largest in the L direction, and is bimodal with the wide peaks at low and the sharp peaks at the edge-resonant frequencies. | 108 |

| | | |
|------|--|-----|
| 5.7 | Comparison of the phonon transmission (at $\kappa_y^* = 0$) from the AMM treatment with the NEGF. The AMM transmission is in good agreement with the NEGF at low frequencies, but does not show the high frequency transmission. | 111 |
| 5.8 | Variations of the phonon conductance ($G_{p,3D,j}$, solid lines) of the three passivated flake junctions with respect to temperature, from the NEGF calculations, and comparison with the bulk behavior (dash lines). . . | 112 |
| 5.9 | Phonon transport channels and the mechanism of phonon transport suppression in the O-H passivated junction. | 113 |
| 5.10 | The contribution of wavevectors to thermal conductance [$G_p^*(\kappa_y^*)$] at $T = 300$ K. | 114 |
| 5.11 | Variations of the electronic thermal conductance ($G_{e,3D,j}$, solid lines) on the left and that scaled with $G_{p,3D,j}$ ($G_{e,3D,j}/G_{p,3D,j}$, dash lines) on the right, without an external bias potential, with respect to temperature. | 115 |
| 5.12 | The charge-density iso-surface ($\rho_e^* = 0.02$) on the left and the wavefunction ($ \psi_e ^2 = 0.01$) of the first eigenstate below the E_F (at the Γ point) on the right, for the bulk and the three junctions. Different colors (blue and red) in the wavefunctions correspond to the opposite signs. | 116 |

| | | |
|------|--|-----|
| 5.13 | The effective thermal conductivity of linear chains composed of graphene flakes with three cases of edge passivated junctions at $T = 300$ K, as a function of the flake length. Two mean free paths, $\lambda_p = 1.0 \mu\text{m}$ ($k_{p,\text{Bulk}} = 4756$ W/m-K) and $\lambda_p = 0.75 \mu\text{m}$ ($k_{p,\text{Bulk}} = 3567$ W/m-K), are used [54, 124]. | 118 |
| 6.1 | Five-level vibrational energy diagram for CO ₂ laser cooling. With the Herzberg notation, the symmetric, bending, and asymmetric vibrational modes are described. The photon wavelength for absorption and emission (λ_i and λ_e) are included, and the relaxation and excitation mechanisms and interaction times (τ 's) are also shown. | 122 |
| 6.2 | Cooling mechanisms for CO ₂ -Xe gas, showing the tube with central laser beam. Due to the anti-Stokes process, the state in (c) has lower energy compared to (a). | 124 |
| 6.3 | Population distribution of energy levels in CO ₂ laser cooling system. | 126 |
| 6.4 | Gas differential energy balance, conduction and cooling/heating rate, and the gas temperature distribution showing local and average change in temperature. ΔT represents the cooling, and $\langle \Delta T \rangle$ is the average cooling. The maximum cooling is achieved at $r = 0$ [$\Delta T_{\text{max}} = \Delta T(r = 0)$]. | 133 |

| | | |
|-----|---|-----|
| 6.5 | Comparison of 9.6 and 10.6 μm wavelength laser cooling, showing variations of cooling with respect for cylinder temperature for both wavelengths. The macroscopic conditions are the same as [38] and the experimental result of [38] for $\lambda_i = 10.6 \mu\text{m}$ is also shown. | 135 |
| 6.6 | Variations of cooling with respect to (a) total gas pressure p and (b) Xe mole fraction x_{Xe} | 137 |
| 6.7 | Variations of cooling with respect to cylinder radius R_t , at several cylinder temperatures, showing the effect of re-absorption (absorption coefficient and emitted photon path length). | 138 |
| 7.1 | Proposed integrated GaN HEMT-HPAB circuit, and variations of Al content, electric potential and field, and temperature. | 146 |
| 7.2 | Electron-LO phonon interaction (absorption and emission) rate in GaN when the LO phonon temperature ($T_{p,\text{LO}}$) is 300 and 500 K. The electron and phonon properties, such as static and optical dielectric constants ($\epsilon_{e,s}$ and $\epsilon_{e,\infty}$), in Refs. [20] and [118] are employed for this polar optical phonon interaction. | 147 |
| 7.3 | Possible HPAB structures for harvesting hot phonons (a) in LED system and (b) in solar and chemisorbed vibration energy relaxation . . . | 149 |
| 7.4 | (a) Primitive cell of Wurtzite GaN. Lattice constants (a and c) and crystal direction [0001] are shown. (b) Atomic configuration of $\text{Al}_{0.25}\text{Ga}_{0.75}\text{N}$. $2 \times 2 \times 1$ supercell is considered and 2 Ga atoms are replaced with Al. | 150 |

| | | |
|-----|---|-----|
| 7.5 | Electronic band structure of wurtzite GaN from <i>ab initio</i> (using VASP). GGA [132] is widely used approximation for exchange correlation potential, but underestimates band gap, $E_{e,g}$. GGA+U (including the Coulomb potential) [4] and HSE (hybrid functional) [65] are employed to have more accurate band structure. <i>Ab initio</i> results (a , c , $E_{e,g}$, band structure, etc.) from HSE agrees well with experiments and literatures [20, 17]. | 151 |
| 7.6 | The diverse applications of molecular junction according to the thermal conductance. | 153 |

A.1 (a) Choice of scattering event. The constant scattering rate ($\dot{\gamma}_o$) is composed of overall scattering ($\sum_{m=1}^j \dot{\gamma}_m$, j is the total number of possible scattering mechanisms) and the self-scattering rates ($\dot{\gamma}_{\text{self}}$), $\dot{\gamma}_o = \sum_{m=1}^j (\dot{\gamma}_m + \dot{\gamma}_{\text{self}})$. If the random number, ran is between $\sum_{m=1}^{i-1} \dot{\gamma}_m / \dot{\gamma}_o$ and $\sum_{m=1}^i \dot{\gamma}_m / \dot{\gamma}_o$, the i -th scattering mechanism is selected. If the self-scattering is selected ($ran > \sum_{m=1}^j \dot{\gamma}_m$), neither energy nor momentum of the carrier changes. (b) The free-flight and scattering sequence. According to randomly assigned scattering time (τ), a carrier can be scattered or drift within a given time step (Δt). Once it finishes its free-flight, a carrier is scattered with randomly selected scattering mechanism and a new scattering time is assigned to the carrier. (c) An algorithm of the self-consistent ensemble MC simulation. Electric potential and field from charge distribution are calculated by solving the Poisson equation, and carrier trajectories are simulated using the MC method with them. Carrier distribution obtained from the simulation is used to update the internal field. 160

| | | |
|-----|---|-----|
| A.2 | Flowcharts of the MC simulation of photon transport using (a) CSDA, and (b) DIS treatment. Photon beam with randomly initialized spatial distribution travels during a photon interaction time, τ_{ph} . If photon escapes the computation domain after the free flight and the prescribed number of simulated beams is not sufficient, new photon beams are simulated. Otherwise, the photon beam is scattered and its new energy is updated (when scattering is inelastic), as well as its directions, etc. In energy absorption, if new energy after scattering is smaller than a prescribed criterion, photon beam is regarded as annihilated and simulation for this beam is stopped. | 162 |
| B.1 | (Color online) Atomic configuration used in MD simulations. The thermostat on each side is three Al layers and its temperature is controlled by the Langevin algorithm. | 165 |
| B.2 | (Color online) (a) Phonon thermal conductance of the biphenyl-dithiol TE junction, obtained via both the MD and NEGF calculations, versus junction temperature. (b) Frequency of occurrence of the biphenyl-dithiol molecular configurations with various torsion angles for three different values of junction temperature. | 168 |

List of Tables

| | | |
|-----|--|-----|
| 4.1 | Si properties from the Stillinger-Weber potential and experiments [61]. | 80 |
| 4.2 | In properties from the developed Morse potential, MEAM and experiments [61]. | 81 |
| 6.1 | Time constants in laser cooling of CO ₂ -Xe gas. | 130 |
| B.1 | Interatomic potential parameters for NEMD simulations. | 166 |

List of Appendices

| | | |
|-----|--|-----|
| A | Monte Carlo Method for Carrier Transport | 157 |
| A.1 | Introduction | 157 |
| A.2 | Electron transport | 158 |
| A.3 | Simulation of phonon, fluid particle, and photon transport | 161 |
| B | Molecular Dynamics for Molecular Junction | 164 |

Nomenclature

| | |
|--------------|--|
| A | area |
| C | elastic constant |
| c | heat capacity |
| D | density of states or diffusion coefficient |
| E | energy |
| e_c | electron charge, 1.602×10^{-19} C |
| e_e | electric field |
| f | occupancy function or frequency |
| G | conductance |
| \mathbf{G} | Green function |
| g | degeneracy |
| H | Hamiltonian |
| H | enthalpy |
| h_P | Planck constant, 6.626×10^{-34} J-s = 4.136×10^{-15} eV-s |
| \hbar | reduced Planck constant, $h_P/2\pi = 1.055 \times 10^{-34}$ J-s = 6.583×10^{-16} eV-s |
| I_{ph} | photon intensity |

| | |
|--------------|---|
| j | flux |
| \mathbf{K} | dynamical matrix (force constant matrix) |
| k | thermal conductivity |
| k_B | Boltzmann constant, 1.381×10^{-23} J/K = 8.618×10^{-5} eV/K |
| L or l | length |
| m | mass |
| n | number density |
| N_p | number of phonon |
| Q | energy transfer |
| \mathbf{q} | thermal energy flux |
| p | pressure |
| \mathbf{p} | momentum vector or potential flux vector |
| R | resistance |
| S | entropy or structure factor |
| \mathbf{s} | polarization vector |
| \dot{S} | energy conversion rate |
| \dot{s} | volumetric energy conversion rate |
| T | temperature |
| T_m | melting temperature |
| $u_{e,d}$ | electron drift velocity |
| u_p | phonon speed |
| u_{ph} | speed of light |

| | |
|-----|--|
| V | volume |
| W | number of microstates |
| x | mole fraction or an axis in the cartesian coordinate |
| Z | partition function |

Greek symbols

| | |
|-----------------------|--|
| α | nonparabolicity |
| $\alpha_{ph,a}$ | absorptance |
| Δ | difference |
| δ_D | Dirac delta function |
| ϵ | permittivity (or dielectric constant) |
| ϵ_0 | vacuum permittivity, $8.854 \times 10^{-12} \text{ C}^2/\text{N}\cdot\text{m}^2$ |
| η | efficiency or infinitesimal constant |
| Γ | force constant |
| $\mathbf{\Gamma}$ | energy-level broadening function |
| $\dot{\gamma}$ | transition rate |
| γ_G | Grüneisen parameter |
| λ | wavelength or mean free path |
| $\boldsymbol{\kappa}$ | wavevector |
| κ | wavenumber |
| $\boldsymbol{\mu}$ | dipole moment |
| μ_c | chemical potential |

| | |
|--------------------|-----------------------------------|
| μ_e | electron mobility |
| ρ | density |
| τ | relaxation time or transmission |
| φ_e | electrochemical potential |
| φ_b | potential barrier height |
| $\varphi_{e-p,A}$ | electron-acoustic phonon coupling |
| $\varphi'_{e-p,O}$ | electron-optical phonon coupling |
| Σ | self-energy |
| $\sigma_{ph,i}$ | absorption coefficient |
| ψ | wave function |
| ω | angular frequency |

Subscripts

| | |
|-------|---|
| A | Acoustic mode |
| BE | Bose-Einstein |
| a | absorption |
| b | boundary |
| c | cutoff, chemical energy, or conduction band |
| $c-c$ | carrier-carrier (c can be p , e , f , or ph .) |
| D | Debye |
| d | dopant |
| dB | de Broglie |

| | |
|--------|---|
| e | electron or emission |
| e, e | effective electron |
| e, d | electron drift |
| F | Fermi |
| FD | Fermi-Dirac |
| f | final or fluid particle |
| g | bandgap, group, or gain |
| i | initial |
| int | interaction |
| L | longitudinal |
| l | liquid |
| MB | Maxwell-Boltzmann |
| m | intermediate |
| O | optical mode |
| o | equilibrium, reference or initial value |
| p | phonon |
| p, c | phonon cutoff |
| ph | photon |
| S | entropy |
| s | solid |
| sp | spontaneous |
| T | transverse |

t translational
 v vibrational or valence band

Others

$\langle \rangle$ average
 $*$ dimensionless
 $'$ nonequilibrium

Abbreviations

| | |
|-------|---------------------------------------|
| 2DEG | two dimensional electron gas |
| AI | <i>ab initio</i> |
| AMM | acoustic mismatch model |
| BCC | body-centered cubic |
| BCT | body-centered tetragonal |
| BTE | Boltzmann transport equation |
| CG | conjugate gradient |
| DFT | density functional theory |
| DOS | density of states |
| DMM | diffuse mismatch model |
| FCC | face-centered cubic |
| FGR | Fermi golden rule |
| GGA | generalized gradient approximation |
| G-K | Green-Kubo |
| GULP | general utility lattice program |
| HCACF | heat current autocorrelation function |

HEMT high electron mobility transistor

HPAB hot-phonon absorbing barrier

HSE Heyd-Scuseria-Ernzerhof exchange-correlation functional

LA longitudinal acoustic

(L)APW(linearized) augmented planewave

LDA local-density approximation

LED light emitting diode

LO longitudinal optical

MC Monte Carlo

MD molecular dynamics

NEGF nonequilibrium Green function

NEMD nonequilibrium molecular dynamics

PBE Perdew-Burke-Ernzerhof

SIESTA spanish initiative for electronic simulations with thousands of atoms

SPV solar photovoltaic

TA transverse acoustic

TE thermoelectricity

TIM thermal interfacial material

TO transverse optical

VASP Vienna *ab initio* simulation package

ABSTRACT

FUNDAMENTAL KINETICS AND INNOVATIVE APPLICATIONS OF
NONEQUILIBRIUM ATOMIC VIBRATION IN THERMAL ENERGY
TRANSPORT AND CONVERSION

by

Seungha Shin

Chair: Massoud Kaviany

All energy conversion inefficiencies begin with emission of resonant atomic motions, e.g., vibrations, and are declared as waste heat once these motions thermalize to equilibrium. The nonequilibrium energy occupancy of the vibrational modes can be targeted as a harvestable, low entropy energy source for direct conversion to electric energy. Since the lifetime of these resonant vibrations is short, special nanostructures are required with the appropriate tuning of the kinetics. These in turn require multiscale, multiphysics treatments.

Atomic vibration is described with quasiparticle phonon in solid, and the optical phonon emission is dominant relaxation channel in semiconductors. These optical modes become over-occupied when their emission rate becomes larger than their decay rate, thus hindering energy relaxation and transport in devices. Effective removal of these phonons by drifting electrons is investigated by manipulating the electron distribution to have higher population in the low-energy states, thus allowing favor-

able phonon absorption. This is done through introduction, design and analysis of a heterobarrier conducting current, where the band gap is controlled by alloying, thus creating a spatial variation which is abrupt followed by a linear gradient (to ensure directed current).

Self-consistent ensemble Monte Carlo simulations based on interaction kinetics between electron and phonon show that up to 19% of the phonon energy is converted to electric potential with an optimized GaAs/Al_xGa_{1-x}As barrier structure over a range of current and electron densities, and this system is also verified through statistical entropy analysis. This direct energy conversion improves the device performance with lower operation temperature and enhances overall energy conversion efficiency. Through this study, the paradigm for harvesting the resonant atomic vibration is proposed, reversing the general role of phonon as only causing electric potential drop.

Fundamentals pertaining to thermal energy transport and conversion are further explored by directly addressing the nonequilibria in phonon and molecular vibration. Enhancement of the laser cooling performance in molecular gas is examined by nonequilibrium interaction kinetics between molecules and photons. Thermal energy transport across interfaces and junctions is also studied, and decomposition of thermal interfacial resistance, atomic restructuring, and phonon wave features are addressed.

Chapter 1

Introduction: Harvesting

Nonequilibrium Atomic Motions

1.1 Fundamentals of energy transport and conversion

Efficient and sustainable energy conversion and transport processes in small and large devices continue to challenge us. Recent advances in areas such as system design, materials characterization, system integration and manufacturing, as well as in the fundamental understanding of energy conversion and transport phenomena have led to major improvements.

In pursuing the fundamentals, the atomic-level physics has been the most important, since the macroscale properties are ultimately derived from these atomic-level treatments. In the atomic perspective, the thermal energy storage, transport, and conversion are examined with regards to the four principal energy carriers, namely, phonon (p), electron (e), fluid particle (f) and photon (ph) [82, 26]. The principal-carrier properties, such as energy, energy occupancy distribution, and speed, and the interaction kinetics among these carriers are central to the understanding of the thermal energy transport and conversion.

According to the second law of thermodynamics, all systems proceed toward the largest entropy state, which is equilibrium. Nonequilibrium energy occupancy of principal energy carriers is the driving force for all energy transport and conversion processes, even though to make property predictions it is customary to assume equilibrium distributions. Addressing and optimizing the nonequilibrium occupancy can lead to new approaches to energy conversion.

This research examines the nonequilibria, especially in phonon or molecular vibrational energy occupancy, with the aim of better understanding and finding innovative solutions to some energy transport and conversion challenges. These are innovative phonon energy conversion device, molecular-gas laser cooling enhancement, and interfacial and junctions transports. These are approached through multiscale analyses (*ab initio*, molecular dynamics, and Boltzmann or meso) with combinations of classical, statistical, and quantum mechanics.

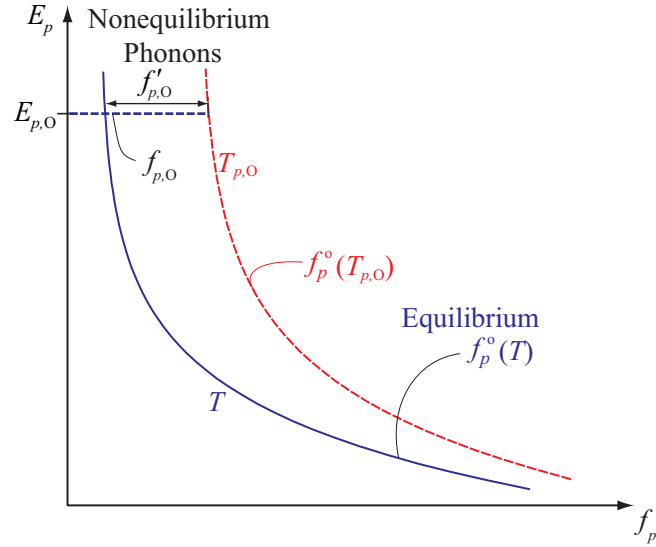


Figure 1.1: Occupancy deviation from equilibrium distribution (f_p°) in nonequilibrium phonon state. One optical mode with $E_{p,O}$ is overpopulated by $f'_{p,O}$ ($= f_{p,O} - f_{p,O}^\circ$). Nonequilibrium mode temperature $T_{p,O}$ (only for this mode) can be defined as temperature where the occupancy corresponds to nonequilibrium occupancy ($f_{p,O}$).

1.2 Nonequilibrium atomic motions

During an energy conversion or a transport process, the energy carrier will be in nonequilibrium occupancy, and once it reaches equilibrium such processes cease. In equilibrium, the distribution of the principal energy carrier follows the equilibrium occupancy function (f_i°) maximizing its entropy, and the occupancy function is determined from the nature of particle, i.e.,

$$\begin{aligned}
 \text{Maxwell-Boltzmann } f_{\text{MB}}^\circ &= \frac{1}{\exp(E_i/k_B T)} && \text{for classical particles,} \\
 \text{Bose-Einstein } f_{\text{BE}}^\circ &= \frac{1}{\exp(E_i/k_B T) - 1} && \text{for bosons, and} \\
 \text{Fermi-Dirac } f_{\text{FD}}^\circ &= \frac{1}{\exp[(E_i - \mu_c)/k_B T] + 1} && \text{for fermions,} \quad (1.1)
 \end{aligned}$$

where E_i is particle energy, k_B is the Boltzmann constant, μ_c is chemical potential, and T is temperature. Nonequilibrium is deviation from the equilibrium, and Fig. 1.1 illustrates a nonequilibrium phonon distribution with overpopulated optical mode (at $E_{p,O}$, $f'_{p,O} = f_{p,O} - f_{p,O}^o > 0$). Although temperature is an equilibrium property determining the maximum entropy occupancy distribution, the nonequilibrium temperature for energy level can be suggested as in Fig. 1.1, e.g., for bosons, $T_p(f_p, E_p) = E_p / \{k_B[\ln(f_p + 1) - \ln(f_p)]\}$ [163]. (In nonequilibrium, the temperature depends on the energy state.)

When the nonequilibrium occupancy is allowed to relax, it finally thermalizes (reaches equilibrium), increasing the system entropy, and in general the atomic vibration is the main relaxation channels toward equilibrium (due to its large heat capacity). Thermalized atomic motion with large entropy and diluted energy would not lead to efficient conversion of the available energy. Thus, it can be said that all energy conversion inefficiencies begin with the emission of resonant atomic motions, e.g., vibrations, and these emissions are declared as waste heat once they thermalize to equilibrium. The nonequilibrium energy occupancy of the vibrational modes, especially with overpopulated high-energy states, can be targeted as a harvestable, low entropy energy source for direct conversion to electric energy. The atomic vibration in solids is described with the quasiparticle phonon. We now proceed to introduce the nonequilibrium phonon in solid and the nonequilibrium molecular vibration in fluid state.

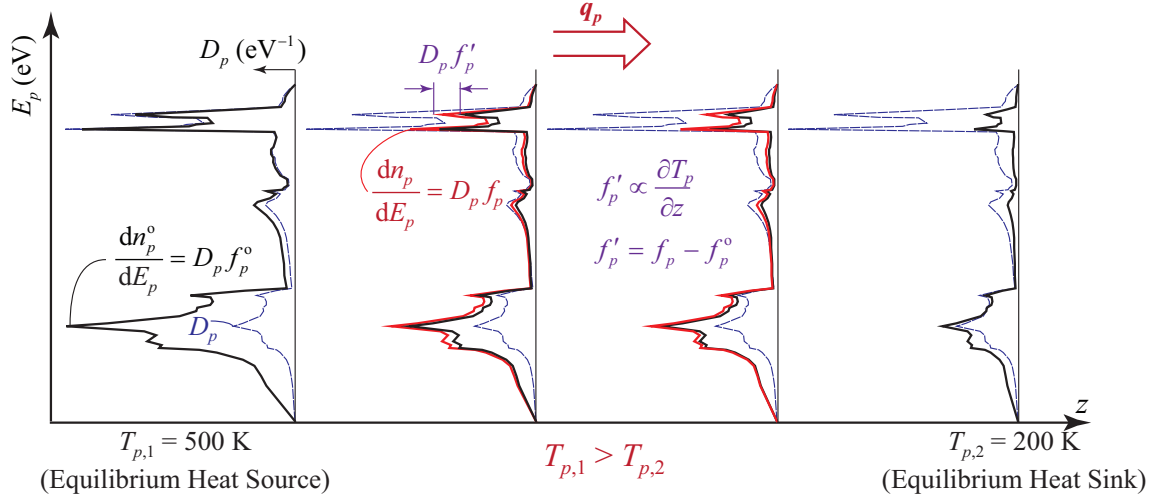


Figure 1.2: Nonequilibrium in phonon transport (GaAs phonon distribution). With temperature distribution in a system (by nonequilibrium temperature setting), phonon distribution is deviated from the equilibrium. This nonequilibrium causes phonon transport for a larger entropy state (finally equilibrium), and the phonon flux (\mathbf{q}_p) increases with the nonequilibrium (f_p'). D_p is the phonon density of states, and dn_p/dE_p is phonon distribution showing phonon population per unit energy.

1.2.1 Nonequilibrium phonons

Phonons in equilibrium can propagate and interact with other phonons or energy carriers, but all the propagations and interactions are balanced with the reverse processes. Once phonons are in nonequilibrium between phonon modes or with other carrier systems, net phonon transports and conversions occur to equilibrate the system; therefore, nonequilibrium is central in energy conversion and transport. Figure 1.2 shows nonequilibrium in phonon transport in gallium arsenide (GaAs), which is derived from nonequilibrium temperature distribution. Large temperature gradients (∇T_p) lead to significant nonequilibrium (f_p'), allowing for larger heat current (\mathbf{q}_p).

In many energy conversion processes in solid, the high-energy carriers (mostly electrons) are relaxed, finally emitting phonons to equilibrate the system. Due to their higher energy compared to acoustic phonons, optical modes are first excited

when available (In particular, phonon emission in optical mode is a dominant relaxation channel in semiconductors). Thus, phonons are emitted by various decays, recombinations and drags in energy conversions, and resistive transport processes (e.g., in electronic circuits). When the optical phonon emission rate is larger than its decay rate, the optical mode is overpopulated over the equilibrium and referred to as "hot phonon" [91]. The sources of these hot optical phonon are presented in Fig. 1.3. Examples include electric field acceleration of the charges in high-power electronic devices [115], nonradiative decay of hot electrons in optoelectric devices [30], lattice electron-stoppage of charged fission fragments [57], frustrated-vibration relaxation of chemisorbed molecules [149], and magnetic field Landau splitting [37]. Some of these sources directly emit phonons, while others first excite an electric or magnetic entity which in turn decays and emits phonons. These hot phonons are generally allowed to thermalized (reaching equilibrium occupancy), converting their energy to waste heat (equilibrium phonons), thus generating entropy.

A large population of hot phonons leads to high temperatures, and also hinders the energy relaxation and transport, which are detrimental in most devices [48, 142]. Therefore, device performance improves by the proper consumption (assisted or unassisted absorption) of these hot phonons. Utilizing hot phonons before their thermalization is expected to be even more efficient, because of their lower entropy. However, due to the small average speed of the optical phonons and the eminence of their downconversion to acoustic phonons, the hot phonons should be used quickly and close to their emission site.

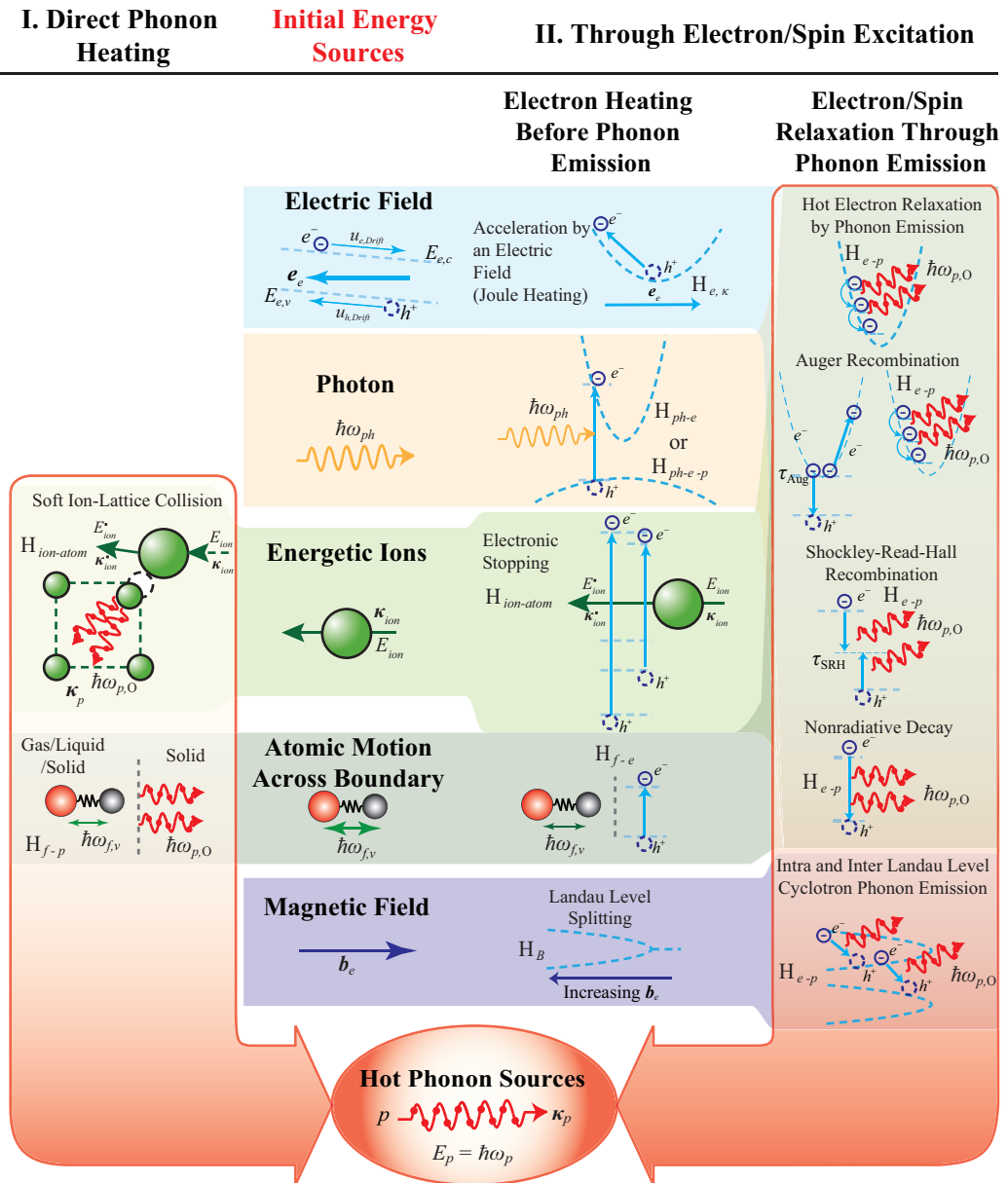


Figure 1.3: Hot phonon emission from various sources. Optical phonons are emitted while electric potential, photon, energetic ion, molecular vibration, and magnetic energy are relaxed. With some sources phonons are directly emitted, and with others electron/spin system is first excited and then phonons are emitted during the electron/spin relaxation.

1.2.2 Nonequilibrium molecular-gas vibration

Polyatomic molecules contain the translational, rotational and vibrational kinetic energies, and these energy modes depend on their atomic constituents and the inter- and intramolecular interactions. In general, because of the high energy [82], the vibrational modes are first excited during the high-energy conversion and transport to fluid particle, and then they are finally decayed to lower kinetic energy mode. The nonequilibrium molecular vibration can be harvested for the laser operation [45] and relaxed to electron or phonon energy by adsorption to the solid substrate [149, 130, 133]. Figure 1.4 shows an example of energy conversion process from catalytic chemical reaction, with the thermalization from high-energy vibrations to low-energy and large-entropy modes. By extracting the vibration energy before thermalization, higher energy efficiency may be achieved.

Energy Conversion from Chemical Reaction

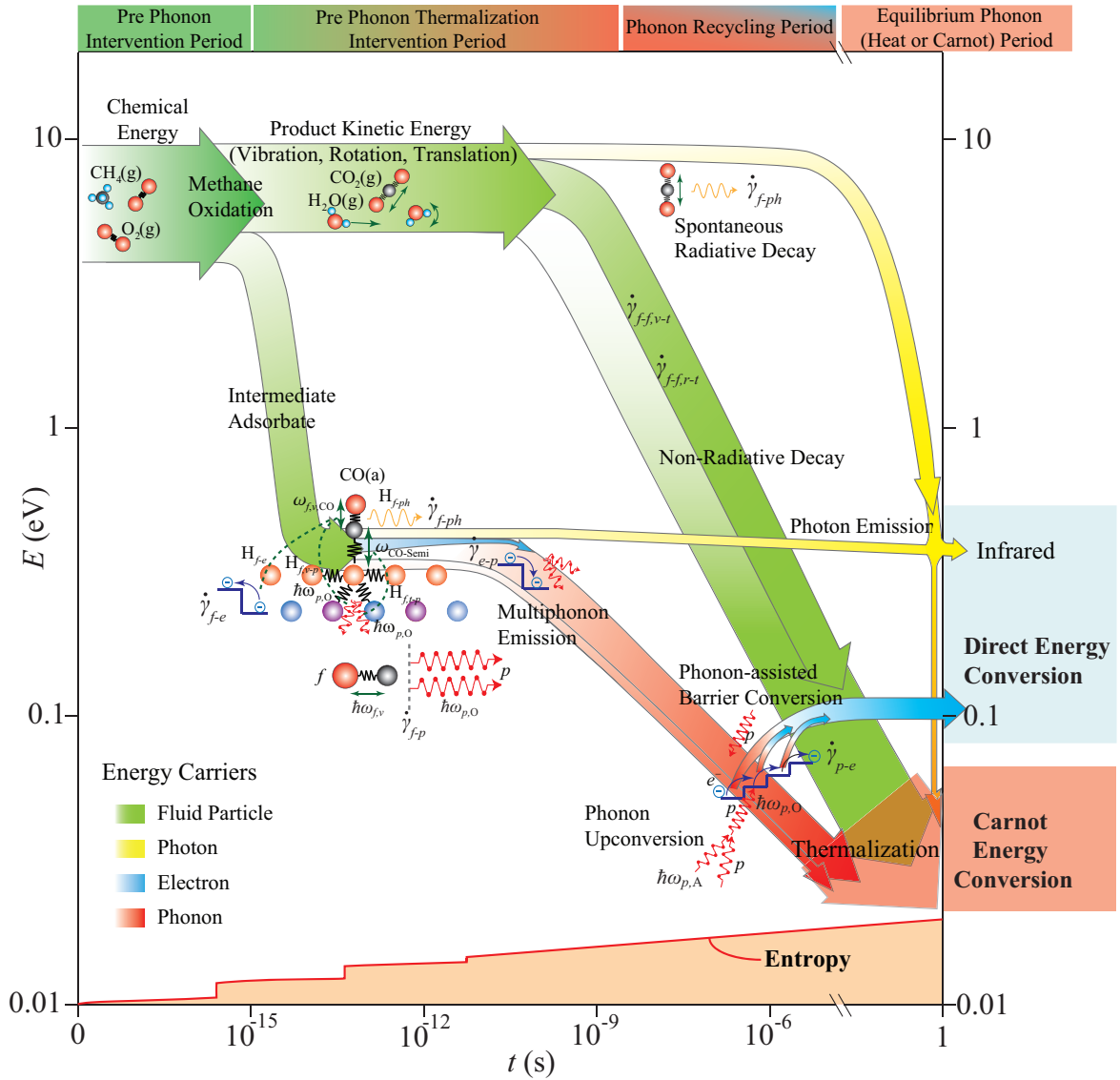


Figure 1.4: Energy relaxation process from chemical reaction (methane catalytic combustion [102]). High-energy vibrational modes are first excited and thermalized to low-energy and large-entropy modes. By extracting energy before thermalization, higher energy conversion efficiency can be achieved.

1.3 Properties of principal carriers and interaction kinetics

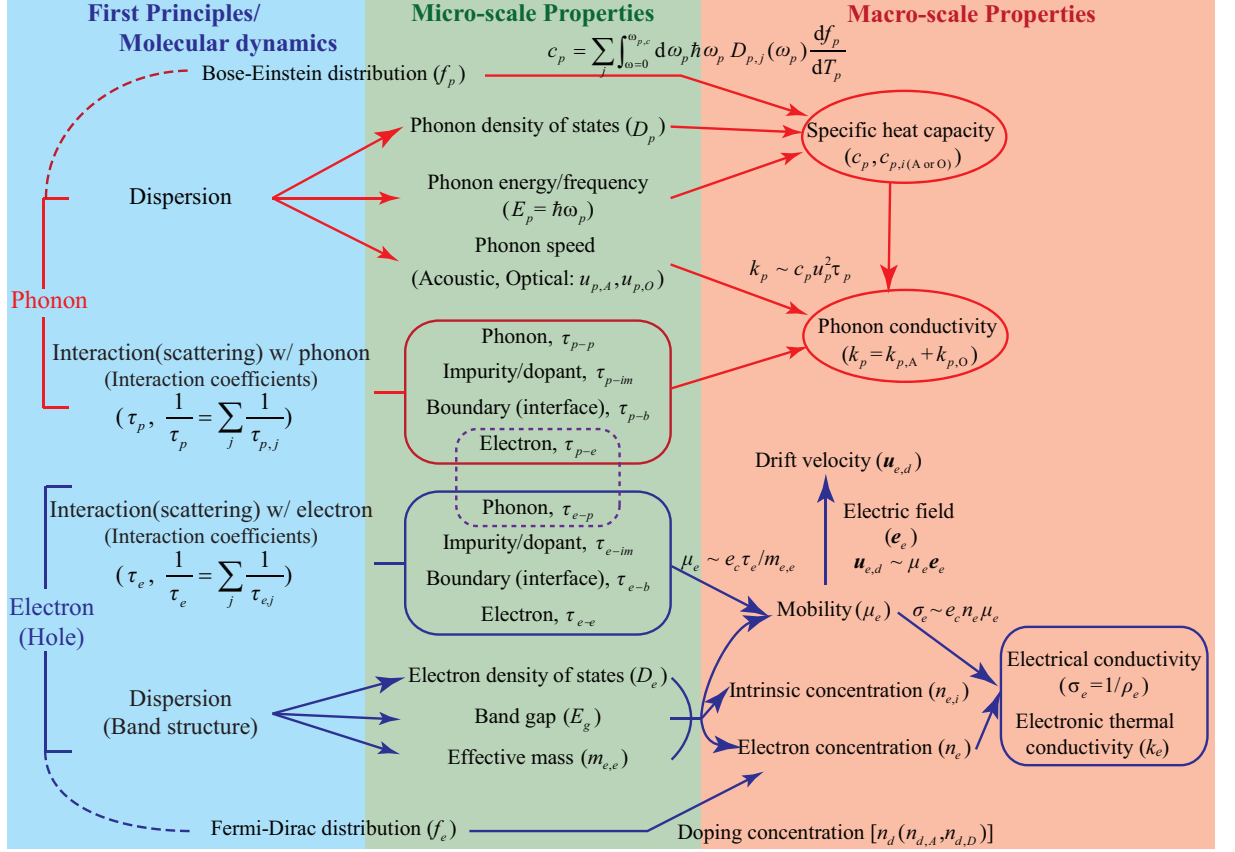


Figure 1.5: Framework for the calculation of material properties in solid. Various carrier properties can be calculated from the carrier dispersion, interaction kinetics and distribution functions.

Energy conversion and transport are characterized by various properties of the principal carriers, and as shown in Fig. 1.5, many properties can be calculated from the carrier dispersion, interaction kinetics and distribution functions. This section discusses how the carrier properties are obtained from their fundamental physics, mainly addressing electron and phonon. Because these carrier properties are determined by the atomic structure and system conditions (e.g., temperature, phase),

desirable properties for applications can be realized through the design of the atomic structure and the control of the system conditions.

1.3.1 Determining properties from atomic structure

By solving the Schrödinger equation ($H_e\psi_{e,x} = E_e\psi_{e,x}$) with the electron Hamiltonian (H_e), the relation between wavevector κ_e and energy E_e is calculated. This relation provides an electronic band structure, and it directly informs band energy dispersion and band gap ($E_{e,g}$). The electron density of states (D_e) is obtained by the projection of the electron band structures. The effective electron mass ($m_{e,e}$) represents the curvature of a valley in the electronic band structures, with a parabolic or nonparabolic band assumption, i.e., (in nonparabolic approach α is nonparabolicity)

$$\begin{aligned} \text{parabolic} & \quad E_e = \hbar^2\kappa_e^2/2m_{e,e}, \quad \text{and} \\ \text{nonparabolic} & \quad E_e(1 + \alpha E_e) = \hbar^2\kappa_e^2/2m_{e,e}. \end{aligned} \quad (1.2)$$

Considering these microscale properties with the Fermi-Dirac occupancy function and the electron scattering mechanisms, mobility (μ_e), electrical conductivity (σ_e) and electronic thermal conductivity (k_e) can be predicted.

As various electronic properties are obtained from the electronic band structure, phonon band structure, which is the relation between the wavevector and the phonon frequency/energy (κ_p vs. ω_p), determines the phonon density of states (D_p), phonon speed ($u_p = d\kappa_p/d\omega_p$) and phonon energy ($E_p = \hbar\omega_p$). Using the microscopic properties derived from the phonon dispersion and the Bose-Einstein function (f_p), phonon

specific heat capacities (c_p), defined as the derivative of internal phonon energy e_p (J/m^3) with respect to temperature T_p (K), is given as

$$c_p = \frac{de_p}{dT_p} = \sum_j \int \hbar\omega_{p,j} D_{p,j}(\omega_{p,j}) \frac{df_{p,j}}{dT_{p,j}} d\omega_{p,j}$$

$$\left(\frac{df_p}{dT_p} = \frac{\hbar\omega_p}{k_B T_p^2} \frac{\exp(\hbar\omega_p/k_B T_p)}{\exp[(\hbar\omega_p/k_B T_p) - 1]^2} \text{ from the Bose-Einstein function} \right), \quad (1.3)$$

where j is a phonon mode. Including the phonon interaction kinetics, the phonon conductivity (k_p) and other transport properties (e.g., boundary resistance) are predicted.

For the gaseous fluid particles, because of the weak intermolecular force compared to intramolecular force, each molecule is generally considered as isolated system differing from the solid system, so the gaseous fluid particle energy is discrete rather than having dispersed band structures. Energy modes and levels are identified based on atomic interaction and configuration, and using the gas kinetic theory and the Maxwell-Boltzmann distribution. Then many macroscale properties can be derived [25, 82].

1.3.2 Interaction kinetics

During energy conversion and transport processes, principal energy carriers experience a variety of interactions, and Figs.1.6 and 1.7 show some phonon and electron interactions. Phonon are emitted when high-energy states of other principal particles are relaxed, or are absorbed to excite them to higher energy states. Phonons interact with other phonons by for example the three-phonon interactions [69], thus up- or

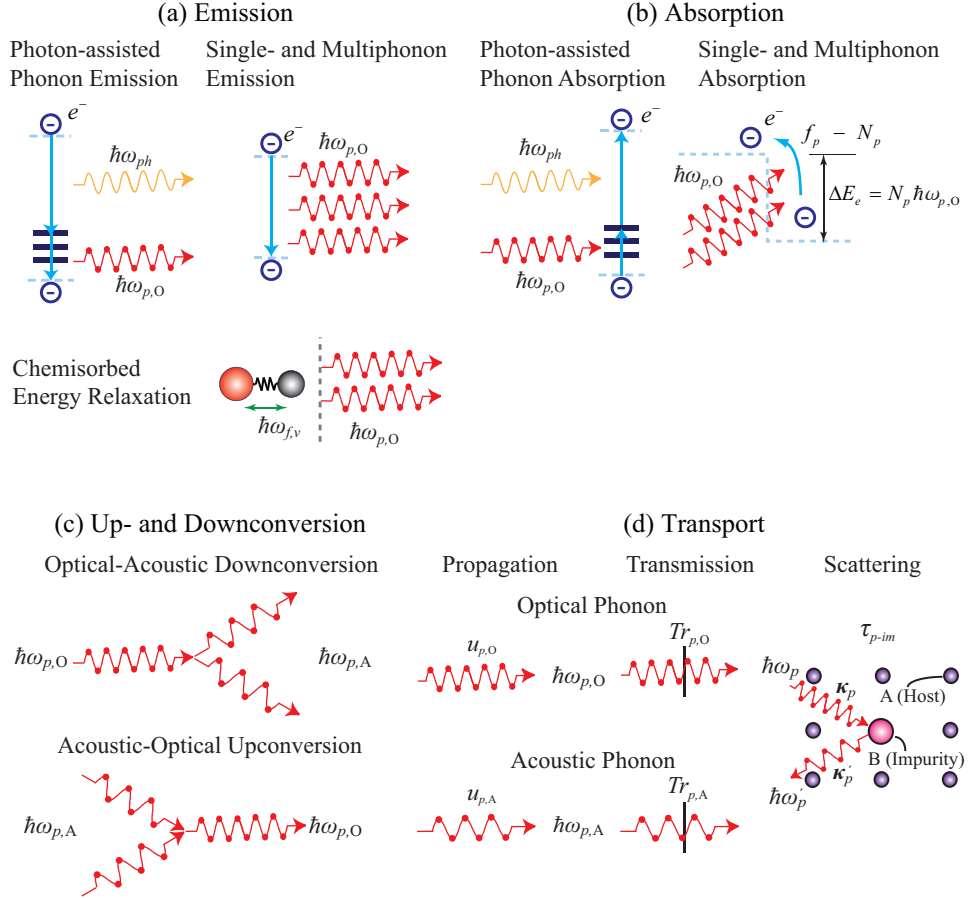


Figure 1.6: Phonon interactions during energy conversion and transport processes. (a) Phonons are emitted when high energy states in other principal particles are relaxed, and (b) they are absorbed to excite other energy states. (c) Through the three-phonon interactions [69], phonon modes can be up- and downconverted. (d) Phonons are propagated with their speed depending on mode and wavevector, and scattered by boundaries and impurities.

downconverting the phonon modes, and they can also be scattered by the boundaries and impurities. Similar to phonons, electrons also interact with other principal carriers as well as with the boundaries and impurities.

The interaction kinetics are characterized by the interaction time constant τ (s) or rate $\dot{\gamma}$ (s^{-1}), and all the interaction rates are calculated based on the Fermi golden rule (FGR) derived from the time-dependent Schrödinger equation using the perturbation theory. Interaction rate (the inverse of the scattering time) is obtained using the

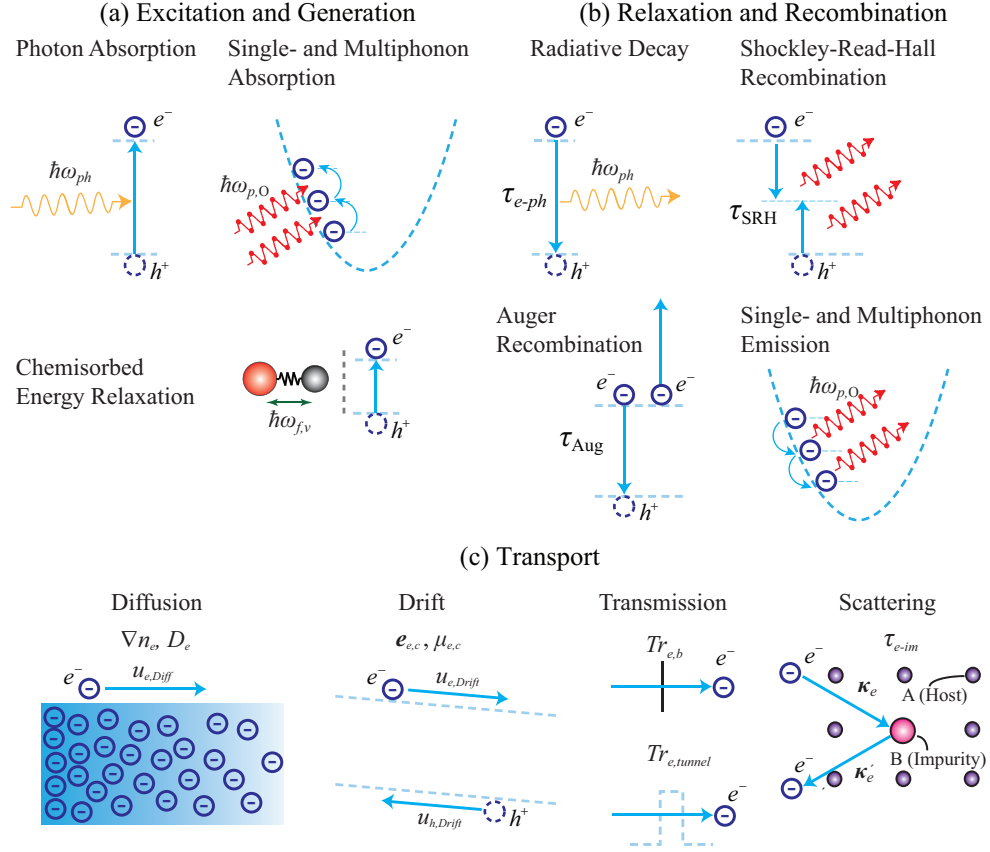


Figure 1.7: Electron energy conversion and transport. (a) Electron state can be excited by photon and phonon absorption, and chemisorbed particle relaxation. (b) During their relaxation and recombination, electrons can emit phonons or photons, or excite other electrons. (c) Electron density distribution and electric field cause electron transport, and the electrons can be also scattered by boundaries and impurities as phonons.

Fermi golden rule [119, 82]

$$\hat{\gamma}_{i,f} = \frac{1}{\tau} = \frac{2\pi}{\hbar} |\langle f | H_{int} | i \rangle|^2 \delta_D(E_f - E_i), \quad (1.4)$$

where $|i\rangle$ and $|f\rangle$ are initial and final wave functions, E_i and E_f are the initial and final energies of the carrier, δ_D is the Dirac delta function and H_{int} is the interaction Hamiltonian. Depending on the interaction, the interaction matrix element $|\langle f | H_{int} | i \rangle|$ varies and can be expanded using the higher order perturbation theory (e.g., the

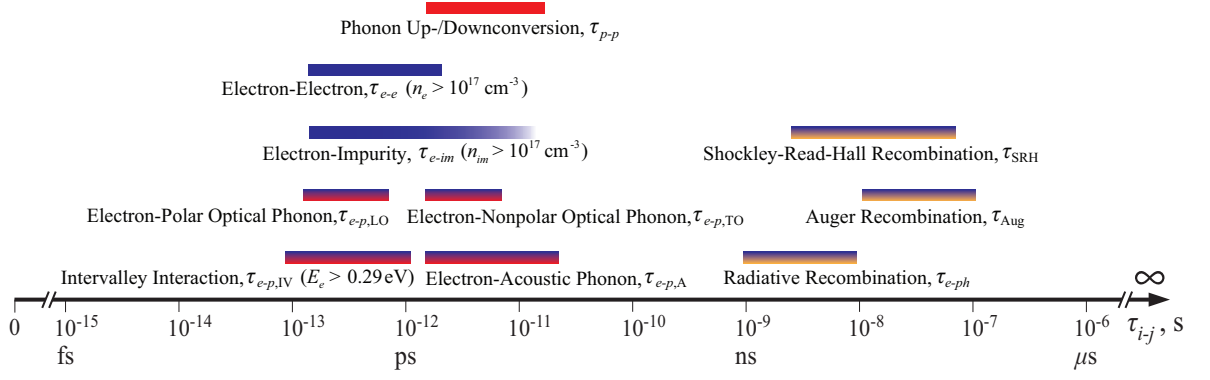


Figure 1.8: Various interaction times in GaAs system.

second-order perturbation theory for the photon-electron-phonon interaction [86]).

Energy carriers can experience various interaction mechanisms, and the interaction rate for each mechanism ($1/\tau_j$) can be separately calculated. The Matthiessen rule is utilized to evaluate the overall interaction rate $\dot{\gamma}$ (or interaction time, τ) as,

$$\dot{\gamma} = \frac{1}{\tau} = \sum_j \frac{1}{\tau_j}, \quad (1.5)$$

where τ_j is an interaction time by mechanism j .

Figure 1.8 shows various interaction times in the GaAs system from experiments and predictions [108, 34, 167] as example, and the energy conversion and transport properties are dependent of these interaction rates. The interaction rates between electrons and phonons are further discussed in Chapter 2, addressing the electron transport and the phonon energy conversion.

1.4 Atomistic computer simulations

In this thesis, the focus is on the fundamentals of the thermal energy transport and conversion. Various simulation techniques are used to calculate the atomic-level properties addressed in the previous section (Section 1.3) and to evaluate the macroscale energy conversion and transport properties (derived from atomic-level properties) and the system performance in some applications. We cover these multiscale (in time and space), diverse simulations using *ab initio*, molecular dynamics and mesoscale simulations such as the ensemble Monte Carlo.

1.4.1 *Ab initio* calculations

Ab initio calculations are based on the first principles of quantum mechanics, through calculations of the electronic structure (generally in ground state). Using this approach, many atomic properties of electrons and phonons (e.g., the electron and phonon band structures and interaction rates between energy carriers) are predicted. For the *ab initio* calculations, the density functional theory (DFT) is one of the most widely used methods [5, 164], and various computer codes based on the DFT {e.g, VASP (Vienna Ab-initio Simulation Package) [94], SIESTA (Spanish Initiative for Electronic Simulations with Thousands of Atoms) [21], WIEN2k [154], ABINIT [58], Quantum Espresso [56]} are available.

The DFT allows for calculating the optimized electronic structures, the relaxed atomic structures, the electronic energy (E_e) in the wavevector (κ_e) space, i.e., the electron band structure, and various other properties. In spite of the limited accuracy

of the DFT in the band structure prediction (because the ground-state wave functions are not sufficient in evaluating the conduction band, especially for the large band gap materials), many compensation techniques have been suggested and widely used [4, 65]. The phonon properties such as phonon band structure are determined by the force field, and this can be calculated with the DFT code with the frozen phonons or the linear response methods [55]. The DFT (or DFPT, density functional perturbation theory) are also employed for the dielectric properties for the polar optical phonon interaction and electron-phonon coupling coefficient for nonpolar phonon interaction [9].

In this research, the electron and phonon band structure, the Hamiltonian and dynamical matrices for the nonequilibrium Green function formalism, and the interatomic potentials used in the molecular dynamics simulations are calculated using the *ab initio* simulations with the commercial DFT codes (e.g., VASP and SIESTA).

1.4.2 Molecular dynamics simulations

Computational molecular dynamics (MD) directly simulates the physical movement of multi-atom systems based on the Newton equations [$\mathbf{F} = -\nabla\varphi = m(d\mathbf{u}/dr)$, \mathbf{F} : force, φ : potential, \mathbf{u} : velocity, r : position] [49], and is a powerful tool for obtaining the phonon (or fluid particle) properties, such as the phonon thermal conductivity (k_p), phonon transmission across interfaces, the phonon density of states, and the phonon-phonon interaction rates (up- and downconversion). In the classical MD, the forces on the ions are calculated using interatomic potential models to update the sys-

tem configuration. Therefore, reliable interatomic potentials are essential, and they are generally developed from the empirical properties and the *ab initio* calculation [75, 162].

As the computing power increases, the *ab initio* molecular dynamics (AIMD) simulations, which are more computationally expensive than the classical MD, have become available [113]. In AIMD, the forces on the ions at each configuration are calculated by the *ab initio* calculations (not by the empirical potential models) to update the ionic positions and velocities (with the Verlet algorithm), and through the iteration of this process, the system trajectory is calculated. The system size in AIMD is limited because of computational cost, but it can reduce the numerical errors from the approximated interatomic potentials (it does not need the empirical interatomic potentials). Using AIMD, not only the phonon properties, but also the electronic properties with the thermal perturbations (temperature dependence) can be examined [84].

The phonon thermal conductivity (k_p) is calculated with both the equilibrium and the nonequilibrium MD simulations (EMD and NEMD). In the equilibrium MD (using constant, uniform temperature setting), k_p is found from the heat flux vector (\mathbf{q}) autocorrelation (representing heat flow fluctuation) decay given by the Green-Kubo (G-K) relation

$$k_p = \frac{V}{k_B T_p^2} \int_0^\infty \langle \mathbf{q}(t) \mathbf{q}(0) \rangle dt,$$

$$(\text{heat flux vector, } \mathbf{q} = \frac{1}{V} \frac{d}{dt} \sum_i E_i \mathbf{r}_i + \frac{\mathbf{r}_{ij}}{2V} \sum_{i,j} \mathbf{F}_{ij} \cdot \mathbf{u}_i), \quad (1.6)$$

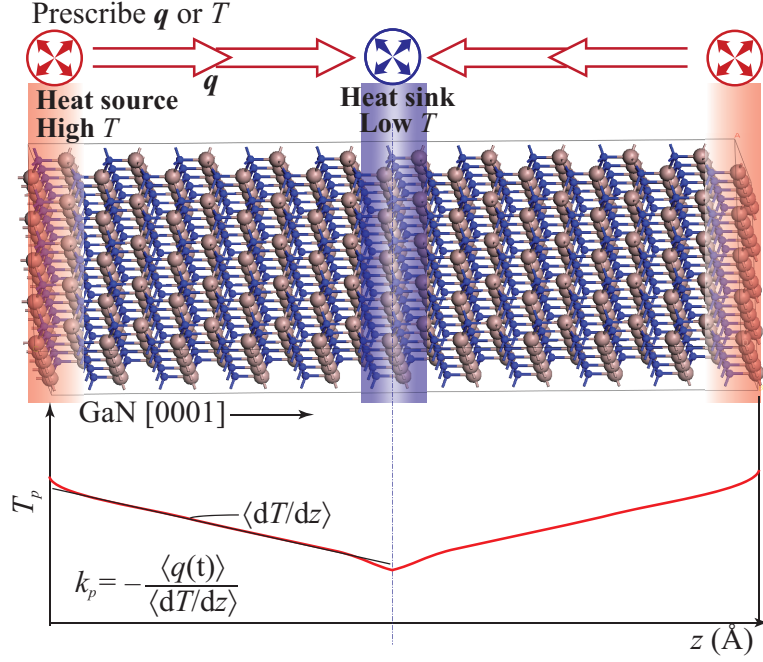


Figure 1.9: Schematics of NEMD simulation for phonon conductivity k_p with gallium nitride GaN structure. Thermal conductivity k_p is obtained by the ensemble average calculation of heat current (with a given ΔT) or temperature profile (with a given q).

where $\langle \rangle$ is for ensemble average, and $\langle q(t)q(0) \rangle$ is known as the heat current autocorrelation function (HCACF) [82]. On the other hand, the NEMD directly prescribes the temperature difference (ΔT) or heat flux (q), and k_p is obtained by the ensemble average calculation of heat current (with a given ΔT) or temperature profile (with a given q) as shown in Fig. 1.9 ($k_p = -\langle q \rangle / \langle dT/dz \rangle$) [162]. Using AIMD, NEMD can be used for the thermal transport, since the *ab initio* codes generally calculate the energy of optimized electronic system not providing potential energy for each ion (problematic in the G-K) [9, 117]. Using the temperature and heat flow across junctions or interfaces in NEMD, the thermal boundary resistance can be calculated. The MD simulations can directly treat the phonon wave, generating phonon wavepackets [151, 178], and the phonon spectral transmission across the boundaries and the

phonon relaxation times can be calculated by tracking the amplitude of the phonon wave. Also, the velocity autocorrelation of the simulated particles is used for the phonon density of states (also discussed in Chapter 4)[162].

NEMD is mainly used for the phonon transport at the interfaces and junctions, which are addressed in Chapter 4 and Appendix B.

1.4.3 Mesoscale simulations: Monte Carlo method

Nonequilibrium behaviors for principal energy carriers [energy distribution in terms of the position (\mathbf{x}_i) and momentum(\mathbf{p}_i)] can be found from the Boltzmann transport equation (BTE) based on the classical Hamiltonian statistical mechanics [19, 103]. The Boltzmann transport equation is expressed as [82]

$$\frac{\partial f_i}{\partial t} + \mathbf{u}_i \cdot \nabla_x f_i + \mathbf{F}_i \cdot \nabla_p f_i = \frac{\partial f_i}{\partial t}|_s + \dot{s}_{f,i}, \quad (1.7)$$

where f_i is the i particle probability, ∇_x and ∇_p are the spatial and momentum gradients, $(\partial f_i/\partial t)|_s$ is the time rate of change of f due to scattering, and $\dot{s}_{f,i}$ is the i carrier source rate. Here, i can be p (phonon), e (electron), f (fluid particle), and ph (photon), and through this equation, transport or conversion of these principal carriers can be addressed.

The BTE is generally solved numerically, and the Monte Carlo (MC) is one of the more widely used and accurate methods for solving the BTE. The Monte Carlo method is a computational algorithm using random sampling to obtain the simulation results, and for the BTE the MC simulates sampled principal particles (i.e.,

updating the states of sampled particles), using the classical equations of motion and randomly selected scattering time and mechanism. The microscale properties (e.g., carrier distribution, effective mass, and interaction rates) for the MC simulation are obtained from the *ab initio* and the MD calculations or experiments. Although the MC simulates with a stochastic process, since the uniformly distributed random numbers decide the scattering sequences using the scattering probabilities based on the physics, it can correctly generate the solution to the BTE [195]. MC only simulates sampled particles instead of all the particles in a simulated system, so larger systems with longer time scale compared to the *ab initio* calculations and MD simulations can be considered.

The MC method is employed in this work to simulate the electron transport and the phonon-electron interactions and energy conversion in Chapter 2, and the detailed algorithm and MC simulations for other principal carriers are explained in Appendix A.

1.5 Statements of objective and scope of thesis

The major objective of this work is to develop fundamental understandings and to find innovative applications of the nonequilibrium systems for thermal energy transport and conversion. Various energy conversion applications and transport systems are examined through theoretical study with various atomistic treatments. The thesis is organized as follows.

Chapter 2 proposes a novel heterobarrier structure for converting hot phonons to

electric potential. The interaction kinetics of the phonons and electrons in semiconductor (GaAs) are examined for the favorable conditions of unassisted absorption of hot phonons. The self-consistent ensemble Monte Carlo simulations based on these kinetics are employed to access the electron transport and energy conversion. Through the simulations, the optimal barrier structure is designed, and the operational conditions of the structure are suggested. The significance and impact of this structure is also addressed.

In Chapter 3, the entropy of the phonon-electron energy conversion systems is examined, and an upper limit for the theoretical conversion efficiency of the above-mentioned heterobarrier is found and compared with the Monte Carlo results.

In Chapter 4, the thermal transport at interfaces between hard and soft solids is studied, and the fundamental roles of the interfacial-region atomic restructuring in the interfacial thermal transport are examined. The Si/In boundary is considered as example, and the nonequilibrium classical molecular dynamics simulation are mainly employed. The *ab initio* calculations are performed for the interatomic potential development, and the simulation results are analyzed with the semi-classical diffuse mismatch model. Decomposition of the interfacial phonon resistance is suggested, and the roles of the interfacial atomic restructuring in the interfacial transport are clarified based on this decomposition method.

In Chapter 5, thermal transport between edge-passivated graphene flakes is investigated considering both the electron and phonon contributions. The thermal conductance is estimated by the Landauer formula with the quantum junction transmission. The nonequilibrium Green function (NEGF) formalism is introduced for

the electron and phonon transmission and the results are compared with the semi-classical acoustic mismatch model. The Hessian and Hamiltonian matrices for NEGF calculation are obtained using the density functional theory (DFT) simulations. The phonon wave features and the effects of passivation are examined, and the effective thermal conductivity of the graphene composites is predicted.

In Chapter 6, the nonequilibrium vibrational energy occupancy in the molecular-gas kinetic energy is studied for the molecular-gas laser cooling application. The anti-Stokes molecular-gas cooling is analyzed using the nonequilibrium interaction kinetics between CO₂ molecules and photons. In order to enhance the laser cooling, the effect of the irradiated photon frequency is examined, and the macroscopic conditions (e.g., temperature, pressure, and Xe diluent atomic fraction), controlling the diffusion and kinetics of the excited vibration levels, are optimized for large excited-level population. Comparison is made with the experimental results and good agreement is found.

Chapter 7 summarizes the important results of this work, and proposes future directions for the related research.

Appendix A gives further details of the Monte Carlo method, and in appendix B the molecular junction thermal conductance is discussed with the phonon transport treated by the classical molecular dynamics.

Chapter 2

Heterobarrier for Hot-Phonon

Absorption by Conduction

Electron

2.1 Heterobarrier for hot-phonon energy conversion

Hot phonons are finally thermalized, converting their energy to waste heat and generating entropy. To improve the energy conversion efficiency and mitigate the heat generation in devices, the thermalized phonons can be recycled by the anti-Stokes

cooling (photo-assisted absorption of phonon), resulting in lower device operating temperatures [145, 87]. Furthermore, unassisted-phonon absorption is more desirable, and utilizing the hot phonons before thermalization is expected to further improve the efficiency because of their lower entropy. Also, this removal of the excess phonon and its harvesting as electric energy will improve the thermal management and device performance (reducing the phonon friction in electron transport) [114].

In this chapter, heterobarrier for converting hot-phonon energy to electric potential by unassisted absorption of the hot phonons is proposed. The barrier structures have been used in thermionics, thermoelectrics and photovoltaics [157, 158, 89, 137], and for selective transmission of the hot electrons (for thermoelectric performance enhancement) and heat absorption to restore the equilibrium electron distribution.

Here, the heterobarrier structure is designed as an embedded structure rather than a stand-alone device, so that we can place the structure near the hot-phonon source for effective pre-thermalization harvesting. This requires kinetics optimization among the phonon absorption and emission (lifetime τ_{p-e}) and up- and downconversion (τ_{p-p}). The Monte Carlo (MC) method is employed to simulate this electron transport and phonon energy conversion in the diffusive regime, showing electric potential gain and phonon energy absorption.

2.1.1 GaAs/Al_xGa_{1-x}As barrier system

A heterobarrier structure composed of GaAs and Al_xGa_{1-x}As (x or x_{Al} is the Al content) is chosen for this study. Since Al_xGa_{1-x}As has a larger bandgap than

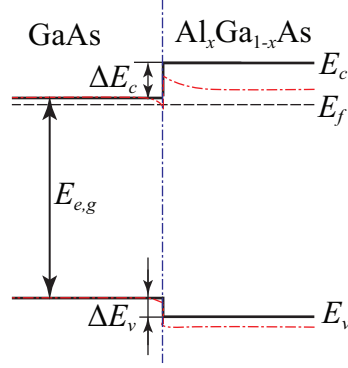


Figure 2.1: Ideal band discontinuity of GaAs/ $\text{Al}_x\text{Ga}_{1-x}\text{As}$. Because of the bandgap difference, the interface has a band edge discontinuity in the conduction ΔE_c and valence bands ΔE_v depending on x_{Al} . Because of the charge redistribution, the bands will be bent as the red dash-dot lines.

GaAs, the interface has a band edge discontinuity in the conduction ($\Delta E_c = 0.79x_{\text{Al}}$, $x_{\text{Al}} < 0.41$) and valence bands ($\Delta E_v = -0.46x_{\text{Al}}$) depending on x_{Al} (type I) as shown in Fig. 2.1 [201, 104]. Here, electrons are considered as the main charge carriers and the band discontinuity in the conduction band is regarded as a potential barrier for electrons in the conduction band, so the barrier height φ_b can be controlled with x_{Al} . Without an external current, electrons are redistributed until the Fermi level is consistent, and this redistribution leads to band bending, shown in Fig. 2.1. No initial prescribed band bending is considered in MC simulations, and the charge redistribution or the bending in the simulations is not significant because of the low electron density and the effective barrier transmission by phonon absorption.

2.1.2 Hot-phonon absorption barrier (HPAB) structure

The potential barriers can cause an adverse (or reverse) current by reflection or potential change, so large, forward local electric field formed by x_{Al} grading is introduced in the barrier to compensate this adverse effect [158]. Figure 2.2 shows the

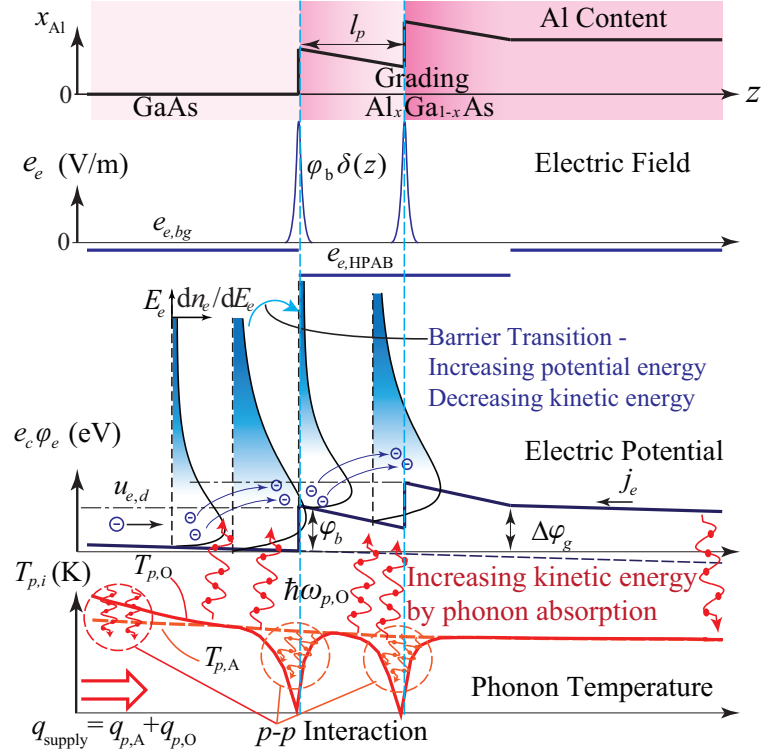


Figure 2.2: Spatial distributions of Al content, electric field and potential, and phonon temperatures in the hot-phonon absorbing barrier structure. x_{Al} abruptly increases, creating the potential barrier (with height φ_b) in the conduction band edge, while the grading maintains the current. Phonon absorption populates electrons with higher energy than barrier height ($E_e > \varphi_b$) before or after the barrier transition, and this energy is converted to electric potential. The population of optical phonons quickly decreases at the barriers and recovers by upconversion.

spatial distributions of (i) x_{Al} , (ii) electric field, e_e , (iii) product of electric potential and electron charge, $e_c \varphi_e$ (in conduction band edge), and (iv) optical and acoustic phonon temperatures, $T_{p,O}$ and $T_{p,A}$, in the hot-phonon absorbing barrier (HPAB) structure. The electric current density j_e , drift velocity $u_{e,d}$, and electron transition processes involving phonon absorption are also shown.

2.2 Interaction kinetics in HPAB

2.2.1 Electron-phonon interaction rate

Interaction rates for the kinetics are calculated using the Fermi golden rule (FGR) [82]. Because the single optical phonon interaction with an electron is based on a perturbation by the displacement d , the Hamiltonian with the electron-phonon (e - p) interaction including the first-order perturbation is expressed as

$$H = H_o + H_{e-p} = (H_{e,o} + H_{p,o}) + \varphi'_{e-p}d, \quad (2.1)$$

where H_o is the unperturbed Hamiltonian ($H_{e,o} + H_{p,o}$), and H_{e-p} is the interaction Hamiltonian (with the first order e - p coupling φ'_{e-p} , $H_{e-p} = \varphi'_{e-p}d$). Since the displacement $d = [\hbar/(2m\omega_{p,o})]^{1/2}(b^\dagger + b)$, where m is the reduced mass of oscillating atoms, $\omega_{p,o}$ is the phonon frequency, and b^\dagger (b) is the creation (annihilation) operator of phonon, the interaction rate from the FGR is expressed as

$$\dot{\gamma}_{e-p} = \frac{\pi}{m\omega_{p,o}} |\langle \psi_{e,f} | \varphi'_{e-p} | \psi_{e,i} \rangle|^2 |\langle f_p \pm 1 | b^\dagger + b | f_p \rangle|^2 \delta_D(E_{e,f} - E_{e,i} \mp E_{p,o}), \quad (2.2)$$

where ψ_e is the electron wave function, f_p is the phonon occupancy, δ_D is the Dirac delta function, and the subscripts i and f represent the initial and final states. The interaction matrix element $|\langle \psi_{e,f} | \varphi'_{e-p} | \psi_{e,i} \rangle|^2$ for the nonpolar optical phonon is $\phi'^2_{e-p} \delta_{D,\kappa}$, where ϕ'_{e-p} is the deformation potential and $\delta_{D,\kappa}$ is for the momentum conservation ($\kappa_{e,f} = \kappa_{e,i} + \kappa_p$, where κ_e and κ_p are the electron and phonon momentum). For the

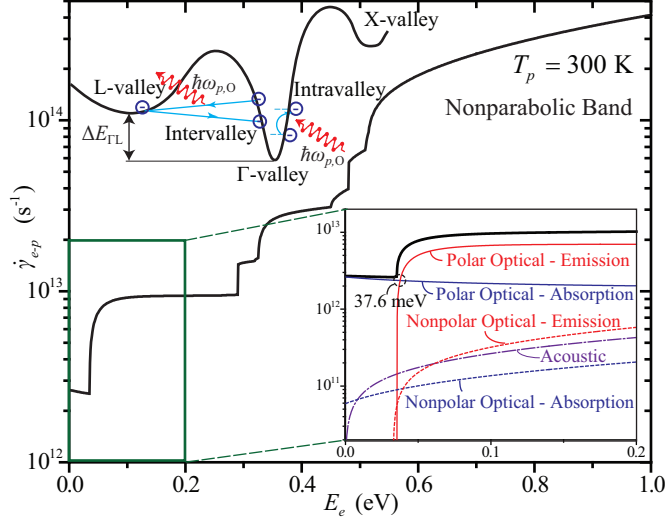


Figure 2.3: Variations of the electron interaction rates in the lowest conduction band, as a function of electron energy (E_e) for $T_p = 300$ K. Insets show the band structure and various interaction mechanisms (left) and the interaction rates for low- E_e Γ -valley electrons (right). Polar optical phonon scattering is dominant at low E_e , and intervalley scattering rates increase with E_e .

anisotropic polar optical phonon interaction which absorbs or emits the longitudinal optical (LO) phonon, the element becomes $(\rho e_c^2 \omega_p^2 / \kappa_p^2)(1/\epsilon_{e,\infty} - 1/\epsilon_{e,s})\delta_{D,\kappa}$, where $\epsilon_{e,s}$ and $\epsilon_{e,\infty}$ are the static and optical dielectric constants, e_c is the electron charge, and ρ is the density [108].

Since $|\langle f_p \pm 1 | b^\dagger + b | f_p \rangle|^2 = f_p + 0.5 \pm 0.5$, the phonon absorption and emission rates ($\dot{\gamma}_{p \rightarrow e}$ and $\dot{\gamma}_{e \rightarrow p}$) are proportional to f_p and $f_p + 1$, respectively. From δ_D for the energy conservation, the phonon emission occurs only when the initial electron energy is larger than the emitted phonon energy ($E_{e,i} > E_{p,O}$), but the emission rate $\dot{\gamma}_{e \rightarrow p}$ increases with E_e faster than the absorption rate $\dot{\gamma}_{p \rightarrow e}$. With higher φ_b , in order to pass through barriers, electrons require a larger momentum or E_e , or the less energetic electrons need to increase their energy through phonon absorption. However, high-energy carriers are emission-favorable and less populated, and multiphonon ab-

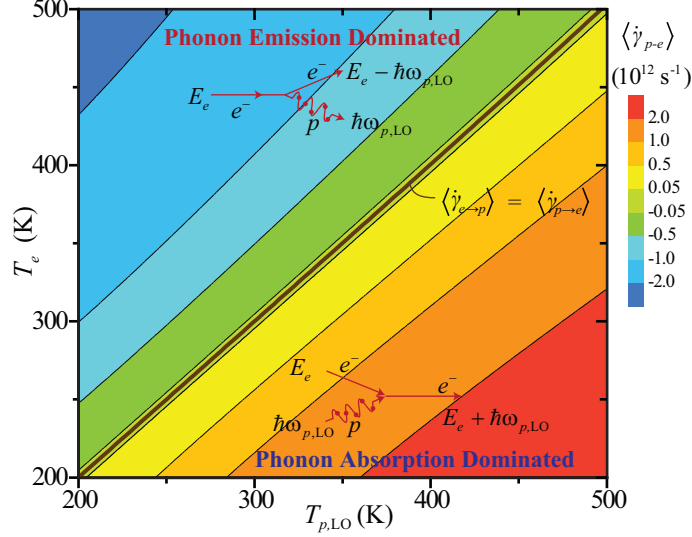


Figure 2.4: Average polar optical phonon absorption (+)/emission (-) rates as functions of T_e and $T_{p,LO}$. The phonon absorption or emission rate becomes faster as nonequilibrium between electron and phonon increases.

sorption for low-energy electron transition is not probable [44]. Thus, tandem-barrier structures with $\varphi_b \leq E_{p,LO} (\simeq 35 \text{ meV})$ (only absorption available) rather than a single barrier with large height are employed for large potential gain.

The lowest conduction band in GaAs has three valleys, at Γ , L and X, where Γ is heavily populated at room temperature. Electrons in the band are scattered through various mechanisms, and the overall interaction rates are shown in Fig. 2.3. The Γ -valley polar optical phonon interaction, which absorbs or emits longitudinal optical (LO) phonon, dominates for low E_e , and intervalley scattering is dominant when $E_e > \Delta E_{TL}$ (energy difference between Γ - and L-valleys). Average absorption $\langle \dot{\gamma}_{p \rightarrow e} \rangle$ and emission $\langle \dot{\gamma}_{e \rightarrow p} \rangle$ rates for Γ -valley is obtained considering LO phonon temperature $T_{p,LO} (= E_{p,LO} / \{k_B [\ln(f_{p,LO} + 1) - \ln(f_{p,LO})]\})$ and electron distribution dn_e/dE_e ($D_e f_e^o$, where D_e is the density of states and f_e^o is the equilibrium electron distribution), and favorable absorption/emission is also shown in Fig. 2.4.

2.2.2 Phonon-phonon interaction rate

The rate of the three-phonon (p - p) interactions (up- and downconversion), competing with the e - p interactions, are [170]

$$\begin{aligned} \dot{\gamma}_{p-p,\text{down/up}} &= \frac{\hbar}{8\pi\rho^3} \frac{|M_{p-p}|^2 R}{u_{p,A}^7 u_{p,O}^2} \omega_{p,A}^2 \omega_{p,O}^3 \\ &\times [f_p(\omega_{p,A}) + 0.5 \pm 0.5]^2 [f_p(\omega_{p,O}) + 0.5 \mp 0.5], \end{aligned} \quad (2.3)$$

where $u_{p,A}$, $u_{p,O}$, $\omega_{p,A}$ and $\omega_{p,O}$ are the acoustic and optical phonon speeds and frequencies, $|M_{p-p}|^2$ is $4\rho^2\gamma_G^2 u_{p,A}^2 u_{p,O}^2$, ρ is the density, γ_G is the Grüneisen parameter, and R is obtained from the force constants estimated by material metrics in [74]. (With $\rho_{\text{GaAs}} = 5317 \text{ kg/m}^3$, $u_{p,A} = 2800 \text{ m/s}$, $\gamma_G = 0.8$ and $R = 0.128$, $\dot{\gamma}_{p-p}$ is 4.3 ps at 300 K, which agrees well with experiments [24, 169].) Since the e - p interaction rate is faster than the p - p , the electron is first excited and relaxed to equilibrium during the hot-phonon relaxation, and thus within a ps, it has large population at high E_e (desirable for barrier transition). (This will be also discussed in Section 3.3.1.) Thus, considering this downconversion of optical phonons along with their low mobility, the HPAB placed near the phonon source is suited for harvesting hot phonons.

2.3 Monte-Carlo simulation

Self-consistent ensemble Monte Carlo (MC) simulates the electron transport and phonon absorption/emission in HPAB with large ensemble of sampled electrons coupling to the Poisson equation to reflect the internal charge redistribution [64, 79, 121].

2.3.1 Electron scattering and transport in simulation

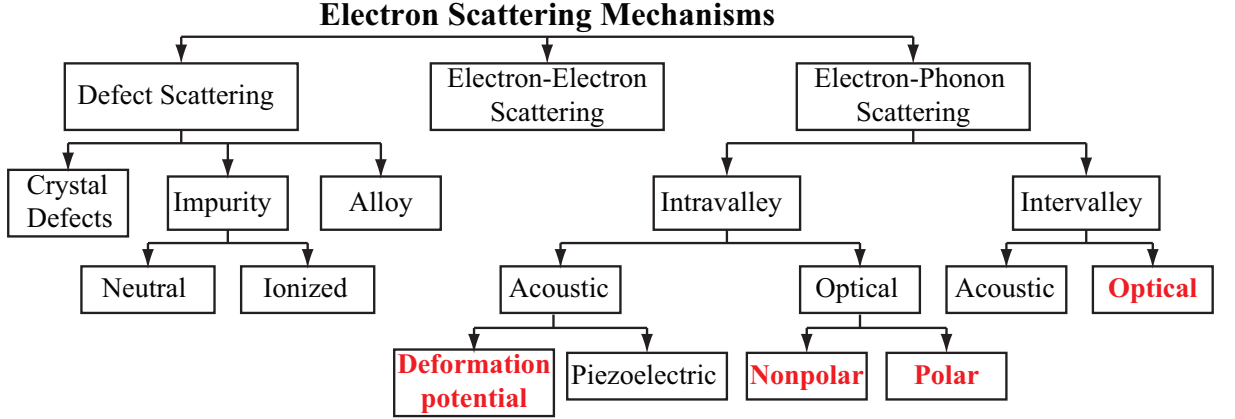


Figure 2.5: Various electron scattering mechanisms. The mechanisms in bold red are included in the Monte-Carlo simulation for this study.

The MC code simulates a large ensemble of electrons in the HPAB with the randomly selected electron scattering events and electron drift. Electrons can be scattered by various mechanisms as shown in Fig. 2.5, and the probability of the random selection in MC is based on those scattering rates. In this study, a few selected scattering mechanisms, such as acoustic, inter- and intravalley optical phonon scatterings in the lowest conduction band, are considered (bold red in Fig. 2.5) and other mechanisms are ignored because of their minor scattering rates. (e.g., The electron density (n_e) is small ($< 10^{17} \text{ cm}^{-3}$) enough to exclude the electron-electron scattering.)

The simulation employs GaAs properties (effective mass $m_{e,e}$, dielectric constants $\epsilon_{e,\infty}$ and $\epsilon_{e,s}$, deformation potential ϕ'_{e-p} , etc.) [34, 108], as the small φ_b requires a small change of x_{Al} and physical properties ($\sim 4\%$ change of x_{Al} per barrier). As Fig. 2.6 shows, the predicted electron drift velocity $u_{e,d}$ and mobility $\mu_e (= u_{e,d}/e_e)$ agrees well with experiments for bulk GaAs ($\mu_{e,\text{GaAs}} = 0.85 \text{ m}^2/\text{V}\cdot\text{s}$ for low e_e and decreases

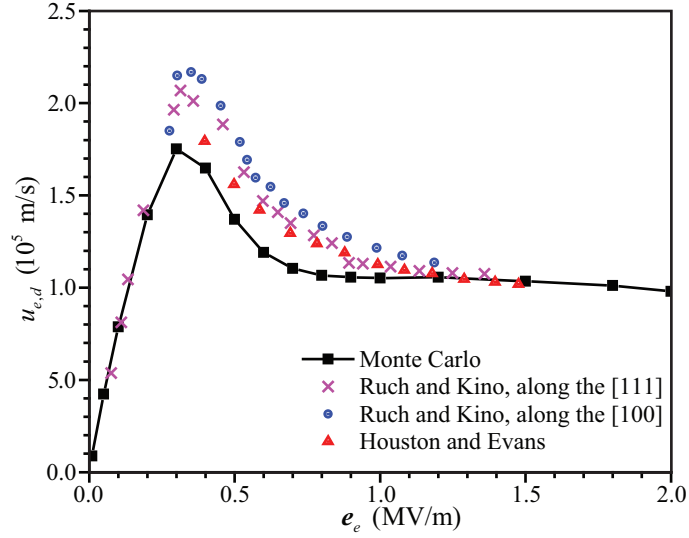


Figure 2.6: Variation of the electron drift velocity ($u_{e,d}$) with respect to electric field (e_e). The drift velocity from the MC simulations (black squares) are in good agreement with experiments (crosses and circles from Ref. [147] and triangles from Ref. [72]). Since the electron mobility μ_e is given as $u_{e,d}/e_e$, μ_e also agrees well with experiments.

with e_e) for all electric fields [147], verifying the algorithm.

Sampled electrons travel with the prescribed electric potential along z as in Fig. 2.2 (the particle distribution in the lateral directions is not considered). Initially 200,000 electrons over $1 \mu\text{m}$ region are sampled, and various numbers of barriers N_b are placed with barrier pitch l_p in the center. Particles are initially in Γ -valley according to the equilibrium distribution with T_e . An appropriate background electric field $e_{e,bg}$ is applied to create a reference current density $j_{e,o}$ (or drift velocity $u_{e,d,o}$) without barrier, and a higher local electric field $e_{e,HPAB}$ (from the x_{Al} grading) is applied to the barrier region. The z -direction boundaries are assumed to have constant charge distribution, and electrons are supplied to compensate for those exiting.

2.3.2 Simulation of phonon population and transport

To maintain the phonon population (depends on T_p through the Bose-Einstein distribution), the phonon flux sufficient for the absorption over the simulation region is prescribed at the left boundary. The phonon transport and distribution are also simulated along with the electrons through the phonon conductivity (k_p), e - p interaction rates (for phonon absorption and emission, $\dot{\gamma}_{p \rightarrow e}$ and $\dot{\gamma}_{e \rightarrow p}$), and p - p up- and downconversion rates ($\dot{\gamma}_{p \rightarrow p, \text{up}}$ and $\dot{\gamma}_{p \rightarrow p, \text{down}}$) [197]. Because the hot phonon effect is prominent only in the LO phonon mode [88], the conservation of the LO phonon (dominant in phonon absorption) and all other phonon modes (A) are separately tracked in each bin. Over the spatial increment ($\Delta z = 5$ nm), the phonon energy change (per area) in the j -th bin (z_j) over a time step ($\Delta t, t \sim t + \Delta t$) is

$$\Delta E_{p,i}(z_j) = \Delta t \{ -(q_{p,i,L} + q_{p,i,R}) + [\dot{s}_{e-p,i}(z_j) \pm \dot{s}_{p-p,\text{up}}(z_j)] \Delta z \}, \quad (2.4)$$

where i is a phonon mode (LO or A, + for LO and - for A), and $q_{p,i,R}$ (or $q_{p,i,L}$) is the phonon flux from the neighboring bins, determined by $T_{p,i}$ and $k_{p,i}$ ($k_{p,A} = 54$ W/K-m and $k_{p,LO} = 1$ W/K-m, approximated from [109]) as

$$q_{p,i,R \text{ or } L} = \frac{k_{p,i}}{\Delta z} [T_{p,i}(z_j) - T_{p,i}(z_j \pm \Delta z)]. \quad (2.5)$$

$q_{p,i,L}$ at the left boundary is prescribed (q_{supply} is set to total phonon absorption), and $q_{p,i,R}$ on the right is calculated using an external thermal resistance (equivalent to 20 μm of GaAs) and the surrounding temperature (T_o). $\dot{s}_{e-p,i}$ and $\dot{s}_{p-p,\text{up}}$ depend

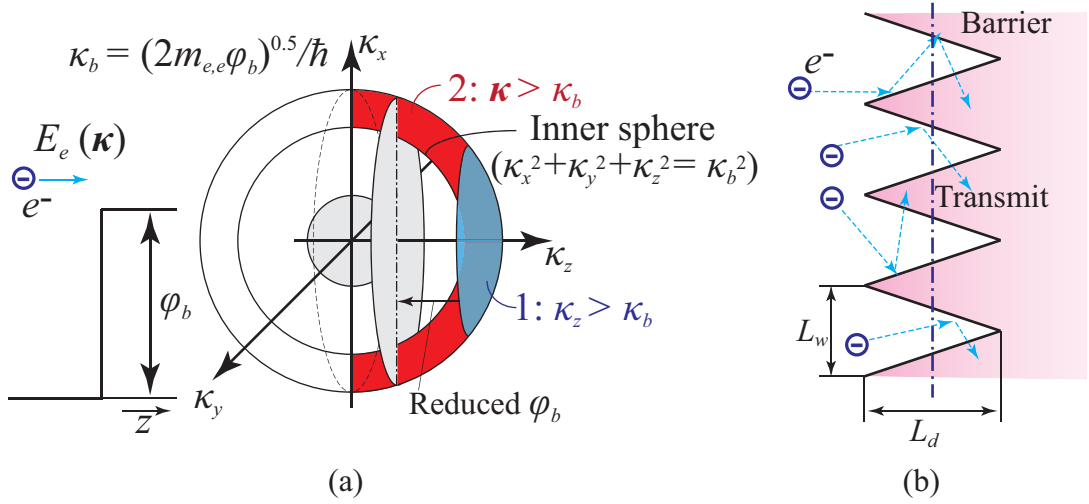


Figure 2.7: (a) Wavevector (κ) space for barrier (φ_b) transition [182]. Region 1 describes the range of momentum vector for electron barrier transition, when the lateral momentum (in x and y direction) is conserved, and region 2 shows the nonconserving lateral momentum scheme. When the lateral momentum is conserved, lower transition efficiency (smaller volume) is expected. (b) The sawtooth interface model and the electron trajectory near the barrier [11]. The electrons can be directed normal to interface through multiple reflections, then more electrons can be transmitted.

on the electron distribution and the phonon temperatures, and are found from MC simulations and Eq. (2.3). The spatial distributions of $T_{p,A}$ and $T_{p,LO}$ are updated, using $\Delta E_{p,i}$, the heat capacity ($c_{p,i}$) [179], and the LO phonon energy ($E_{p,LO} \simeq 35$ meV).

2.3.3 Simulation of barrier transition

During the barrier transition in this MC simulation, electrons lose (forward) or gain (backward) a momentum corresponding to φ_b with the nonconserving lateral momentum [89, 182], and tunneling is not considered. With the lateral momentum conservation, smaller barrier transition efficiency is expected because more electrons can participate in the barrier transition as Fig. 2.7(a) describes. Although the epi-

taxial planar GaAs/AlGaAs heterostructures have shown that lateral momentum is mostly conserved, introducing a surface roughness is expected to break the conservation and enhance the barrier transition [182, 11]. For a sawtooth roughness interface shown in Fig. 2.7(b), more electrons (including those having energy larger than φ_b but not having sufficient energy in the z direction) can contribute to the transport due to larger effective interface area and multiple reflections. Small period (L_w) and large depth (L_d) are desirable for the transport [11], but the period is limited by the quantum mechanical wavelength (the de Broglie wavelength, $\lambda_{dB} = h_P/|\mathbf{p}_{e,\kappa}|$) of electron (~ 25 nm when the energy is closed to the barrier height, $\varphi_b \simeq 35$ meV) and the depth is also limited by the barrier size (l_p). Therefore, the interface roughness can be optimized for an effective barrier transmission, and the maximum transmission corresponds to the non-conserving lateral momentum.

2.3.4 Analysis of simulation results

The Fermi level, away from the HPAB, is expected to have the same distance from the band edge, due to the same level of doping and electron distribution. The potential gain through each barrier structure is estimated as $\Delta\varphi_{g,o} = \varphi_b + e_{e,HPAB}l_p$ (when the internal field by charge redistribution is not significant), and the total potential gain is proportional to the number of barriers ($\Delta\varphi_g = N_b\Delta\varphi_{g,o}$). Note that $\Delta\varphi_g$ increases the required x_{Al} , which changes the properties (increase in the optical phonon energy $E_{p,LO}$ and decrease in the electron mobility μ_e due to larger $m_{e,e}$ and intervally scattering). The simulation results using GaAs properties can be more

safely accepted for the lower $\Delta\varphi_g$. The properties from simulations (e.g., electron and phonon distribution, drift velocity, temperatures, and phonon absorption rate) are obtained by the ensemble average of the sampled particles from 0.5 to 1 ns.

2.4 Results and discussions

2.4.1 Electron transport

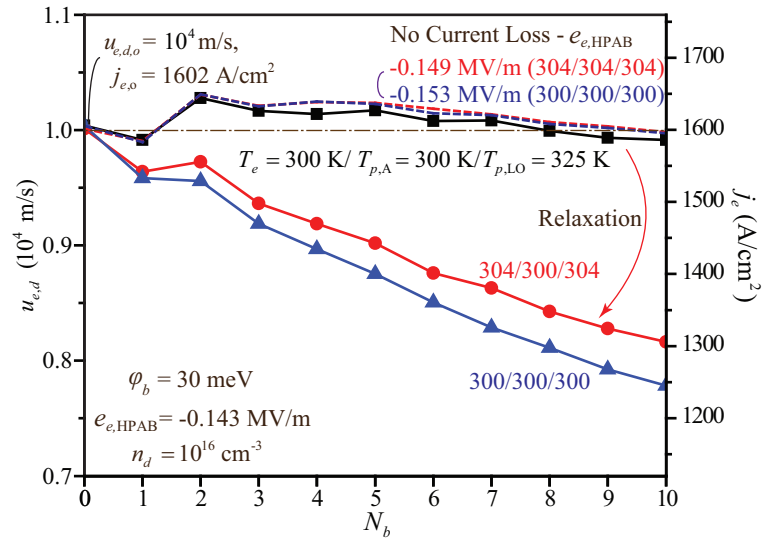


Figure 2.8: Variations of drift velocity ($u_{e,d}$, left) and current density (j_e with doping density $n_d = 10^{16} \text{ cm}^{-3}$, right) with respect to the number of barriers (N_b) for different temperatures (T_e , $T_{p,A}$ and $T_{p,LO}$. Constant temperatures are used in the simulation). High $T_{p,LO}$ reduces the current loss under the same $e_{e,HPAB}$, and as hot phonon system is relaxed (T_e and $T_{p,A} = 300 \text{ K}$, $T_{p,LO} = 325 \text{ K} \Rightarrow T_e, T_{p,A}$ and $T_{p,LO} = 304 \text{ K}$), less potential gain or electrical power is expected without current loss. ($\Delta\varphi_g = 20.03 \text{ meV} \Rightarrow 19.57 \text{ meV}$).

The MC simulations demonstrate that the HPAB produces electric potential gain without current loss through a proper combination of the local barrier electric field ($e_{e,HPAB}$), the optical phonon population ($f_{p,LO}$), and the barrier height (φ_b), and the potential energy gain is based on phonon absorption. As Fig. 2.4 shows, insufficient

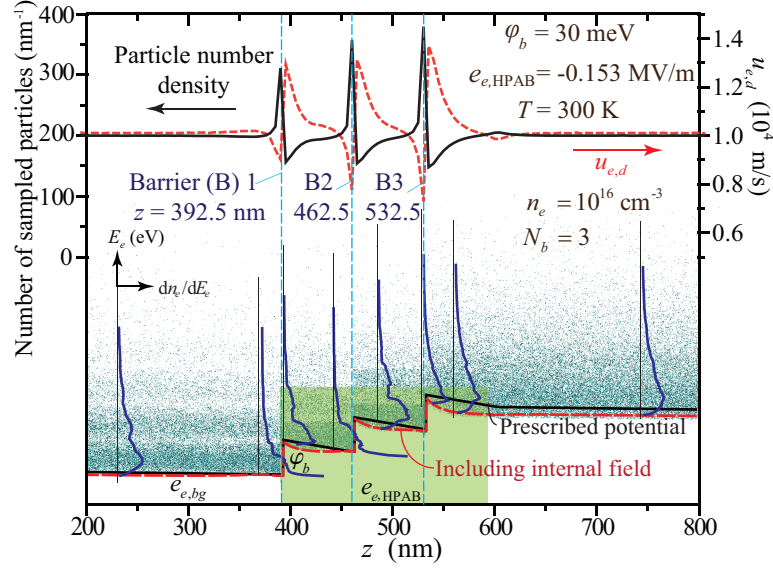


Figure 2.9: Sampled particle number density, drift velocity ($u_{e,d}$), and particle-energy distributions over the simulation cell. Electrons are accumulated behind barriers and low-energy electrons are highly populated near barriers.

phonon absorption (by low $T_{p,LO}$ or $f_{p,LO}$) or $e_{e,HPAB}$ (grading field) leads to a large current loss. Since the adverse current caused by the barrier decreases with increasing $f_{p,LO}$ (or $T_{p,LO}$) due to large phonon absorption rate, larger $\Delta\varphi_g$ with smaller $e_{e,HPAB}$ can be achieved at higher $T_{p,LO}$ as in Fig. 2.4. However, a large phonon population also increases the scattering rate, thus decreasing μ_e . The acoustic phonons do not contribute to electron upconversion, so low $T_{p,A}$ and high $T_{p,LO}$ are desirable. With constant $T_{p,A}$ and $T_{p,LO}$, HPAB operating under high $T_{p,LO}$ has smaller current loss and larger $\Delta\varphi_g$ compared to the thermal equilibrium system. (Nonequilibrium $T_{p,LO} = 325$ K and $T_{p,A} = 300$ K in GaAs relaxes to an equilibrium temperature of 304 K from the energy conservation, and $\Delta\varphi_{g,o}$ reduces from 20.03 to 19.57 meV (Fig. 2.8). Barrier transition is more effective in hot phonon systems [88].)

The particle density and velocity distributions in Fig. 2.9 show the electron accumulation and the low electron velocity behind the barriers. As the local electron

density (n_e) increases, the local electron average velocity ($u_{e,d}$) decreases, so that the current density j_e ($= e_c n_e u_{e,d}$) remains as constant. As Fig. 2.9 also shows, the potential profile near the barriers is bent by this nonuniform charge distribution, and this effect is not significant for small n_e ($< 10^{17}$ cm $^{-3}$). While the electron energy distribution dn_e/dE_e without a barrier is consistent and close to equilibrium, the low-energy electron density is large in the proximity of the barriers because of low transmission and energy loss by barrier.

The distribution recovers to equilibrium within a short distance from the barrier (by populating high-energy electrons due to large phonon absorption as well as field acceleration). Unless the electron distribution recovers its population over φ_b before the next barrier, large adverse current is induced by this ineffective barrier transition, and therefore, HPAB should have sufficiently large l_p to enable recovery. However, a long l_p leads to larger potential loss through $e_{e,\text{HPAB}}$, and needs to be optimized. Phonon absorption must occur at least once to recover the energy loss ($\leq E_{p,\text{LO}}$), so the required distance can be approximated as $l_p = u_{e,z} \tau_{p \rightarrow e,\text{LO}}$, where $u_{e,z}$ is the electron velocity in the z direction and $\tau_{p \rightarrow e,\text{LO}}$ is the time constant of LO phonon absorption ($1/\dot{\gamma}_{p \rightarrow e,\text{LO}}$), and this increases with φ_b . Considering an average $u_{e,z} = 1.5 \times 10^5$ m/s (from the isotropic velocity distribution) and $\tau_{p \rightarrow e,\text{LO}} = 0.4$ ps for equilibrium electrons moving with the forward direction below $E_{p,\text{LO}}$, we estimate $l_p = 60$ nm for LO phonon absorption and we choose $l_p = 70$ nm for this work. The MC results also demonstrate that the adverse current by two barriers is almost saturated with $l_p \geq 70$ nm and $\varphi_b \leq E_{p,\text{LO}}$.

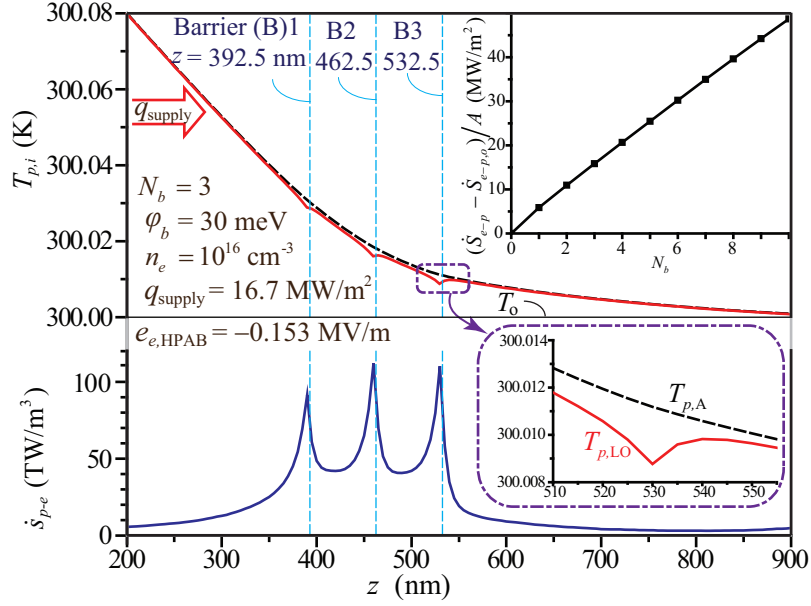


Figure 2.10: Distributions of phonon temperatures ($T_{p,A}$ and $T_{p,LO}$) and phonon energy absorption rate (\dot{s}_{p-e}). Large phonon absorption occurs around the barriers because of the large population of low-energy electrons, and this leads to the extended nonequilibrium between phonon modes. The total phonon absorption rate in HPAB (\dot{S}_{p-e}/A) is proportional to the number of barriers, as in the inset (top right).

2.4.2 Phonon population and absorption distribution

The phonon energy absorption rate ($\dot{s}_{p-e} = \dot{S}_{p-e}/V$, W/m^3) is determined by the electron energy distribution (dn_e/dE_e), i.e.,

$$\dot{s}_{p-e} = \sum_j \int_{E_e} [\dot{\gamma}_{p \rightarrow e,j}(E_e) - \dot{\gamma}_{e \rightarrow p,j}(E_e)] E_{p,j} \frac{dn_e(E_e)}{dE_e} dE_e, \quad (2.6)$$

where j is an interaction mechanism. Because of the large population at low E_e and no phonon emission with $E_e < E_{p,j}$, the large \dot{s}_{p-e} is observed near the barriers as in Fig. 2.10.

As shown in Fig. 2.10, the variation of $T_{p,i}$ in simulation region ($< 1 \mu\text{m}$) is rather small ($< 1 \text{ K}$), unless $q_{p,i}$ is extremely large ($> 55 \text{ MW}/\text{m}^2$), but a rather large

difference between $T_{p,LO}$ and $T_{p,A}$ appears near the barriers due to the large \dot{s}_{p-e} . However, since the phonon density ($n_{p,LO} = f_{p,LO}/V_{prim} = 7.56 \times 10^{21} \text{ cm}^{-3}$ at 300 K, V_{prim} is the primitive cell volume) is more than the four order-of-magnitude larger than n_e ($< 10^{17} \text{ cm}^{-3}$), the depletion of LO phonons is not significant and is quickly made up by upconversion of acoustic phonons (in spite of smaller $\dot{\gamma}_{p-p}$ than $\dot{\gamma}_{e-p}$). As phonons are absorbed, q_p (gradient of T_p) decreases with z , and vanishes when q_{supply} is completely absorbed. This also shows that hot phonons do not propagate due to the fast relaxation, and therefore, HPAB should be near the hot phonon generation site for high absorption efficiency.

The total phonon absorption rate for the HPAB operation (\dot{S}_{p-e}/A , W/m²) is the integration of \dot{s}_{p-e} over the simulation region, and is almost proportional to n_e (more electrons absorbing more phonons), especially when n_e is low (because of small effect of the charge redistribution). Also, \dot{S}_{p-e}/A increases with N_b or $\Delta\varphi_g$ due to increase in the transitions (linear proportionality for more than two barriers). So, \dot{S}_{p-e}/A can be expressed as $a_{p-e}n_e\Delta\varphi_g$ by introducing the parameter a_{p-e} (A/m).

2.4.3 Energy conversion efficiency

The electrical current (j_e) in this HPAB structure is maintained constant by carefully selecting the potential barrier height (φ_b) and the electric field following the barriers ($e_{e,HPAB}$). We note that the barrier structure generally decreases electron mobility (μ_e) hindering the electron transport. However, the large $e_{e,HPAB}$ recovers the current loss in the potential barrier. This is at cost to gained potential, i.e., it

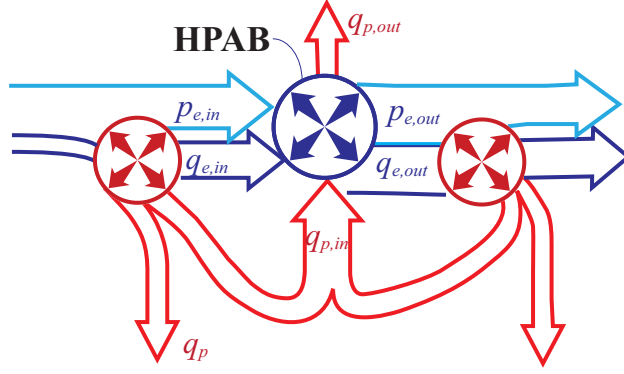


Figure 2.11: Energy (electric potential p and thermal energy q) flow in HPAB. Red arrows show phonon flows and blue and light blue arrows show electronic thermal and potential flow. Absorbed phonon energy (q_p) is used to increase electric potential (p_e).

decreases the net potential gain ($\Delta\varphi_g$). Without a current loss the phonon energy conversion to electrical power per unit area is $p_g = \Delta\varphi_g j_e$ (W/m²). The phonon absorption decreases the phonon energy flux, and the large field increases the electron kinetic energy flux. Considering the energy flow as in Fig. 2.11 ($p_g = p_{e,out} - p_{e,in}$, $q_e = q_{e,out} - q_{e,in}$, and $\dot{S}_{p-e}/A = q_{p,in} - q_{p,out}$), electrical energy balance in HPAB is

$$\dot{S}_{p-e}/A - q_e = p_g [= N_b(\varphi_b + e_{e,HPAB}l_p)n_e e_c u_{e,d}], \quad (2.7)$$

where q_e is the kinetic energy flux of egressing electrons.

Thus, the HPAB efficiency (η_{HPAB}) is the ratio of the power gain (electric potential) and the absorbed phonon energy rate,

$$\eta_{HPAB} = \frac{p_g}{\dot{S}_{p-e}/A} = \frac{e_c u_{e,d}}{a_{p-e}} \quad (\text{using } p_g = \Delta\varphi_g e_c n_e u_{e,d} \text{ and } \dot{S}_{p-e}/A = a_{p-e} n_e \Delta\varphi_g). \quad (2.8)$$

Higher $u_{e,d}$ yields larger p_g , but it also leads to larger potential drop from the

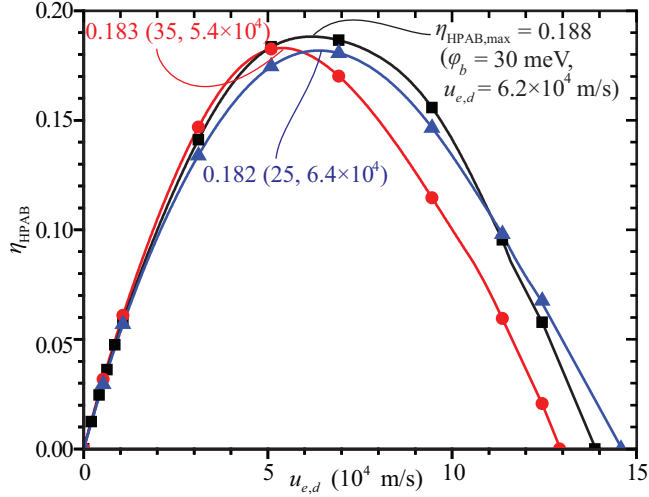


Figure 2.12: Variations of the HPAB efficiency (η_{HPAB}) with respect to the drift velocity ($u_{e,d}$). η_{HPAB} first increases with $u_{e,d}$ due to increase in the electrical power gain ($p_g = \Delta\varphi_g j_e$) and then decreases because of smaller $\Delta\varphi_g$. The maximum efficiency $\eta_{\text{HPAB,max}}$ is 18.8% for $u_{e,d} = 6.2 \times 10^4$ m/s and $\varphi_b = 30$ meV.

increased electric field ($u_{e,d}$ larger than 1.38×10^5 m/s cannot gain potential with $\varphi_b = 30$ meV), and thus a_{p-e} increases with $u_{e,d}$ (because of smaller $\Delta\varphi_g$). Since the increase in a_{p-e} becomes more pronounced with higher $u_{e,d}$, η_{HPAB} has a maximum ($\eta_{\text{HPAB,max}}$). \dot{S}_{p-e}/A and $\Delta\varphi_g$ also depend on φ_b because higher φ_b requires larger $e_{e,\text{HPAB}}$ and more phonon absorption per barrier. The simulation results for various $u_{e,d}$ and φ_b show that $\eta_{\text{HPAB,max}}$ is 18.8% when $u_{e,d} = 6.2 \times 10^4$ m/s and $\varphi_b = 30$ meV, as presented in Fig. 2.12. The phonons are provided by an external source, so higher η_{HPAB} is expected by including the phonons emitted in HPAB.

2.4.4 Operational Regime

HPAB requires sufficient phonon supply, otherwise phonon depletion reduces $T_{p,\text{LO}}$ and the adverse current increases, which in turn results in charge redistribution diminishing the potential gain. The required phonon energy for low $u_{e,d}$ ($< 10^4$ m/s)

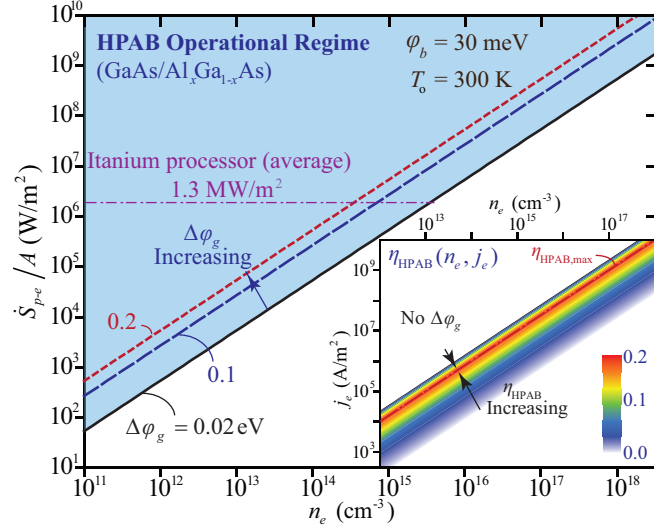


Figure 2.13: HPAB operational regime and variations of phonon energy absorption rate \dot{S}_{p-e}/A with respect to n_e , for $\Delta\varphi_g = 0.02, 0.1$, and 0.2 eV, and $u_{e,d} < 10^4$ m/s. Inset shows variations of η_{HPAB} with respect to n_e and j_e . \dot{S}_{p-e}/A (for $\Delta\varphi_g$ and j_e corresponding to $\eta_{\text{HPAB,max}}$) increases with n_e .

and various n_e and $\Delta\varphi_g$ is estimated by extrapolation from the simulations of low n_e ($= 10^{11} \text{ cm}^{-3}$) with $\varphi_b = 30 \text{ meV}$ and is shown Fig. 2.13.

In order for HPAB to operate in a system with larger n_e or $\Delta\varphi_g$, more \dot{S}_{p-e}/A should be provided. The j_e required for high η_{HPAB} is selected depending on n_e due to the dominant dependence of η_{HPAB} on $u_{e,d}$. (j_e for $\eta_{\text{HPAB,max}}$ also increases with n_e .) In the conventional electron density ranges (10^{16} to 10^{18} cm^{-3}), large \dot{S}_{p-e}/A ($> 10^6 \text{ W/m}^2$) and j_e (10^6 to 10^{10} A/m^2) are necessary for high η_{HPAB} , and heat dissipation from some state-of-the-art integrated processors is in this range [136]. Since HPAB is placed close to phonon source, this is local value at a site (e.g. drain-source channel in high-mobility electron transistors) [148, 129].

2.5 Summary

The novel heterobarrier structure is designed for the direct energy conversion from phonon energy to electric potential. This heterobarrier or hot-phonon absorption barrier (HPAB) structure combines an abrupt barrier with a gradual potential decrease which creates favorable condition for unassisted phonon absorption by increasing the low-energy electron population. The absorbed phonon energy turns into harvestable electric potential without current loss. The HPAB reverses the phonon role, which generally hinders electron transport, by harvesting hot phonons which would otherwise turn into waste heat.

Through MC simulations, we estimate up to 19% of the phonon energy conversion with proper phonon flux and current. In addition to gaining electric potential (or recovery), integrating HPAB in electronic devices will reduce heat dissipation, lowering operation temperature and enhancing the electron transport (higher mobility) through the effective removal of excess phonons as a heat sink.

Chapter 3

Phonon-Electron Energy

Conversion Entropy and Efficiency

3.1 Introduction

In the electron-phonon interactions the final states correspond to the maximum system entropy. This system entropy increase is accompanied by decrease in the availability of the carriers to do work. In the limit of reversible interaction, there is no net entropy increase, and the maximum energy conversion efficiency is achieved, i.e., the Carnot efficiency, which is determined from the equilibrium temperatures and heat flow rate.

Chapter 2 introduced the phonon recycling, which results in a reduction in heat

generation and a gain of electric potential, i.e., phonon-electron direct energy conversion system using a heterobarrier [163]. The barrier (with height nearly that of optical phonons) can effectively absorb the overpopulated nonequilibrium (i.e., hot) phonons, as the structure creates large population of low-energy electrons. Through the entropy analysis, this conversion system can be verified and the upper limit of its conversion efficiency can be theoretically predicted. A similar process, the anti-Stokes laser cooling has been originally analyzed in Ref. [97] and recently in Ref. [146], predicting the maximum cooling performance.

Here we analyze the system entropy change during the phonon-phonon and electron-phonon interactions and its energy conversion efficiency, including that of the heterobarrier conversion system.

3.2 Entropy analyses

3.2.1 Statistical entropy

Entropy is the conjugate property for the temperature, so in the classical thermodynamic treatment it is a challenge to define the entropy under nonequilibrium populations, since it requires a corresponding definition of the nonequilibrium temperatures. This can be overcome by using the statistical entropy of the microstates under nonequilibrium conditions [22].

In the Boltzmann formulation [19], the statistical entropy is $S = k_B \ln W$, where k_B is the Boltzmann constant and W is the number of microstates for a given macrostate.

Considering a system with discrete energy level i with energy ε_i , each level has D_i states and n_i particles, and then the numbers of possible combinations of the microstates in the Bose-Einstein (BE, identical and indistinguishable particles), the Fermi-Dirac (FD, with Pauli exclusion, $n_i \leq D_i$), and the Maxwell-Boltzmann (MB, distinguishable particles) are

$$W_{\text{BE}} = \prod_i \frac{(n_i + D_i - 1)!}{n_i!(D_i - 1)!}, \quad W_{\text{FD}} = \prod_i \frac{D_i!}{n_i!(D_i - n_i)!}, \quad \text{and} \quad W_{\text{MB}} = \prod_i \frac{(D_i)^{n_i}}{n_i!}. \quad (3.1)$$

With the Stirling approximation $[\ln(x!) \sim x \ln x - x]$, the total entropy S is approximated as

$$\frac{S}{k_{\text{B}}} = \ln W \simeq \frac{E - \mu_c N}{k_{\text{B}} T} + \sum_i \frac{D_i}{a} \ln \left[1 + a \exp\left(-\frac{\varepsilon_i - \mu_c}{k_{\text{B}} T}\right) \right], \quad (3.2)$$

with the total energy $E (= \sum_i \varepsilon_i n_i)$, the chemical potential μ_c and the particle number $N (= \sum_i n_i)$. This is maximized by using the method of Lagrange undetermined multipliers, and the occupancy ($f_i = n_i/D_i$) for the maximum entropy becomes

$$f_i^{\circ} = \frac{n_i}{D_i} = \frac{1}{\exp(\alpha + \beta \varepsilon_i) + \gamma}, \quad \alpha = -\frac{\mu_c}{k_{\text{B}} T}, \quad \text{and} \quad \beta = \frac{1}{k_{\text{B}} T}, \quad (3.3)$$

where $\gamma = -1$ for BE, 0 for MB, and $+1$ for FD. This is identical to the occupancy functions in Eq. (1.1). Then, the statistical entropies for phonon and electrons (in a

unit volume) are [46, 18]

$$S_p = \int_0^{E_{p,c}} k_B D_p [(f_p + 1) \ln(f_p + 1) - f_p \ln f_p] dE_p, \quad (3.4)$$

$$S_e = - \int_{-\infty}^{\infty} k_B D_e [(1 - f_e) \ln(1 - f_e) - f_e \ln f_e] dE_e. \quad (3.5)$$

From the occupancy functions (f_p and f_e), nonequilibrium temperatures are defined as (using the Fermi level E_F as the chemical potential μ_c)

$$T_p(f_p, E_p) = \frac{E_p}{k_B [\ln(f_p + 1) - \ln f_p]}, \quad (3.6)$$

$$T_e(f_e, E_e) = \frac{E_e - E_F}{k_B [\ln(1 - f_e) - \ln f_e]}. \quad (3.7)$$

3.2.2 Interactions between phonon subsystems

The longitudinal optical (LO) phonon mode in polar semiconductors (e.g., GaAs, GaN, and SiC) are most significant in the e - p coupling [88] due to the high interaction rate, and the low momentum and smaller decay rate which lead to the overpopulation of LO phonons. These hot phonons are decayed by the downconversion to the acoustic phonon modes with decay rate $\dot{\gamma}_{p-p,down}$ until equilibrium is reached. The entropy change by interactions between phonon subsystems (LO and other phonon modes) during the hot LO phonon relaxation is addressed below, and the non-dispersed, single-phonon energy approximation ($E_{p,LO} = \hbar\omega_{p,LO}$) is employed for the LO phonons. In a primitive cell with two atoms, $\int_0^{\infty} D_{p,LO} dE_{p,LO} = 1$, and

using Eq. (3.4), the energy and entropy of the LO phonon mode are

$$\langle E_{p,\text{LO}} \rangle(T_{p,\text{LO}}) = f_{p,\text{LO}} E_{p,\text{LO}}, \quad (3.8)$$

$$S_{p,\text{LO}}(T_{p,\text{LO}}) = k_{\text{B}}[(f_{p,\text{LO}} + 1)\ln(f_{p,\text{LO}} + 1) - f_{p,\text{LO}}\ln f_{p,\text{LO}}]. \quad (3.9)$$

Through the relaxation, the energy and entropy of each subsystem changes, and the rates are

$$\frac{d\langle E_{p,\text{LO}} \rangle}{dt} = \frac{df_{p,\text{LO}}}{dt} E_{p,\text{LO}}, \quad \text{and} \quad \frac{dS_{p,\text{LO}}}{dt} = k_{\text{B}} \frac{df_{p,\text{LO}}}{dt} \ln\left(\frac{f_{p,\text{LO}} + 1}{f_{p,\text{LO}}}\right). \quad (3.10)$$

Using the relaxation time approximation ($df_{p,\text{LO}}/dt = -\dot{\gamma}_{p-p,\text{down}} f_{p,\text{LO}}$), the rate of energy change in a primitive cell is

$$\frac{d\langle E_{p,\text{LO}} \rangle}{dt} = -\dot{\gamma}_{p-p,\text{down}} f_{p,\text{LO}} E_{p,\text{LO}} (= -\dot{\gamma}_{p-p,\text{down}} \langle E_{p,\text{LO}} \rangle). \quad (3.11)$$

With the temperature defined in Eq. (3.6), the entropy change is

$$\frac{dS_{p,\text{LO}}}{dt} = \frac{1}{T_{p,\text{LO}}} \frac{d\langle E_{p,\text{LO}} \rangle}{dt} = -\frac{\dot{\gamma}_{p-p,\text{down}} \langle E_{p,\text{LO}} \rangle}{T_{p,\text{LO}}}. \quad (3.12)$$

Assuming that other phonon modes (p, A) are in equilibrium (because of the faster relaxation rate between other modes), only the nonequilibrium between LO and A phonon modes are considered. Without any external source, the total phonon system energy is conserved ($dE_p/dt = dE_{p,\text{LO}}/dt + dE_{p,\text{A}}/dt = 0$), and then from Eq. (3.11),

we have

$$\frac{d\langle E_{p,A} \rangle}{dt} = -\frac{d\langle E_{p,LO} \rangle}{dt} = \dot{\gamma}_{p-p,down} f_{p,LO} E_{p,LO}, \quad (3.13)$$

where the total phonon energy with mode A in a primitive cell is $\langle E_{p,A} \rangle = \int D_{p,A} f_{p,A} E_p dE_p$.

The entropy production rate is

$$\begin{aligned} \frac{dS_{p,A}}{dt} &= \int k_B D_{p,A} \frac{df_{p,A}}{dt} \ln\left(\frac{f_{p,A} + 1}{f_{p,A}}\right) dE_p \\ &= \int D_{p,A} \frac{df_{p,A}}{dt} \frac{E_{p,A}}{T'_{p,A}(E_{p,A})} dE_{p,A}. \end{aligned} \quad (3.14)$$

With an equilibrium temperature $[T_{p,A} = T'_{p,A}(E_{p,A})]$, the total phonon entropy production rate is

$$\begin{aligned} \frac{dS_p}{dt} &= \frac{dS_{p,A}}{dt} + \frac{dS_{p,LO}}{dt} = \frac{1}{T_{p,A}} \frac{d\langle E_{p,A} \rangle}{dt} + \frac{1}{T_{p,LO}} \frac{d\langle E_{p,LO} \rangle}{dt} \\ &= \left(\frac{1}{T_{p,LO}} - \frac{1}{T_{p,A}}\right) \frac{d\langle E_{p,LO} \rangle}{dt} = \left(\frac{1}{T_{p,A}} - \frac{1}{T_{p,LO}}\right) \dot{\gamma}_{p-p,down} \langle E_{p,LO} \rangle. \end{aligned} \quad (3.15)$$

In the presence of hot LO phonons ($T_{p,LO} > T_{p,A}$), the total entropy increases, and the rate of entropy increase is higher under a more pronounced nonequilibrium (larger temperature difference between LO phonon and other phonon modes).

3.2.3 Electron-phonon interactions

The energy and entropy changes in the electron-phonon ($e-p$) interactions are determined based on their kinetics. The electron interaction with the LO phonons

is the dominant scattering mechanism in many polar semiconductors. With phonon absorption and emission rates ($\dot{\gamma}_{p \rightarrow e}$ and $\dot{\gamma}_{e \rightarrow p}$), the rates in the LO phonon energy and entropy changes are (emission increases $f_{p,LO}$ and absorption decreases it)

$$\frac{d\langle E_{p,LO} \rangle}{dt} = \int (\dot{\gamma}_{e \rightarrow p} - \dot{\gamma}_{p \rightarrow e}) f_e D_e E_{p,LO} dE_e, \quad (3.16)$$

$$\frac{dS_{p,LO}}{dt} = \frac{1}{T_{p,LO}} \frac{d\langle E_{p,LO} \rangle}{dt} = \frac{E_{p,LO}}{T_{p,LO}} \int (\dot{\gamma}_{e \rightarrow p} - \dot{\gamma}_{p \rightarrow e}) f_e D_e dE_e. \quad (3.17)$$

Using the energy conservation and the total electron energy $\langle E_e \rangle = \int (E_e - E_F) D_e f_e dE_e$, the electron energy change becomes

$$\frac{d\langle E_e \rangle}{dt} = \int (E_e - E_F) D_e \frac{df_e}{dt} dE_e = -\frac{d\langle E_{p,LO} \rangle}{dt}. \quad (3.18)$$

The electron entropy production rate is obtained from the time derivative of Eq. (3.5), and using the definition of the electron temperature in Eq. (3.7) it can be written as

$$\frac{dS_e}{dt} = \int_{-\infty}^{\infty} k_B D_e \frac{df_e}{dt} \ln\left(\frac{1-f_e}{f_e}\right) dE_e = \int_{-\infty}^{\infty} D_e \frac{df_e}{dt} \frac{E_e - E_F}{T'_e(E_e)} dE_e. \quad (3.19)$$

If the electrons are in equilibrium, T_e is constant [$T_e = T'_e(E_e)$] and dS_e/dt becomes simply $(1/T_e)d\langle E_e \rangle/dt$. Then, the total entropy production rate in e - p coupling system is given as

$$\frac{dS_p}{dt} + \frac{dS_e}{dt} = \left(\frac{1}{T_{p,LO}} - \frac{1}{T_{p,e}} \right) \frac{d\langle E_{p,LO} \rangle}{dt} \geq 0. \quad (3.20)$$

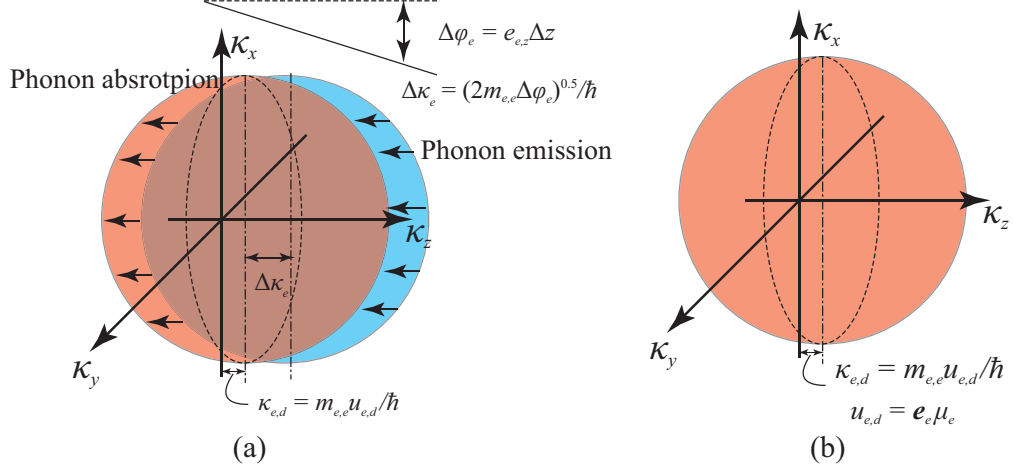


Figure 3.1: (a) Electron acceleration by an electric field. Electron distribution is shifted, but electrons with higher energy (larger distance from the origin) have the favorable condition for phonon emission, whereas the low-energy electrons are absorption favorable. (b) Electron distribution with a drift velocity $\mathbf{u}_{e,d}$. Due to the phonon scattering (absorption and emission), the electron distribution has a finite bias in κ -space showing the electron drift velocity.

Again, if the heat flows from the higher to lower temperature subsystem, the entropy always increases, and entropy increase originates from the nonequilibrium between the subsystems.

3.2.4 Steady electrical current

3.2.4.1 Electron drift

In the wavevector (κ_e) space, the electron distribution (without an average drift) is isotropic in equilibrium. With a parabolic band structure, the electron kinetic energy ($E_{e,\kappa}$) is proportional to the square of distance from the origin in the κ -space ($E_{e,\kappa} = \hbar^2|\boldsymbol{\kappa}_e|^2/2m_{e,e}$), as in Eq. (1.2). In the presence of an electrical field (\mathbf{e}_e), the electrons accelerate and gain a momentum ($\Delta\mathbf{p}_e = \hbar\Delta\boldsymbol{\kappa}_e$) in the applied field direction. As Fig. 3.1 shows, considering \mathbf{e}_e only in the z direction ($\mathbf{e}_e = e_{e,z}\mathbf{z}$), the

electrical potential drop over Δz is $\Delta\varphi_e = e_{e,z}\Delta z$, and this potential drop leads to a kinetic energy or momentum gain, which corresponds to the momentum change $\Delta\kappa_e = (2m_{e,e}\Delta\varphi_e)^{0.5}/\hbar$. As a result, the electron distribution shifts, and the electron distribution changes to nonequilibrium. However, due to the e - p scattering, electrons cannot be continuously accelerated. Since the electrons with higher energy (larger distance from the origin) have larger phonon emission rates than absorption (whereas low-energy electrons are phonon absorption favorable), the electron distribution has a finite bias in the κ -space ($\kappa_{e,d}$), showing an average drift velocity ($u_{e,d} = \hbar\kappa_{e,d}/m_{e,e}$) as shown in Fig. 3.1(b). With a low electric field (\mathbf{e}_e), the electron drift is linearly proportional to the field, ($\mathbf{u}_{e,d} = \mu_e\mathbf{e}_e$) and here the ratio of $\mathbf{u}_{e,d}$ to \mathbf{e}_e is the electron mobility (μ_e).

For electrons in the Γ -valley ($0 < E_{e,\kappa} < 0.29$ eV) in the GaAs system using the parabolic band assumption and $m_{e,e} = 0.63m_e$, a drift velocity ($u_{e,d}$) 2.3×10^4 m/s results in only 0.1 meV bias. (Even with the saturation velocity of GaAs 1.2×10^5 m/s, the bias is only 2.5 meV.) Therefore, the bias caused by the electric current does not have a large effect on the distribution, and a symmetric and equilibrium distribution can be assumed in the simple electron drift cases (i.e., under no abrupt perturbation such as the barrier).

3.2.4.2 Electrochemical potential

Each particle contains the electrochemical potential (φ_e), which is composed of a chemical potential (μ_c , or Fermi level E_F) and an electrostatic component (e_cV , e_c : the electron charge and V : the electrostatic potential). The change in the local

Fermi level is generally referred to as the change in the electrochemical potential in the analysis of electric circuit ($\Delta\varphi_e = \Delta E_F$). Including this electrochemical potential, the total electron energy is $\langle E_e \rangle + E_F N_e$ or $\langle E_{e,\kappa} \rangle + \varphi_e N_e$, where N_e is the number of electrons ($= \int D_e f_e dE_e$) and $\langle E_{e,\kappa} \rangle$ is the total electron kinetic energy [59].

Under the steady-state condition ($\partial E/\partial t = 0$, no internal energy change), the total energy generation in a system is equivalent to the integral of the divergence of energy flux \mathbf{j}_E (W/m²) and is zero (by energy conservation). Using the Gauss divergence theorem (and the surface normal unit vector \mathbf{s}_A), this becomes

$$\frac{dE}{dt} = \int_V \nabla \cdot \mathbf{j}_E dV = \int_A \mathbf{j}_E \cdot \mathbf{s}_A dA = 0. \quad (3.21)$$

Here, the energy flux can be decomposed as

$$\mathbf{j}_E = \mathbf{q}_p + \mathbf{q}_e + \mathbf{p}_e (= \mathbf{q}_p + \mathbf{q}_e + \varphi_e \mathbf{j}_{n,e}), \quad (3.22)$$

where \mathbf{q}_p and \mathbf{q}_e are the phonon and electron energy (heat) flux vectors respectively, and $\varphi_e \mathbf{j}_{n,e}$ (or \mathbf{p}_e) is the electrochemical energy flux. $\mathbf{j}_{n,e}$ (m⁻²s⁻¹) is the electron number flux given as

$$\mathbf{j}_{n,e} = \int \mathbf{u}'_{e,d} D_e f_e dE_e, \quad (3.23)$$

where $\mathbf{u}'_{e,d}$ is the drift velocity at E_e , and the electrical current is $\mathbf{j}_e = -e_c \mathbf{j}_{n,e}$.

Considering a 1-D transport in the z direction as illustrated in Fig.3.2 (the properties in the lateral directions are assumed uniform, so the lateral transport is ignored),

the net energy flux from Eq. (3.21) is

$$\int_A \mathbf{j}_E \cdot \mathbf{s}_A dA = A_z(j_{E,R} - j_{E,L}) = 0, \quad (3.24)$$

where A_z is the area normal to the transport direction z , and $j_{E,R/L}$ is z -direction component of energy flux at for the right or left boundary. This shows that only the energy fluxes at the left and right boundaries are required for the energy conservation. The total energy flux should be conserved ($j_{E,z} = j_{E,R} = j_{E,L}$), but each component in \mathbf{j}_E [Eq. (3.22)] varies because of interactions. The phonon absorption and emission by e - p interactions change the phonon energy flux in the z direction, so

$$\Delta q_{p,z} = q_{p,R} - q_{p,L} = -\dot{S}_{p \rightarrow e}/A = -\int_0^{\Delta z} \dot{s}_{p \rightarrow e} dz. \quad (3.25)$$

Here, the volumetric phonon absorption $\dot{s}_{p \rightarrow e} = \int (\dot{\gamma}_{p \rightarrow e} - \dot{\gamma}_{e \rightarrow p}) E_{p,LO} f_e D_e dE_e$ [Eq. (3.17)], when only the LO phonon scattering is included. The change in electron energy flux (in the z direction) is

$$\Delta q_{e,z} = q_{e,R} - q_{e,L} = \int (q'_{e,R} - q'_{e,L}) dE_e. \quad (3.26)$$

Here $q'_{e,R/L}$ is the energy flux of the electrons with E_e at the right or left boundaries, i.e., $q'_{e,R/L} = u'_{e,d} E_{e,\kappa} D_{e,R/L} f_{e,R/L} = u'_{e,d} (E_e - E_{c,R/L}) D_{e,R/L} f_{e,R/L}$, where the electron kinetic energy is $E_{e,\kappa} = E_e - E_c$, and E_c is the conduction band edge. From the

particle number conservation, $j_{n,e,z}$ is constant, i.e.,

$$\Delta j_{n,e,z} = j_{n,e,R} - j_{n,e,L} = \int (u'_{e,d,R} D_e f_{e,R} - u'_{e,d,L} D_e f_{e,L}) dE_e = 0, \quad (3.27)$$

and with the electrochemical potential gain $\Delta\varphi_e (= E_{F,R} - E_{F,L})$, the change in the electrochemical potential flux ($\Delta p_{e,z}$) in the z direction is

$$\Delta p_{e,z} = \Delta\varphi_e j_{n,e,z} = (E_{F,R} - E_{F,L}) j_{n,e}. \quad (3.28)$$

From the energy conservation

$$\begin{aligned} \int_A \mathbf{j}_E \cdot \mathbf{s}_A dA &= \Delta q_{p,z} + \Delta q_{e,z} + \Delta p_{e,z} = 0 \\ -\dot{S}_{p \rightarrow e}/A + \int (q'_{e,R} - q'_{e,L}) dE_e + \Delta\varphi_e j_{n,e,z} &= 0. \end{aligned} \quad (3.29)$$

The entropy production rate under steady state is equal to the net entropy flux ($\Delta j_{S,z}$)

as in energy flux. The net electron entropy flux is

$$\Delta j_{S,e,z} = j_{S,e,R} - j_{S,e,L} = \int \left(\frac{q'_{e,R}}{T'_{e,R}} - \frac{q'_{e,L}}{T'_{e,L}} \right) dE_e, \quad (3.30)$$

where $q'_{e,R/L}$ and $T'_{e,R/L}$ are the E_e -dependent heat flux contribution and temperature, and if the electrons are in equilibrium on both boundaries, this becomes

$$\Delta j_{S,e,z} = \frac{q_{e,R}}{T_{e,R}} - \frac{q_{e,L}}{T_{e,L}}. \quad (3.31)$$

The net phonon entropy flux or phonon entropy production is (with the LO phonon mode only)

$$\Delta j_{S,p,z} = \frac{dS_{p,LO}}{dt} = \frac{1}{T_{p,LO}} \frac{d\langle E_{p,LO} \rangle}{dt} = -\frac{\dot{S}_{p \rightarrow e}/A}{T_{p,LO}} \quad (= -\frac{\Delta q_p}{T_{p,LO}}), \quad (3.32)$$

and using the energy conservation in Eq. (3.29), this can be written as

$$\Delta j_{S,p,z} = -\frac{\int (q'_{e,R} - q'_{e,L}) dE_e + \Delta \varphi_e j_{n,e,z}}{T_{p,LO}}. \quad (3.33)$$

According to the second law of thermodynamics, the production rate should not be smaller than 0, i.e.,

$$\begin{aligned} \Delta j_{S,e,z} + \Delta j_{S,p,z} &\geq 0 \\ \int \left(\frac{q'_{e,R}}{T'_{e,R}} - \frac{q'_{e,L}}{T'_{e,L}} \right) dE_e - \frac{\Delta \varphi_e j_{n,e} + \int (q'_{e,R} - q'_{e,L}) dE_e}{T_{p,LO}} &\geq 0. \end{aligned} \quad (3.34)$$

Figure 3.2 describes the energy (j_E) and entropy flux (j_S) for a steady, electrical current. Without scattering (friction), the conversion between the electron kinetic and potential energies ($E_{e,\kappa}$ and $E_{e,p}$) will be reversible as in the mechanical system ($E_{e,\kappa} = E_e - E_c$ and $E_{e,p} = E_c - E_F$). However, as a result of the electron-phonon interactions, electron system has a constant drift velocity in spite of the loss of electrochemical potential. Assuming the constant electron and phonon occupancy distributions, the temperatures on both boundaries are the same, and the electron heat flux (\mathbf{q}_e) is consistent [i.e., $D_e f_e$ for $(E_e - E_F)$, and $D_p f_p$ for E_p do not change]. Thus, the net

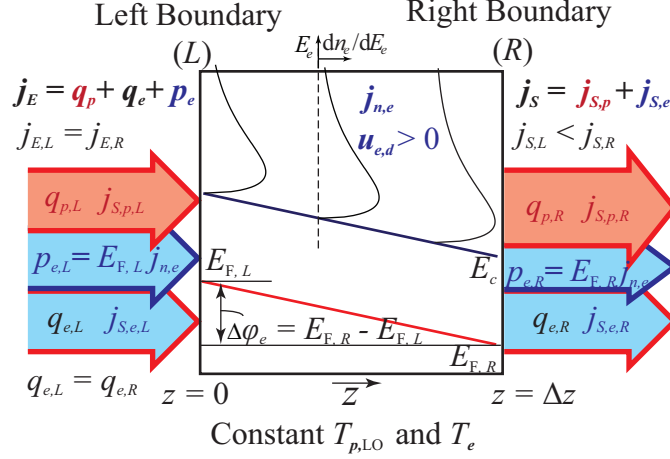


Figure 3.2: Energy (\mathbf{j}_E) and entropy flux (\mathbf{j}_S) in a steady electrical current. With constant temperatures (i.e., constant electron and phonon occupancies), the electrochemical potential is converted to phonon energy, and this results in the entropy production.

phonon flux Δq_p is $-\Delta\varphi_e j_{n,e}$ (according to the energy conservation, Eq. (3.29)), which is the known Joule heating $\dot{S}_{e,J}$. The total entropy production rate ($\Delta j_{S,e,z} + \Delta j_{S,p,z}$) becomes $-\Delta\varphi_e j_{n,e,z}/T = \dot{S}_{e,J}/T$, and this shows that the entropy in the electrical currents always increases, because of the voltage drop ($\Delta\varphi_e < 0$) and electron drift ($j_{n,e,z} > 0$).

3.3 Entropy in energy conversion systems

In this section, the entropy is examined in the phonon-electron energy conversion systems, i.e., the hot-phonon relaxation system and the barrier energy conversion discussed in Chapter 2. The conduction electrons in Γ -valley in GaAs are considered for their interaction and transport, and with the parabolic band approximation from

Eq. (1.2), the electron density of states D_e is

$$D_e(E_{e,\kappa}) = \frac{2^{1/2} m_{e,e}^{3/2} E_{e,\kappa}^{1/2}}{\pi^2 \hbar^3}. \quad (3.35)$$

3.3.1 Hot phonon relaxation by e - p and p - p interactions

3.3.1.1 Distributions and interaction kinetics

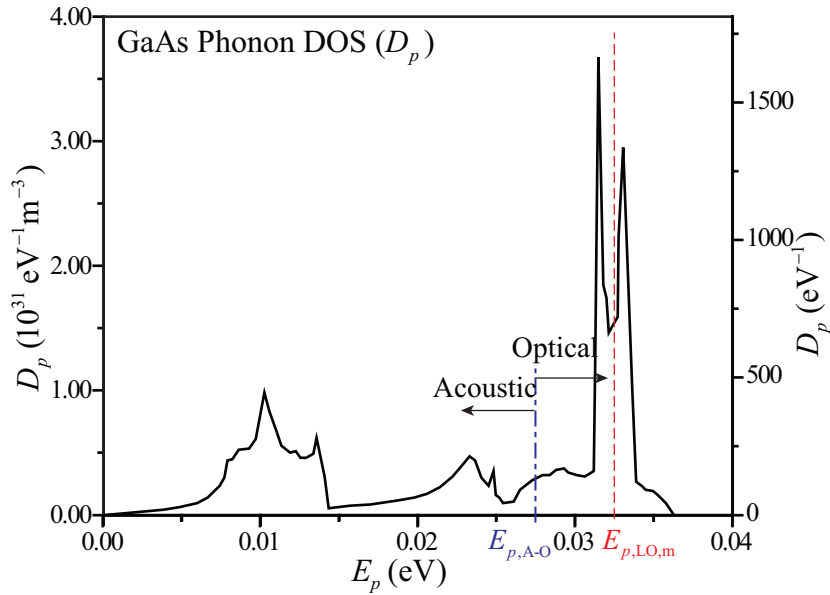


Figure 3.3: Phonon density of states (D_p) in GaAs [55]. D_p in the left y -axis shows the density of state per unit volume and unit energy ($\text{eV}^{-1}\text{m}^{-3}$), and the right one represents D_p per a primitive cell and unit energy (eV^{-1}). Since GaAs has 6 modes in a primitive cell, $\int_0^\infty D_p dE_p = 6$, and in this analysis, phonons with energy less than $E_{p,\text{LO},m}$ are regarded as other phonon modes (p,A) when $\int_0^{E_{p,\text{LO},m}} D_p dE_p = 5$ ($E_{p,\text{LO},m} = 32.7 \text{ meV}$).

Hot phonons (in LO mode) in GaAs are decayed by the e - p as well as the p - p interactions, and the hot phonon relaxation process is determined by these interaction kinetics and the population distributions of the electron and phonon modes.

The primitive cell of GaAs has six phonon modes, i.e., three acoustic and three

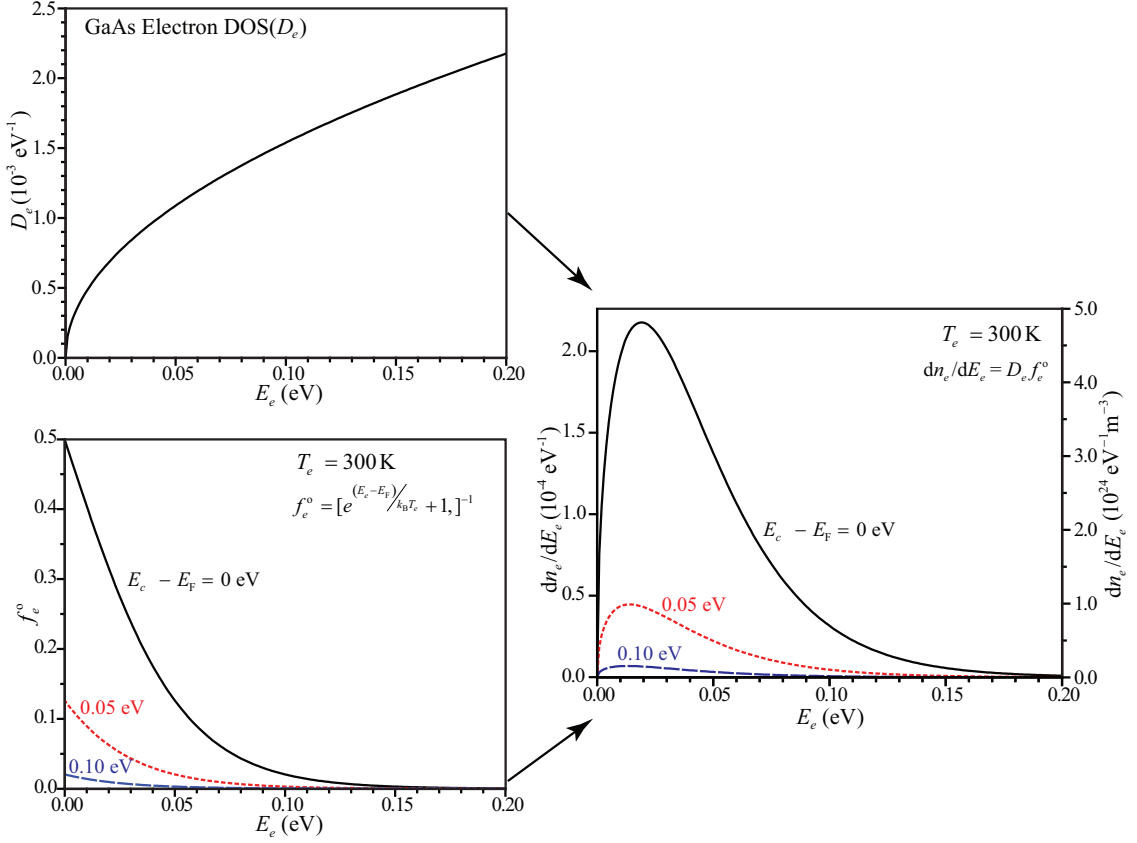


Figure 3.4: Electron density of states (D_e), equilibrium electron occupancy (f_e^o) and population distribution (dn_e/dE_e) with a parabolic band approximation in GaAs. Using D_e and f_e^o , the equilibrium electron population distribution is found. Since the occupancy is a function of the Fermi energy and temperature, the population distribution also varies with E_F and T_e .

optical modes, and the LO phonon is the highest-energy phonon mode. Phonon population distribution (dn_p/dE_p , phonon population in unit volume and unit energy range) is found using the density of states (D_p) in Fig. 3.3 and the occupancy (f_p), that is, $dn_p/dE_p = D_p f_p$. As in the previous sections, two phonon subsystems, namely, LO phonon and other phonon modes, are considered, and in this analysis, the phonons with energy less than $E_{p,LO,m}$ are regarded as the other phonon modes (p,A), so $\int_0^{E_{p,LO,m}} D_p dE_p = 5$ ($E_{p,LO,m} = 32.7 \text{ meV}$). The LO phonon mode is assumed to have a single energy, $E_{p,LO} = 35 \text{ meV}$.

With a parabolic band structure, the electron density of states (D_e) is calculated through Eq. (3.35). The equilibrium population distribution (dn_e/dE_e) is obtained using this D_e and the equilibrium electron occupancy (f_e^0), as shown in Fig. 3.4, and this distribution dn_e/dE_e is dependent on the Fermi energy and the electron temperature.

The LO phonon absorption and emission rates ($\dot{\gamma}_{p,LO \rightarrow e}$ and $\dot{\gamma}_{p,LO \rightarrow e}$) can be found using Eq. (2.2) with the interaction Hamiltonian for the polar optical phonon. (These interaction rates are shown in Fig. 2.3.) The three-phonon interactions (up- and downconversion, $\dot{\gamma}_{p,A \rightarrow p,LO}$ and $\dot{\gamma}_{p,LO \rightarrow p,A}$) are calculated using Eq. (2.3) based on the Fermi golden rule. The p - p interactions among the phonon modes other than LO are fast enough to assume equilibrium occupancy for those phonon mode A.

3.3.1.2 System evolution during relaxation

Initially, the electron and phonon temperatures (except for LO phonon mode) are set to 300 K ($T_e = T_{p,A} = 300$ K), and for a hot phonon system, we assume that LO mode phonons are singly excited ($f_{p,LO} = 1.0$), thus the LO phonon temperature is $T_{p,LO} = 600$ K. The Fermi level is assumed to be constant ($E_c - E_F = 0.05$ eV) during the relaxation. Based on the interaction rates ($e \rightleftharpoons p,LO$ and $p,LO \rightleftharpoons p,A$) and the electron and phonon distributions, the evolutions of the population distribution and entropy in electron and phonon systems during the hot phonon relaxation process are examined. Electron and phonon population distributions are updated at every time step ($\Delta t_s = 10$ fs), and their entropies are calculated using Eqs. (3.5) and (3.4).

In Chapter 2, barrier height (φ_b) near $E_{p,LO}$ is considered, and the large popu-

lation over the barrier energy is desirable for the barrier transition. Figure 3.5(a) shows the variations of the number density ($n_{e,OB}$) and fraction ($n_{e,OB}^o$) of the electrons with $E_e > E_{p,LO}$ with respect to time, and these can be used to estimate the barrier conversion efficiency with the barrier height $\varphi_b = E_{p,LO}$. This number density and the fraction is maximized around 1 ps after the hot phonon relaxation begins. This shows the optimum time for the barrier transition. During the relaxation, the electron distribution is not in equilibrium, so no single temperature exists. Thus, multiple effective temperatures at which equilibrium distribution has the same fraction ($n_{e,OB}^o$), density ($n_{e,OB}$), and total energy (E_e) are possible. As Fig. 3.5(b) shows, the effective T_e first increases and then decreases, whereas $T_{p,LO}$ decreases and $T_{p,A}$ increases monotonically. Because the e - p interaction rate is faster than the p - p , the electron is first excited by the dominant e - p interactions and then other phonon modes (p,A) are excited by p - p .

Figure 3.6(a) shows the electron (e , blue) and phonon (p , red) distributions at elapsed time of 1 ps since the hot-phonon relaxation begins, and this also demonstrates that larger electron population over the barrier height is expected (compared to the initial distribution). The electron and phonon entropies (S_e and S_p) evaluated using the population distributions indicate a continuous increase in total entropy ($S_e + S_p$), as shown in Fig. 3.6(b), even though the electron entropy decreases after 1 ps and the total entropy production rate is reduced.

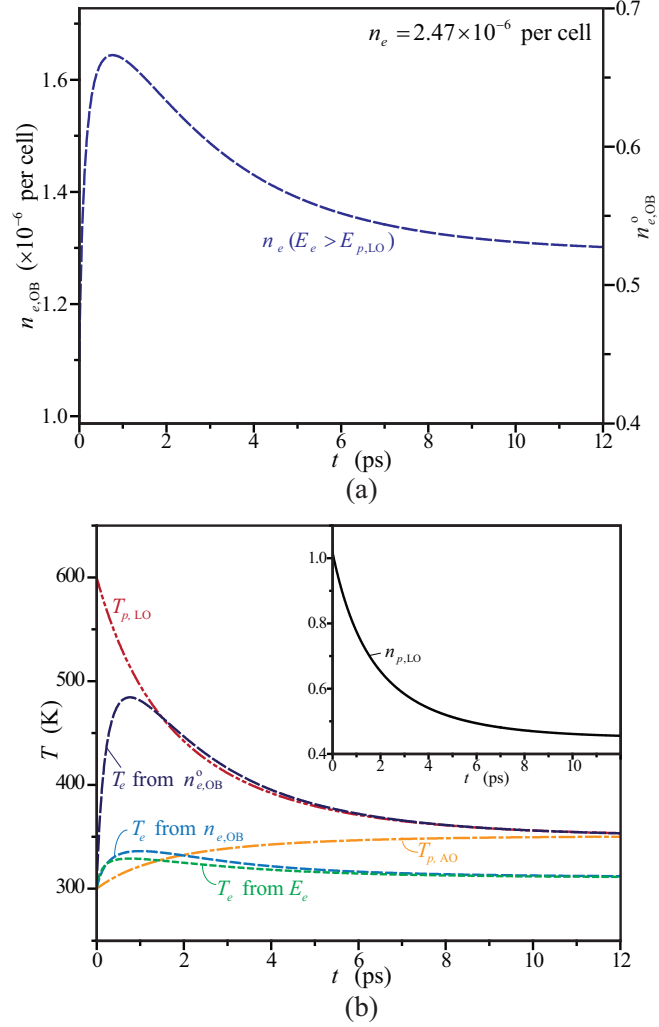


Figure 3.5: (a) Variations of the number density ($n_{e,OB}$) and fraction ($n_{e,OB}^0$) of electrons with $E_e > E_{p,LO}$ with respect to time. This number density is maximized near 1 ps since hot phonon relaxation begins. (b) Time evolution of the temperatures. For nonequilibrium electrons, temperatures at which equilibrium distribution has the same fraction ($n_{e,OB}^0$), density ($n_{e,OB}$), and total energy (E_e), are used. T_e first increases and then decreases, whereas $T_{p,LO}$ decreases and $T_{p,A}$ increases monotonically.

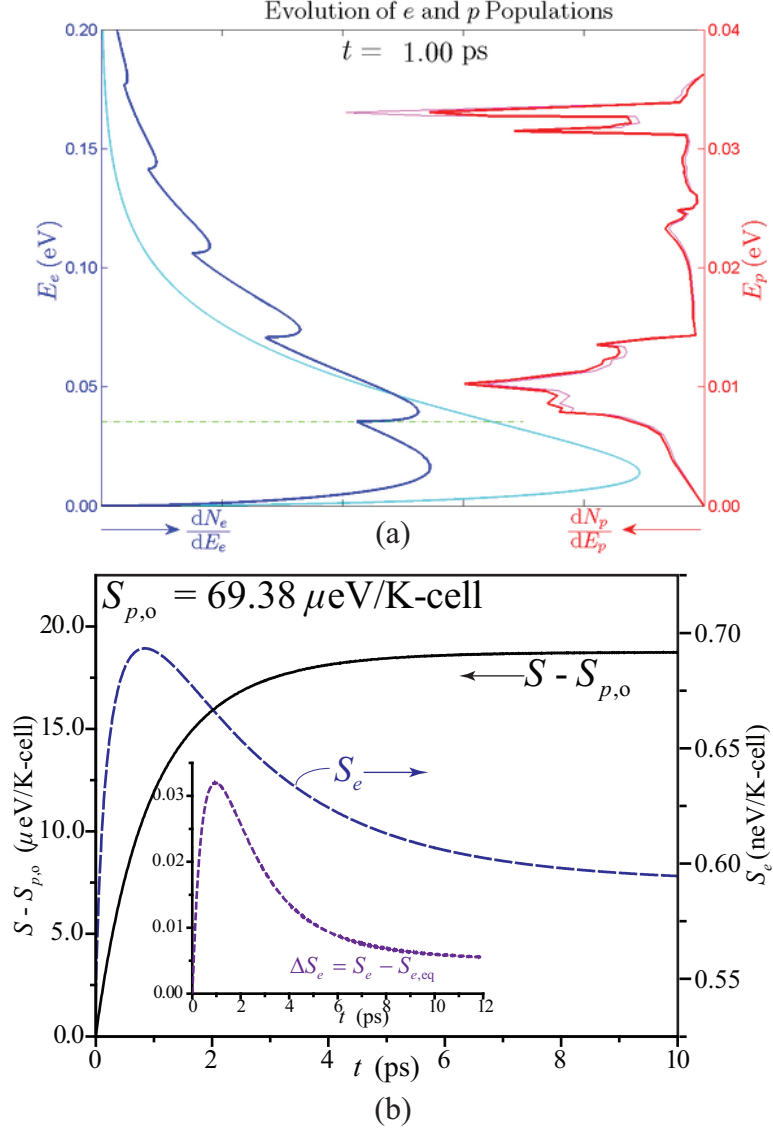


Figure 3.6: (a) Electron (e , blue) and phonon (p , red) distributions at 1 ps since the hot phonon relaxation begins. [Initial e (cyan) and p (magenta) distributions are also presented. Initially T_e and $T_p = 300$ K, and $T_{p,LO} = 600$ K]. (b) Entropy (S) evolution of hot phonon relaxation process ($S_{p,o}$ is initial phonon entropy). Total entropy S increases with time.

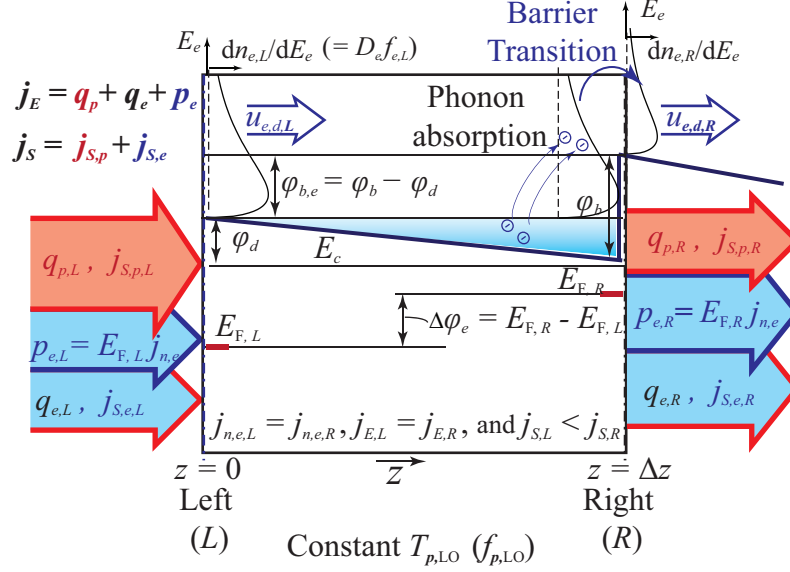


Figure 3.7: Energy and entropy flux in a barrier structure under a steady state. The barrier is located just before the right boundary, and the effective barrier height is defined as the increase in the conduction band edges, ($\varphi_{b,e} = \varphi_b - \varphi_d$). Phonon temperature is fixed as $T_{p,LO}$, and the injected electron distribution ($dn_{e,L}/dE_e$) is equilibrium while the exiting distribution ($dn_{e,R}/dE_e$) is not. With electrochemical potential gain ($\Delta\varphi_e = E_{F,R} - E_{F,L}$), the system produces entropy, conserving electron number and energy.

3.3.2 Barrier transition conversion

3.3.2.1 Analysis scheme

The energy and entropy in a heterobarrier for converting phonon energy to electrical potential are now examined to find the theoretical potential gain and the conversion efficiency. As in Chapter 2, the GaAs/ $\text{Al}_x\text{Ga}_{1-x}\text{As}$ system is considered for a steady state, 1-D transport (z -direction), and the flux vectors for the entropy, energy, and particle number density are described in Fig. 3.7

This analysis includes only the e -(p,LO) interactions dominant in GaAs, and the phonon temperature ($T_{p,LO}$) is assumed to be constant. This is because of the small phonon temperature variation in the small dimension (due to large up- and downcon-

version rate and large phonon density as demonstrated in Chapter 2). The injected electron distribution (at the left boundary, $dn_{e,L}/dE_e$) is that of the equilibrium, and the electron temperature ($T_{e,L}$), number density ($n_{e,L}$), and the Fermi energy are related. In this analysis, $T_{e,L} = 300$ K and $n_{e,L} = 10^{16}$ cm⁻³ are used, then $E_{F,L}$ is 0.094 eV below the conduction band edge (E_c).

The barrier (with a height φ_b) is located just before the right boundary and the potential drop (φ_d) before the barrier is introduced to ensure the electron drift (current). Then, the effective barrier height $\varphi_{b,e}$ is defined as the difference between these two potential changes (or the increase in the conduction band edges), i.e., $\varphi_{b,e} = \varphi_b - \varphi_d$. Due to the barrier transition, the exiting electron distribution ($dn_{e,R}/dE_e$) deviates from the equilibrium. The E_F at the right boundary is higher than the left boundary for the electrochemical potential gain ($\Delta\varphi_e = E_{F,R} - E_{F,L}$).

Under steady-state electron transport, the particle number and the energy conservation are given by Eqs. (3.27) and (3.29), and Eq. (3.34) should be satisfied for the second law of thermodynamics. To use these equations, the electron distributions and the Fermi levels are needed, and since the electron distribution at the right boundary is nonequilibrium, the temperature for the energy level E_e , i.e., $T'_{e,R}(E_e)$, is required and this is calculated using Eq. (3.7) with $E_{F,R}$ and $f_{e,R}$.

The energy conversion efficiency (from the phonon energy to electrical potential) is the ratio of the power gain (from potential gain) and is [similar to Eq. (2.8)]

$$\eta_{p \rightarrow e} = \frac{\Delta p_{e,z}}{\dot{S}_{p \rightarrow e}/A} = \frac{\Delta\varphi_e j_{n,e,z}}{\Delta\varphi_e j_{n,e,z} + \int (q'_{e,R} - q'_{e,L}) dE_e}. \quad (3.36)$$

3.3.2.2 Barrier transition

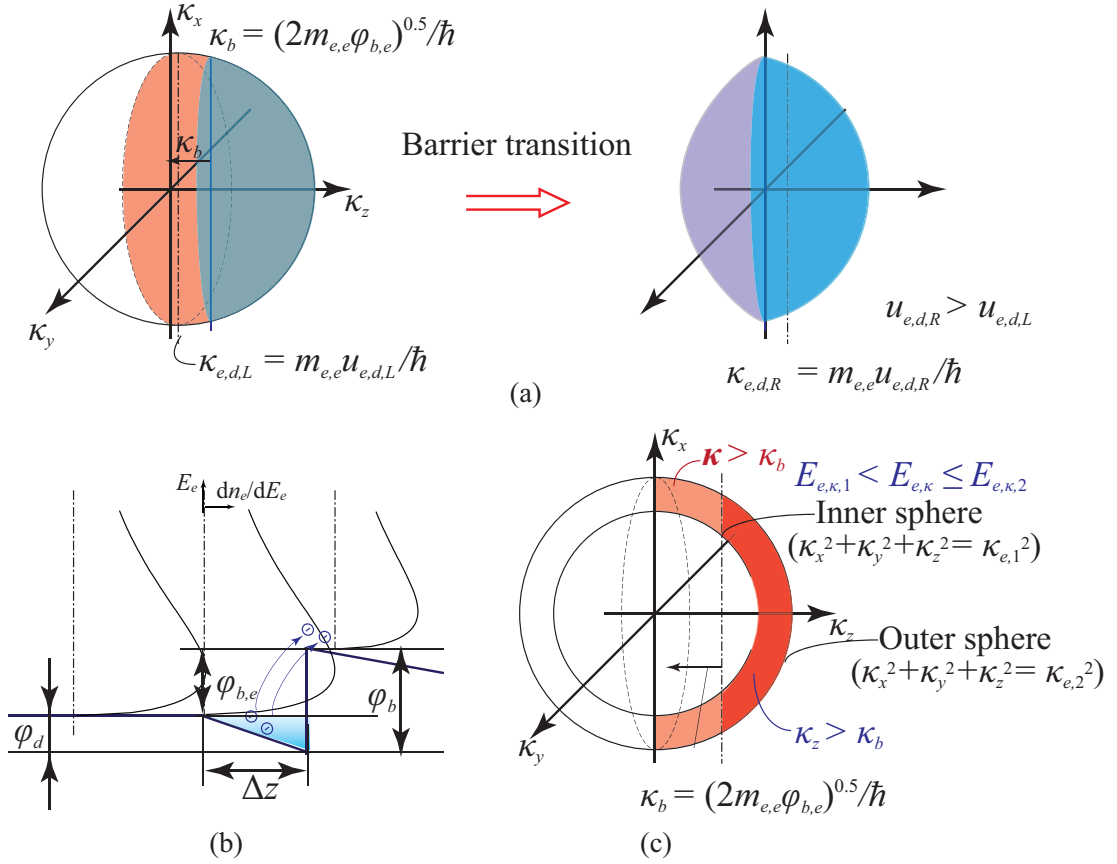


Figure 3.8: (a) Momentum change by barrier transition. With the lateral momentum conservation, electrons lose their momentum by κ_b in z direction. Smaller electron number density after transition leads to a larger drift velocity. (b) Phonon absorption for constant electrical current. With a short distance (Δz) from equilibrium and sufficient phonon absorption, equilibrium distribution before the barrier can be approximated despite faster depletion of high energy electrons. (c) Fraction of transmitted electron population at energy level $E_{e,\kappa}$ ($E_{e,\kappa,1} < E_{e,\kappa} < E_{e,\kappa,2}$). The fraction is the ratio of volume of spherical shell with dark red and volume with dark and light red.

Here, the electron population distribution at the right boundary (right after a barrier transition) is estimated using the lateral momentum conservation (no momentum changes in x and y directions) as described in Fig. 3.8(a). Since scattering

at the barrier (because of small dimension) is not considered (i.e., neither $e-p$, nor $e-e$), there is only energy conversion between electron kinetic and potential. The potential varies only in the transport direction, and the z -direction momentum (κ_z) will decrease after the barrier transition. Therefore, the electrons with $\kappa_z \leq \kappa_b$ will be reflected, and the ones with $\kappa_z > \kappa_b$ will lose their momentum by κ_b , where κ_b is the barrier momentum corresponding to the barrier height $[=(2m_{e,e}\varphi_{b,e})^{0.5}/\hbar]$. For $E_{e,\kappa} \leq \varphi_{b,e}$, no electron can have κ_z larger than κ_b , and even with larger electron kinetic energy ($E_{e,\kappa} > \varphi_{b,e}$), the electrons with smaller κ_z than κ_b are reflected. As a result, smaller electron density is expected after the barrier transition, and the drift velocity should be increased for the particle conservation, $u_{e,d,R} > u_{e,d,L}$. (The drift velocity can change with E_e , but a constant $u_{e,d}$ for all E_e is assumed.)

The injected equilibrium electron distribution is accelerated because of the potential drop (φ_d , introduced for the electron drift), and the accelerated electrons decayed, emitting phonons. Within a short distance (Δz) from the equilibrium injection site or with a sufficient phonon absorption (enhanced by the low-energy electron accumulation by the barrier), the consistent equilibrium distribution up to the barrier is assumed (despite faster depletion of high energy electrons, due to larger $u_{e,d,R}$) as shown in Fig. 3.8(b).

The fraction of transmitted electron population can be obtained using a simple geometric calculation, as shown in Fig. 3.8(c). The electrons with $E_{e,\kappa}$ ranging from $E_{e,\kappa,1}$ to $E_{e,\kappa,2}$ (where $E_{e,\kappa,1} = E_{e,\kappa} - 0.5\Delta E_{e,\kappa}$, $E_{e,\kappa,2} = E_{e,\kappa} + 0.5\Delta E_{e,\kappa}$, and $\Delta E_{e,\kappa}$ is an energy step) are uniformly distributed in the spherical shell between $E_{e,\kappa,1}$ and $E_{e,\kappa,2}$, and then the fraction for barrier transition is the ratio of the spherical shell

volume with dark red and the volume with dark and light red in Fig. 3.8(c).

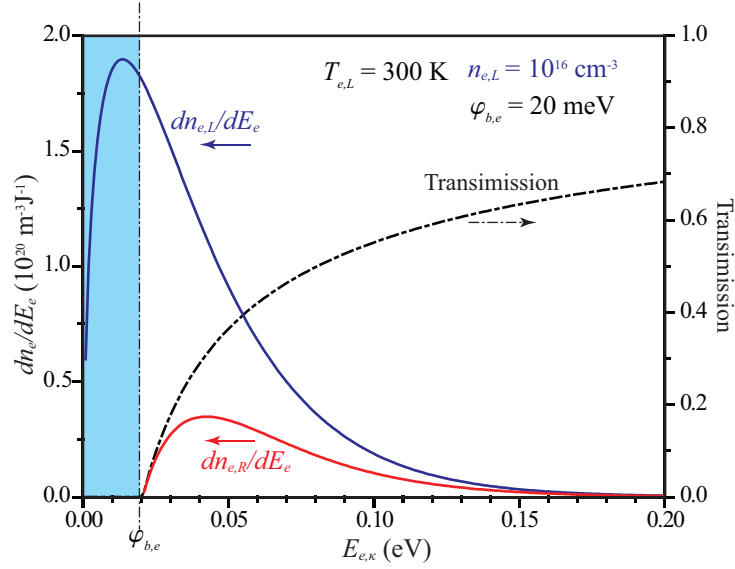


Figure 3.9: Electron population distributions at the left and right boundaries ($dn_{e,L}/dE_e$ and $dn_{e,R}/dE_e$) and variation of barrier transmission with respect to electron kinetic energy ($E_{e,\kappa}$). Electrons at the left boundary are equilibrium with $T_{e,L} = 300$ K and $n_{e,L} = 10^{16}$ cm^{-3} , and the effective barrier height $\phi_{b,e} = 20$ meV. As the energy increases, larger number of electrons can have momentum over κ_b , and this results in higher transmission.

Using this barrier transition mechanism, the electron distribution at the right boundary is calculated. Figure 3.9 shows an example of the electron population distributions at the left and right boundaries ($dn_{e,L}/dE_e$ and $dn_{e,R}/dE_e$) with a barrier structure, when equilibrium electrons are injected at the left boundary and the effective barrier height is $\phi_{b,e} = 20$ meV. Below the barrier height, no electron can transmit the barrier, and the transmission increases with the electron kinetic energy ($E_{e,\kappa}$) (because a larger number of electrons can have momentum larger than κ_b). The electron number density $n_{e,R}$ is smaller than $n_{e,L}$, and this difference increases with the $\phi_{b,e}$. (In Fig. 3.9, 21.5% of total electrons are transmitted.) For the constant

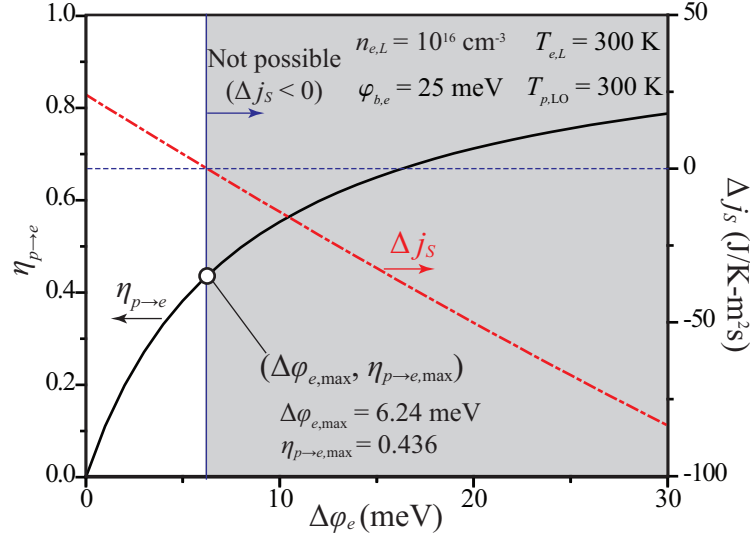


Figure 3.10: Variations of energy conversion efficiency ($\eta_{p \rightarrow e}$) and the net entropy flux (Δj_S) with respect to the potential gain ($\Delta \varphi_e$). Δj_S represents the entropy production rate per unit area in the 1-D transport system. As $\Delta \varphi_e$ increases, $\eta_{p \rightarrow e}$ increases and the entropy production rate decreases. The maximum efficiency $\eta_{p \rightarrow e, \max}$ and potential gain ($\Delta \varphi_{e, \max}$) are found when $\Delta j_S = 0$.

particle flux, the average electron drift velocity at the right boundary ($u_{e,d,R}$) should be inversely proportional to $n_{e,R}$.

3.3.2.3 Maximum potential gain and efficiency

Once the electron distributions at both boundaries are found, the theoretical range of the electrochemical potential gain $\Delta \varphi_e$ is calculated using the continuity equation and the first and second laws of thermodynamics [Eqs. (3.27), (3.29), and (3.34)].

In the electrical current, the phonon temperature cannot be higher than electron temperature, because the energy flows from electron to phonon systems as electric potential is the source for the Joule heating. With interest in recycling the Joule heating as in the HPAB system (Chapter 2), the case of the phonon temperature ($T_{p,LO}$) equal to $T_{e,L}$ (as the maximum possible temperature) is considered first.

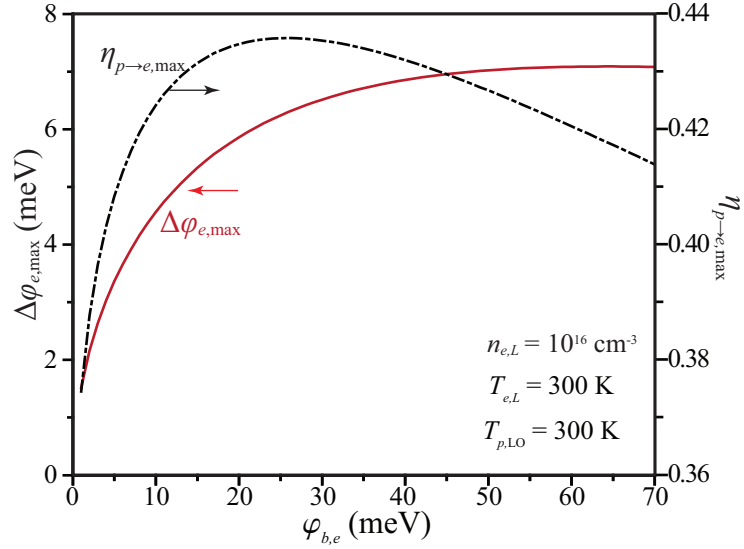


Figure 3.11: Variations of the maximum potential gain ($\Delta\varphi_{e,\max}$) and the maximum energy conversion efficiency ($\eta_{p\rightarrow e,\max}$) with respect to the potential barrier height ($\varphi_{b,e}$). $\Delta\varphi_{e,\max}$ increases with $\varphi_{b,e}$ while $\eta_{p\rightarrow e,\max}$ has the maximum with $\varphi_{b,e} = 25$ meV.

The nonequilibrium $T'_{e,R}$ and the electron heat flux component $q'_{e,R}$ at E_e depend on $E_{F,R}$, and the net entropy flux Δj_S is calculated through the numerical integration of $T'_{e,R}$ and $q'_{e,R}$ using variable $E_{F,R}$. Using Eq. (3.36), the energy conversion efficiency (for phonon to electric potential) $\eta_{p\rightarrow e}$ is calculated. Figure 3.10 demonstrates that $\eta_{p\rightarrow e}$ increases and Δj_S decreases as $\Delta\varphi_e$ increases. For the 1-D, steady-state transport system, Δj_S represents the entropy production rate per unit area, and this rate should be positive. Therefore, the maximum efficiency $\eta_{p\rightarrow e,\max}$ and the potential gain ($\Delta\varphi_{e,\max}$) are found when $\Delta j_S = 0$. When $T_{p,LO} = T_e = 300$ K and $\varphi_{b,e} = 25$ meV, the predicted theoretical maximum efficiency is 43.6% with 6.24 meV as the maximum potential gain.

For variable effective potential barrier heights ($\varphi_{b,e}$), the values of $\Delta\varphi_{e,\max}$ and $\eta_{p\rightarrow e,\max}$ are calculated under zero entropy production ($\Delta j_S = 0$). As Fig. 3.11 shows,

$\Delta\varphi_{e,\max}$ increases with $\varphi_{b,e}$, while $\eta_{p\rightarrow e,\max}$ has a maximum at $\varphi_{b,e} = 25$ meV.

Assuming an external phonon source, this barrier system is also analyzed for variable LO phonon temperatures ($T_{p,\text{LO}}$). High $T_{p,\text{LO}}$ leads to large $\Delta\varphi_{e,\max}$ and $\eta_{p\rightarrow e,\max}$, as shown in Fig. 3.12. Nonequilibrium among phonon modes (LO and A) are also considered, and with an overpopulated LO phonons ($T_{p,\text{LO}} > T_{p,\text{A}}$), the inclusion of the p - p interactions (LO phonon downconversion) decreases $\Delta\varphi_{e,\max}$ and $\eta_{p\rightarrow e,\max}$.

As this analysis shows (and is expected), the theoretical maximum efficiency is higher than the results of the MC simulations (19% for $T_e = T_{p,\text{A}} = T_{p,\text{LO}} = 300$ K [163]). Because there should be electron-phonon interactions and any spontaneous interaction produces entropy, the entropy production in the energy conversion system should be larger than zero, so the efficiency $\eta_{p\rightarrow e}$ is smaller than $\eta_{p\rightarrow e,\max}$. In addition, since the electron distribution decays before the barrier (shown in Fig. 3.8), the barrier transmission of the electrons (the fraction of transmitted electrons) becomes less efficient. The inclusion of more interaction mechanisms, such as the p - p and e - e , will further decrease the efficiency. Due to the assumptions made, the results do not depend on electron drift velocity ($u_{e,d}$), but in the actual system, the $u_{e,d}$ is related to the electron distribution and the electric field (or potential), and these affect the conversion efficiency.

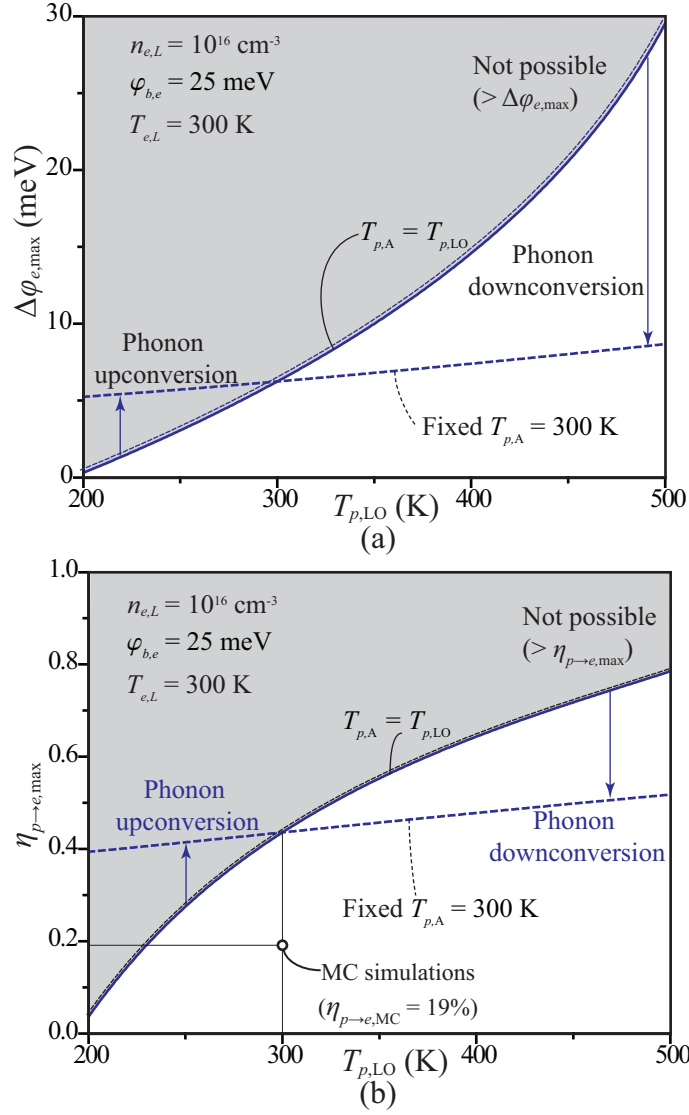


Figure 3.12: Effects of the LO phonon temperature ($T_{p,LO}$) on (a) the maximum potential gain ($\Delta\varphi_{e,\max}$) and (b) the maximum conversion efficiency ($\eta_{p \rightarrow e, \max}$). High phonon temperature leads to large $\Delta\varphi_{e,\max}$ and high $\eta_{p \rightarrow e, \max}$. The efficiency from the MC simulations (in Chapter 2) is lower than this theoretical upper limit $\eta_{p \rightarrow e, \max}$. With an overpopulated LO phonons ($T_{p,LO} > T_{p,A}$), the inclusion of the p - p interactions reduces $\eta_{p \rightarrow e, \max}$ and $\Delta\varphi_{e,\max}$.

3.4 Summary

In this chapter, addressing the statistical entropy of the phonon and electron systems, their entropy production is studied under the phonon-phonon and electron-phonon interactions and phonon-electric potential conversion. We note that spontaneous interaction will increase the system entropy, and the temperatures indicate the direction of energy flow.

In the entropy analysis and its applications, we use the first and the second laws of thermodynamics (i.e., energy conservation and entropy production), and predict the maximum efficiency under zero entropy production condition. For the heterobarrier structure introduced and discussed in Chapter 2, the spontaneous phonon absorption is achieved through lower electron temperatures created by converting electron kinetics to potential in a barrier structure, and the upper limit of phonon-electron potential conversion efficiency is found using this entropy analysis. As expected, the non-ideal, irreversible MC simulation results for efficiency are lower than this theoretical upper limit.

Chapter 4

Interfacial Atomic Restructuring and Phonon Conductance

4.1 Interfacial thermal transport

Heat transfer across interfaces is central in design and performance of micro/nano devices, because of the dominance of the interfacial thermal resistance over the bulk resistances on each side of the interface. In this chapter, the interfacial thermal energy transport is examined with particular attention to the role of interfacial-region atomic structure (which depends strongly on how the interface of the two solids is formed) and its effect on the phonon density of states. As an example with application in thermal management of high-power circuits, the thermal transport across the interface of

Si with a soft, low melting temperature metal such as indium is examined. In this application, In is allowed to melt (phase change) to absorb high peak in cyclic heating. So, to address reducing the circuit temperature via solid-liquid phase change energy storage, we also consider the molten phase of In.

4.1.1 Treating interfacial phonon transport

The acoustic mismatch model (AMM) (for specular surfaces) and diffuse mismatch model (DMM) have been used to estimate the phonon boundary resistance [176]. The DMM assumes all phonons are diffusely scattered at the boundary and then transported in proportion to the phonon density of states D_p and the phonon speed u_p of each side, so the transmission probability (from material 1 to 2) $\tau_{1\rightarrow 2}(\omega)$, is [176]

$$\tau_{1\rightarrow 2}(\omega) = \frac{\sum_j u_{p,2,j} D_{p,2,j}(\omega)}{\sum_j u_{p,1,j} D_{p,1,j}(\omega) + \sum_j u_{p,2,j} D_{p,2,j}(\omega)}, \quad (4.1)$$

where j is the phonon mode and ω is the phonon frequency.

While the AMM is limited to low temperatures (~ 30 K) and smooth surfaces, the DMM provides relatively good agreements with the experiments at room or higher temperatures [31]. Since the DMM is based on the Debye approximations and the bulk properties of the materials in contact, it only applies to interfaces with high and similar Debye temperatures T_D . Otherwise, the measured bulk phonon dispersion and D_p [134, 139], the joint phonon properties for the interfacial region [70], or the virtual crystal representing the disordered interfacial region [10] have been used in the DMM.

To verify the theoretical models, molecular dynamics (MD) simulations with no restrictions on the boundary phonon scattering have been used [100, 173]. However, more realistic interfaces and theoretical models for them have not been addressed, and more accurate predictions are expected with guidance from the *ab initio* calculations, e.g., advances in computing methods have enabled prediction of the interfacial structures [191] and phonon properties [50] using the density functional theory (DFT).

Here, the interfacial-region phonon properties are addressed mainly using nonequilibrium molecular dynamics (NEMD), with the NEMD employing cross-boundary reaching force fields (potentials) from the *ab initio* simulations. Also, the semi-classical DMM is employed for the comprehensive analysis of the simulation results, noting that this Si/In (phase change material) interface is challenging to treat with the DMM due to the strong contrast in material properties [176].

4.1.2 Electronic thermal transport

The NEMD allows only for treating the phonon transport with interphonon scattering, however electrons contribute to thermal energy transport, especially in metals. For the semiconductor/metal interface considered, the electron (metal)–electron (semiconductor) and the electron (metal)–phonon (semiconductor) interactions are addressed for boundary transport involving electrons.

The electronic thermal resistance due to the electron–electron interaction across

the boundary is found from the Wiedemann-Franz law given as [32, 82]

$$AR_{e,k} = \frac{AR_{e,e}}{N_{L,o}T}, \quad (4.2)$$

where $AR_{e,k}$ is the electronic thermal resistance, $AR_{e,e}$ is the electrical resistance, $N_{L,o}$ is the Lorenz constant ($= \pi^2 k_B^2 / 3e_c^2 = 2.442 \times 10^{-8} \text{ W}\cdot\Omega/\text{K}^2$), and T is the temperature. $AR_{e,e}$ can be estimated by considering the tunneling probability across the Schottky barrier (formed by the metal and semiconductor contact) [32, 177]. Unless the semiconductor is very heavily doped, thermal transport by the electron-electron interaction is minor compared with phonon transport, due to the low density and tunneling probability of the electrons to pass through the carrier depletion region from the contact [83]. [In the Si/In interface with doping concentration 10^{20} cm^{-3} for n -type Si, $AR_{e,k} = 100$ to $1000 \text{ nK}/(\text{W}/\text{m}^2)$ depending on T , which is 10 to 100 times larger than the calculated phonon resistance.]

The transport by electron–phonon coupling can be negligible at low temperatures, but is more significant in the interfacial transport at the high temperatures [155]. Recent experiments [111] and theoretical calculations [112] show that without special control the coupling may have small contribution to the interfacial transport. Here, the phonon transport is only considered using NEMD and DMM.

Table 4.1: Si properties from the Stillinger-Weber potential and experiments [61].

| Properties | Stillinger-Weber | Experiments |
|-----------------------------|------------------|-------------|
| Lattice constant, Å | 5.431 | 5.431 |
| Bulk Modulus, GPa | 101.4 | 100.0 |
| Elastic constant, GPa | C_{11} | 151.4 |
| | C_{12} | 76.4 |
| | C_{44} | 56.4 |
| Thermal conductivity, W/m-K | 139 | 149 |

4.2 Nonequilibrium molecular dynamics (NEMD)

4.2.1 Interatomic potentials

In MD, interatomic potentials are necessary to calculate the forces on ions to update the system configuration, and for the Si/In layer simulation, the Si-Si, In-In and Si-In interatomic potentials are required. The Stillinger-Weber potential is a well known potential model for Si interactions [174], and also employed in this work. Interatomic potentials can be verified by comparing physical properties derived from the potential models with experimental values, and the properties are calculated by molecular dynamics and lattice dynamics using GULP (General Utility Lattice Program) [52]. Thermal and mechanical properties from the Stillinger-Weber potential agree well with experiments, as shown in Table 4.1.

For the In-In interaction, the pair-wise Morse potential is developed from the *ab initio* simulations with the Vienna *ab initio* simulation package (VASP) by fitting the experimental thermal properties. The developed In-In interatomic potential has the parameters set as $\varphi_{o,In-In} = 0.1336$ eV, $a_{In-In} = 0.961$ Å⁻¹, $r_{o,In-In} = 3.41$ Å, and $r_{c,In-In}$

Table 4.2: In properties from the developed Morse potential, MEAM and experiments [61].

| Properties | | Morse | MEAM | Experiments |
|--|-----------------|--------|--------|-------------|
| Atomic structure* | | FCC | BCT | BCT |
| Bulk Modulus, GPa | | 14.945 | 43.2 | 35.3 |
| Elastic constant C_{11} , GPa | | 19.583 | 58.6 | 44.5 |
| Density, kg/m ³ | at 300 K | 7344 | 7314.5 | 7310 |
| | Solid at T_m | 7176 | | 7214 |
| | Liquid at T_m | 7095.7 | | 7024 |
| Melting T_m , K | | 430 | 645 | 429.75 |
| ΔV of melting [‡] , % | | 1.131 | 0.41 | 2.0 |
| ΔH_m , kJ/mol [†] | | 1.118 | 7.24 | 3.28 |
| c_p (0-100°C), J/mol-K | | 25.850 | 21.8 | 27.9 |

* FCC: face-centered cubic, BCT:body-centered tetragonal

[‡] volume change in melting, [†] melting enthalpy change

(cut-off radius) = 5.235 Å in the Morse potential model,

$$\varphi_{\text{Morse}}(r_{ij}) = \varphi_o[(1 - \exp[-a(r_{ij} - r_o)])^2 - 1]. \quad (4.3)$$

Other In potentials such as the modified embedded atom model (with stronger bond) [39] were considered, however the developed Morse potential predicts the thermal properties most accurately as shown in Table 4.2.

For the Si-In interactions which affect the interfacial structure, the Morse potential was developed from the force field between Si slab and In atom from the *ab initio* calculations (with parameter set as $\varphi_{o,\text{Si-In}} = 0.3990$ eV, $a_{\text{Si-In}} = 0.8965$ Å⁻¹, $r_{o,\text{Si-In}} = 3.402$ Å, and $r_{c,\text{Si-In}} = 5.0$ Å) instead of using the combinative rule between Si and In potential models (because of the different forms of the Si and the In potentials).

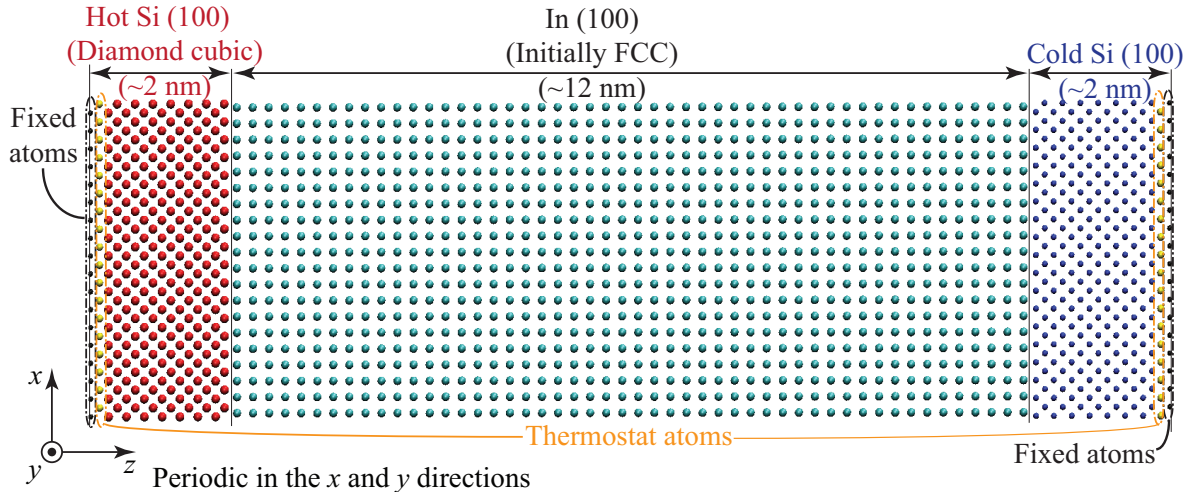


Figure 4.1: NEMD simulation scheme and the initial structure. In and Si have initially face-centered cubic (FCC) and diamond cubic (or zinc-blende) structures, respectively. The simulated structure is periodic in the x and y directions, and different temperatures are prescribed on both sides through the Langevin thermostats.

4.2.2 NEMD simulation scheme and equations

NEMD simulations employing the potentials discussed in the previous subsection are performed with the initial system configuration described in Fig. 4.1, the code for the simulations was developed with Fortran90. The simulations also employ the NVT ensemble (constant number of particles, volume, and temperature) with average temperatures from 200 to 700 K, and the velocity-Verlet algorithm for the equations of motions. The temperature of the system is controlled by the Langevin thermostat, which stochastically adds or removes kinetic energy of the thermostat atoms [184]. Periodic boundary conditions are imposed in the x and y directions, and Si layers are placed on both sides of the In layers in the z direction (the Si end-atoms are fixed and the next-to-end atoms are used as the thermostat atoms). 10000 In atoms and 5184 Si atoms (2592 each side) are simulated in a rectangular parallelepiped simulation

cell of volume $4.8 \times 4.8 \times 16 \text{ nm}^3$ (Si: 2 nm/In: 12 nm/Si: 2 nm). The interfaces are initially connected as diamond cubic (100) Si surface and face-centered cubic (100) In surface. The initial simulation cell size and density are selected to minimize the lattice mismatch, based on the MD equilibrium density in NpT ensemble (constant number of particles, pressure, and temperature). To examine the interfacial thermal transport, a temperature difference is prescribed across the Si/In/Si system, and the steady-state temperature distribution and heat flux are calculated.

4.2.3 Heat flow and phonon properties

The temperature distribution is from the ensemble-average kinetic energy within divided position bins and the heat flux q_{MD} is the net kinetic, potential and pressure energy flow, i.e., [77]

$$q_{\text{MD}} = \frac{1}{V} \left[\sum_i \frac{1}{2} m_i (\mathbf{u}_i \cdot \mathbf{u}_i) u_{i,z} + \sum_i \varphi_i u_{i,z} + \frac{1}{2} \sum_i \sum_j z_{ij} (\mathbf{u}_i \cdot \mathbf{F}_{ij}) \right], \quad (4.4)$$

where V is the volume, m_i is the mass of particle i , \mathbf{u}_i is the velocity vector, $u_{i,z}$ is the z -component of \mathbf{u}_i , φ_i is the potential energy, z_{ij} is the z -component of the interatomic separation, and \mathbf{F}_{ij} is the interaction force between i and j particles. q_{MD} can be also estimated by calculating stochastically added or removed kinetic energy in the Langevin thermostats on both sides, and the results from this method are similar to the ones from Eq.(4.4). Using the temperature distribution (only considered in the z direction) and heat flux, the thermal conductivity and the interfacial resistance are

calculated as

$$k_p = -\frac{q_{\text{MD}}}{dT_p/dz} \quad \text{and} \quad AR_b = \frac{\Delta T_{p,\text{interface}}}{q_{\text{MD}}}, \quad (4.5)$$

where $\Delta T_{p,\text{interface}}$ is the temperature difference across the interface.

For the DMM calculations, we use bosons $f_p^o = [\exp(\frac{\hbar\omega}{k_B T}) - 1]^{-1}$, where \hbar is the reduced Planck constant and k_B is Boltzmann constant, and D_p from the Fourier transform of the velocity autocorrelation function, $u^{2*}(t)$ of the MD simulation results [82]

$$u^{2*}(t) = \frac{\sum_i \langle \mathbf{u}_i(t) \cdot \mathbf{u}_i(0) \rangle}{\sum_i \langle \mathbf{u}_i(0) \cdot \mathbf{u}_i(0) \rangle} \quad \text{and} \quad D_p(\omega) = \int_0^\tau u^{2*}(t) \cos(\omega t) dt, \quad (4.6)$$

where $\langle \rangle$ is an ensemble average and τ is taken as 15 ps which is based on the $\Delta\omega$ resolution for D_p taken as 2.094×10^{11} rad/s ($= \pi/\tau$).

4.3 Results and analysis

Various results, such as the atomic structure, temperature distribution and heat flux, are obtained from the NEMD simulations over 2 ns. The ensemble averages for the temperature distribution and heat flux are taken over more than 1 ns after the simulated system is stabilized.

4.3.1 Atomic structure

Si remains solid, while In, with the Morse potential model, melts at 430 K. Even below this temperature, due to force fields from the adjacent-layer atoms, the Si and

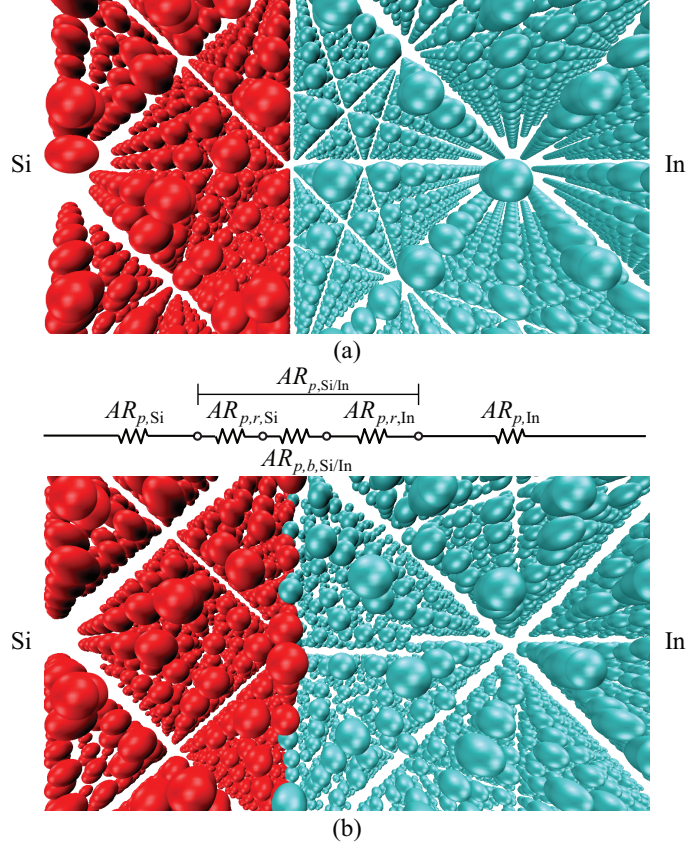


Figure 4.2: (a) Interfacial Si and In atomic structures without interactions (initial equilibrium condition), and (b) with interactions and restructuring obtained from the MD simulations at 300 K. The bulk resistances ($AR_{p,Si}$ and $AR_{p,In}$) and the total interfacial resistance ($AR_{p,Si/In}$) [decomposed into the boundary ($AR_{p,b,Si/In}$) and two interfacial-region resistances ($AR_{p,r,Si}$ and $AR_{p,r,In}$)] are shown through the thermal circuit diagram.

In atoms adjacent to the boundary are restructured to satisfy the energy minimization, as presented in Fig. 4.2(b), compared to the initial equilibrium non-restructured lattice structure in Fig. 4.2(a). The structure disorder by restructuring can be quantified using the static structure factor, given by [36]

$$|S(\mathbf{k})|^2 = \left[\frac{1}{N} \sum_i \cos(\mathbf{k} \cdot \mathbf{r}_i) \right]^2 + \left[\frac{1}{N} \sum_i \sin(\mathbf{k} \cdot \mathbf{r}_i) \right]^2, \quad (4.7)$$

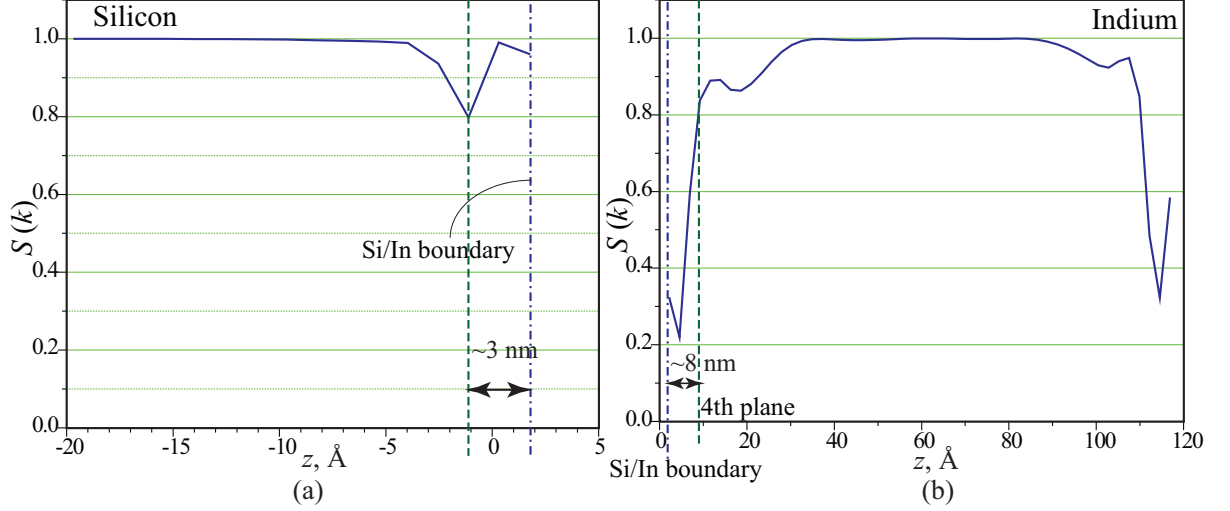


Figure 4.3: Structure factor, $S(\mathbf{k})$ in (a) Si and (b) In layers at 300 K. $S(\mathbf{k})$ decreases around the Si/In boundary, showing non-crystalline by restructuring. Softer In has longer restructuring layers than Si.

where i is the index for atoms, \mathbf{k} is a reciprocal lattice vector in the x - y plane [for the planar $S(\mathbf{k})$], and \mathbf{r} is the position vector. With the perfect crystallinity, $S(\mathbf{k})$ is unity, and more disordered structure has smaller $S(\mathbf{k})$. As Fig. 4.3 shows, $S(\mathbf{k})$ is reduced around the Si/In boundary, showing non-crystalline by restructuring. The change of $S(\mathbf{k})$ in In is more significant and appears in larger number of layers, and this demonstrates that the softer In is more restructured than Si.

4.3.2 Thermal conductivity

From the thermal analysis of the Si/In interface, we calculate the phonon conductivity of Si and In in phase i (s for solid, and l for liquid phase) [$k_{p,\text{Si or In},i} = -q_{\text{MD}}/(dT/dz)$] and the thermal resistance ($AR_i = \Delta T_i/q_{\text{MD}}$) from the heat flux q_{MD} and the temperature distribution, as shown in Fig. 4.4.

Due to the boundary scattering, phonon conductivity from the NEMD is size-

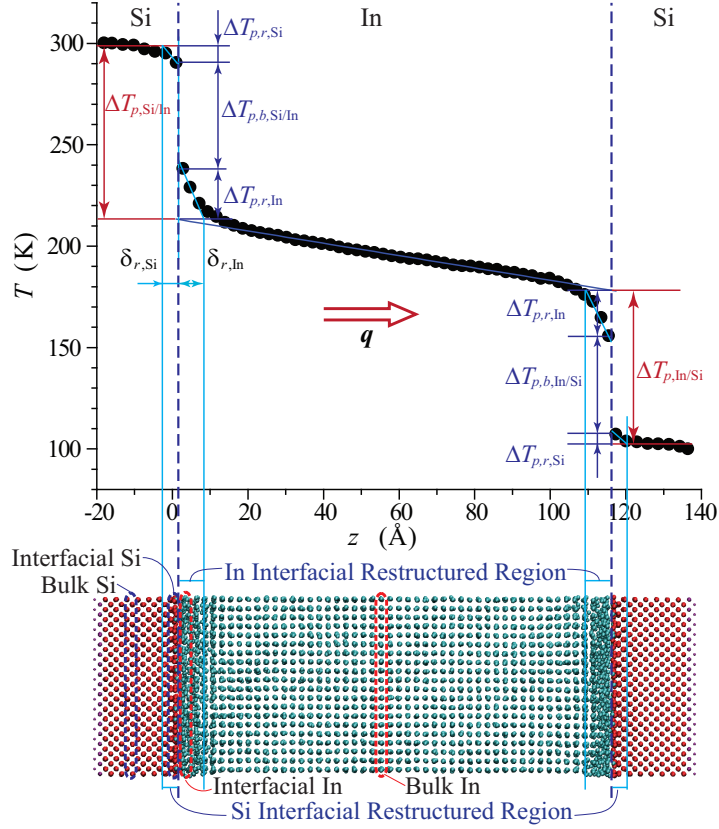


Figure 4.4: Temperature distribution with heat flowing along direction z (cold thermostat at 100 and hot at 300 K).

dependent, so smaller simulation cell results in smaller conductivity [150]. Therefore, considering this finite-size effect, the bulk thermal conductivity can be extrapolated as shown in Fig. 4.5. From the NEMD, the Si phonon conductivity $k_{p,\text{Si}}$ (obtained using the simulations only with Si atoms) is 139.1 W/m-K at 300 K, which is in good agreement with the experiment (149 W/m-K in [61]).

When the acoustic phonons are the main transport carriers and the three-phonon processes (at high temperatures, normally above $1/4$ – $1/5$ of the Debye temperature), the phonon conductivity of the crystals is predicted by the Slack relation [168, 74]

$$k_p = k_{p,S} = \frac{3.1 \times 10^4 \langle M \rangle V_a^{1/3} T_{D,\infty}^3}{T \langle \gamma_G^2 \rangle N_o^{2/3}}, \quad (4.8)$$

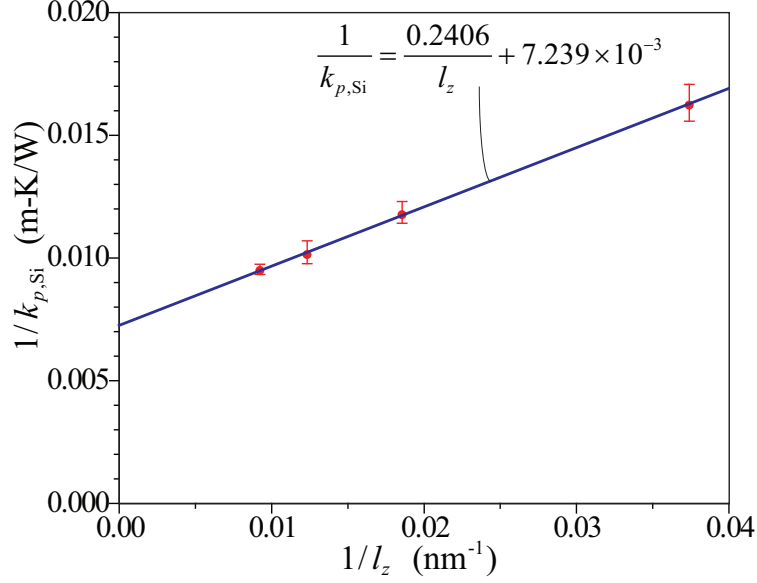


Figure 4.5: Size dependence of Si phonon conductivity, $k_{p,Si}$. Inverse conductivity is proportional to inverse simulation cell size [150]. Using this relation and extrapolation, the bulk thermal conductivity can be obtained.

where $\langle M \rangle$ is the mean atomic weight of the atoms in a primitive cell, $V_a = 1/n$ is the average volume per atom, $T_{D,\infty}$ is the high-temperature Debye temperature, T is the temperature, N_o is the number of atoms in a primitive cell, and $\langle \gamma_G^2 \rangle$ is the mode-averaged square of the Grüneisen parameter. Here, $T_{D,\infty}$ is extracted from the phonon density of states D_p , i.e.,

$$T_{D,\infty}^2 = \frac{5h_P^2 \int_0^\infty f^2 D_p(f) df}{3k_B^2 \int_0^\infty D_p(f) df}, \quad (4.9)$$

where h_P is the Planck constant, k_B is the Boltzmann constant, and f is the phonon frequency. Indium contains only acoustic phonon modes, and the Debye temperature is low, thus the Slack relation can be used.

Figure 4.6 shows the variation of In phonon conductivity ($k_{p,In}$) with respect to temperature, and $k_{p,In,s}$ decreases from 1.7 to 0.72 W/m-K, as the temperature in-

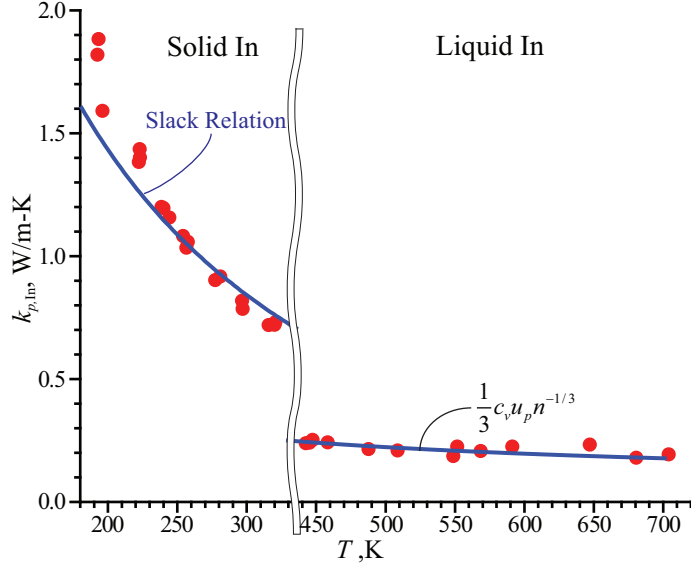


Figure 4.6: Variation of In phonon conductivity ($k_{p,\text{In}}$) with respect to temperature (T). Conductivity decreases with T . The phonon conductivity of solid In agrees well with the Slack relation, and the kinetic theory with the Kittel model for the mean free path works well in liquid.

creases from 200 to 320 K. As expected, these are in good agreement with the Slack relation [168, 74] using D_p and density from NEMD, but as expected much smaller than the total thermal conductivity including electronic contribution, i.e., 81.6 W/m-K at 300 K [61]. Electronic thermal conductivity $k_{e,\text{In},s}$ is much larger than $k_{p,\text{In},s}$, so the electronic thermal transport is dominant in the bulk In transport. Upon melting, the thermal conductivity of In drops and slightly decreases with temperature (0.24 W/m-K at 450 K, 0.21 W/m-K at 700 K), in good agreement with the Kittel model [90] for disordered structures. With the phonon mean free path λ_p equal to the average interatomic spacing l_a (from atomic number density n), the kinetic theory gives [82]

$$k_p = \frac{nc_v u_p \lambda_p}{3}, \quad (4.10)$$

where $u_{p,A}$ is the average phonon propagation speed from elastic constants, and c_v is the specific heat capacity calculated from the MD results for D_p and f_p^o .

4.3.3 Decomposition of interfacial resistance

Despite the exclusion of electronic thermal transport, most of the temperature drop occurs near the boundary, as shown in Fig. 4.4, thus the bottleneck in thermal transport is the interfacial thermal resistance. Adjacent to the interfaces temperature distributions are nonlinear, because the atomic restructuring and boundary interaction lead to extra phonon scattering and lower local thermal conductivities. The restructured regions (with nonlinear temperature distributions) extend only on the order of the cut-off radii of the force fields on each side. The extra scattering in these regions is represented with the interfacial-region resistance, which is traditionally included in the thermal boundary resistance. So, the total interfacial resistance $AR_{p,\text{Si/In}}$ is the sum of the boundary resistance $AR_{p,b,\text{Si/In}}$ and the two interfacial-region resistances $AR_{p,r,\text{Si}}$ and $AR_{p,r,\text{In}}$ (the corresponding temperature jumps for the three resistances are shown in Fig. 4.4), i.e.,

$$AR_{p,\text{Si/In}} = AR_{p,b,\text{Si/In}} + AR_{p,r,\text{Si}} + AR_{p,r,\text{In}}. \quad (4.11)$$

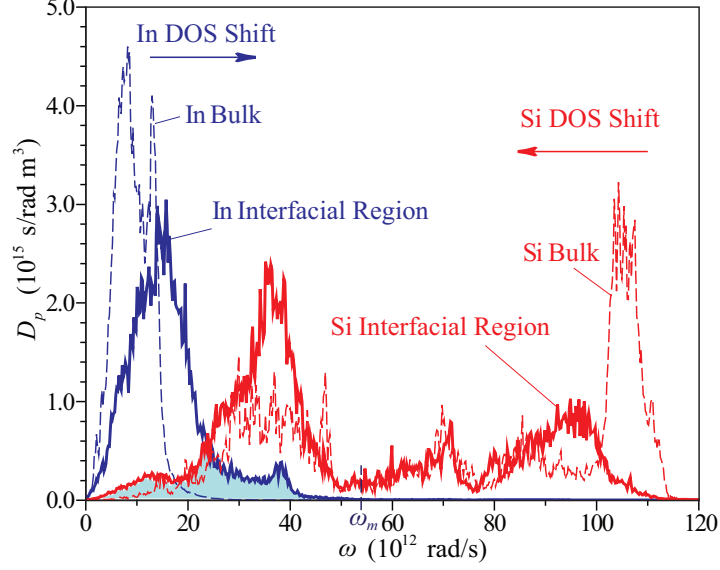


Figure 4.7: MD phonon density of states of Si and In, in the bulk and the interfacial regions [within $0.5r_{c,\text{Si-In}}$ from the nominal interface]. Due to the interpenetration of force fields and atomic restructuring, D_p is distorted in the interfacial region. The blue shaded region represents shared phonon states between Si and In in the interfacial region. The interfacial D_p s (solid lines) have more shared phonon states participating in the boundary transport, compare to the bulk D_p s (dashed lines).

4.3.4 Analysis of interfacial resistance

4.3.4.1 Phonon spectrum in interfacial region

In these interfacial regions, D_p is modified due to the atomic restructuring and interactions between Si and In atoms, as presented in Fig. 4.7. The interfacial-region $D_{p,\text{Si}}$ and $D_{p,\text{In}}$ are calculated using Eq. (4.6) within the region bounded by the nominal interface and $0.5r_{c,\text{Si-In}}$, while the bulk values are calculated with 200 atoms in the central region (in z direction), as marked in Fig. 4.4. The $D_{p,\text{Si}}$ shifts to the lower energies and $D_{p,\text{In}}$ moves to higher energies, and the changes in $D_{p,\text{In}}$ are more pronounced than $D_{p,\text{Si}}$.

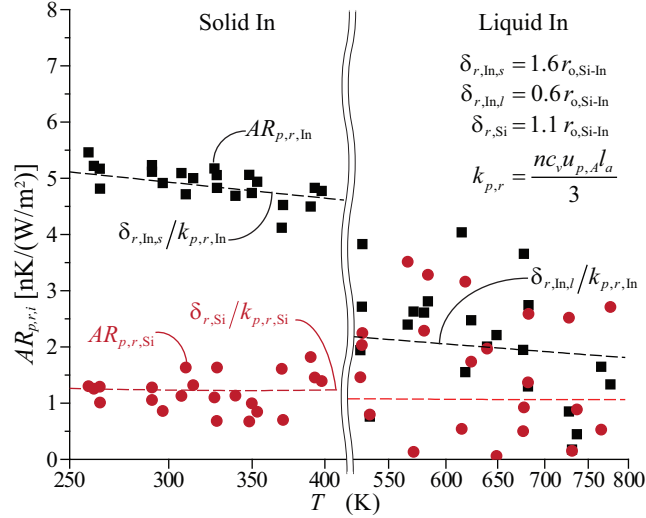


Figure 4.8: Comparison of the variations of the NEMD Si/In thermal boundary resistance as a function of temperature, with the DMM theory. The liquid NEMD simulation results have larger scatter due to the local temperature fluctuations. The scatter increases with increase in temperature (larger kinetic energy) and with smaller heat flux (lower thermal conductivity).

4.3.4.2 Interfacial-region resistance

A sample temperature distribution in the restructured regions, shown in Fig. 4.4, suggests lower thermal conductivity $k_{p,r}$ or reduced λ_p , due to the enhanced scattering. Then the $k_{p,r}$ decreases as the boundary is approached because the λ_p decreases to l_a near the diffusely scattering boundary. Moreover, asymmetric force field near the boundary reduces $u_{p,A}$ (depending on the interaction potential), it additionally decreases the phonon conductivity.

Using n and c_v from the MD density and D_p in the interfacial region with $\lambda_p = l_a = (2^{1/2}/n)^{1/3}$ and the MD interfacial region phonon conductivity $k_{p,r} = (nc_v u_{p,A} l_a)/3$ ($k_{p,r,In} \simeq 0.1$ and $k_{p,r,Si} \simeq 0.3$ W/m-K), the interfacial-region $u_{p,A}$ is estimated to be 0.4 to 0.5 of the bulk $u_{p,A}$.

The restructuring length is defined as $\delta_{r,i} \equiv k_{p,r,i} AR_{p,r,i}$, and the dimensionless $\delta_{r,i}^*$

($= \delta_{r,i}/r_{o,\text{Si-In}}$) from the NEMD results are $\delta_{r,\text{In},s}^* \simeq 1.6$, $\delta_{r,\text{In},l}^* \simeq 0.6$, and $\delta_{r,\text{Si}}^* \simeq 1.1$, as listed in Fig. 4.8. [These solid-phase restructuring lengths are in a good agreement with the locations where the average (over three principal reciprocal vectors) static structure factor in Fig. 4.3 is 0.5.] These indicate that the interfacial restructuring for solid/solid extends further into the softer material, and the solid In restructuring extends over the cut-off radius $r_{c,\text{Si/In}}$ of the effective force (potential) of interaction with Si. Since the interfacial-region resistance is the decrease in thermal conductivity in the interfacial region, the softer In with extended restructured region has the larger interfacial-region resistance [$\sim 5 \text{ nK}/(\text{W}/\text{m}^2)$] compared to the harder Si [$\sim 1.3 \text{ nK}/(\text{W}/\text{m}^2)$]. The liquid-phase In interfacial-region resistance is smaller than the solid phase, because the liquid already has a disordered structure and lower thermal conductivity, as shown in Fig. 4.8.

4.3.4.3 Boundary resistance

For $AR_{p,b}$, all phonons with energy $\hbar\omega$ are assumed to travel to the boundary region with average speed $u_{p,A}$ and are then completely scattered as assumed in the DMM theory, because here the diffuse interfacial scattering is dominant at temperatures over 200 K and in the presence of the non-crystalline phases at the boundary. Using this phonon speed and D_p for both interfacial regions, with the DMM $\tau_{1\rightarrow 2}(\omega)$ from Eq. (4.1), the phonon boundary resistance is [176]

$$\begin{aligned} \frac{1}{AR_{p,b,\text{DMM}}} &= \frac{q_{net}}{T_1 - T_2} \\ &= \frac{1}{4} \int_{\omega=0}^{\omega_m} \frac{[f_p^o(\omega, T_1) - f_p^o(\omega, T_2)]}{T_1 - T_2} D_{p,1}(\omega) \hbar\omega u_{p,A,1} \tau_{1\rightarrow 2}(\omega) d\omega, \end{aligned} \quad (4.12)$$

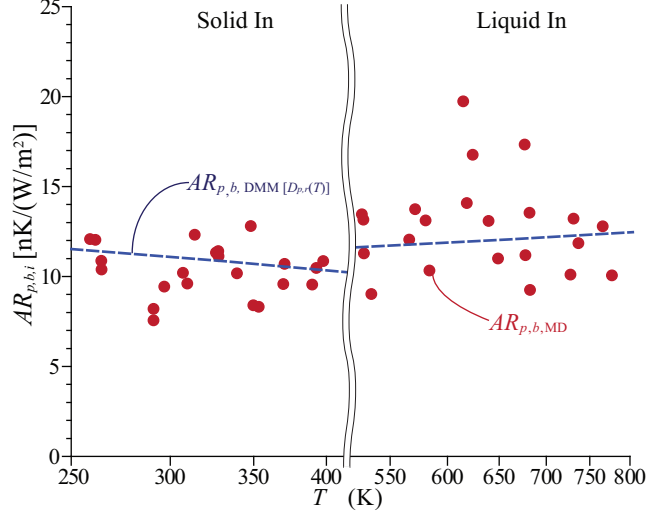


Figure 4.9: Comparison of the variations of the NEMD thermal interfacial-region resistances (in In and Si) as a function of temperature, with the approximate relation $\delta_{r,i}/k_{p,r,i}$.

where ω_m is the cut-off frequency of the softer material. From Eq. (4.1), only phonons which can exist on the both sides contribute to the phonon transport with nonzero $\tau_{1 \rightarrow 2}(\omega)$. Figure 4.7 shows in their interfacial regions In and Si have larger range of shared phonon states, about four times compared to the bulk (and these participate in the boundary transport). The retarded $u_{p,A}$ in the interfacial region also reduces the phonon energy flux at the boundary.

In Fig. 4.9, the DMM phonon boundary resistances $AR_{p,b,DMM[D_{p,r}(T)]}$ calculated with the interfacial properties [11 to 13 nK/(W/m²)] are in good agreement with the NEMD results ($AR_{p,b,MD} = \Delta T_{p,b}/q_{MD}$), whereas using the Debye D_p ($AR_{p,b,DMM[D_{Debye}]}$) and the bulk phonon properties ($AR_{p,b,DMM[D_{p,bulk}(T)]}$) overestimates $AR_{p,b}$ [using the bulk MD properties of Si and In gives 21.55, while the Debye model give 82.43 nK/(W/m²)].

At higher temperatures, the controlling, softer material In has more high-energy

phonons participating in the transport, and $AR_{p,b}$ decreases. For the liquid In, the reverse occurs because D_p will have more low-energy (longer wavelength) modes due to the increased anharmonicity.

4.4 Summary

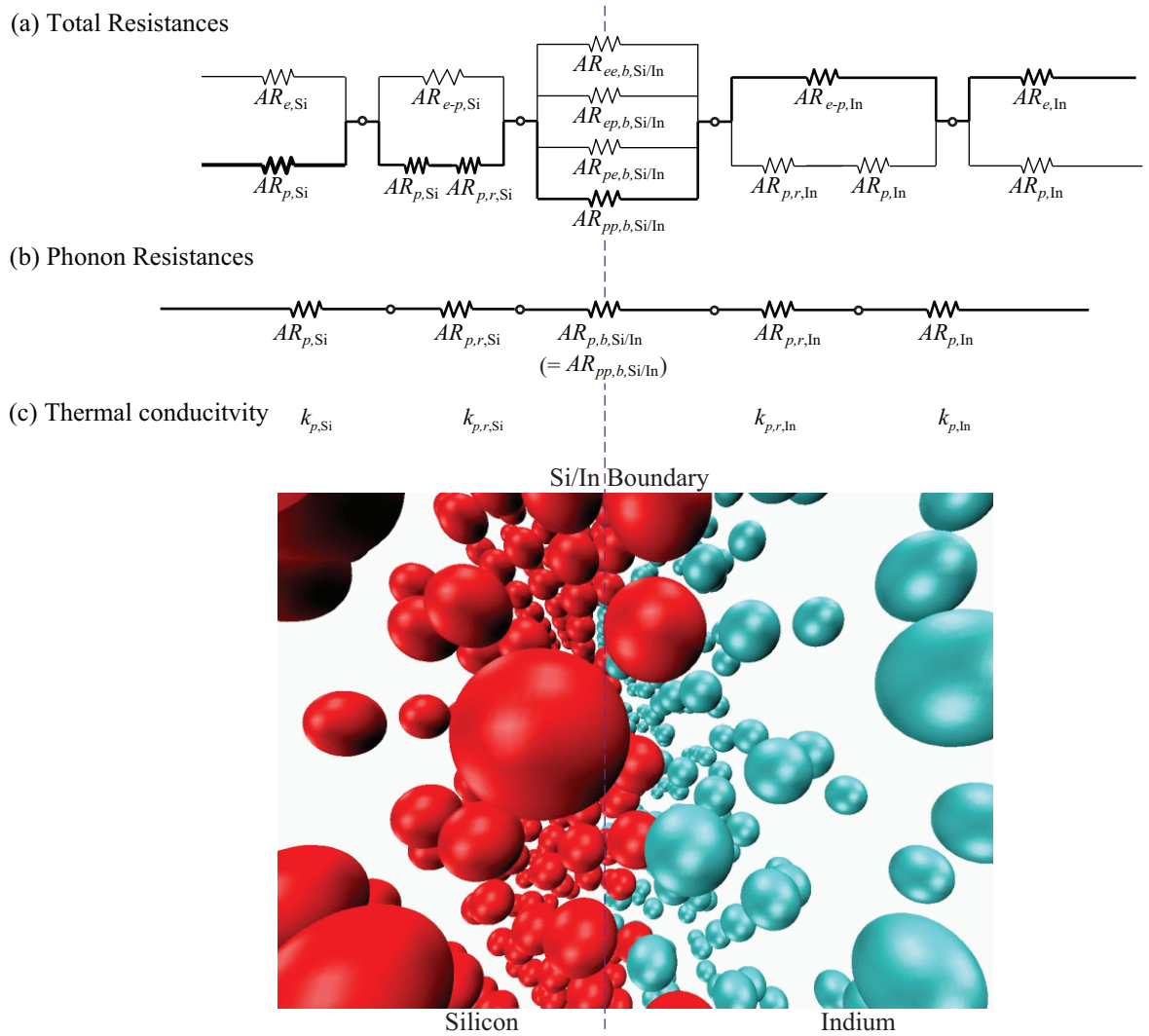


Figure 4.10: Overall thermal circuit diagram. (a) All the resistances in the Si/In contact are described, and the main transport channels are shown with thicker lines. (b) This work mainly considers phonon resistances, and the decomposition of interfacial resistance (into $AR_{p,b}$ and $AR_{p,r}$) is suggested. (c) The interfacial region has a lower thermal conductivity ($k_{p,r}$) due to the atomic restructuring.

In this chapter, the interfacial thermal transport is analyzed by treating the interfacial atomic restructuring and its phonon transport with NEMD, for Si/In interface. The electron contribution to the thermal transport is also addressed, while phonon transport is dominant. The thermal circuit for the interfacial transport is shown in Fig. 4.10, and the thermal resistances as the main transport channels are shown with thicker lines. While electrons are the main transport carriers in metal In, phonons dominate in the boundary and in semiconductor Si.

The interfacial phonon resistance is decomposed into the boundary and interfacial-region components. The atomic restructuring and the boundary interactions were found to reduce the boundary resistance by providing additional phonon transport channels (modes), while adding an extra scattering resistance by the non-crystalline interfacial regions. The DMM using the interfacial-region phonon properties predicts the boundary resistance in good agreement with NEMD, even with low T_D materials, and this is also the case when one material is in the liquid phase. For the interfacial-region resistances, a simple model is provided based on the minimum λ_p . In the NEMD thermal contact analysis, without the interfacial-region resistances (due to the non-crystalline region, which has lower local thermal conductivity than crystalline phase), the bulk behavior away from the interface is not recovered. Adding the boundary resistance from the DMM and the interfacial-region resistances, this is the total interfacial resistance found in experiments. While for the Si/In example considered the total interfacial resistance is less than that predicted by the DMM based on bulk properties, this cannot be generalized for less contrasting material pairs. More accurate predictions of the interfacial-region atomic structures and phonon properties,

such as the *ab initio* MD, will improve on these treatments.

Chapter 5

Low Dimensionality Effect: Passivated-Graphene Interflake Junction Electron and Phonon Conductance

5.1 Introduction

5.1.1 Graphene composite and edge passivation

Graphene, which is a flat monolayer of (sp^2 -bonded) carbon atoms tightly packed into a 2D honeycomb lattice, has attracted much attention for its superior electrons, phonons, and spin transport properties [41, 7, 54]. The graphene-based composites [171] have also been considering for similar superior effective properties. The graphene flakes commonly used in such composites are readily and unintentionally edge (and side) passivated with various gaseous atoms [68, 51] under non-vacuum handling, and these edge passivations influence the graphene composite properties [101]. In this chapter we examine the roles of edge-passivation on the interfacial thermal transport by electron and phonon across the graphene flakes

5.1.2 Thermal transport bottleneck in Graphene composite

Due to the very weak interflake interactions compared to the strong covalent bonds in the graphene flakes, the bottleneck in the electronic and phonon transport is expected in the interflake. Here, the interflake thermal energy transport is examined using the quantum thermal energy transport treatments, while considering that applications of graphene may include its inevitable passivated form. The O- or H-passivations of graphene flake edges, which do not corrugate the graphene plane, are studied (i.e., three interflake junction arrangements, O-H, O-O and H-H). Then the carrier scattering is concentrated in the interflakes junction when considering the long intragraphene mean free path for the energy carriers compared with the flake

dimension [54, 127].

5.1.3 Treatments of nanoscale thermal transport

The nanoscale thermal transport addresses the quantum features and the carrier wave effects [76], and within that the nonequilibrium Green function (NEGF) formalism is the treatment we use [120]. Also, for the phonon transport in the heterostructures, the semi-classical acoustic mismatch model (AMM) [106] or diffuse mismatch model (DMM) [176], or the molecular dynamics (MD) [151] can provide limited, but more intuitive insights into the phonon transport. However, MD based on the classical Newtonian mechanics has limitation in considering the quantum effects even though it can easily include the anharmonic effects, and the conventional semi-classical AMM and DMM do not include the atomic details of the interfaces and the quantum and wave natures of the phonon transport [183, 71, 198].

In this chapter, both the NEGF formalism and the AMM treatment are employed for the interflake phonon transport across the edge-passivated graphene and although the electronic thermal transport is expected to be small in this system [124, 190], it is also included for gaining insight into the force fields and to complete the treatment of the thermal transport.

5.2 Phonon thermal transport

5.2.1 Nonequilibrium Green function (NEGF) formalism

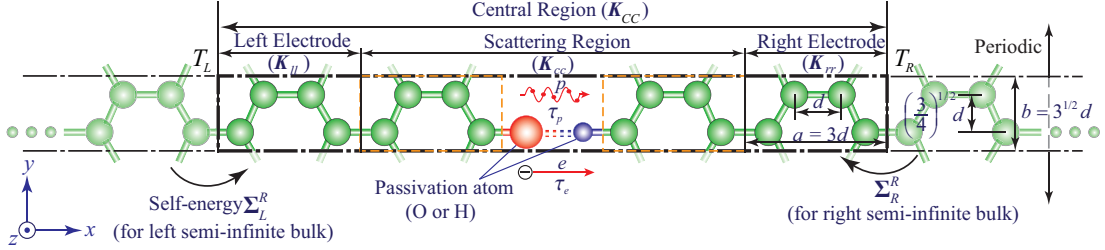


Figure 5.1: The edge-passivated graphene-flake junction used for the thermal transport calculations. The entire domain is divided into a central and two semi-infinite regions, and the central region is divided into a scattering and two electrode regions. The temperatures T_L and T_R are prescribed. d is the interatomic distance, and a and b is the width and height of the periodic bulk cell.

In analogy to the NEGF for the electronic transport [35], we calculate the Green functions using the Hessian matrix with elements $\partial^2 E / \partial x_i \partial x_j$ (E is the energy and x_i and x_j are the i -th and j -th degree of freedom) [156]. These matrices are calculated using the density functional theory (DFT) calculation with finite differences (0.015 Å) provided in the Vienna *ab initio* simulation package (VASP) [94]. The equilibrium structures for the Hessian matrix calculations are obtained by the relaxation of the considered structure with the conjugate gradient (CG) method, and all the atoms are relaxed until the maximum absolute force is less than 0.01 eV/Å. The DFT calculation in VASP employs the Perdew-Burke-Ernzerhof (PBE) parameterization of the generalized gradient approximation (GGA) for exchange and correlation [132] with the projector augmented wave method [16, 95].

The relaxed structures of the joined, passivated graphene flakes (zigzag edges) show restructuring within the first four C atoms from the edge (and negligible dif-

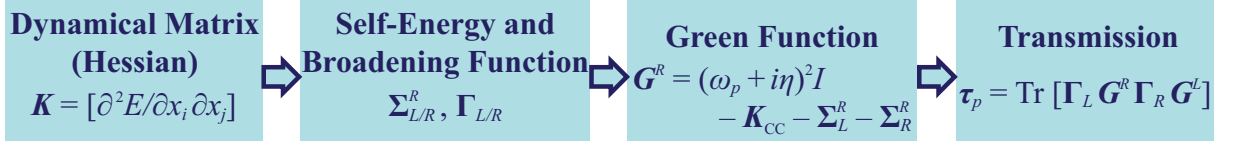


Figure 5.2: NEGF calculation processes for the carrier transmission at interfaces. The self energies and Green functions are calculated with the dynamical (Hessian) matrices from the DFT calculation. Using the Caroli formula with the Green functions, the transmission at interfaces can be found.

ference from the bulk, within less than 0.01 Å, beyond that). In the Green function formalism, we consider a central region connected to two semi-infinite regions representing the bulk graphene, as shown in Fig. 5.1. The central region is divided into two "contact cells or electrodes" on each side with four carbon atoms and a "scattering region or junction" with four carbon atoms on each side of the passivated atoms, also shown in Fig. 5.1. The interaction of the nearest-neighbor cells is taken into consideration and the energy flow from the left to the right with the temperatures T_L and T_R is prescribed. The interatomic distance (d) is 1.42 Å from the DFT relaxation, and the width (a) and the height (b) of the periodic bulk cell is $3d$ and $3^{1/2}d$. Since the interflake contact is 1-D (in the y direction), in addition to the carriers with the transport direction ($\kappa_y^* = 0$, where $\kappa_y^* = \kappa_y b$ and κ_y is the wavenumber in the y direction), other transport directions ($\kappa_y^* \neq 0$) should be included. For this, 200 κ_y^* points are sampled considering the upper and lower neighboring cells in the y direction.

The NEGF calculation processes for the carrier transmission at interfaces are described in Fig. 5.2. From the orthogonalized dynamical matrix with elements,

$-1/(m_i m_j)^{1/2}(\partial^2 E/x_i x_j)$, (m_i and m_j are the mass of atoms) [120], the matrix of the central region with κ_y^* is extracted as [199]

$$\mathbf{K}_{CC}(\kappa_y^*) = \begin{bmatrix} \mathbf{K}_{ll}(\kappa_y^*) & \mathbf{K}_{lc}(\kappa_y^*) & 0 \\ \mathbf{K}_{cl}(\kappa_y^*) & \mathbf{K}_{cc}(\kappa_y^*) & \mathbf{K}_{cr}(\kappa_y^*) \\ 0 & \mathbf{K}_{rc}(\kappa_y^*) & \mathbf{K}_{rr}(\kappa_y^*) \end{bmatrix}, \quad (5.1)$$

where for each element $\mathbf{K}_{ij}(\kappa_y^*) = \mathbf{K}_{M_i U_j} e^{-i\kappa_y^*} + \mathbf{K}_{M_i M_j} + \mathbf{K}_{M_i L_j} e^{i\kappa_y^*}$. Here, i and j can be l , c or r (for the left electrode, the scattering region or the right electrode. The subscripts, U , M and L represent upper, middle and lower cells in the vertical (y) direction. $\mathbf{K}_{M_i M_j}$ is the dynamical matrix for the interaction between the i and j cells which are in the middle strip, and $\mathbf{K}_{M_i U_j}$ (or $\mathbf{K}_{M_i L_j}$) is the matrix for the interaction between the i cell in the middle strip and the j cell in the upper (or lower) strip.

To represent the interaction of the semi-infinite bulk graphenes, the self-energy (Σ_L^R or Σ_R^R) is obtained employing the decimation technique suggested by Lopez-Sancho *et al.* [107]. The phonon-retarded Green function of the central region is given by [186]

$$\mathbf{G}^R(\kappa_y^*, \omega_p) = [(\omega_p + i\eta)^2 \mathbf{I} - \mathbf{K}_{CC}(\kappa_y^*) - \Sigma_L^R(\kappa_y^*, \omega_p) - \Sigma_R^R(\kappa_y^*, \omega_p)]^{-1}, \quad (5.2)$$

where ω_p is the phonon frequency, η is an infinitesimal number corresponding to the phonon energy dissipation [198]. The phonon transmission across the central region

is written as [35, 27],

$$\tau_p(\kappa_y^*, \omega_p) = \text{Tr}[\mathbf{\Gamma}_L(\kappa_y^*, \omega_p) \mathbf{G}^R(\kappa_y^*, \omega_p) \mathbf{\Gamma}_R(\kappa_y^*, \omega_p) \mathbf{G}^A(\kappa_y^*, \omega_p)], \quad (5.3)$$

where \mathbf{G}^A is the phonon advanced Green function equivalent to $(\mathbf{G}^R)^\dagger$ and $\mathbf{\Gamma}_L$ ($\mathbf{\Gamma}_R$) is the energy-level broadening function caused by the left (right) electrode and described by

$$\mathbf{\Gamma}_{L/R}(\kappa_y^*, \omega_p) = i[\mathbf{\Sigma}_{L/R}^R(\kappa_y^*, \omega_p) - \mathbf{\Sigma}_{L/R}^A(\kappa_y^*, \omega_p)]. \quad (5.4)$$

With these Green functions, the phonon density of states is [186]

$$D_p(\kappa_y^*, \omega_p) = -\frac{2\omega_p}{\pi} \text{Im}\{\text{Tr}[\mathbf{G}^R(\kappa_y^*, \omega_p)]\}. \quad (5.5)$$

5.2.2 Transmission at interfaces

5.2.2.1 Lattice dynamics and dispersion

For calculations of the self-energy and the bulk graphene properties, the scattering region is replaced with the same structure as the left and right electrodes. The graphene phonon dispersion is obtained using the dynamical matrix from the DFT calculations with the lattice dynamics relation with the Born-von Karman boundary condition [187]

$$[\omega_p^2(\kappa_x^*, \kappa_y^*, \alpha) \mathbf{I} - \mathbf{K}_{cc}(\kappa_y^*) - \mathbf{K}_{cl}(\kappa_y^*) e^{i\kappa_x^*} - \mathbf{K}_{cr}(\kappa_y^*) e^{-i\kappa_x^*}] \mathbf{s}(\kappa_x^*, \kappa_y^*, \alpha) = 0, \quad (5.6)$$

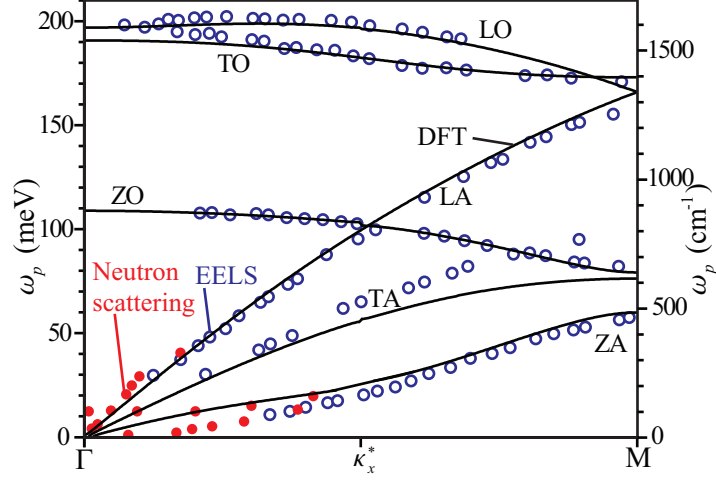


Figure 5.3: The phonon dispersion from Γ to M for the bulk graphene. The solid line is from the DFT dynamical matrix calculations. The red solid circles are from the neutron scattering data and the blue open circles are from the electron energy loss spectroscopy (EELS) data [128].

where κ_x^* is the dimensionless wave number in the transport direction ($\kappa_x^* = \kappa_x a$ and κ_x is the wavenumber in the x direction), α is the polarization [4 atoms in each unit cell and three degrees of freedom per each atom, the number of total branches (α) is 12], \mathbf{s} is the eigenvector, and \mathbf{K}_{cl} (\mathbf{K}_{cr}) is the dynamical matrix for the interaction between the left (right) electrode and the scattering region.

The phonon dispersion found from Eq. (5.6) is unfolded to show it for the primitive cell of graphene composed of two C atoms. The dispersion curve from Γ to M ($\kappa_y^* = 0$) is in good agreement with the experiments [128], as demonstrated in Fig. 5.3.

5.2.2.2 NEGF transmission

Because the passivated atoms are linearly aligned and the transport with the $\boldsymbol{\kappa}$ vector (wavevector) propagating in the transport direction is expected to dominate (when expanding to the longer functional groups, it would be more dominant), the

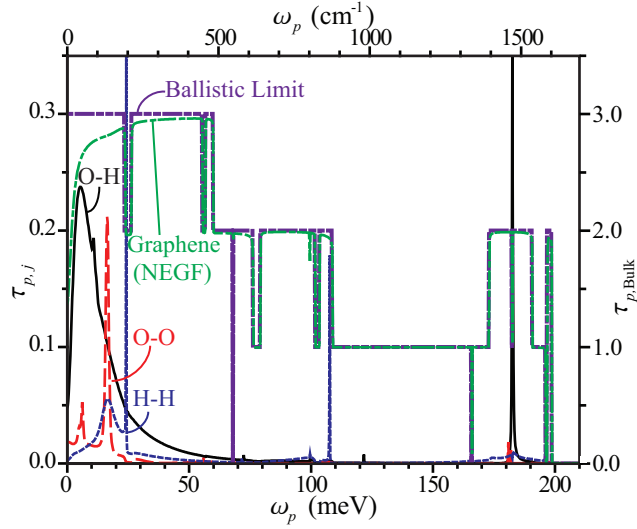


Figure 5.4: The variations of the phonon transmission with the transport direction ($\kappa_y^* = 0$) with respect to the phonon energy, for the bulk graphene and the passivated junctions. The transmissions for the passivated junctions are largely suppressed, while the O-H junction has the largest transmission.

dominant transport direction ($\kappa_y^* = 0$) is first calculated. In the ideal ballistic transport, when all modes are transmitted without scattering, the phonon transmission is the number of modes at frequency ω_p [187], and the NEGF transmission for graphene is similar to this ballistic limit with a small η , as shown in Fig. 5.4. Phonons incident from the graphene are transported through the passivated edges in the three junctions with significantly suppressed transmissions. The τ_p for the O-H junction is the largest among the three, and in all three the phonons with the low energy (less than 30 meV) and some high energies have relatively high transmissions.

Figures 5.5(a), (b), (c) and (d) show the phonon transmissions as functions of the component κ_y^* in the $\boldsymbol{\kappa}$ vector space and the phonon energy, for the graphene and passivated graphene junctions. The bulk graphene in the ballistic limit has integer transmission for all $\boldsymbol{\kappa}$ directions, and the phonon transmissions through interflake junctions are limited by the bulk graphene transmission. The transmissions are sym-

metric and larger near the transport direction ($\kappa_y^* = 0$).

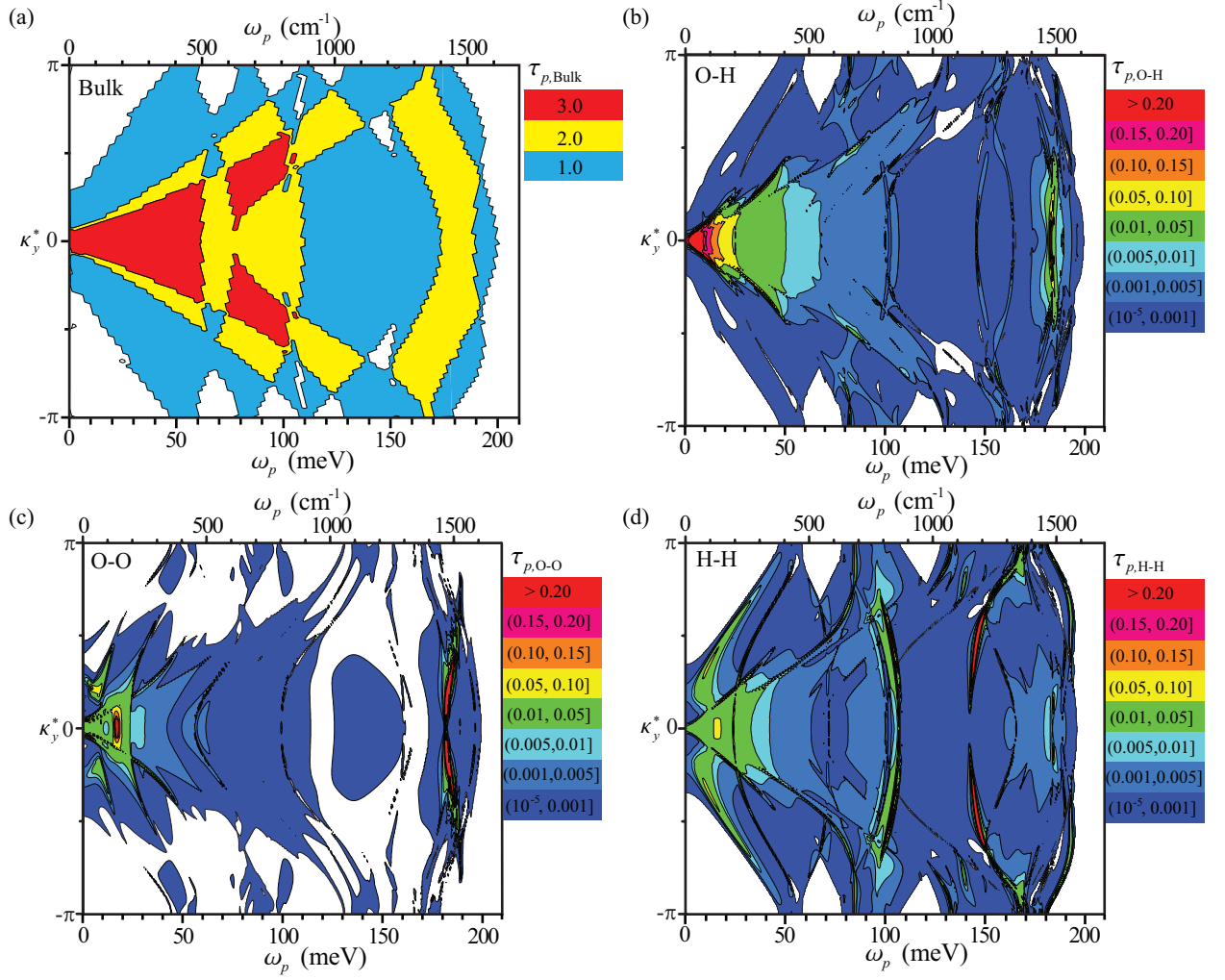


Figure 5.5: Phonon transmissions as functions of the component κ_y^* in the wavevector space and the phonon energy for (a) bulk graphene, (b) O-H, (c) O-O and (d) H-H junctions. The transmissions are symmetric and larger near the transport direction ($\kappa_y^* = 0$).

5.2.2.3 Polarization

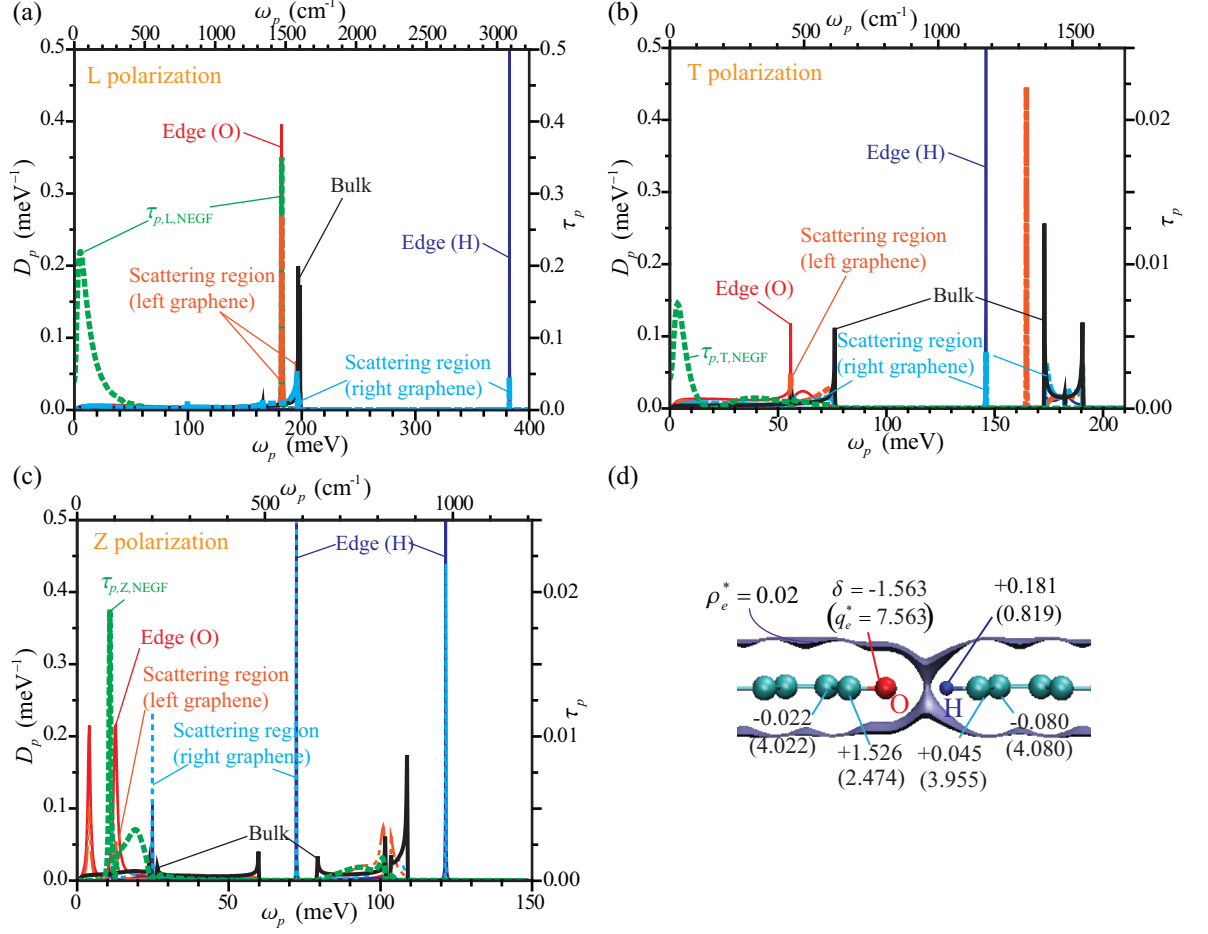


Figure 5.6: Variations of the phonon density of states and transmissions (at $\kappa_y^* = 0$) with respect to the phonon energy for (a) the longitudinal (L), (b) transverse (T), and (c) out-of-plane (Z) directions, for the O-H passivated junction. Due to the interaction with the junction atoms and the atomic restructuring, D_p is distorted in the interfacial regions. The iso-surface of the charge density ($\rho_e^* = 0.02$), the charge (q_e^*) associated with each atom, and the difference from the valence charges (δ) are shown in (d). Note that τ_p is the largest in the L direction, and is bimodal with the wide peaks at low and the sharp peaks at the edge-resonant frequencies.

Since the dynamical matrices demonstrate that the couplings between the different polarizations are weak, we consider the three polarizations separately, which are the longitudinal (L or the transport direction), transverse in plane (T), and out-of-plane (Z) directions. Figures 5.6(a), (b) and (c) show the phonon density of states

and transmissions, as a function of phonon energy, for the three polarizations of wavevectors with the transport direction, for the O-H interflakes. The D_p for the carbon atoms near the flake edges are distorted compared to the bulk D_p , due to the restructuring in the edges and the interaction with the passivated atoms [162]. The D_p for the edge atoms have sharp peaks due to the asymmetric coupling and the non-periodicity, and their frequencies mostly depend on the interaction with the nearest C atoms [$\sim (\Gamma_{ij}/m_{ij})^{0.5}$, where Γ_{ij} is the force constant and m_{ij} is the reduced mass] [82]. Because of the much smaller mass of the H atom compared to O, H acquires high frequencies in spite of the stronger interaction of O with the nearest C atom.

The asymmetric charge distribution in the O-H is shown from the Bader charge analysis [62] as Fig. 5.6(d), which shows the iso-surface of the charge density ($\rho_e^* = 0.02$), the charge associated with each atom according to Bader partitioning (q_e^*), and the net charge (δ) which is the difference from the valence charges. This induces the Coulomb interaction between the two flakes, and the interaction with the transport direction enhances the phonon transport polarized with the L direction. Thus, in the O-H junction, the phonon transmission in the L polarization is much larger than the other polarizations, (T and Z), and most of the phonon energy is transported by the phonons polarized in the L direction. Differing from the O-H junction, the O-O and H-H junctions cause much weaker coupling between the two flakes and do not show the dominance of the phonons with a particular polarization (because the transport in the L polarization is suppressed as much as the other directions).

The transmission in the L polarization in the O-H junction is bimodal showing the broad peak at the low frequency and the sharp peak at the high frequency for

the O-resonant vibration. Only phonons with the energies available in the graphene reservoirs can contribute to the phonon transport and the frequencies for H are over the cutoff of the graphene (L) or are in the phonon bandgaps (in the T and Z polarizations), so the phonons with the H-resonant frequencies cannot contribute to the transport for wavevectors vectors with the transport direction. Despite the absence of the phonon energy states in the H atom, the phonons with the resonant frequency of O can be transmitted through the tunneling. This resonant tunneling is enhanced by the strong interaction of the passivated atoms with the opposite flake, so the L-polarized phonon has a higher τ_p at the resonance of the passivated atom. The long-wave phonons with the low energy (resonant with the weak couplings between two flakes) are less scattered and dominate in the phonon transport. This bimodal transport leads to different channels depending on the temperature (high energy phonons have higher population at high temperature).

5.2.3 Semi-classical Transmission

In relating the semi-classical treatment to the NEGF, we calculate the τ_p in the AMM employing the specular scattering as an analogy to the electromagnetic waves. In the AMM [106], the phonon transmission is obtained with the acoustic impedance (Z_p) as

$$\tau_{p,L/R,AMM} = \frac{4Z_{p,L}Z_{p,R}}{(Z_{p,L} + Z_{p,R})^2}, \quad (5.7)$$

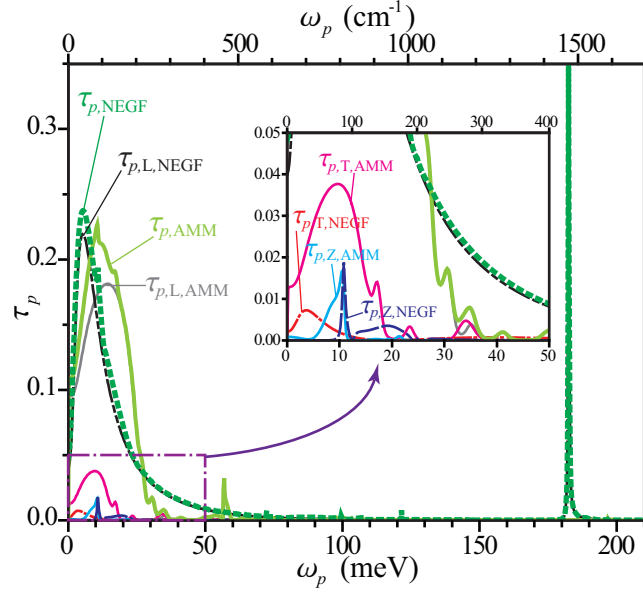


Figure 5.7: Comparison of the phonon transmission (at $\kappa_y^* = 0$) from the AMM treatment with the NEGF. The AMM transmission is in good agreement with the NEGF at low frequencies, but does not show the high frequency transmission.

where $\tau_{p,L/R,AMM}$ is the phonon transmission from the left to right region, $Z_{p,L}$ is the impedance for the left and $Z_{p,R}$ is for the right region, and Z_p is commonly used as ρu_p , where ρ is the density and u_p is the phonon speed (u_p is proportional to D_p^{-1} in 1-D systems).

Here, scattering is due to the mismatch in the phonon spectra (phonon speed, density, etc.). (The maximum transmission is unity with the same phonon properties for both sides, as in the bulk.) Because D_p in the central region is heterogeneous, due to the restructuring as confirmed in Fig. 5.6, we consider the phonon scattering at the interface of neighboring atoms ($\tau_{p,i/i+1,AMM}$) using the local Z_p proportional to the D_p^{-1} , and combine all interfacial $\tau_{p,i/i+1,AMM}$ in the central region to find the

overall transmission $\tau_{p,\text{AMM}}$,

$$\tau_{p,\text{AMM}} = \tau_{p,1/2,\text{AMM}}\tau_{p,2/3,\text{AMM}}\cdots\tau_{p,17/18,\text{AMM}} = \prod_{i=1}^{17} \tau_{p,i/i+1,\text{AMM}}. \quad (5.8)$$

Since the semi-classical treatments, e.g., the AMM applied here, assume a quasi-particle carrier, the wave natures (e.g. interference) are not addressed. In spite of that, we observe that $\tau_{p,\text{AMM}}$ is in good agreement with the NEGF results as in Fig. 5.7, except for the high-frequency transmission, by treating the atomic details with D_p at every atomic location in the scattering region. Small disagreement is ascribed to the omitted wave natures in the AMM and the simple combination which only counts the nearest-neighbor interactions, thus excluding the interference, the tunneling and the multiple reflections and transmissions.

5.2.4 Phonon conductance

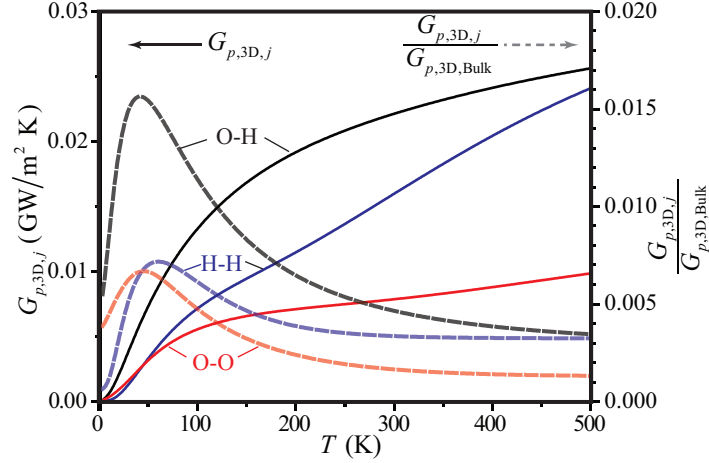


Figure 5.8: Variations of the phonon conductance ($G_{p,3D,j}$, solid lines) of the three passivated flake junctions with respect to temperature, from the NEGF calculations, and comparison with the bulk behavior (dash lines).

In 1-D transport with a given κ_y^* , the phonon conductance is evaluated using the Landauer formula [99, 141],

$$G_{p,1D}(\kappa_y^*) \text{ [W/K]} = \int_0^\infty \frac{d\omega_p}{2\pi} \hbar\omega_p \tau_p(\kappa_y^*, \omega_p) \left[\frac{\partial f_p^o(\omega_p, T)}{\partial T} \right], \quad (5.9)$$

where T is the temperature, \hbar is the reduced Planck constant, the equilibrium Bose-Einstein distribution function is $f_p^o(\omega_p, T) = [\exp(\hbar\omega_p/k_B T) - 1]^{-1}$, and k_B is the Boltzmann constant. To include contributions from all wavevectors (as well as $\kappa_y^* = 0$), we sample κ_y^* values (200 points in the first Brillouin zone, $-\pi \leq \kappa_y^* < \pi$) and integrate 1-D conductance for each direction for the 2-D conductance as [199],

$$G_{p,2D} \text{ [W/m-K]} = \frac{1}{b} \int_{-\pi}^{\pi} d\kappa_y^* G_{p,1D}(\kappa_y^*). \quad (5.10)$$

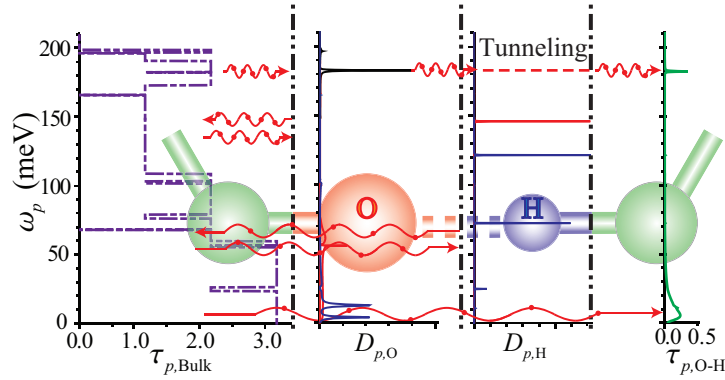


Figure 5.9: Phonon transport channels and the mechanism of phonon transport suppression in the O-H passivated junction.

The phonon conductance per unit width ($G_{p,2D}$, W/m-K) is calculated by Eqs. (5.9) and (5.10) with the transmission in Fig. 5.5 and using the layer separation distance (0.335 nm) in the graphite as the thickness, we find the phonon conductance

per unit area ($G_{p,3D}$, W/m²-K), which is shown in Fig. 5.8.

The $G_{p,3D}$ reduces for the edge-passivated graphene junctions are largely suppressed to less than one percent of bulk graphene $G_{p,3D,Bulk}$ at 300 K (4.76 GW/m²-K from this work) because only phonons with the low energy or the tunneled resonant energy can be transmitted through the interflakes, as shown in Fig. 5.9.

Figure 5.10 shows the contribution of wavevectors to thermal conductance [$G_p^*(\kappa_y^*) = G_{p,1D}(\kappa_y^*)/(bG_{p,2D})$ satisfying $\int_{-\pi}^{\pi} d\kappa_y^* G_p^*(\kappa_y^*) = 1$] and it confirms that the phonons with the transport direction are dominant. This is further clear for the passivated graphene junctions at lower temperature.

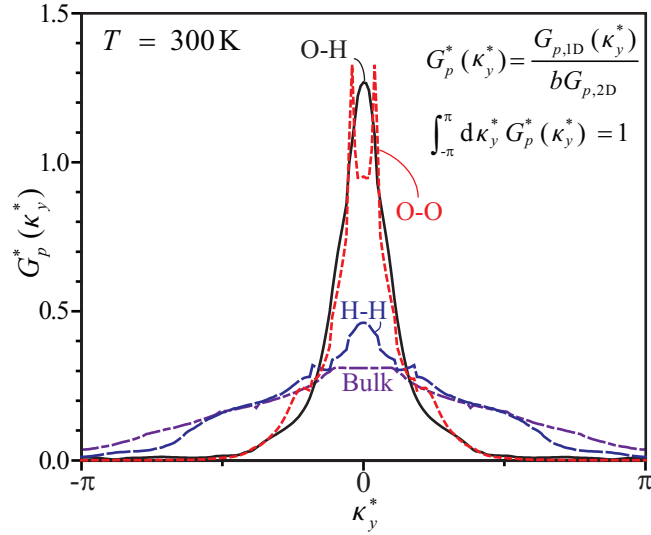


Figure 5.10: The contribution of wavevectors to thermal conductance [$G_p^*(\kappa_y^*)$] at $T = 300$ K.

5.3 Electronic thermal transport

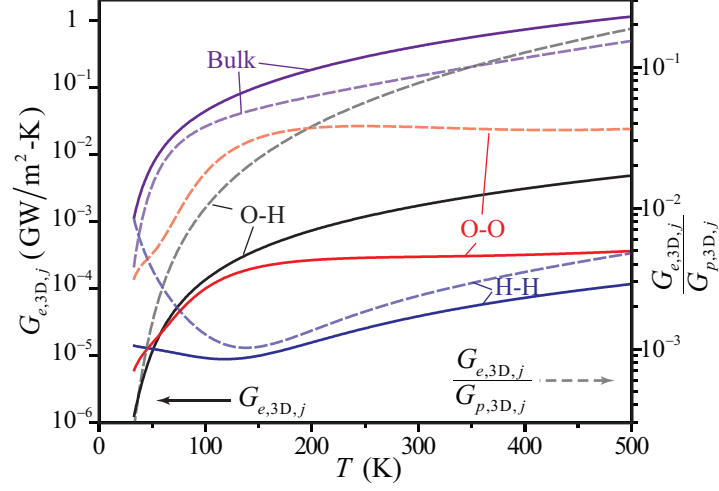


Figure 5.11: Variations of the electronic thermal conductance ($G_{e,3D,j}$, solid lines) on the left and that scaled with $G_{p,3D,j}$ ($G_{e,3D,j}/G_{p,3D,j}$, dash lines) on the right, without an external bias potential, with respect to temperature.

The electronic thermal conductance is calculated using the NEGF and the TranSIESTA module within the SIESTA code (with the GGA-PBE exchange correlation, the CG relaxation, and a single ζ -plus-polarization basis set) [21] and the same configuration shown in Fig. 5.1. For infinitesimal voltage and temperature differences, the electronic thermal conductance is [47]

$$G_{e,2D} [\text{W/m-K}] = \frac{1}{bT} (K_2 - \frac{K_1^2}{K_0}), \quad (5.11)$$

where K_n is defined as $K_n = (1/\pi\hbar) \int dE_e (E_e - E_F)^n \tilde{\tau}_e(E_e) [-\partial f_e^o(E_e, T)/\partial E_e]$, E_F is the Fermi-level defined by the external electrode, $\tilde{\tau}_e$ is the average electron transmission over the sampled κ vectors (200 points in the y direction) with regard to the electron energy, and f_e^o is for the equilibrium fermion, $f_e^o(E_e, T) = \{\exp[(E_e - E_F)/k_B T] + 1\}^{-1}$. $G_{e,3D}$ for bulk and three junctions are calculated with the layer

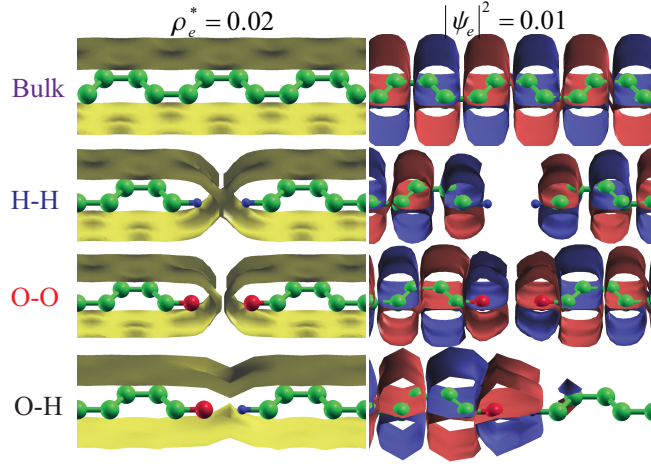


Figure 5.12: The charge-density iso-surface ($\rho_e^* = 0.02$) on the left and the wavefunction ($|\psi_e|^2 = 0.01$) of the first eigenstate below the E_F (at the Γ point) on the right, for the bulk and the three junctions. Different colors (blue and red) in the wavefunctions correspond to the opposite signs.

separation distance as in $G_{p,3D}$ and compared with $G_{p,3D}$ in Fig. 5.11. The reduction of G_e from the bulk value is more pronounced than G_p , when no external bias potential is applied.

Figure 5.12 presents the charge-density iso-surface ($\rho_e^* = 0.02$) and the wavefunction of the first eigenstate below the E_F (at the Γ point). The low charge density presents between the flakes and the localized orbital exists near the passivated edge for the symmetric junctions differing from the chemical σ - or π -bond between the passivation atom and the nearest C [101] and the delocalized π -bond in the bulk graphene. These lead to the large drop in the magnitude of G_e . For the asymmetric junction O-H, the G_e is less suppressed because of the delocalization in the molecular orbital due to the asymmetric charge distribution. As shown to right of Fig. 5.11, the G_e for all the three junctions is smaller than the G_p , especially at low temperatures, with the O-H junction suffering the least reduction.

5.4 Prediction of composite effective conductivity

As hetero-structure systems experience large decrease in the transport by the Kapitza resistance at the interfaces, the reduction in thermal conductance of the graphene junctions with the edge passivation drastically reduce the effective thermal conductivity of the graphene composite. As the previous sections demonstrate, thermal transport by phonons is dominant over electrons, and thus phonon conductivity is mainly considered in graphene composite.

The total thermal resistance of the linear chain of graphene flakes ($1/G_{p,3D,Chain}$) is the sum over the resistances for the graphene flakes and the interflakes junctions, i.e.,

$$\frac{1}{G_{p,3D,Chain}} = n_j \left(\frac{1}{G_{p,3D,GF}} + \frac{1}{G_{p,3D,j}} \right) + \frac{1}{G_{p,3D,GF}}, \quad (5.12)$$

where n_j is the number of the interflake junctions in the chain, and $G_{p,3D,GF}$ and $G_{p,3D,j}$ are the thermal conductance of the graphene flake and the interflake junction. With uniform length for the graphene flakes (l_{GF}), the effective thermal conductivity of the chain with sufficiently long length $L_c = (n_j + 1)l_{GF}$ is

$$\langle k_{p,Chain} \rangle = G_{p,3D,Chain} L_c = \frac{G_{p,3D,GF} G_{p,3D,j}}{G_{p,3D,GF} + G_{p,3D,j}} l_{GF}. \quad (5.13)$$

Since the conductance calculated in this work is based on the ballistic transport, the thermal conductivity of graphene flakes depends on l_{GF} and the phonon mean

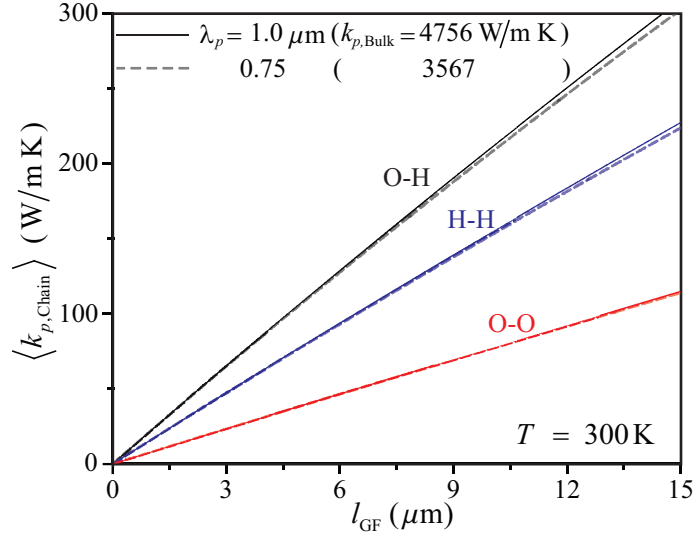


Figure 5.13: The effective thermal conductivity of linear chains composed of graphene flakes with three cases of edge passivated junctions at $T = 300\text{ K}$, as a function of the flake length. Two mean free paths, $\lambda_p = 1.0\ \mu\text{m}$ ($k_{p,\text{Bulk}} = 4756\text{ W/m-K}$) and $\lambda_p = 0.75\ \mu\text{m}$ ($k_{p,\text{Bulk}} = 3567\text{ W/m-K}$), are used [54, 124].

free path λ_p [124], i.e.,

$$k_{p,\text{GF}} = G_{p,3\text{D},\text{GF}} l_{\text{GF}} = G_{p,3\text{D},\text{Bulk}} \frac{l_{\text{GF}} \lambda_p}{l_{\text{GF}} + \lambda_p}. \quad (5.14)$$

The phonon thermal conductivity of undisrupted graphene $k_{p,\text{Bulk}}$ (i.e., $l_{\text{GF}} \rightarrow \infty$) is $G_{p,3\text{D},\text{Bulk}} \lambda_p$ (4756 W/m-K with $\lambda_p = 1.0\ \mu\text{m}$ and 3567 W/m-K with $\lambda_p = 0.75\ \mu\text{m}$). Then, the effective thermal conductivity of the linear chain composed of graphene flakes with uniform length ($\langle k_{p,\text{Chain}} \rangle$) can be estimated using the phonon conductance of interflake junction and the graphene flake. Figure 5.13 shows variation of the effective thermal conductivity as a function of the flake length. ($\langle k_{p,\text{Chain}} \rangle$ increases with l_{GF} .) Here the large reduction of the effective thermal conductivity compared to the undisrupted graphene is also confirmed.

5.5 Summary

In this chapter, the interflake electronic and phonon thermal conductances of the edge-passivated graphene flakes are calculated. Using the NEGF, it is demonstrated that a bimodal phonon transmission at the low and high frequencies caused by the weak coupling between two flakes and the tunneling resonant peaks of the passivated atoms, whereas the AMM treatment with the multiple interfaces predicts only the low frequency transmission. This transmission also explains the different phonon transport mechanisms at low and high temperatures. The relatively strong interaction between O- and H-passivated graphene flakes leads to a high conductance and the dominance of the phonon polarized in the transport direction. The mode or frequency dependence of the phonon transport is controlled by the edge passivation, and this may provide a tool for the phonon engineering of the graphene compounds. Thermal conductance noticeably decreases due to the edge-passivated graphene junctions and the phonon thermal transport dominates over the electronic except for the asymmetric junction at high temperatures. Since the bottleneck of the effective phonon transport in the graphene composites is the junction conductance between the flakes (or fibers), these findings can benefit the design of such high effective thermal conductivity composites.

Chapter 6

Selecting Molecular Vibrations for Molecular-Gas Laser Cooling

6.1 Introduction

Cooling of molecular gases continues to be a challenge, due to the limiting transition kinetics. In this chapter, nonequilibrium occupancy in the molecular-gas kinetic energy is addressed while considering the molecular-gas cooling by laser irradiation. Laser irradiation leads to a nonequilibrium population distribution of the molecular gas, and this low-entropy nonequilibrium population distribution can be exploited (before it equilibrates and increases entropy). We address manipulation of the nonequilibrium population to enhance energy conversion, especially for enhanced

gas cooling. The example of CO₂ gas composite cooling is considered, and a new molecular vibrational state is identified for improved cooling.

6.1.1 Prior studies on gas laser cooling

While a number of studies have been published on atomic gas laser cooling [125, 193, 81, 135] for trapped ultracold atoms, studies on molecular-gas laser cooling have been rather limited in number [6, 8]. Cooling of molecules such as the alkaline-earth monohydrides via magneto-optical trapping has been suggested [143]; several other attempts have been made to produce ultracold gaseous molecules, but so far they have not been successful [28]. Kinetic cooling has also been suggested and observed with CO₂ and other molecules, but it is only transient with negligible cooling [165, 53]. So far, the only successful net cooling of molecular gases has been achieved in CO₂ gas cooling by the anti-Stokes fluorescence [38]. However, this cooling only reached 1 K at 600 K using 10.6 μm CO₂ laser irradiation with Xe as the diluent.

6.2 Model for molecular-gas laser cooling system

6.2.1 Vibrational states in molecular gas

Molecular-gas laser cooling employs vibrational states, in contrast to solid-state anti-Stokes laser cooling, which uses doped-ion electronic energy levels and phonons [86]. The Herzberg notation [63], $(v_1 v_2' v_3)$, is used for vibrational states, where v_1 , v_2 , and v_3 are the symmetric, bending, and asymmetric vibrational quantum numbers

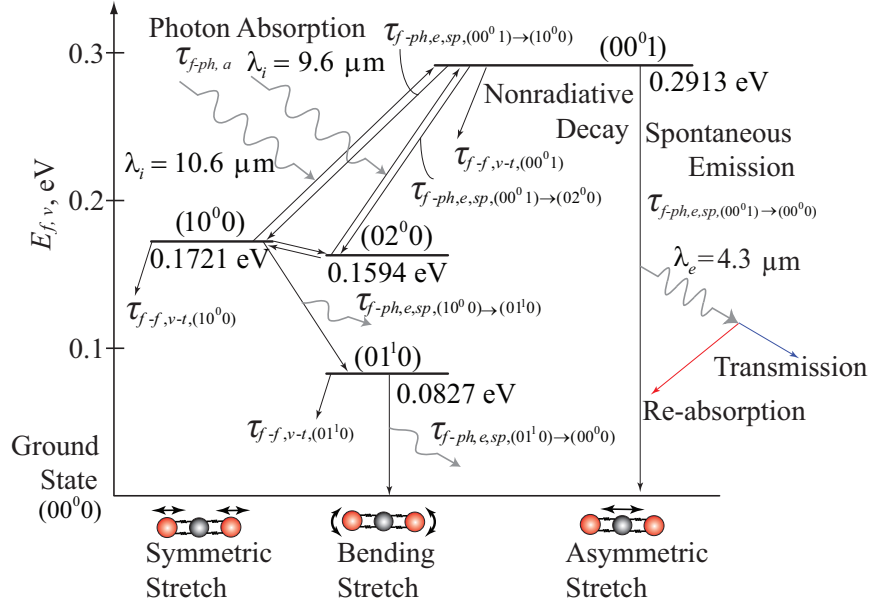


Figure 6.1: Five-level vibrational energy diagram for CO₂ laser cooling. With the Herzberg notation, the symmetric, bending, and asymmetric vibrational modes are described. The photon wavelength for absorption and emission (λ_i and λ_e) are included, and the relaxation and excitation mechanisms and interaction times (τ 's) are also shown.

and l is the angular quantum number of the bending mode. Because the population of overtone vibration levels is low at low vibration temperatures, only levels under (00^1) are considered. Among these, (00^0) , (10^0) , and (02^0) are possible levels for radiative excitation to (00^1) , according to the vibration mode transition selection rule [42]. Covering the above-mentioned levels, a five-level vibration energy system is employed in this analysis, as shown in Fig. 6.1 [63]. Compared to the three-level analysis in [38], other possible resonant irradiations can be considered using this energy level system, so that the selections of other laser frequencies as well as more accurate results and predictions are allowed.

6.2.2 System description and cooling mechanism

The addition of Xe improves cooling by lowering the mixture thermal conductivity and deactivating collisional relaxation [29]. At high temperatures, Ne, Ar, Kr and He have larger deactivation effects than Xe [172], but Xe lowers the mixture thermal conductivity [181] due to its heavy atomic mass. Thus, Xe is still considered the most effective diluent for gas cooling. The gas mixture is contained in a long cylinder of radius R_t and prescribed wall temperature T_o , and irradiated with a laser beam of radius R_l traveling at the cylinder center.

Laser cooling can be achieved by the following processes. First, laser irradiation excites (10^00) or (02^00) level to (00^01) level by absorbing photons. Then, the excited CO_2 molecules undergo radiative decay by spontaneous emission, and the emitted photons from the spontaneous emissions are absorbed in tube wall or re-absorbed by the gas. Population distribution reaches thermal equilibrium through vibration-translation energy transport by collision. When the emitted photon has higher energy than absorbed photon (anti-Stokes), the total system energy decreases and the system is cooled. This cooling process is also described as in Fig. 6.2.

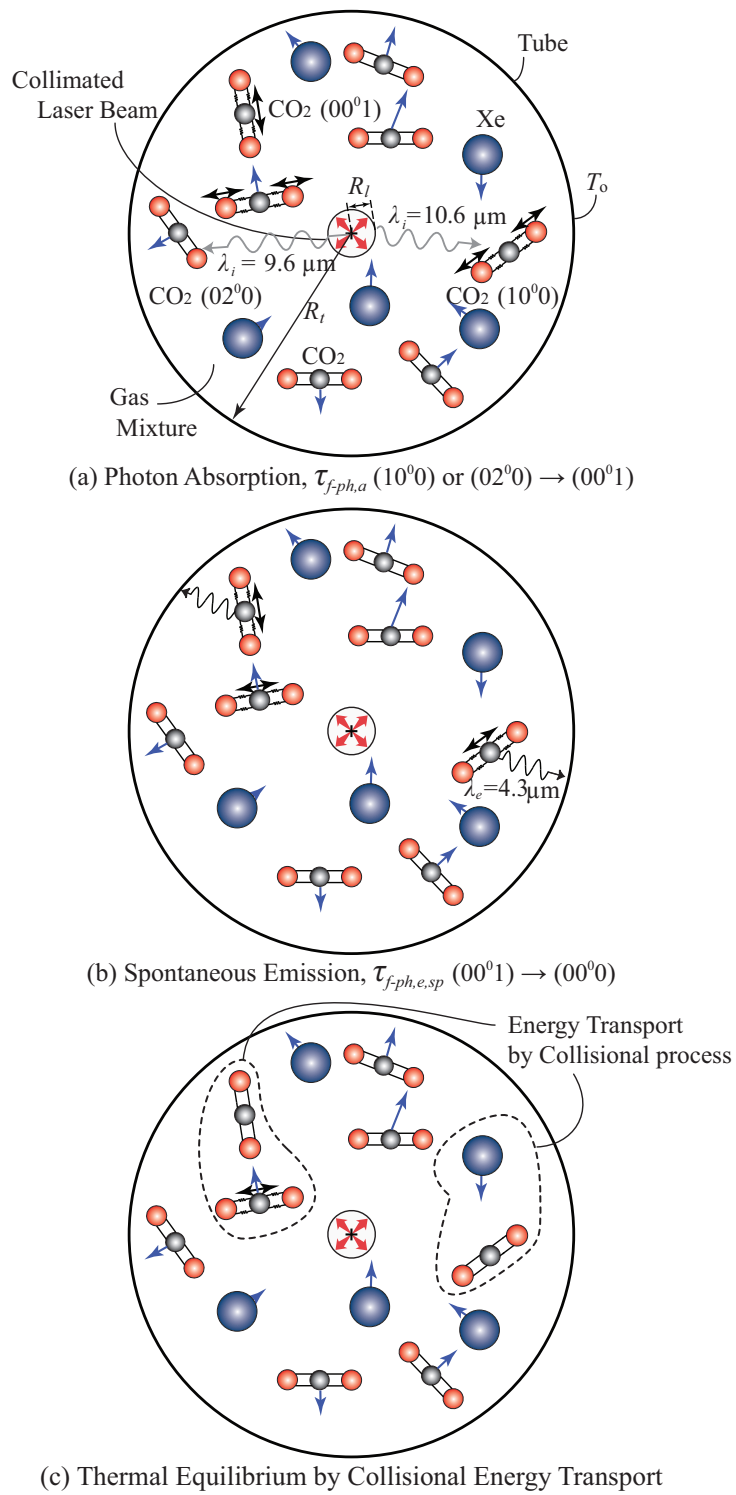


Figure 6.2: Cooling mechanisms for CO₂-Xe gas, showing the tube with central laser beam. Due to the anti-Stokes process, the state in (c) has lower energy compared to (a).

6.3 Analysis

6.3.1 Population distribution

The CO₂-Xe gas mixture system is assumed to be in equilibrium before the laser irradiation. All kinetic temperatures (vibrational, rotational and translational) are therefore equal. The population of each vibration level generally follows the Boltzmann distribution. The population of energy level ($v_1v_2^lv_3$) is proportional to

$$f_{v_1v_2^lv_3}^o = \exp\left(-\frac{\Delta E_{v_1v_2^lv_3}}{k_B T}\right), \quad (6.1)$$

where k_B is the Boltzmann constant, $\Delta E_{v_1v_2^lv_3}$ is the energy difference between the vibrational level ($v_1v_2^lv_3$) and ground level (00⁰0), and T is the gas mixture temperature. Since the bending mode of CO₂ molecule is doubly degenerated, the vibration partition function becomes [33]

$$Z_{f,v} = (1 - f_{10^00}^o)^{-1}(1 - f_{01^10}^o)^{-2}(1 - f_{00^01}^o)^{-1}. \quad (6.2)$$

Thus the population density of energy level ($v_1v_2^lv_3$) is

$$n_{v_1v_2^lv_3} = \frac{n_{\text{CO}_2} f_{v_1v_2^lv_3}^o g_{v_1v_2^lv_3}}{Z_{f,v}}, \quad (6.3)$$

where $g_{v_1v_2^lv_3}$ is the degeneracy of the level ($v_1v_2^lv_3$) and n_{CO_2} is the population density of CO₂.

Photon absorption causes a deviation in population distribution from the Boltz-

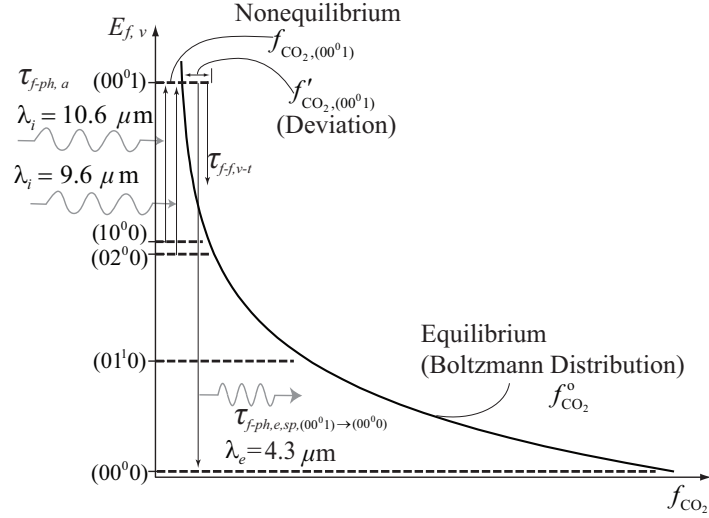


Figure 6.3: Population distribution of energy levels in CO₂ laser cooling system.

mann distribution. In this analysis, (00⁰1) becomes populated by laser irradiation; the populated (00⁰1) level then decays, emitting larger-energy photons with a large spontaneous relaxation rate when compared to the nonradiative decay. Cooling is thus achieved by generating the nonequilibrium, asymmetric (00⁰1) level population fraction designated by $f_{\text{CO}_2,(00^0 1)}$ in Fig. 6.3.

6.3.2 Transition Kinetics

Gas species diffusion and thermal energy transport are controlled by the transition kinetics, and the molecular kinetics (represented by D_f and k_f) of the gas mixture [181, 40, 15, 78]. With a constant total number density, slow relaxation and large pumped molecules are desirable for maintaining large deviations from the equilibrium population across the cylinder. Relaxation of the (00⁰1) level $\tau_{f-ph-f,(00^0 1)}$ involves spontaneous emission $\tau_{f-ph,e,sp}$ and nonradiative decay $\tau_{f-f,v-t}$ through vibration-translation or vibration-vibration energy transport (by collisions between CO₂ and CO₂ or CO₂

and Xe). The spontaneous emission rate for transition from i to j state is [82]

$$\tau_{f-ph,e,sp,i-j}^{-1} = \frac{64\pi^4 f_{e,g}^3 |\mu_{e,i-j}|^2}{3h_P u_{ph}^3}, \quad (6.4)$$

where $f_{e,g}$ is the emitted frequency, u_{ph} is photon speed, h_P is the Planck constant, and $|\mu_{e,i-j}|$ is the transition dipole moment between the i and j states. Transition dipole moments have been estimated by *ab initio* calculations [105]; here we use the dipole moment from the measured absorption coefficient because of the higher accuracy [93].

The time constant of the collisional nonradiative process $\tau_{f-f,v-t}$ is [153]

$$\tau_{f-f,v-t} = \frac{\tau_{f-f}}{P_{f-f,v-t}}, \quad (6.5)$$

where τ_{f-f} is the time constant of the molecular collision (from molecular kinetics) [?], and $P_{f-f,v-t}$ is the transition probability per collision, estimated using a combination of experimental results [29, 172, 126] and theoretical models {Landau-Teller [98] and Schwartz-Slowsky-Herzfeld (SSH) [153]}.

During collisional energy transport, relaxations are allowed from (00^01) to all lower levels $(v_1 v_2^l 0)$. Transitions to the closest levels [such as (11^10) and (04^00)] dominate (00^01) relaxation despite its small mole fraction, because a transition with a large energy exchange has a low probability [122]. Adding diluent Xe lowers the probability of (00^01) nonradiative relaxation because of the large collisional reduced mass, and because Xe only has translational energy. The addition of Xe also increases relaxation rates in the lower levels [29, 196]. The nonradiative relaxation time of a

CO₂-Xe gas mixture, generally dependent on pressure p , is reported in [126]

$$(p\tau_{f-f,v-t})^{-1} = x_{\text{CO}_2}(p\tau_{f-f,v-t,\text{CO}_2-\text{CO}_2})^{-1} + x_{\text{Xe}}(p\tau_{f-f,v-t,\text{CO}_2-\text{Xe}})^{-1}, \quad (6.6)$$

where x_{CO_2} and x_{Xe} are the mole fraction of Xe and CO₂, $\tau_{f-f,v-t,\text{CO}_2-\text{CO}_2}$ is the relaxation time constant by collisions between CO₂ molecules, and $\tau_{f-f,v-t,\text{CO}_2-\text{Xe}}$ is the relaxation time constant by collisions between CO₂ and Xe. From the time constants of nonradiative and radiative decay, the overall relaxation time of (00⁰1) is found as follows by the Matthissen rule,

$$\tau_{f-ph-f,(00^01)}^{-1} = \sum \tau_{f-f,v-t,A-B,(00^01)}^{-1} + \sum \tau_{f-ph,e,sp,(00^01) \rightarrow (v_1 v_2^1 0)}^{-1}. \quad (6.7)$$

The (00⁰1) level population in the beam region also varies according to photon absorption rate and pumped-level population (10⁰0) or (02⁰0). The lower levels have larger populations according to the equilibrium Boltzmann distribution, so resonant irradiation with transition between the lower (02⁰0) and (00⁰1) levels leads to a larger number density for (00⁰1). Absorption and gain coefficients for the transition between (02⁰0) with rotational level j and (00⁰1) with j' are derived from stimulated absorption and emission rates. Using the time constant for spontaneous emission in decay from (02⁰0) and (00⁰1), these are [66]

$$\begin{aligned} \sigma_{ph,a,(02^00),j \rightarrow (00^01),j'} &= \frac{n_{\text{CO}_2,(02^00)}}{\tau_{f-ph,e,sp,(00^01) \rightarrow (02^00)} \int_{\omega} d\omega} \frac{g_{(00^01),j'}}{g_{(02^00),j}} \left(\frac{\pi u_{ph}}{\omega_{(00^01) \rightarrow (02^00)}} \right)^2 \\ \sigma_{ph,g,(00^01),j' \rightarrow (02^00),j} &= \frac{n_{\text{CO}_2,(00^01)}}{\tau_{f-ph,e,sp,(00^01) \rightarrow (02^00)} \int_{\omega} d\omega} \left(\frac{\pi u_{ph}}{\omega_{(00^01) \rightarrow (02^00)}} \right)^2, \end{aligned} \quad (6.8)$$

where $\int_{\omega} d\omega$ is over a small bandwidth centered around $\omega_{(00^01) \rightarrow (02^00)}$, $g_{(02^00),j}$ and $g_{(00^01),j'}$ are the degeneracies of rotational levels of (02^00) and (00^01) , and $n_{\text{CO}_2,(02^00)}$ and $n_{\text{CO}_2,(00^01)}$ are the number density of (02^00) and (00^01) .

From the absorption relation (the Bouguer law), the rate equation under laser irradiation is

$$\begin{aligned} \frac{dn_{\text{CO}_2,(00^01)}}{dt} = & -\frac{n_{\text{CO}_2,(00^01)}}{\tau_{f-ph-f,(00^01)}} \\ & + I_{ph} \left(\frac{\sigma_{ph,a,(02^00),j \rightarrow (00^01),j'}}{\hbar\omega_{(00^01) \rightarrow (02^00)}} - \frac{\sigma_{ph,g,(00^01),j' \rightarrow (02^00),j}}{\hbar\omega_{(00^01) \rightarrow (02^00)}} \right), \end{aligned} \quad (6.9)$$

where I_{ph} is laser intensity. Even though here we address laser irradiation causing rotational transition and population deviation for levels j and j' , the populations of all rotational levels in (02^00) and (00^01) are affected by irradiation (due to the fast relaxation of the rotational levels).

Thus, the absorption and emission rates by laser irradiation depend upon I_{ph} and vibration population distribution. When a 9.6 μm wavelength laser on the P(28) line (the strongest transition in the group [131]) is selected and I_{ph} is larger than 100 W/cm^2 , these rates are much higher than the overall relaxation, and the excited level population can be saturated close to the pumped energy level (99.99 %). Therefore, the net absorption time constant $\tau_{f-ph,a}$ is limited to $\tau_{f-ph-f,(00^01)}$ under steady state.

The essential time constants for this analysis are shown in Table 6.1. The transition from (00^01) to (00^00) has the largest spontaneous decay rate, and this radiative relaxation is faster than nonradiative decay under very low pressure. Hence, high occupancy of the (00^01) level under the low pressure with a properly-selected Xe

Table 6.1: Time constants in laser cooling of CO₂-Xe gas.

| Mechanism | Time Constant | Magnitude |
|------------------------|--|---------------------------------------|
| Radiative ^a | $\tau_{f-f,e,sp, (00^01) \rightarrow (00^00)}$ | 2.383 ms |
| Decay | $\tau_{f-f,e,sp, (00^01) \rightarrow (02^00)}$ | 2172 |
| | $\tau_{f-f,e,sp, (00^01) \rightarrow (10^00)}$ | 2378 |
| | $\tau_{f-f,e,sp, (01^10) \rightarrow (00^00)}$ | 326.3 |
| | Nonradiative ^b | $p\tau_{f-f,v-t,CO_2-CO_2,(00^01)}^c$ |
| Decay | $p\tau_{f-f,v-t,CO_2-CO_2,(10^00)}^d$ | 0.454 |
| | $p\tau_{f-f,v-t,CO_2-CO_2,(01^10)}^d$ | 5.18 |
| | $p\tau_{f-f,v-t,CO_2-Xe,(00^01)}^d$ | 33.3 |

^a: Calculated using transition dipole values from Ref. [93]

^b: Data for 300 K, and data for other temperatures estimated using combination of experimental results [29, 172, 126] and theoretical models (Landau-Teller [98] and SSH [153])

^c: Ref. [126], and ^d: Ref. [29]

concentration is desirable for effective cooling.

6.3.3 Re-absorption

The cooling/heating rate is the difference between the absorbed photons under an overall relaxation rate and the photon emission rate by spontaneous processes. However, not all emitted photons from excited molecules reach the cylinder wall (once they reach there, it is assumed that they are completely absorbed). The average gas absorptance of the emitted photon depends on the integrated product of the absorption coefficient and path length, i.e.,

$$\langle \alpha_{ph,a,(00^00) \rightarrow (00^01)}(r) \rangle = \frac{1}{4\pi} \int_{\varphi=0}^{2\pi} \int_{\theta=0}^{\pi} \{1 - \exp[-\sigma_{ph,a,(00^00) \rightarrow (00^01)} l_{ph}(r, \theta, \varphi)]\} \sin\theta d\theta d\varphi, \quad (6.10)$$

where $\sigma_{ph,a,(00^00) \rightarrow (00^01)}$ is the absorption coefficient of a 4.3 μm wavelength and $l_{ph}(r, \theta, \varphi)$ is the photon path length at radial position r and angular directions

θ and φ . We only consider re-absorption of the 4.3 μm emission, which has the largest absorption cross-section area (from the PNNL database) and the highest spontaneous emission rate. Radiative decay rates of other spontaneous emissions are negligible compared to this. $\sigma_{ph,a,(00^00)\rightarrow(00^01)}$ is the product of the average absorption cross-section area (considering all branches in transition of rotational levels) $A_{ph,a,(00^00)\rightarrow(00^01)}$ and the number density difference of CO_2 molecules involved in the absorption process, $n_{\text{CO}_2,(00^00)} - n_{\text{CO}_2,(00^01)}$. Thus $\sigma_{ph,a,(00^00)\rightarrow(00^01)}$ increases with an increase in pressure and a decrease in temperature. The cooling/heating rate then becomes [144]

$$\begin{aligned} \frac{dE_{c,h}(r)}{dt} = & \frac{\hbar\omega_i}{\tau_{f-ph-f,(00^01)}} - \frac{\sum \hbar\omega_{(00^01)\rightarrow(v_1v_2^l0)}}{\tau_{f-ph,e,sp,(00^01)\rightarrow(v_1v_2^l0)}} \\ & + \frac{\langle \alpha_{ph,a,(00^00)\rightarrow(00^01)}(r) \rangle \hbar\omega_{(00^01)\rightarrow(00^00)}}{\tau_{f-ph,e,sp,(00^01)\rightarrow(00^00)}}, \end{aligned} \quad (6.11)$$

where ω_i is the absorbed photon wavelength.

6.3.4 Temperature Distribution

Using symmetry, only the radial variations of temperature and species concentration are considered in this study. The laser beam is smaller than the cylinder, and therefore excited CO_2 molecules diffuse outward. Their mass diffusion is governed by through the Fick law,

$$\dot{m}_{\text{CO}_2,(00^01)}(r) = -D_f \nabla n_{\text{CO}_2,(00^01)}(r)M, \quad (6.12)$$

where $\dot{m}_{\text{CO}_2,(00^01)}$ is the mass change rate, D_f is the diffusion coefficient, $n_{\text{CO}_2,(00^01)}$ is the number density of (00^01) level species, and M is the molecular mass. Using the species conservation equation with the Fick law,

$$\nabla \cdot \dot{m}_{\text{CO}_2,(00^01)} = -\nabla \cdot (D_f \nabla n_{\text{CO}_2,(00^01)} M) = \dot{n}_{\text{CO}_2,(00^01)} M, \quad (6.13)$$

and using the effective relaxation time of (00^01) ($\tau_{f-ph-f,(00^01)}$) only with the radial variation of properties,

$$\frac{D_f}{r} \frac{d}{dr} \left[r \frac{dn_{\text{CO}_2,(00^01)}}{dr} \right] - \frac{n_{\text{CO}_2,(00^01)}}{\tau_{f-ph-f,(00^01)}} = 0. \quad (6.14)$$

Then, the number density distribution of the excited state (00^01) is given as

$$\begin{aligned} n_{\text{CO}_2,(00^01)}(r) &= n_o && \text{for } 0 \leq r < R_l \text{ and} \\ n_{\text{CO}_2,(00^01)}(r) &= n_o \frac{K_o[r/(D_f \tau_{f-ph-f,(00^01)})^{0.5}]}{K_o[R_l/(D_f \tau_{f-ph-f,(00^01)})^{0.5}]} && \text{for } R_l \leq r < R_t, \end{aligned} \quad (6.15)$$

where n_o is the saturated number density and K_o is the zeroth-order modified Bessel's function of the second kind.

The steady-state energy equation is

$$\nabla \cdot q_k(r) = -k_f \left[\frac{1}{r} \frac{d}{dr} \left(r \frac{d\Delta T(r)}{dr} \right) \right] = \dot{s}_{ph-v-ph}(r), \quad (6.16)$$

where ΔT is the temperature difference from T_o (or the cooling effect), k_f is the thermal conductivity, and $\dot{s}_{ph-v-ph}$ is the volumetric source rate given as $n_{\text{CO}_2,(00^01)} dE_{c,h}(r)/dt$.

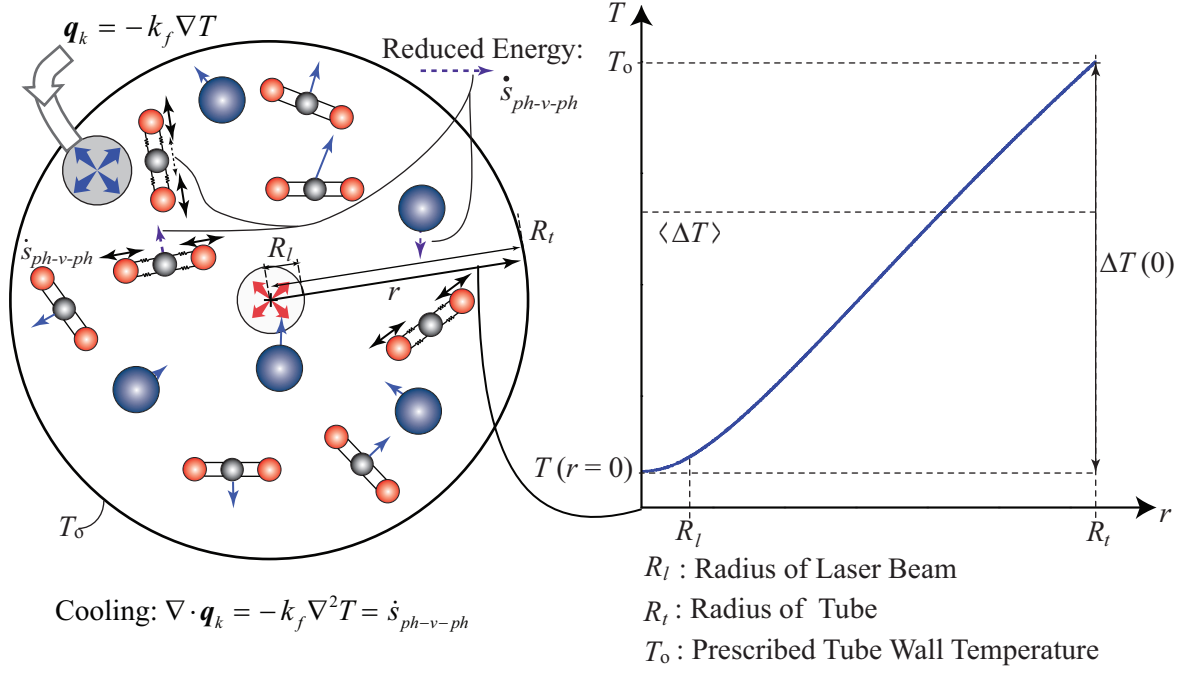


Figure 6.4: Gas differential energy balance, conduction and cooling/heating rate, and the gas temperature distribution showing local and average change in temperature. ΔT represents the cooling, and $\langle \Delta T \rangle$ is the average cooling. The maximum cooling is achieved at $r = 0$ [$\Delta T_{\max} = \Delta T(r = 0)$].

[$dE_{c,h}(r)/dt$ is obtained by Eq. (6.11)]

Solving Eq. (6.16), the cooling (ΔT) is given as

$$\Delta T(r) = T_o - T(r) = \frac{2}{R_t^2} \sum_{n=1}^{\infty} \frac{\langle \dot{s}_{ph-v-ph}(\alpha_n) \rangle J_0(\alpha_n r)}{k_f \alpha_n^2 [J_1(\alpha_n R_t)]}, \quad (6.17)$$

where $\alpha_n R_t$ is the n -th root of $J_0 = 0$ and $\langle \dot{s}_{ph-v-ph}(\alpha_n) \rangle = \int_0^{R_t} r \dot{s}_{ph-v-ph}(r) J_0(\alpha_n r) dr$.

The temperature distribution in the laser cooling system from this analysis is shown

in Fig. 6.4, and Ref. [38] also shows these results.

6.3.5 Dimensionless analysis

A dimensionless form of the steady-state temperature distribution is used to facilitate the analysis of cooling effectiveness. With the excited-population penetration length defined as

$$\delta_D = (D_f \tau_{f-ph-f,(00^01)})^{1/2}, \quad (6.18)$$

where D_f is the mass diffusivity for the excited (00^01) state and $\tau_{f-ph-f,(00^01)}$ is the overall relaxation time of the (00^01) state including radiative and nonradiative relaxations. The dimensionless cylinder and beam radii are $R_t^* = R_t/\delta_D$ and $R_l^* = R_l/\delta_D$. The reference temperature difference found from the energy equation is

$$\Delta T_o = \frac{n_{\text{CO}_2,(00^01),o} \delta_D^2}{k_f} \frac{dE_{c,h}}{dt}, \quad (6.19)$$

where k_f is gas thermal conductivity, $n_{\text{CO}_2,(00^01),o}$ is the number density of the (00^01) state in the irradiated beam region, and $dE_{c,h}/dt$ is the cooling/heating rate (cooling < 0). This rate is uniform in the irradiated region if re-absorption of the $4.3 \mu\text{m}$ spontaneous emission is not considered.

Thus, dimensionless cooling is

$$\begin{aligned} \Delta T^*(r^*) &= \frac{\Delta T(r^*)}{\Delta T_o} \\ &= 2R_t^{*2} \sum_{n=1}^{\infty} \frac{\int_0^\beta r^* J_o(\alpha_n r^*) dr^* + [\int_\beta^1 r^* K_o(r^* R_t^*) J_o(\alpha_n r^*) dr^* / K_o(R_t^*)]}{\alpha_n^2 [J_1(\alpha_n)]^2}, \end{aligned} \quad (6.20)$$

where α_n represents roots of the Bessel function J_0 , $\beta = R_l/R_t$ is the ratio of beam to cylinder radius, and $r^* = r/R_t$ is the dimensionless radial position. For $\beta = 1$, there is no spatial variation of $n_{\text{CO}_2,(00^0_1)}$, i.e., $\Delta T(r^*)$ is independent of D_f . Cooling is enhanced using large ΔT_o , i.e., small energy transport k_f , large species diffusion D_f , large nonequilibrium population $n_{\text{CO}_2,(00^0_1),o}$, and large quantum efficiency.

6.4 Results and Discussion

6.4.1 Laser irradiation wavelength

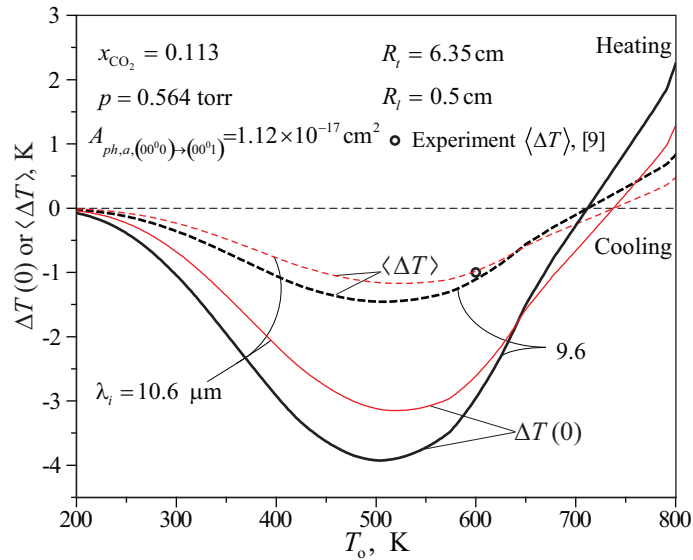


Figure 6.5: Comparison of 9.6 and 10.6 μm wavelength laser cooling, showing variations of cooling with respect for cylinder temperature for both wavelengths. The macroscopic conditions are the same as [38] and the experimental result of [38] for $\lambda_i = 10.6 \mu\text{m}$ is also shown.

In spite of the slightly larger photon energy absorption and lower absorption rate due to the smaller transition dipole, when compared to 10.6 μm [93], 9.6 μm resonance with excitation of (02^0_0) enhances cooling because of the increase in pumped

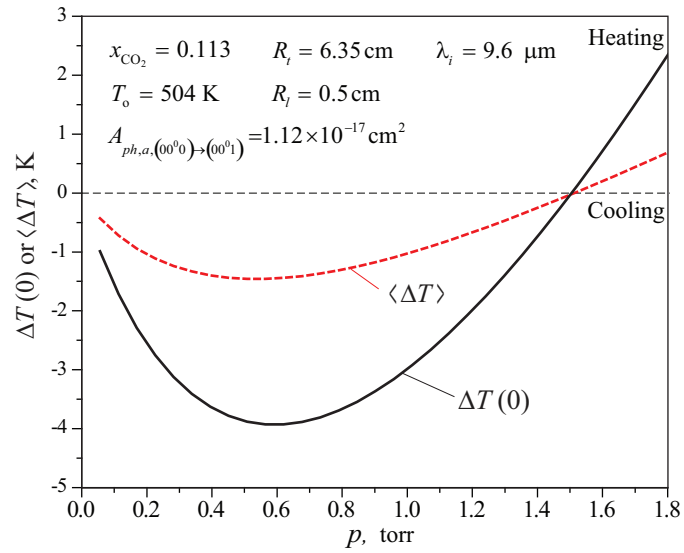
population. The 10.6 and 9.6 μm dual-beam irradiation appears to raise the excited population, but the (00^01) level population cannot exceed the saturated population with a 9.6 μm irradiation. Also, dual irradiation with the 15 μm laser changes the population of other energy levels that have smaller radiative relaxation rates (compared to nonradiative), and this deteriorates cooling. The cooling enhancement of the 9.6 μm wavelength in Fig. 6.5 shows 3.93 K cooling at a cylinder temperature of 504 K, and 1.05 K with the cylinder at room temperature. All macroscopic conditions are the same as in [38], and the experimental result of [38] is also shown in Fig. 6.5. Comparison of laser wavelengths shows that the shorter wavelength results in improved cooling.

6.4.2 Gas condition: T , p , and x_{Xe}

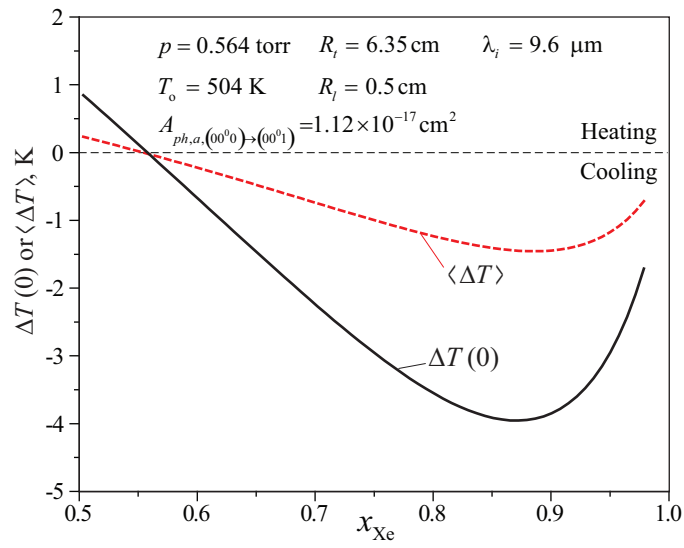
Even though k_f and $P_{f-f,v-t}$ increases at higher temperatures, the pumped energy level (02^00) population also rises with an increase in (00^01) . Higher temperatures increase D_f and maintain a large deviation in (00^01) , even in the non-irradiated region. $\sigma_{ph,a,(00^00)\rightarrow(00^01)}$ decreases with temperature due to a decrease in CO_2 number density. Therefore, the maximum cooling temperature is found when the deteriorating factors—i.e., increased k_f and $P_{f-f,v-t}$ —are properly compensated by the enhancing factors—i.e., large $n_{\text{CO}_2,(00^01)}$, D_f and small $\sigma_{ph,a,(00^00)\rightarrow(00^01)}$.

Figures 6.6(a) and (b) show cooling variations with respect to macroscopic conditions (a) pressure p and (b) Xe diluent atomic fraction x_{Xe} ; both show optima. Low total pressures reduce re-absorption and nonradiative relaxation, but high pres-

sures are desirable for significant species diffusion. Likewise, the larger x_{Xe} leads to lower k_f , larger D_f , smaller $\sigma_{ph,a}$, and lower $P_{f-f,v-t}$, while the smaller x_{Xe} the larger $n_{CO_2,(00^0 1)}$.



(a)



(b)

Figure 6.6: Variations of cooling with respect to (a) total gas pressure p and (b) Xe mole fraction x_{Xe} .

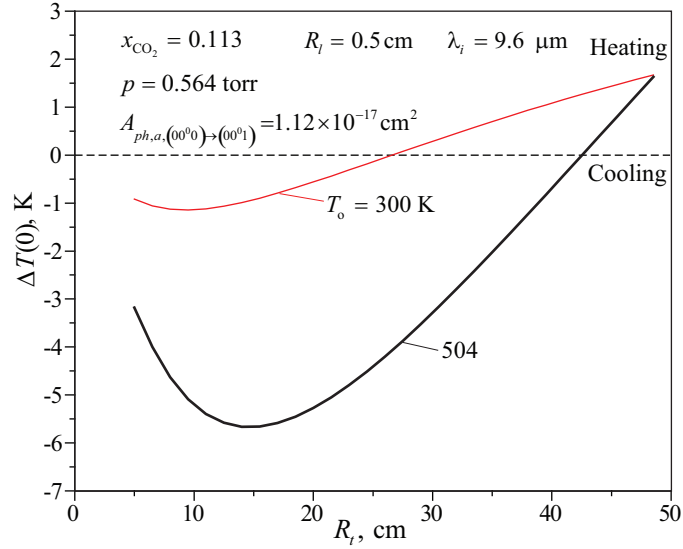


Figure 6.7: Variations of cooling with respect to cylinder radius R_t , at several cylinder temperatures, showing the effect of re-absorption (absorption coefficient and emitted photon path length).

6.4.3 Geometrical condition: reabsorption effects

As cylinder radius R_t increases, the heat flow rate from the wall decreases, and re-absorption increases due to the longer photon path length. Selection of optimal R_t is also influenced by macroscopic conditions, which in turn influence $\sigma_{ph,a,(00^0) \rightarrow (00^1)}$. Figure 6.7 shows the variation of cooling with respect to R_t at different cylinder temperatures. Optimal R_t for cooling increases with temperature as re-absorption reduces, as a result of small $\sigma_{ph,a,(00^0) \rightarrow (00^1)}$ at high temperatures.

The large beam radius and larger threshold irradiation required to populate the (00^01) level yield a large laser power. The maximum cooling limit occurs when the (00^01) level is saturated throughout the gas ($R_l = R_t$, i.e., $\beta = 1$), so it requires a high laser power. The maximum cooling for $T_o = 300$ K ($R_l = R_t = 10$ cm, $p = 0.67$ torr and $x_{Xe} = 0.89$) is $\Delta T(0)_{\max} = 8.07$ K (with cooling rate of 317.6 K/s). Also,

at the optimal temperature $T_o = 504$ K ($R_l = R_t = 14$ cm, $p = 0.56$ torr and $x_{Xe} = 0.89$), the maximum cooling limit is $\Delta T(0)_{\max} = 44.9$ K (with cooling rate of 2427 K/s).

6.5 Summary

In this chapter, the anti-Stokes molecular-gas laser cooling and its enhancement by manipulating the population distribution are analyzed. Deviation of the excited vibrational state population of CO_2 from the equilibrium population is central in the laser cooling enhancement. In our analysis, in order to enhance the laser cooling, the vibrational energy population distribution is manipulated by choosing laser photon frequency, and in particular, irradiation with a $9.6 \mu\text{m}$ wavelength in resonance with (02^0_0) improves the cooling performance by increasing the population of the (00^0_1) level. The availability of tunable dye lasers to achieve the desired wavelength makes it possible to target vibrational population inversions for the most effective cooling. With this ability to select the excitation, the optimal cooling of CO_2 has been addressed. The desired nonequilibrium population distribution for laser cooling can be achieved by resonance with other energy carriers, such as electrons or phonons. Thus, a possible extension of population manipulation for cooling enhancement is to increase the population of (10^0_0) by low-energy electron impact along with $10.6 \mu\text{m}$ laser irradiation, which would improve cooling through the large population of the (00^0_1) level [192, 92]. Also, the internal vibrational energy of the bounding solid (phonon) can excite the vibrational energy level of gas molecules adsorbed on the

solid surface [200]. Therefore, finding the relaxation channel of phonons resonating with excited energy levels is another possible extension to improve the cooling.

Optimal macroscopic conditions (T , p and x_{Xe}) allow for large excited-level population through control of species diffusion and kinetics of the excited vibration levels, which improves cooling with hindered energy transport. Inclusion of re-absorption determines the optimal geometry. With (02^00) excitation and selection of gas conditions and geometry, enhanced anti-Stokes cooling of CO_2 -Xe gas is predicted even at or around room temperature. Then cooling is effective at low pressures, but the cooling rate is fast and it is non-mechanical, with possible applications in space telescope or satellite and where there is a need for fast cooling of not easily accessible regions.

Chapter 7

Summary and Future Work

7.1 Contributions

Nonequilibrium (deviation from equilibrium energy distribution) is omnipresent in energy transport and conversion, but the nonequilibrium features are not generally addressed. This study examines the fundamentals pertaining to thermal energy transport and conversion with direct inclusion of nonequilibrium carrier energy distribution, especially in phonons and molecular vibrations. The study is motivated by the idea of harvesting nonequilibrium states for innovative new energy conversion applications and for enhancing energy conversion efficiency among principal energy carriers (electrons, phonons, photons and fluid particles). Also, nonequilibrium populations provide fundamental understanding in atomic-level transport. In particular,

the interfacial transport (resistance) is generally a transport bottleneck, and the findings of this work can have significant impact in thermal analysis of micro/nanoscale devices or high-conductivity composites.

This theoretical study applies diverse atomistic simulations and theories including *ab initio* (based on the first principle), molecular dynamics (with classical equations) and mesoscale simulations (ensemble Monte Carlo). The results from these multiscale simulations are analyzed using various theoretical models in semiclassical mechanics, lattice dynamics, and Green function formalism. Comprehensive and systematic multiscale analyses improve the theoretical interpretation and the models in addition to providing fundamental insights with respect to quantum and classical physics.

The significant contributions of this work are summarized below.

- *Development of novel heterobarrier structures for converting hot-phonon energy to electrical potential* [163]. The heterobarrier or hot-phonon absorption barrier (HPAB) structure proposed in Chapter 2 reverses the general phonon roles (i.e., deteriorating device performance by hindering transport and increasing operating temperature) through harvesting phonons as energy commodity. This HPAB structure is designed as an embedded (integrated) structure, so that it can be placed near the hot-phonon source for effective pre-thermalization harvesting. Through the direct energy conversion from phonon energy to electric potential in this structure, the following effects are predicted. (i) Electric potential is gained (or recovered) and this will enhance energy conversion efficiency. (ii) Heat dissipation will be reduced, lowering operation temperature. (iii) The

electron transport is enhanced through the effective removal of excess phonons (reducing the phonon friction).

- *Theoretical analysis of the entropy production and efficiency of phonon-electron energy conversion* [161]. In Chapter 3, entropy production in energy conversion systems including the phonon-phonon and phonon-electron interactions is examined, and the hot-phonon converting heterobarrier system of Chapter 2 is analyzed. This analysis demonstrates the validity of the introduced heterobarrier hot-phonon energy conversion and gives a theoretical upper limit for the conversion efficiency. As expected, this efficiency is larger than that obtained from the MC simulations.
- *Proposed decomposition of interfacial resistance and introduction of roles of atomic restructuring in thermal interfacial transport* [162]. The bottleneck in the thermal transport in micro/nano scale devices is at the interfaces; therefore, the study of interfacial transport is essential in the thermal transport analysis of small systems. The decomposition of the interfacial phonon resistance into boundary and interfacial-region components is suggested in Chapter 4, and this new method enables more systematic analysis of interfacial transport. The effects of interfacial atomic restructuring on these decomposed resistance components (boundary and interfacial-region) are introduced. The phonon spectrum broadening by atomic restructuring reduces the boundary resistance by providing additional phonon transport channels (modes), while non-crystalline structure adds extra scattering resistance in the interfacial regions. This work

provides enhanced understanding and suggests a more accurate prediction of the interfacial transport using the interfacial-region phonon properties, and this tool allows for avoiding computationally expensive simulations.

- *Thermal transport across low-dimensional graphene junctions.* [160]. In Chapter 5, thermal transport across graphene junctions was investigated considering both electron and phonon contributions, and the results from this study benefit the design of graphene composite as a promising high-conductivity material. Also, some interesting characteristics in the low-dimensional thermal transport in atomic dimensions (less than a few nanometer) were observed, such as a bimodal phonon transmission at the low and high frequencies caused by the weak coupling between two flakes and the tunneling resonant peaks of the passivated atoms. The mode or frequency dependence of the phonon transport is controlled by the edge passivation, and this may provide a tool for the phonon engineering of the graphene compounds. With regards to methodology, since NEGF formalism has not been widely used for phonon transport, this study, introducing and showing NEGF application, can guide further study of phonon junction transport. In addition, by relating NEGF to the semiclassical acoustic mismatch model, a more comprehensive understanding of both quantum and classical interfacial and junction transport is suggested.
- *Enhancement of cooling performance in molecular-gas laser system* [159]. Nonequilibrium dynamics based on the interaction kinetics between molecules and photons is studied for molecular-gas laser cooling system, and through this study

the conditions for cooling enhancement have been found (Chapter 6). The cooling by laser is attractive and useful for many applications because of fast and non-mechanical process, but its low cooling efficiency in molecular-gas system has been a major challenge for applications. Therefore, the finding of the cooling enhancement and the systematical analysis of the cooling system are significant steps toward the practical applications of molecular-gas laser cooling.

7.2 Recommendation for further studies

Further studies of the nonequilibrium physics of the four principal energy carriers will provide physical understanding and new, innovative solutions for a variety of thermal energy transport and conversion challenges. Here, possible extensions of the energy conversion and transport issues are suggested.

7.2.1 Further studies of hot-phonon energy conversion

Since more energy is wasted as heat than converted to useful energy, reducing the waste heat contributes much to the conversion efficiency enhancement, helping with the energy needs. Harvesting the nonequilibrium energy carriers (e.g., hot phonons and electrons) before their thermalization decreases the waste heat and enhances device performance. Expanding on the hot phonon research of Chapters 2 and 3, converting nonequilibrium energy-carrier states (which have smaller entropy) can be further studied for practical, integrated circuit systems and energy conversion systems (e.g., chemical reaction, solar photovoltaic cell, and laser). For the further studies,

more advanced and rigorous predictions for the material properties and system evaluation are recommended, and this will not only improve the system analysis but also inspire other fundamental findings in the carrier interaction kinetics and transport.

7.2.1.1 Phonon energy conversion in high electron mobility transistor

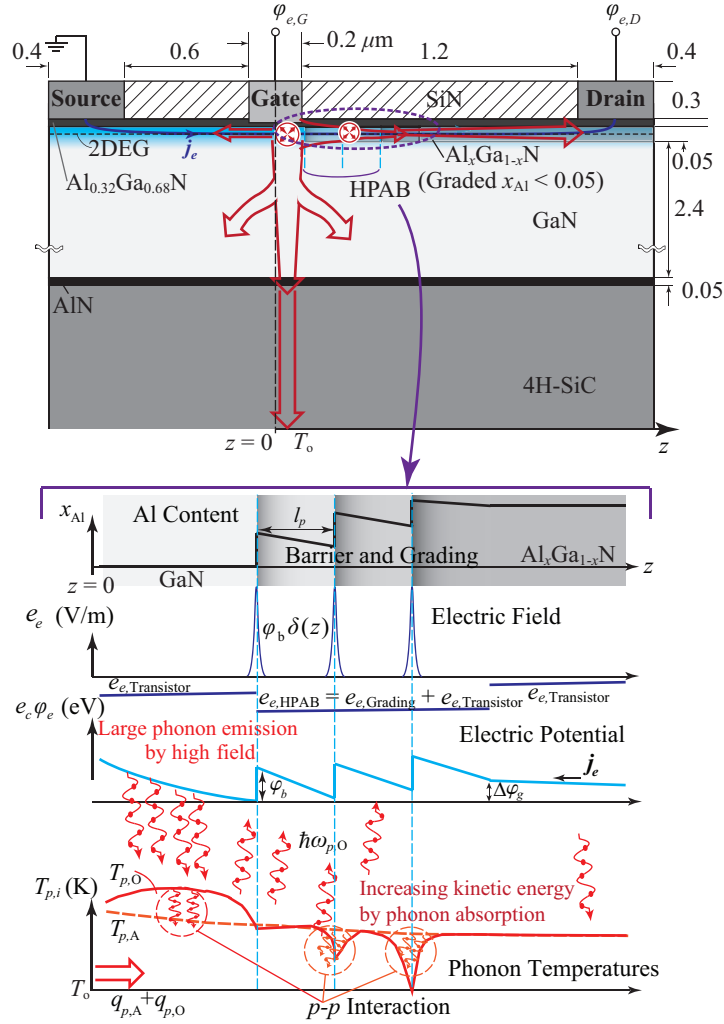


Figure 7.1: Proposed integrated GaN HEMT-HPAB circuit, and variations of Al content, electric potential and field, and temperature.

The HPAB structure has potential to be integrated into the high-power circuits where resistance to electron current emits a large number of optical phonons, as

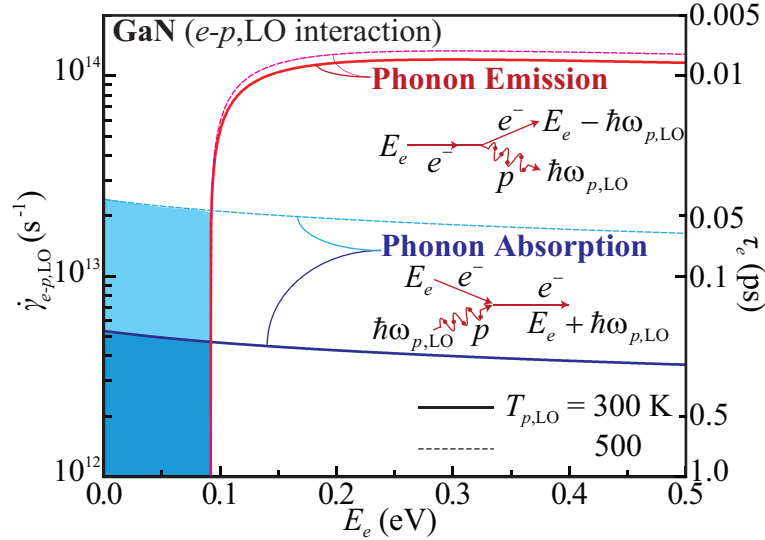


Figure 7.2: Electron-LO phonon interaction (absorption and emission) rate in GaN when the LO phonon temperature ($T_{p,LO}$) is 300 and 500 K. The electron and phonon properties, such as static and optical dielectric constants ($\epsilon_{e,s}$ and $\epsilon_{e,\infty}$), in Refs. [20] and [118] are employed for this polar optical phonon interaction.

shown in Fig. 2.13. The state of the art GaN-based high-electron-mobility transistors (HEMT) can be a good candidate for the HPAB structure application. GaN-based high-electron-mobility transistors are promising in the high-frequency (microwave) and high-power applications [43, 123]. The polarization and piezoelectric fields in an undoped AlGaIn/GaN interface form a high-density two-dimensional electron gas (2DEG) channel in GaN at the heterojunction [1], and the electron mobility in 2DEG channel is high in the absence of impurity scattering. However, due to the strong electron-phonon (especially LO mode) coupling in GaN, electrons accelerated by high field, emit a large number of optical phonons, and these phonons limit the capabilities of GaN-HEMTs [2]. In a GaN 2DEG channel, the hot-phonon lifetime (~ 350 fs) is much longer than the time for spontaneous LO-phonon emission (~ 10 fs), and the hot phonons tend to accumulate [114]. These hot phonons are finally relaxed to the

acoustic phonons, increasing the temperature, and cause an additional friction for the drifting electrons (larger than the friction imposed by the equilibrium phonons), thus reducing the electron mobility and the drain current (the self-heating effect). Introduction of the HPAB structure in GaN-HEMT, as shown in Fig. 7.1, can resolve this self-heating problem.

Similar to the GaAs/AlGaAs interface, GaN/AlGaN has a band discontinuity, because of the larger AlGaN bandgap [23], therefore the barrier structure can be controlled by Al alloying. As shown in Fig. 7.2, with larger population of the low-energy electrons by the barrier structure, the GaN can also have favorable conditions for the phonon absorption with high population of the low-energy electrons ($< E_{p,LO}$).

7.2.1.2 Other applications of hot-phonon absorption barrier system

Although the light-emitting diode (LED) has 3-fold larger efficiency than the incandescent lighting, more energy is wasted as heat than used for lighting (currently has up to 35% plug-in-efficiency) [152]. The wasted heat originates from the large optical phonon emission by the nonradiative relaxation and resistive transport processes. As Ref. [85] suggested, in phonon recycling in LED the HPAB integration can harvest the emitted phonons. This is shown in Fig. 7.3(a), when the emitted phonons in LED operation layers and transport processes will be absorbed in the HPAB converted into electric potential energy.

Hot phonons are also generated in chemisorbed vibration energy relaxation and solar photovoltaic cell, but based on the results so far, sufficient phonon generation for significant power gain is not expected. However, with the enhanced design or

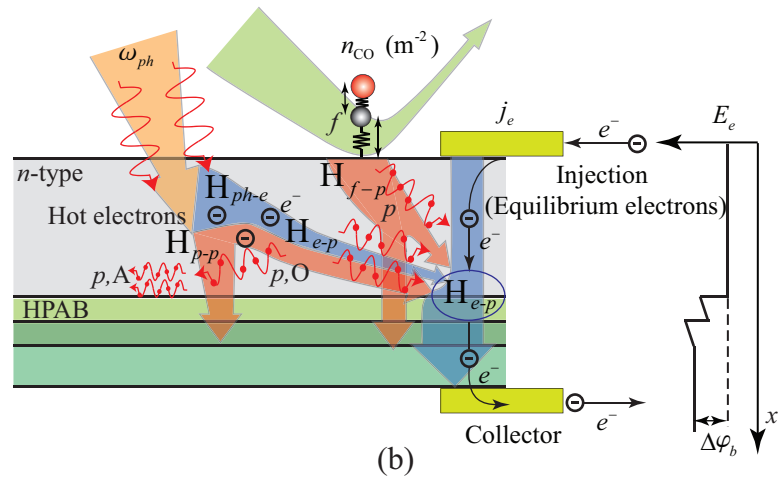
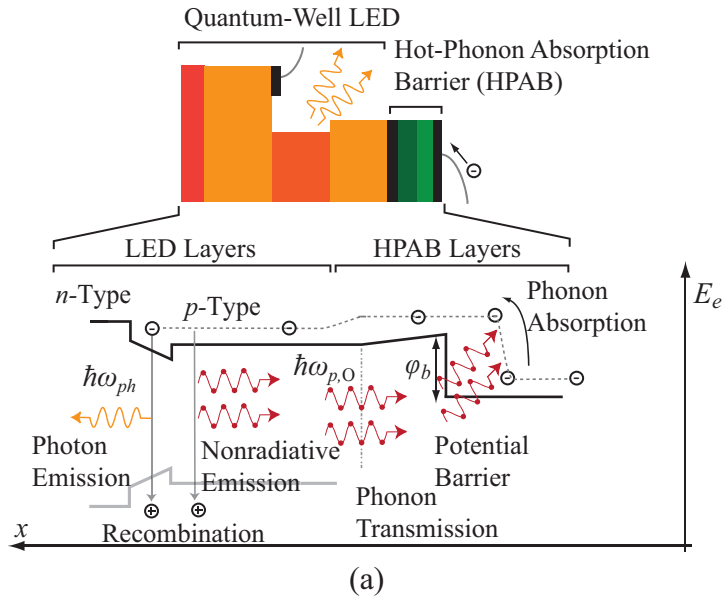


Figure 7.3: Possible HPAB structures for harvesting hot phonons (a) in LED system and (b) in solar and chemisorbed vibration energy relaxation

by finding the desirable heterobarrier structures, the hot phonons may be harvested.

Figure 7.3(b) suggests this HPAB application.

7.2.1.3 Advance simulations

The material properties (electron and phonon properties, interaction rates, etc.) should be identified for the HPAB analysis, and these properties are obtained from the

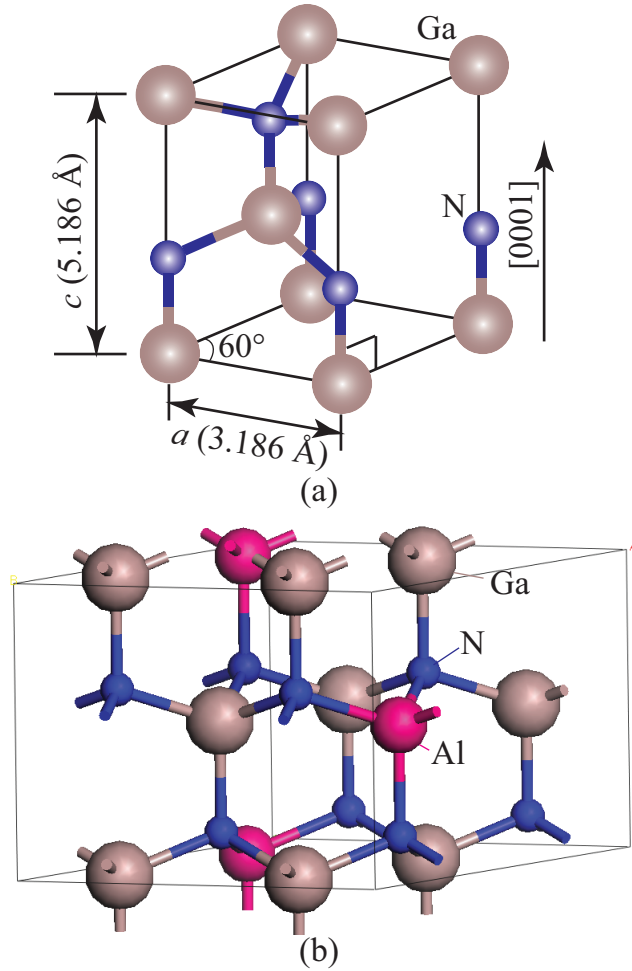


Figure 7.4: (a) Primitive cell of Wurtzite GaN. Lattice constants (a and c) and crystal direction $[0001]$ are shown. (b) Atomic configuration of $\text{Al}_{0.25}\text{Ga}_{0.75}\text{N}$. $2 \times 2 \times 1$ supercell is considered and 2 Ga atoms are replaced with Al.

ab initio and molecular dynamics simulation methods. Based on the properties, the HPAB efficiency and overall system performance can be assessed and optimized using the meso- (Monte Carlo) and macroscale energy conversion and transport analyses.

The findings in this work employ many assumptions in order to make computationally reasonable calculations, but more advanced and rigorous simulations will improve the system analysis, and further insight into the fundamental physics of the carrier interaction and transport can be found in advanced studies.

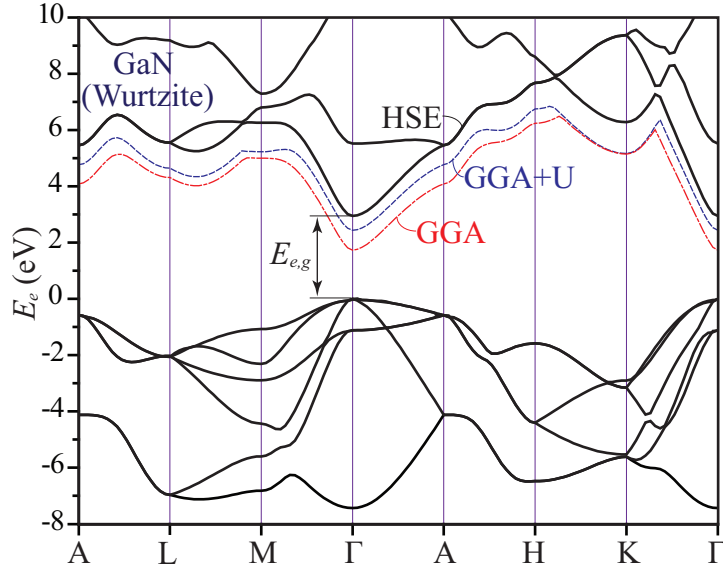


Figure 7.5: Electronic band structure of wurtzite GaN from *ab initio* (using VASP). GGA [132] is widely used approximation for exchange correlation potential, but underestimates band gap, $E_{e,g}$. GGA+U (including the Coulomb potential) [4] and HSE (hybrid functional) [65] are employed to have more accurate band structure. *Ab initio* results (a , c , $E_{e,g}$, band structure, etc.) from HSE agrees well with experiments and literatures [20, 17].

Constant material properties (i.e., pure GaAs properties from experiments) are assumed in the Chapter 2, but the electron and phonon properties will vary with the Al alloying content. Due to the lack of the experimental data, various simulations should be carried out for the electron and phonon properties of the alloyed semiconductors. Many properties, such as the electron effective mass, phonon and electron density of state, and phonon speed, can be found from the electron and phonon band properties, obtained from the *ab initio* methods. [Various computer codes based on density function theory (DFT) such as VASP, SIESTA, and WIEN2k can be utilized.]

For the alloyed systems, the simulated unit cell structure should be adjusted depending on the Al content and material composition. Figures 7.4(a) and (b) show examples of unit cells for alloyed system for AlGaIn HPAB suggested in Section 7.2.1.1.

(Larger unit cells will be required for alloying systems to have the prescribed Al content.) In spite of the limited accuracy of the DFT in the band structure calculation (because the ground-state wave functions are not sufficient for evaluation of the conduction band, especially in the large band gap materials), many compensational techniques have been proposed. Figure 7.5 shows the improvements in the *ab initio* electronic band structure calculations for the GaN using various functionals [132, 4, 65].

The carrier interaction kinetics (e.g., *e-p* interaction) can also be investigated by the advanced simulations. For example, the dielectric properties ($\epsilon_{e,s}$ and $\epsilon_{e,\infty}$) for the polar optical phonon interactions and the *e-p* coupling coefficients for the nonpolar phonon interactions can be calculated using the *ab initio* software (VASP and Quantum Espresso will be mainly tried) using the electron system response to the linear perturbation in the DFT (or DFPT, density functional perturbation theory) [9]. The *ab initio* molecular dynamics (AIMD) simulations [113] can be used for an atomic structure with the thermal perturbation (depending on temperature) [84] and phonon transport properties for the barrier system. In spite of the limit in the computational resources, this approach is now widely used and becomes more available as the computing technology advances.

Material and transport properties from new simulations can be employed in the self-consistent ensemble MC code used, and this will improve the MC code. In addition, various scattering mechanisms (e.g., *e-e* scattering and impurity scattering) and barrier transition algorithms [64, 79, 121] can be added.

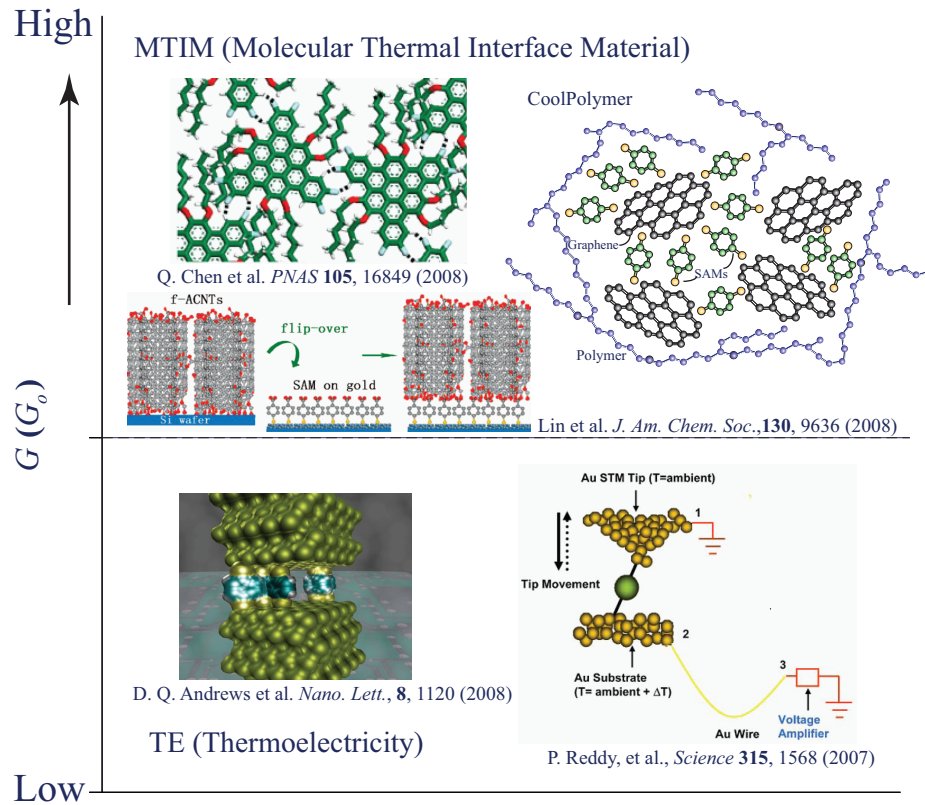


Figure 7.6: The diverse applications of molecular junction according to the thermal conductance.

7.2.2 Further studies of thermal interfacial and junction transports

The thermal energy transport (characterized by thermal conductance/resistance G/R or conductivity k) is central in performance of many devices. Figure 7.6 shows the molecular junction applications, where the thermal conductance should be manipulated according to the application. For thermoelectricity (TE), the low thermal conductance is desirable, whereas high thermal conductance is necessary for the effective heat dissipation in electronic components or in the thermal interfacial materials (TIMs).

Based on the significance of the thermal interfacial transport as a bottleneck, the study can be expanded to various types of interfaces and junctions. The transport across repeated (periodic) interfaces in superlattices, promising structures for thermoelectrics (suppression of phonon conductivity) and solar photovoltaics, is a good example of extending the interfacial study. Also, molecular-junction transport (phonon and electron) can be studied further for the thermoelectrics, interfacial materials, and nanostructured-based organic solar and fuel cells.

For these interfacial studies, both the particle and wave features (with classical and quantum mechanics) of the phonons and electrons need to be considered (because the transport is at the atomic scale). Molecular dynamics and the Green function formalism, employed in this work, give new perspectives to these thermal transport phenomena.

Chapter 4 suggests that the interfacial atomic restructuring and interaction play an important role in the thermal interfacial transport, and those interfacial properties can be more accurately predicted by *ab initio* MD (with fewer assumptions than MD). (Using the *ab initio* MD, the approximations connected with the empirical potentials or relaxation times are not necessary; thus, the analysis will be improved.) The ballistic conductance from the Green function in Chapter 5 can be also compared with the MD or the *ab initio* MD. This comprehensive interfacial transport research will improve our understandings of the phonon energy transport, will identify key factors, such as the interfacial atomic structure and the bonds, controlling the thermal transport properties, and will enable accurate predictions and better device design.

7.2.3 Experimental studies

Since the realistic systems have too many variables (including uncontrollable features), many simplifications and assumptions are necessary for theoretical studies, and the simplifications limit their applicability. On the other hand, theoretical studies are economical in time and cost, and facilitates systematic analysis of a new systems.

This work proposes novel energy conversion systems and new atomic-level theoretical treatments and insights in the energy conversion and transport. However, the approximations need to be verified through experimental studies. As extensions of the studies presented in this thesis, it is recommended to fabricate the heterobarrier structure for converting hot-phonon energy (Chapter 2 and Section 7.2.1) and to test its performance. Also, comparison of the predicted interfacial transport with experiments is also recommended to verify the theoretical treatments.

The combination of theoretical and experimental studies is expected to create useful synergy. The unexpected results in the experiments can lead to further theoretical studies and the re-examinations of the assumptions and approximations. Also, theoretical treatment can inspire new experimental studies.

7.3 Outlook

Traditionally, the heat transfer engineering has concentrated on thermal energy transport at macroscale, and considered the related materials as given. However, with advances in the synthesis of new materials, and with the emergence and importance of the energy conversion technologies and the micro/nanoscale devices, there is a shift

to the atomic-level understanding and design of the energy-related materials. So, the field has expanded, with more fundamental and innovative studies of the principal energy carriers, i.e., the heat transfer physics.

The kinetics of interactions among the principal energy carriers (phonon, electron, fluid particle and photon) is central to heat transfer physics. Also ever present and central are the nonequilibrium energy occupancy of the carriers. These kinetics in turn depend on the vibrational and electronic band structure of materials. This thesis presents through various examples, how the nonequilibrium vibrational and electronic energy occupancies can be described and applied in energy conversion. Ideas, such the heterobarrier for direct conversion of hot phonons to electricity, are beginning steps in using the heat transfer physics and the atomic-level materials, insights and syntheses to introduce new energy conversion systems or improve the efficiency of the existing systems. The future of such discoveries and innovation is very promising.

Appendix A

Monte Carlo Method for Carrier Transport

A.1 Introduction

The Monte Carlo (MC) is a broad term and describes an approach to solving problems that involves generating a sequence of random numbers. This can be employed to solve the Boltzmann transport equation (BTE) for the phonon, electron, fluid particle and photon transport phenomena. At first glance, one may raise the question on how the randomness in the MC can generate a correct solution to the transport equation. However, the energy carriers travel according to the scattering probabilities based on the physics, and the uniformly distributed random number

decides the scattering sequences using the probabilities [195].

A.2 Electron transport

The MC simulation is widely used for the electron transport and is regarded as one of the most accurate approaches for simulating device performance [108]. The semiclassical MC simulation employs randomly selected scattering mechanisms and relaxation times, which are theoretical based on the quantum mechanical Fermi golden rule, and the classical equations of motion for charge (e.g., electron) carrier transport between scattering events. This is represented by

$$\frac{d\mathbf{r}_e}{dt} = \frac{1}{\hbar} \nabla_{\kappa_e} E_e(\kappa_e) \text{ and } \frac{d\kappa_e}{dt} = \frac{q\mathbf{e}_e}{\hbar}, \quad (\text{A.1})$$

where \mathbf{r}_e is the position, E_e is the energy, κ_e is the momentum wave vector of the simulated carrier, \mathbf{e}_e is electric field vector and q is the electric charge. The energy dispersion relation, or the band structure, $E_e(\kappa_e)$, should be identified for the drift (free-flight) of carriers. The random selection procedure for the scattering mechanisms can be simplified through introduction of the self scattering [140]. Otherwise, we need the full integral form of the free-flight probability density function for all scattering mechanisms. Scattering rates are generally functions of the energy, so the overall rate (by the Matthiessen rule) changes with carrier energy. However, with the self-scattering mechanism, we can use a constant total scattering rate ($\dot{\gamma}_o$), then by the use of only one random number can cover the various scattering models. This is illustrated in Figure A.1(a). The relaxation time of each carrier (τ) is randomly

assigned (with a random number, ran) based on the constant total relaxation time ($\tau_o = 1/\dot{\gamma}_o$) as

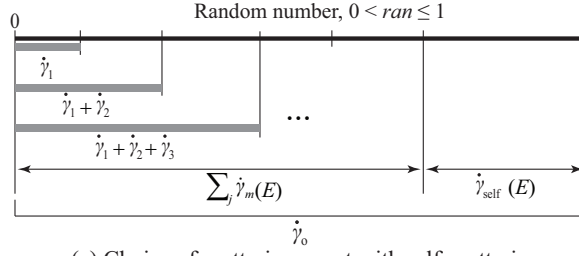
$$\tau = -\frac{1}{\dot{\gamma}_o} \ln(ran). \quad (\text{A.2})$$

Each carrier is scattered or drifted during a simulation time step and Fig. A.1(b) outlines an algorithm for this process [67]. The lookup tables for scattering rates of various mechanisms can save calculation time.

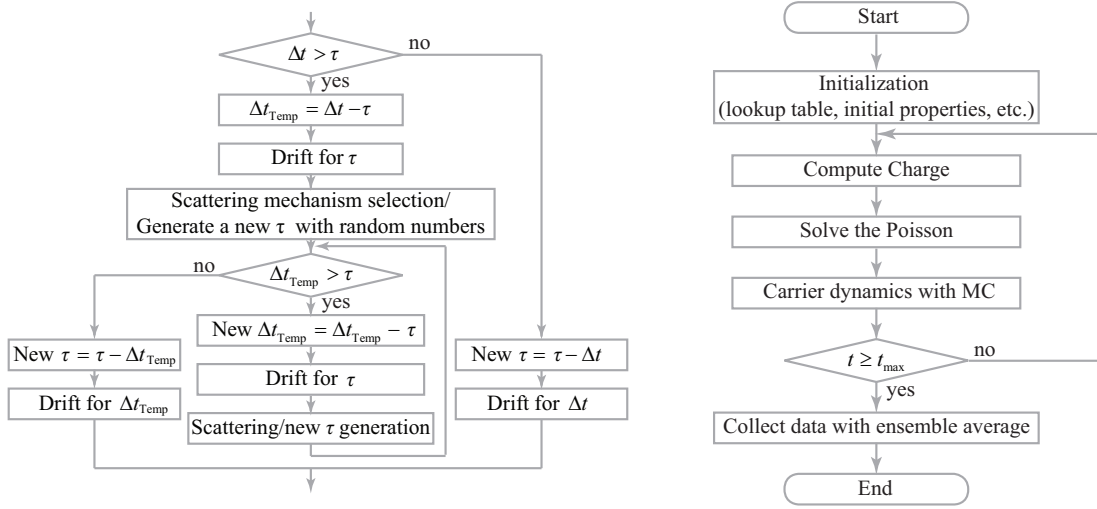
In many electron transport Monte Carlo simulations, the so called "ensemble Monte Carlo simulations", a large ensemble of electrons are simulated at the same time. Then the ensemble average over long enough time is taken for the calculation of properties such as the electric mobility. The carrier distribution influences the electric field and the field influences the carrier trajectory, as described with the Poisson equation as

$$-\nabla \cdot (\epsilon_o \epsilon_e \nabla \varphi_e) = e_c n_e, \quad (\text{A.3})$$

where ϵ_e is the permittivity, n_e is the charge density, and φ_e is the electric potential. The ensemble MC simulation is coupled with the Poisson equation by the iteration process, so-called "self-consistent process" to make charge distribution consistent with field, and field consistent with distribution as shown in Fig. A.1(c). This self-consistent ensemble Monte Carlo method is widely used for device simulations [67, 79, 121, 64].



(a) Choice of scattering event with self-scattering



(b) Free-flight and scattering sequence for each carrier within Δt (c) Algorithm of self-consistent ensemble MC simulation

Figure A.1: (a) Choice of scattering event. The constant scattering rate ($\dot{\gamma}_o$) is composed of overall scattering ($\sum_{m=1}^j \dot{\gamma}_m$, j is the total number of possible scattering mechanisms) and the self-scattering rates ($\dot{\gamma}_{self}$), $\dot{\gamma}_o = \sum_{m=1}^j (\dot{\gamma}_m + \dot{\gamma}_{self})$. If the random number, ran is between $\sum_{m=1}^{i-1} \dot{\gamma}_m / \dot{\gamma}_o$ and $\sum_{m=1}^i \dot{\gamma}_m / \dot{\gamma}_o$, the i -th scattering mechanism is selected. If the self-scattering is selected ($ran > \sum_{m=1}^j \dot{\gamma}_m$), neither energy nor momentum of the carrier changes. (b) The free-flight and scattering sequence. According to randomly assigned scattering time (τ), a carrier can be scattered or drift within a given time step (Δt). Once it finishes its free-flight, a carrier is scattered with randomly selected scattering mechanism and a new scattering time is assigned to the carrier. (c) An algorithm of the self-consistent ensemble MC simulation. Electric potential and field from charge distribution are calculated by solving the Poisson equation, and carrier trajectories are simulated using the MC method with them. Carrier distribution obtained from the simulation is used to update the internal field.

A.3 Simulation of phonon, fluid particle, and photon transport

The MC simulations are also applied to solve BTE for the phonon transport phenomena, in a similar manner to the electron transport, despite its differences [116]. The equilibrium phonon occupation number is given by the Bose-Einstein distribution and the phonon group velocity ($u_{p,g}$) and density of states (D_p) calculated from the phonon dispersion. Phonons travel with the group velocity and engage in scattering with other phonons, impurity, lattice boundary, electrons, etc. The ensemble of phonon trajectories are calculated with a stochastic sampling of the scattering events. Phonons can be annihilated and created during the three-phonon interactions, which is representative phonon scattering as normal and Umklapp processes. During the Umklapp process, energy is not conserved posing resistance in energy transport. The MC approach have been applied to phonon transport at nanoscales because of its flexibility in accounting for complicated geometries and use of proper phonon dispersion relation and different polarization branches [194, 96, 138, 60, 80].

Fluid particles in the transitional-flow regime have been simulated with this method. Both interparticle and particle-surface collisions are considered in the transition regime ($10^{-2} < \text{Kn}_l < 1$, Kn_l is the Knudsen number defined as λ_f/l , where λ_f is the molecular spacing and l is clearance distance.). The MC for fluid particle transport [also called direct simulation Monte Carlo (or DSMC)], treats the fluid particle motion and intermolecular collision separately based on dilute gas assumption and the kinetic theory [14]. Thus, the DSMC cannot be applied to dense gases

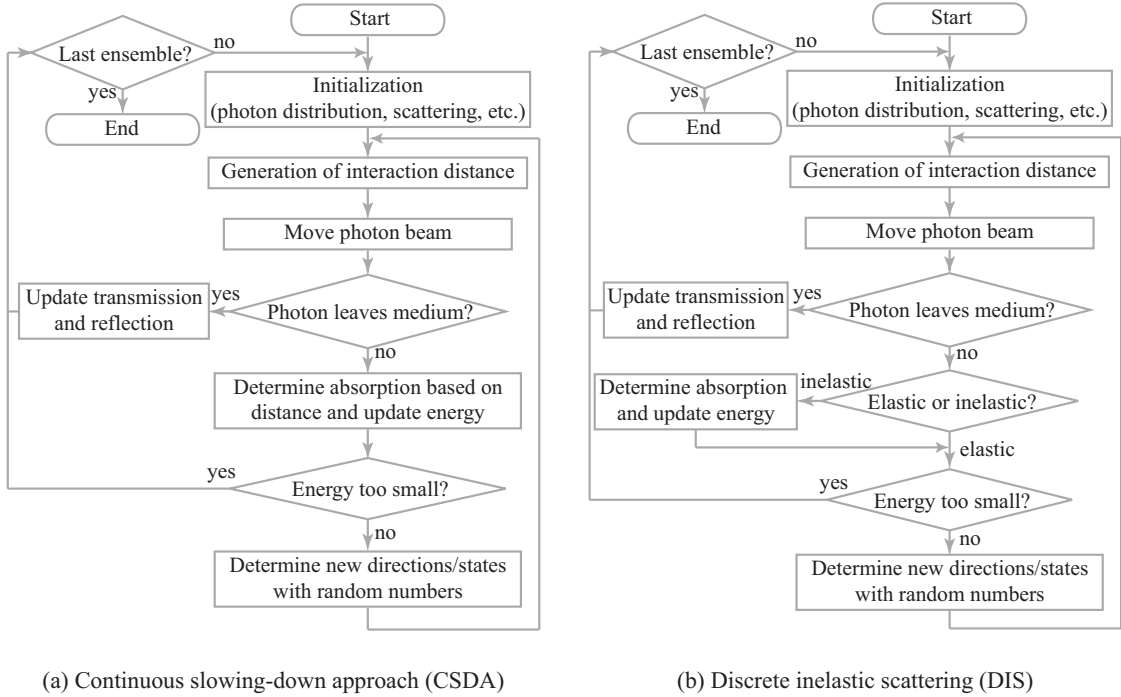


Figure A.2: Flowcharts of the MC simulation of photon transport using (a) CSDA, and (b) DIS treatment. Photon beam with randomly initialized spatial distribution travels during a photon interaction time, τ_{ph} . If photon escapes the computation domain after the free flight and the prescribed number of simulated beams is not sufficient, new photon beams are simulated. Otherwise, the photon beam is scattered and its new energy is updated (when scattering is inelastic), as well as its directions, etc. In energy absorption, if new energy after scattering is smaller than a prescribed criterion, photon beam is regarded as annihilated and simulation for this beam is stopped.

or to highly ionized plasmas dominated by the long-range interactions (although it is applied to weakly ionized gases with the Poisson equation to include the electric field effect [175]). This approach was first used for the homogeneous gas relaxation problem, and has been used in the flow analysis, such as shock structure [12, 13].

The MC method for photon transport employs the concept of particle-beam based on the radiative transfer equation (ERT), and it has its distinct features compared to for example electron transport [195, 166]. There are two photon transport treatment, i.e., the continuous slowing-down approach (CSDA) and the discrete inelastic

scattering (DIS). Both initialize photon beam (photon packet) profiles with random numbers and generally use a spatial uniform or Gaussian beam intensity distribution. The main difference between two treatments is that the CSDA treats inelastic scattering as a continuous event, so energy change corresponds to the distance traveled, but in the DIS, the energy change in inelastic scattering events depends on the scattering mechanism [195]. Their algorithms are described in Fig. A.2 with the flowcharts. These are applied to various biomedical applications for measurements of phonon transport as well as similar treatment of electron-beam transport as in the scanning electron microscope (SEM) [166, 189, 188].

Appendix B

Molecular Dynamics for Molecular Junction

In Chapter 5, the thermal energy transport in the molecular junctions (graphene junctions) was examined by the nonequilibrium Green function formalism (NEGF), and the results were compared with the semi-classical acoustic mismatch model. Here, the phonon transport in the biphenyl junctions is studied with the nonequilibrium molecular dynamics (NEMD) [156].

The molecular dynamics (MD) simulations is employed to investigate the stability with respect to the torsion angle and the phonon transport properties of biphenyl-dithiol junction. Since the NEGF formalism for phonon transport employs the dynamical matrices, the phonon conductance $G_{t,p}$ calculated above does not include the anharmonicity. However, the anharmonicity in phonon transport is omnipresent, especially at high temperatures. $G_{t,p}$ is calculated from the temperature distribution

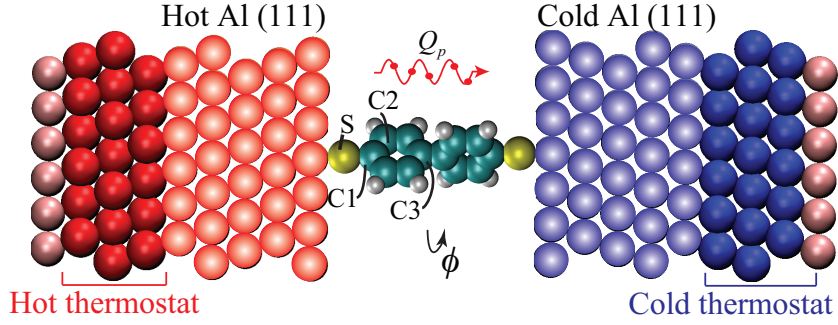


Figure B.1: (Color online) Atomic configuration used in MD simulations. The thermostat on each side is three Al layers and its temperature is controlled by the Langevin algorithm.

(ΔT) and heat flow (Q) in non-equilibrium MD (NEMD), where the temperature is controlled by the Langevin thermostat [162].

The NEMD simulations cover a temperature range of 280-500 K in the NVT ensemble (constant number of particles, volume, and temperature) with the hot (T_{hot}) and cold (T_{cold}) thermostat temperatures set 10% higher and 10% lower than the average temperature respectively. The temperature gradient is large enough to mask the effects of temperature fluctuations [73]. In our model the biphenyl-dithiol molecule is sandwiched between two Al electrodes represented by 324 atoms each (see in Fig. B.1). Periodic boundary conditions are imposed in lateral x and y directions for Al. The calculations are over 5 ns with 0.5 fs time steps. The interatomic potentials used in the molecular mechanics simulations are fit against DFT calculations. Two, three, and four-body potentials are employed and are listed in Table B.1. Instead of direct inclusion of H atoms, the C-H groups are treated each as one entity (adding mass of H to that of C) [75].

A quantum correction scheme is invoked to the MD simulations. The correction

Table B.1: Interatomic potential parameters for NEMD simulations.

| Interaction | Potential model | Parameters |
|--|--|---|
| <i>Pair</i> | | |
| Al-S | $\varphi_o[(1 - \exp[-a(r - r_o)])^2 - 1]$ | $\varphi_o = 0.909$ eV, $r_o = 2.600$ Å, $a = 1.375$ Å ⁻¹ |
| S-C1 | $\varphi_o[(1 - \exp[-a(r - r_o)])^2 - 1]$ | $\varphi_o = 2.843$ eV, $r_o = 1.823$ Å, $a = 1.781$ Å ⁻¹ |
| C1/2/3-C2 ^a | $\varphi_o[(1 - \exp[-a(r - r_o)])^2 - 1]$ | $\varphi_o = 8.196$ eV, $r_o = 1.388$ Å, $a = 1.680$ Å ⁻¹ |
| C3-C3 | $\varphi_o[(1 - \exp[-a(r - r_o)])^2 - 1]$ | $\varphi_o = 7.436$ eV, $r_o = 1.489$ Å, $a = 1.639$ Å ⁻¹ |
| Al-Al | $0.5k_r(r - r_o)^2$ | $k_r = 3.989$ eV, $r_o = 2.864$ Å |
| <i>Angular</i> | | |
| S-C1-C2 ^b | $0.5k_\theta(\cos \theta - \cos \theta_o)^2$ | $k_\theta = 3.745$ eV, $\theta_o = 120^\circ$ |
| C1/3-C2-C2, C2-C1/3-C2 ^a | $0.5k_\theta(\cos \theta - \cos \theta_o)^2$ | $k_\theta = 11.732$ eV, $\theta_o = 120^\circ$ |
| C2-C3-C3 ^a | $0.5k_\theta(\cos \theta - \cos \theta_o)^2$ | $k_\theta = 9.599$ eV, $\theta_o = 120^\circ$ |
| <i>Torsional</i> | | |
| C2-C3-C3-C2 | $k_\phi[1 - \cos(\phi - \phi_o)]$ | $k_\phi = 2.499$ eV, $\phi_o = 31.6^\circ$ |

r , θ and ϕ are the distance, the bond angle and the torsion angle.

a - Ref.[75], b - Ref. [3]

terms takes the following form [82, 185, 187]:

$$k_B T_{\text{MD}} = \int d\omega D_p(\omega) \hbar \omega (f_p^o + \frac{1}{2}), \quad G_{t,p} = G_{t,p,\text{MD}} \frac{dT_{\text{MD}}}{dT}. \quad (\text{B.1})$$

Here f_p^o is the phonon distribution defined as $f_p^o = [\exp(\hbar\omega/k_B T) - 1]^{-1}$, and D_p is the phonon density of states (DOS) of Al (within a harmonic approximation). Figure B.2(a) shows the MD phonon conductance ($G_{t,p,\text{MD}}$), the quantum-corrected one ($G_{t,p}$), and the phonon conductance obtained via the NEGF first-principles approach. Both the MD (top axis) and corrected temperatures are indicated in the figure.

The quantum correction of the thermal transport is generally applied to the bulk properties and is rather controversial [180]. Nevertheless, the MD thermal conduc-

tance trend is found to be similar to the NEGF approach [see Fig. B.2(a)]. This agreement is originated from the relatively small model size that results in non-interacting phonons at low temperatures. At this limit the phonon-phonon (p - p) effect not included in the NEGF approach are negligible. The MD results, which include the p - p scattering, show a slightly decreasing phonon thermal conductance at high temperatures (over 431 K, which is associated with the anharmonicity), while the NEGF results with non-interacting phonons show the saturation (plateau) at high temperatures.

Overall the phonon contribution to the thermal conductance of the biphenyl-dithiol junction is relatively small compared to the electron contribution. Therefore, the anharmonic effect will only slightly enhance the TE figure of the merit (ZT) of the junction at high temperatures.

The MD calculations also analyze the torsion stability of the biphenyl-dithiol junction. In order to do so, the frequency of occurrence of the biphenyl-dithiol molecule is computed with the particular torsion angle between the phenyl rings, as shown in Fig. B.2(b). Clearly, the molecular geometries with the torsion angle of 30 degrees occur most frequently. This is in agreement with the results of the conformational study within the first-principles approach discussed in the previous subsections. At higher temperatures the frequency of occurrence becomes broadened suggesting that the molecule is likely to deviate more from the stable configuration. Furthermore, the MD results suggest the decrease in the phonon conductance at high temperatures due to the anharmonic effects [110].

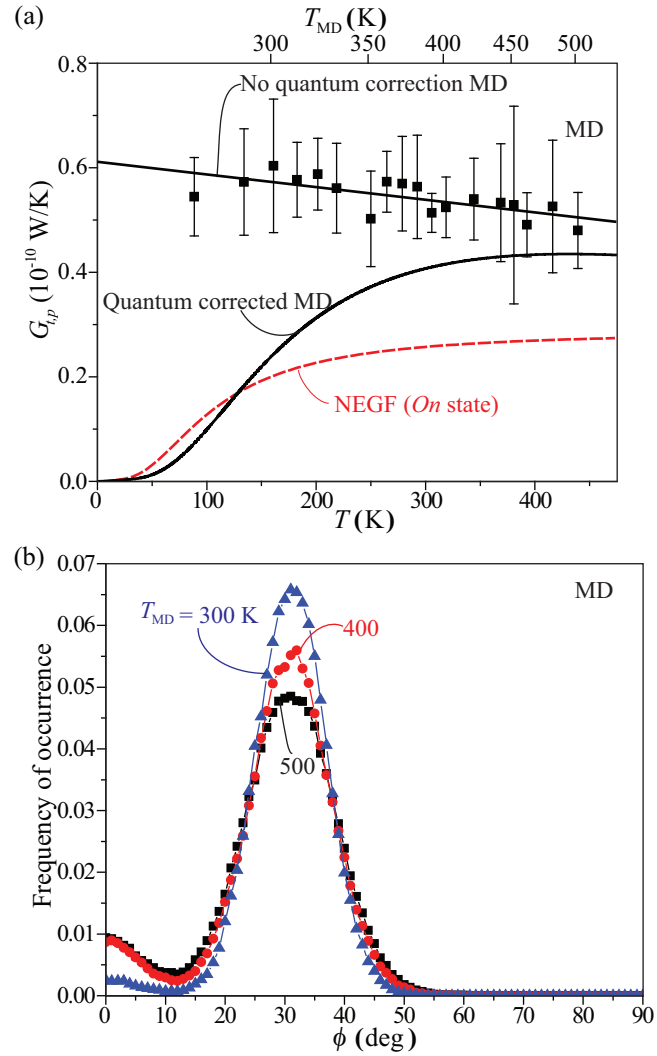


Figure B.2: (Color online) (a) Phonon thermal conductance of the biphenyl-dithiol TE junction, obtained via both the MD and NEGF calculations, versus junction temperature. (b) Frequency of occurrence of the biphenyl-dithiol molecular configurations with various torsion angles for three different values of junction temperature.

Bibliography

- [1] O. Ambacher, B. Foutz, J. Smart, J. R. Shealy, N. G. Weimann, K. Chu, M. Murphy, A. J. Sierakowski, W. J. Schaff, L. F. Eastman, R. Dimitrov, A. Mitchell, and M. Stutzmann. Two dimensional electron gases induced by spontaneous and piezoelectric polarization in undoped and doped AlGa_N/Ga_N heterostructures. *J. Appl. Phys.*, 87:334, 2000.
- [2] T. J. Anderson, M. J. Tadjer, K. D. Hobart, T. I. Feygelson, J. D. Caldwell, M. A. Mastro, J. K. Hite, C. R. Eddy Jr., F. J. Kub, and B. B. Pate. Profiling the temperature distribution in AlGa_N/Ga_N HEMTs with nanocrystalline diamond heat spreading layers. *CS MANTECH Conference, Boston, Massachusetts, USA*, 2012.
- [3] D. Q. Andrews, R. P. Van Duyne, and M. A. Ratner. Stochastic modulation in molecular electronic transport junctions: Molecular dynamics coupled with charge transport calculations. *Nano Lett.*, 8:1120–1126, 2008.
- [4] V. I. Anisimov, F. Aryasetiawan, and A. I. Lichtenstein. First-principles calculations of the electronic structure and spectra of strongly correlated systems: the LDA+U method. *J. Phys., Condens. Matter.*, 9:767, 1997.

- [5] N. Argaman and G. Makov. Density functional theory: An introduction. *Am. J. Phys.*, 68:69–79, 2000.
- [6] J. T. Bahns, W. C. Stwalley, and P. L. Gould. Laser cooling of molecules: A sequential scheme for rotation, translation, and vibration. *J. Chem. Phys.*, 104:9689, 1996.
- [7] A. A. Balandin, S. Ghosh, W. Bao, I. Calizo, D. Teweldebrhan, F. Miao, and C. N. Lau. Superior thermal conductivity of single-layer graphene. *Nano Lett.*, 8:902, 2008.
- [8] S. Banerjee and G. Gangopadhyay. Laser cooling of vibrational degrees of freedom of a molecular system. *J. Chem. Phys.*, 123:114304, 2005.
- [9] S. Baroni, S. de Gironcoli, A. D. Corso, and P. Giannozzi. Phonons and related crystal properties from density-functional perturbation theory. *Rev. Mod. Phys.*, 73:515–562, 2001.
- [10] T. Beechem, S. Graham, P. E. Hopkins, and P. M. Norris. Role of interface disorder on thermal boundary conductance using a virtual crystal approach. *Appl. Phys. Lett.*, 90:054104, 2007.
- [11] Z. Bian and A. Shakouri. Enhanced solid-state thermionic emission in nonplanar heterostructures. *Appl. Phys. Lett.*, 88:012102, 2006.
- [12] G. A. Bird. Approach to translational equilibrium in a rigid sphere gas. *Phys. Fluids*, 6:1518–1519, 1963.

- [13] G. A. Bird. *Shock wave structure in a rigid sphere gas*, In *Rarefied gas dynamics*. Academic Press, New York, 1965.
- [14] G. A. Bird. *Molecular Gas Dynamics and the Direct Simulation of Gas Flow*. Oxford University Press, Oxford, 1994.
- [15] R. B. Bird, W. E. Stewart, and E. N. Lightfoot. *Transport Phenomena*. Wiley, New York, 1960.
- [16] P. E. Blöchl. Projector augmented-wave method. *Phys. Rev. B*, 50:17953, 1994.
- [17] S. Bloom, G. Harbeke, E. Meier, and I. B. Ortenburger. Band structure and reflectivity of GaN. *Phys. Stat. Solidi.*, 66:161–168, 1974.
- [18] P. D. Bogdanoff, B. Fultz, J. L. Robertson, and L. Crow. Temperature dependence of the phonon entropy of vanadium. *Phys. Rev. B*, 65:014303, 2001.
- [19] L. Boltzmann. *Lecture Notes on Gas Theory, Translated from the German Editions (Part 1; 1896, and Part 2; 1898)*. Dover, New York, 1964.
- [20] V. Bougrov, M. E. Levinshtein, S. L. Rumyantsev, and A. Zubrilov. *Properties of Advanced Semiconductor Materials GaN, AlN, InN, BN, SiC, SiGe*. John Wiley & Sons, Inc., New York, 2001.
- [21] M. Brandbyge, J.-L. Mozos, P. Ordejón, J. Taylor, and K. Stokbro. Density-functional method for nonequilibrium electron transport. *Phys. Rev. B*, 65:165401, 2002.

- [22] E. Bringuier. Nonequilibrium statistical mechanics of drifting particles. *Phys. Rev. E*, 61:6351–6358, 2000.
- [23] D. Brunner, H. Angerer, E. Bustarret, F. Freudenberg, R. Hopler, R. Mimitrov, O. Ambacher, and M. Strutzmann. Optical constants of epitaxial AlGaIn films and their temperature dependence. *J. Appl. Phys.*, 82:5090, 1997.
- [24] W. Cai, M. C. Marchetti, and M. Lax. Nonequilibrium phonon effect on time-dependent relaxation of hot electrons in semiconductor heterojunctions. *Phys. Rev. B*, 35:1369, 1987.
- [25] V. P. Carey. *Statistical thermodynamics and microscale thermophysics*. Cambridge University Press, Cambridge, 1999.
- [26] V. P. Carey, G. Chen, C. Grigoropoulos, M. Kaviany, and A. Majumdar. A review of heat transfer physics. *Nanoscale and Microscale Thermophysical Engineering*, 12:1–60, 2008.
- [27] C. Caroli, R. Combescot, P. Nozieres, and D. Saint-James. Direct calculation of the tunneling current. *J. Phys. C: Solid St. Phys.*, 4:916, 1971.
- [28] L. D. Carr, D. DeMille, R. V. Krems, and J. Ye. Cold and ultracold molecules: science, technology and applications. *New J. Phys.*, 11:055049, 2009.
- [29] P. K. Cheo. Relaxation of CO₂ laser levels by collisions with foreign gases. *IEEE J. Quantum Electron.*, 4:587–593, 1968.

- [30] G. Conibeer, R. Patterson, L. Huang, J.-F. Guillemoles, D. König, S. Shrestha, and M. A. Green. Modelling of hot carrier solar cell absorbers. *Sol. Energ. Mat. Sol. Cells*, 94:1516, 2010.
- [31] R. M. Costescu, M. A. Wall, and D. G. Cahill. Thermal conductance of epitaxial interfaces. *Phys. Rev. B*, 67:054302, 2003.
- [32] L. W. da Silva and M. Kaviany. Micro-thermoelectric cooler: Interfacial effects on thermal and electrical transport. *Int. J. Heat Mass. Tran.*, 47:2417–2435, 2004.
- [33] C. Dang, J. Reid, and B. K. Garside. Detailed vibrational population distributions in a CO₂ laser discharge as measured with a tunable diode laser. *Appl. Phys. B*, 27:145–151, 1982.
- [34] A. Dargys and J. Kundrotas. *Handbook on Physical Properties of Ge, Si, GaAs and InP*. Science and Encyclopedia Publishers, 1994.
- [35] S. Datta. *Electronic Transport in Mesoscopic Systems*. Cambridge University Press, Cambridge, 1997.
- [36] T. G. Desai. Molecular dynamics study of screening at ionic surfaces. *J. Chem. Phys.*, 127:154707, 2007.
- [37] C. Diaz-Pinto, S. Lee, V. G. Hadjiev, and H. Peng. Probing phonon emission via hot carrier transport in suspended graphitic multilayers. *Solid State Commun.*, 151:1645–1649, 2011.

- [38] N. Djeu and W. T. Whitney. Laser cooling by spontaneous anti-stokes scattering. *Phys. Rev. Lett.*, 46:236–239, 1981.
- [39] E. C. Do, Y.-H. Shin, and B.-J. Lee. A modified embedded-atom method interatomic potential for indium. *CALPHAD*, 32:82–88, 2008.
- [40] L. Doyennette, M. Margottin-Maclou, H. Gueguen, A. Carion, and L. Henry. Temperature dependence of the diffusion and accommodation coefficients in nitrous oxide and carbon dioxide excited into the (0001) vibrational level. *J. Chem. Phys.*, 60:697–702, 1974.
- [41] X. Du, I. Skachko, A. Barker, and E. Y. Andrei. Approaching ballistic transport in suspended graphene. *Nature Nanotechnol.*, 3:491–195, 2008.
- [42] W. Duley. *CO₂ Lasers: Effects and Applications*. Academic Press, London, 1976.
- [43] L. F. Eastman, V. Tilak, V. Kaper, J. Smart, R. Thompson, B. Green, J. R. Shealy, and T. Prunty. Progress in high-power, high frequency AlGa_N/Ga_N HEMTs. *phys. stat. sol. (a)*, 194:433, 2002.
- [44] S. A. Egorov and J. L. Skinner. On the theory of multiphonon relaxation rates in solids. *J. Chem. Phys.*, 103:1533, 1995.
- [45] M. Endo and R. F. Walter. *Gas Laser*. CRC Press, Taylor & Francis Group, 2007.

- [46] O. Eriksson, J. M. Wills, and D. Wallace. Electronic, quasiharmonic, and anharmonic entropies of transition metals. *Phys. Rev. B*, 46:5221–5228, 1992.
- [47] K. Esfarjani, M. Zebarjadi, and Y. Kawazoe. Thermoelectric properties of a nanocontact made of two-capped single-wall carbon nanotubes calculated within the tight-binding approximation. *Phys. Rev. B*, 73:085406, 2006.
- [48] J. N Fehr, M.-A. Dupertuis, T. P. Hessler, L. Kappei, D. Marti, F. Salleras, M. S. Nomura, B. Deveaud, J.-Y. Emery, and B. Dagens. Hot phonons and auger related carrier heating in semiconductor optical amplifiers. *IEEE J. Quantum Elect.*, 38:674, 2002.
- [49] D. Frenkel and B. Smit. *Understanding Molecular Simulation: From Algorithms to Applications*. Academic Press, 2002.
- [50] J. Fritsch and U. Schröder. Density functional calculation of semiconductor surface phonons. *Physics Reports*, 309:209–331, 1999.
- [51] S. Fujii and T. Enoki. Cutting of oxidized graphene into nanosized pieces. *J. Am. Chem. Soc.*, 132:10034–10041, 2010.
- [52] J. D. Gale and A. L. Rohl. The general utility lattice program. *Mol. Simul.*, 29:291–341, 2003.
- [53] F. G. Gebhardt and D. C. Smith. Kinetic cooling of a gas by absorption of CO₂ laser radiation. *Appl. Phys. Lett.*, 20:129–132, 1972.

- [54] S. Ghosh, I. Calizo, D. Teweldebrhan, E. P. Pokatilov, D. L. Nika, A. A. Balandin, W. Bao, F. Miao, and C. N. Lau. Extremely high thermal conductivity of graphene: Prospects for thermal management applications in nanoelectronic circuits. *Appl. Phys. Lett.*, 92:151911, 2008.
- [55] P. Giannozzi, S. de Gironcoli, P. Pavone, and S. Baroni. *Ab initio* calculation of phonon dispersions in semiconductors. *Phys. Rev. B*, 43:7231–7242, 1991.
- [56] P. Giannozzi et al. Quantum espresso: a modular and open-source software project for quantum simulations of materials. *J. Phys.: Condens. Matter*, 21:395502, 2009.
- [57] A. N. Goland and A. Paskin. Model for fissionfragment damage in thin polycrystalline metal films. *J. Appl. Phys.*, 35:2188, 1964.
- [58] X. Gonze et al. Abinit : First-principles approach of materials and nanosystem properties. *Computer Phys. Commun.*, 180:2582–2615, 2009.
- [59] C. Goupil, W. Seifert, K. Zabrocki, E. Müller, and G. J. Snyder. Thermodynamics of thermoelectric phenomena and applications. *Entropy*, 13:1481–1517, 2011.
- [60] Q. Hao, G. Chen, and M.-S. Jeng. Frequency-dependent monte carlo simulations of phonon transport in two dimensional porous silicon with aligned pores. *J. Appl. Phys*, 106:114321, 2009.
- [61] W. M. Haynes. *CRC Handbook of Chemistry and Physics, 91st edition*. CRC Press, 2009.

- [62] G. Henkelman, A. Arnaldsson, and H. Jónsson. A fast and robust algorithm for Bader decomposition of charge density. *Comput. Mater. Sci.*, 36:354–360, 2006.
- [63] G. Herzberg. *Molecular Spectra and Molecular Structure vol.II-Infrared and Raman Spectra of Polyatomic Molecules*. Van Nostrand, New York, 1945.
- [64] K. Hess. *Monte Carlo Device Simulation: Full Band and Beyond*. Kluwer Academic Publishers, 1991.
- [65] J. Heyd, G. E. Scuseria, and M. Ernzerhof. Hybrid functionals based on a screened coulomb potential. *J. Chem. Phys.*, 118:8207, 2003.
- [66] R. C. Hilborn. Einstein coefficients, cross sections, f values, dipole moments, and all that. *Am. J. Phys.*, 50:982–986, 1982.
- [67] R. W. Hockney and J. W. Eastwood. *Computer simulation using particle*. Adam Hilger, 1988.
- [68] O. Hod, V. Barone, J. E. Peralta, and G. E. Scuseria. Enhanced half-metallicity in edge-oxidized zigzag graphene nanoribbons. *Nano Lett.*, 7:2295–2299, 2007.
- [69] M. G. Holland. Analysis of lattice thermal conductivity. *Phys. Rev.*, 132:2461–2471, 1963.
- [70] P. E. Hopkins and P. M. Norris. Effects of joint vibrational states on thermal boundary conductance. *Nanoscale Microscale Thermophys. Eng.*, 11:247–257, 2007.

- [71] P. E. Hopkins, P. M. Norris, M. S. Tsegaye, and A. W. Ghosh. Extracting phonon thermal conductance across atomic junctions: Nonequilibrium greens function approach compared to semiclassical methods. *J. Appl. Phys.*, 106:063503, 2009.
- [72] P. A. Houston and A. G. R. Evans. Electron drift velocity in n-gaas at high electric fields. *Solid State Electron.*, 20:197, 1977.
- [73] J. Hu, X. L. Ruan, and Y. P. Chen. Thermal conductivity and thermal rectification in graphene nanoribbons: A molecular dynamics study. *Nano Lett.*, 9:2730–2735, 2009.
- [74] B. L. Huang and M. Kaviany. Structural metrics of high-temperature lattice conductivity. *J. Appl. Physics*, 100:123507–1–12, 2006.
- [75] B. L. Huang and M. Kaviany. Thermal conductivity of metal-organic framework 5 (MOF-5): Part i. molecular dynamics simulations. *Int. J. Heat Mass. Tran.*, 50:393–404, 2007.
- [76] Z. Huang, T. S. Fisher, and J. Y. Murthy. Simulation of phonon transmission through graphene and graphene nanoribbons with a greens function method. *J. Appl. Phys.*, 108:094319, 2010.
- [77] G. S. Hwang and M. Kaviany. Molecular dynamics simulation of effective thermal conductivity of vapor-filled nanogap and nanocavity. *J. App. Phys.*, 106:024317, 2009.

- [78] F. I. Irwine. *Thermophysical Properties, in Handbook of Heat Transfer*. McGraw-Hill, New York, 1998.
- [79] C. Jacoboni and P. Lugli. *The Monte Carlo Method for Semiconductor Device Simulation*. Springer-Verlag, 1989.
- [80] M.-S. Jeng, R. Yang, D. Song, and G. Chen. Modeling the thermal conductivity and phonon transport in nanoparticle composites using monte carlo simulation. *J. Heat Transfer*, 130:042410, 2008.
- [81] P. S. Julienne and F. H. Mies. Collisions of ultracold trapped atoms. *J. Opt. Soc. Am. B*, 6:2257–2269, 1989.
- [82] M. Kaviany. *Heat Transfer Physics*. Cambridge University Press, Cambridge, 2008.
- [83] A. Kikuchi. Calculation of ohmic contact resistance at a metal/silicon interface. *Phys. Stat. Sol. (a)*, 175:623–629, 1999.
- [84] H. Kim and M. Kaviany. Effect of thermal disorder on high figure of merit in PbTe. *Phys. Rev. B*, 86:045213, 2012.
- [85] J. Kim. *Phonon Tuning and Recycling in Photonic Energy Conversion: Atomic-Structure Metrics and Examples*. Ph.D. thesis, University of Michigan, Ann Arbor, Michigan, 2011.
- [86] J. Kim, A. Kapoor, and M. Kaviany. Material metrics for laser cooling of solids. *Phys. Rev. B*, 77:115127, 2008.

- [87] J. Kim and M. Kaviany. Phonon recycling in ion-doped lasers. *Appl. Phys. Lett.*, 95:074103, 2009.
- [88] K. Kim, K. Hess, and F. Capasso. Monte carlo study of electron heating and enhanced thermionic emission by hot phonons in heterolayers. *Appl. Phys. Lett.*, 52:1167, 1988.
- [89] R. Kim, C. Jeong, and M.S. Lundstrom. On momentum conservation and thermionic emission cooling. *J. Appl. Phys.*, 107:054502, 2010.
- [90] C. Kittel. Interpretation of the thermal conductivity of glasses. *Phys. Rev.*, 75:972–974, 1949.
- [91] P. Kocevar. Hot phonon dynamics. *Physica B*, 134:155, 1985.
- [92] K. H. Kochem, W. Sohn, N. Hebel, K. Jung, and H. Ehrhardt. Elastic electron scattering and vibrational excitation of CO₂ in the threshold energy region. *J. Phys. B: At. Mol. Opt. Phys.*, 18:4455–4467, 1985.
- [93] T. D. Kolomiřtsova, A. V. Lyaptsev, and D. N. Shchepkin. Determination of parameters of the dipole moment of the CO₂ molecule. *Opt. Spectrosc.*, 88:648–660, 2000.
- [94] G. Kresse and J. Furthmüller. Efficient iterative schemes for *ab initio* total-energy calculations using a plane-wave basis set. *Phys. Rev. B*, 54:11169–11186, 1996.

- [95] G. Kresse and D. Joubert. From ultrasoft pseudopotentials to the projector augmented-wave method. *Phys. Rev. B*, 59:1758, 1999.
- [96] D. Lacroix, K. Joulain, and D. Lemonnier. Monte carlo transient phonon transport in silicon and germanium at nanoscales. *Phys. Rev. B*, 72:064305, 2005.
- [97] L. Landau. On the thermodynamics of photoluminescence. *J. Phys. (Moscow)*, 10:503–506, 1946.
- [98] L. D. Landau and E. Teller. in *Collected Papers of L. D. Landau, edited by D. ter Haar (Gordon and Breach, Science Publishers, Inc. and Pergamon Press Ltd., New York, 1965), p.147; Phys. Z. Sowjetunion*, 10:34, 1936.
- [99] R. Landauer. Spatial variation of currents and fields due to localized scatterers in metallic conduction. *IBM J. Res. Dev.*, 1:223–231, 1957.
- [100] E. S. Landry and A. J. H. McGaughey. Thermal conductance of epitaxial interfaces. *Phys. Rev. B*, 80:165304, 2009.
- [101] G. Lee and K. Cho. Electronic structures of zigzag graphene nanoribbons with edge hydrogenation and oxidation. *Phys. Rev. B*, 79:165440, 2009.
- [102] J. H. Lee and D. L. Trimm. Catalytic combustion of methane. *Fuel Processing Technology*, 42:339–359, 1995.
- [103] R. G. Lerner and G. L. Trigg. *Encyclopaedia of Physics (2nd Edition)*. VHC Inc., 1991.

- [104] M. E. Levinshtein, S. L. Rumyantsev, and M. Shur. *Handbook Series on Semiconductor Parameters*. World Scientific, London, 1996.
- [105] Z. Liang and H. L. Tsai. Determination of vibrational energy levels and transition dipole moments of CO₂ molecules by density functional theory. *J. Mol. Spectrosc.*, 252:108–114, 2008.
- [106] W. Little. The transport of heat between dissimilar solids at low temperatures. *Can. J. Phys.*, 37:334, 1959.
- [107] M. P. Lopez Sancho, J. M. Lopez Sancho, and J. Rubio. Highly convergent schemes for the calculation of bulk and surface green functions. *J. Phys. F*, 15:851–858, 1985.
- [108] M. Lundstrom. *Fundamentals of Carrier Transport*. Cambridge University Press.
- [109] T. Luo, J. Garg, J. Shiomi, K. Esfarjani, and G. Chen. Gallium arsenide thermal conductivity and optical phonon relaxation times from first-principles calculations. *Europhys. Lett.*, 101:16001, 2013.
- [110] T. Luo and J. R. Lloyd. Non-equilibrium molecular dynamics study of thermal energy transport in Au-SAM-Au junctions. *Int. J. Heat Mass Transf.*, 63:1–11, 2010.
- [111] H. K. Lyo and D. G. Cahill. Thermal conductance of interfaces between highly dissimilar materials. *Phys. Rev. B*, 73:144301, 2006.

- [112] G. D. Mahan. Kapitza thermal resistance between a metal and a nonmetal. *Phys. Rev. B*, 79:075408, 2009.
- [113] D. Marx and J. Hutter. *Ab Initio Molecular Dynamics: Basic Theory and Advanced Methods*. Cambridge University Press, Cambridge, 2009.
- [114] A. Matulionis. Hot phonons in GaN channels for HEMTs. *Phys. Stat. Sol. (a)*, 203:2313, 2006.
- [115] A. Matulionis, J. Liberis, I. Matulionien, H. Y. Cha, L. F. Eastman, and M. G. Spencer. Hot-phonon temperature and lifetime in biased 4H-SiC. *J. Appl. Phys.*, 96:6439, 2004.
- [116] S. Mazumder and A. Majumdar. Monte carlo study of phonon transport in solid thin films including dispersion and polarization. *J. Heat Transfer*, 123:749, 2001.
- [117] A. J. H. McGaughey and M. Kaviani. Thermal conductivity decomposition and analysis using molecular dynamics simulations. part i. lennard-jones argon. *Int. J. Heat and Mass Transfer*, 47:1783–1798, 2004.
- [118] O. Medelung. *Semiconductors: Data Handbook*. Springer Verlag, 3rd edition, 2004.
- [119] E. Merzbacher. *Quantum Mechanics*. John Wiley & Sons, Inc., 1998.
- [120] N. Mingo and L. Yang. Phonon transport in nanowires coated with an amorphous material: An atomistic greens function approach. *Phys. Rev. B*, 68:245406, 2003.

- [121] C. Moglestue. *Monte Carlo Simulation for Semiconductor Device*. Chapman and Hall, 1993.
- [122] C. B. Moore, R. E. Wood, B. L. Hu, and J. T. Yardley. Vibrational energy transfer in CO₂ lasers. *J. Chem. Phys.*, 46:4222–4231, 1967.
- [123] H. Morkoç. *Semiconductors: Data Handbook*. Springer, Berlin, 2006.
- [124] E. Muñoz, J. Lu, and B. I. Yakobson. Ballistic thermal conductance of graphene ribbons. *Nano Lett.*, 10:1652–1656, 2010.
- [125] W. Neuhauser, M. Hohenstatt, P. Toschek, and H. Dehmelt. Optical-sideband cooling of visible atom cloud confined in parabolic well. *Phys. Rev. Lett.*, 41:233–236, 1978.
- [126] V. V. Nevdakh, L. N. Orlov, and N. S. Leshenyuk. Temperature dependence of the vibrational relaxation rate constants of CO₂ (00⁰1) in binary mixture. *J. Appl. Spectrosc.*, 70:276–284, 2003.
- [127] K. S. Novoselov, A. K. Geim, S. V. Morozov, D. Jiang, Y. Zhang, S. V. Dubonos, I. V. Grigorieva, and A. A. Firsov. Electric field effect in atomically thin carbon films. *Science*, 306:666–669, 2004.
- [128] C. Oshima, T. Aizawa, R. Souda, Y. Ishizawa, and Y. Sumiyoshi. Atomistic structure of band-tail states in amorphous silicon. *Solid State Commun.*, 65:1601, 1988.

- [129] T. Palacios, A. Chakraborty, S. Heikman, S. Keller, S. P. DenBaars, and U. K. Mishra. AlGa_N/Ga_N high electron mobility transistors with InGa_N back-barriers. *IEEE Electr. Device L.*, 27:13, 2006.
- [130] J. Y. Park and G. A. Somorjai. The catalytic nanodiode: Detecting continuous electron flow at oxide-metal interfaces generated by a gas-phase exothermic reaction. *ChemPhysChem*, 7:1409–1413, 2006.
- [131] C. K. N. Patel. Continuous-wave laser action on vibrational-rotational transitions of CO₂. *Phys. Rev.*, 136:A1187–A1193, 1964.
- [132] J. P. Perdew, K. Burke, and M. Ernzerhof. Generalized gradient approximation made simple. *Phys. Rev. Lett.*, 77:3865–3868, 1996.
- [133] B. N. J. Persson and R. Ryberg. Vibrational line shapes of low-frequency adsorbate modes: CO on Pt(111). *Phys. Rev. B*, 40:10273, 1989.
- [134] P. E. Phelan. Application of diffuse mismatch theory to the prediction of thermal boundary resistance in thin-film high-*t_c* superconductors. *J. Heat. Trans.*, 120:37–43, 1998.
- [135] W. D. Phillips. Nobel lecture: Laser cooling and trapping of neutral atoms. *Rev. Mod. Phys.*, 70:721–741, 1998.
- [136] F. J. Pollack. In *32nd IEEE Annual International Symposium on Microarchitecture*, 1999.

- [137] F. W. Ragay, E. W. M. Ruigrok, and J. H. Wolter. GaAs-AlGaAs heterojunction solar cells with increased open-circuit voltage. *IEEE WCPEC.*, 2:1934, 1994.
- [138] J. Randrianalisoa and D. Baillis. Monte carlo simulation of steady-state microscale phonon heat transport. *J. Heat Transfer*, 130:072404, 2008.
- [139] P. Reddy, K. Castelino, and A. Majumdar. Diffuse mismatch model of thermal boundary conductance using exact phonon dispersion. *Appl. Phys. Lett.*, 87:211908, 2005.
- [140] H. D. Rees. Calculation of distribution functions by exploiting the stability of the steady state. *J. Phys. Chem. Solids*, 30:643, 1969.
- [141] L. G. C. Rego and G. Kirczenow. Quantized thermal conductance of dielectric quantum wires. *Phys. Rev. Lett.*, 81:232, 1998.
- [142] B. K. Ridley, W. J. Schaff, and L. F. Eastman. Hot-phonon-induced velocity saturation in GaN. *J. Appl. Phys.*, 96:1499, 2004.
- [143] M. D. Di Rosa. Laser-cooling molecules. *Eur. Phys. J. D*, 31:395–402, 2004.
- [144] X. L. Ruan and M. Kaviani. Enhanced laser cooling of rare-earth-ion-doped nanocrystalline powders. *Phys. Rev. B*, 73:155422, 2006.
- [145] X. L. Ruan and M. Kaviani. Advances in laser cooling of solids. *ASME J. Heat Transfer*, 129:3–10, 2007.

- [146] X. L. Ruan, S. C. Rand, and M. Kaviani. Vibrational entropy and efficiency in laser cooling of solids. *Phys. Rev. B*, 75:214304, 2007.
- [147] J. G. Ruch and G. S. Kino. Transport properties of GaAs. *Phys. Rev.*, 174:921, 1968.
- [148] W. Saito, Y. Takada, M. Kuraguchi, K. Tsuda, I. Omura, T. Ogura, and H. Ohashi. High breakdown voltage algan-gan power-hemt design and high current density switching behavior. *IEEE Trans. Electron Dev.*, 50:2528, 2003.
- [149] S. Sakong, P. Kratzer, X. Han, K. Laß, O. Weingart, and E. Hasselbrink. Density-functional theory study of vibrational relaxation of CO stretching excitation on Si(100). *J. Chem. Phys.*, 129:174702, 2008.
- [150] P. K. Schelling, S. R. Phillpot, and P. Keblinski. Comparison of atomic-level simulation methods for computing thermal conductivity. *Phys. Rev. B*, 65:144306, 2002.
- [151] P. K. Schelling, S. R. Phillpot, and P. Keblinski. Phonon wave-packet dynamics at semiconductor interfaces by molecular-dynamics simulation. *Appl. Phys. Lett.*, 80:2484, 2002.
- [152] E. F. Schubert. *Light-Emitting Diodes*. Cambridge University Press, 2nd edition, Cambridge, 2006.
- [153] R. N. Schwartz, Z. I. Slawsky, and K. F. Herzfeld. Calculation of vibrational relaxation times in gases. *J. Chem. Phys.*, 20:1591–1599, 1952.

- [154] K. Schwarz and P. Blaha. Solid state calculations using WIEN2k. *Comput. Mater. Sci.*, 28:259–273, 2003.
- [155] A. V. Sergeev. Electronic kapitza conductance due to inelastic electron-boundary scattering. *Phys. Rev. B*, 58:R10199–R10202, 1998.
- [156] N. Sergueev, S. Shin, M. Kaviany, and B. Dunietz. Efficiency of thermoelectric energy conversion in biphenyl-dithiol junctions: Effect of electron-phonon interactions. *Phys. Rev. B*, 83:195415, 2011.
- [157] A. Shakouri and J. E. Bowers. Heterostructure integrated thermionic coolers. *Appl. Phys. Lett.*, 71:1234, 1997.
- [158] A. Shakouri, E. Y. Lee, D. L. Smith, V. Narayanamurti, and J. E. Bowers. Thermoelectric effects in submicron heterostructure barriers. *Microscale Thermophys. Eng.*, 2:37, 1998.
- [159] S. Shin and M. Kaviany. Enhanced laser cooling of CO₂-Xe gas using (02⁰0) excitation. *J. Appl. Phys.*, 106:124910, 2009.
- [160] S. Shin and M. Kaviany. Interflake thermal conductance of edge-passivated graphene. *Phys. Rev. B*, 84:235433, 2011.
- [161] S. Shin and M. Kaviany. Entropy production in phonon-electron energy conversion in semiconductors. *Phys. Rev. B (submitted)*, 2013.
- [162] S. Shin, M. Kaviany, T. Desai, and R. Bonner. Roles of atomic restructuring in interfaical phonon transport. *Phys. Rev. B*, 82:081302, 2010.

- [163] S. Shin, C. Melnick, and M. Kaviany. Heterobarrier for converting hot-phonon energy to electric potential. *Phys. Rev. B*, 87:075317, 2013.
- [164] D. Sholl and J. A. Steckel. *Density Functional Theory: A Practical Introduction*. Wiley-Interscienc, 2009.
- [165] D. R. Siebert, F. R. Grabiner, and G. W. Flynn. Time-resolved thermal lensing studies of laser-induced translational energy fluctuations in CD₄, SO₂, and OCS. *J. Chem. Phys.*, 60:1564–1574, 1996.
- [166] R. Siegel and J. R. Howell. *Thermal radiation Heat Transfer*. Hemisphere, Washington, D.C., 1992.
- [167] J. Singh. *Electronic and Optoelectronic Properties of Semiconductor Structures*. Cambridge University Press, Cambridge, 2003.
- [168] G. A. Slack. The thermal conductivity of nonmetallic crystals. *Solid State Phys.*, 34:1–71, 1979.
- [169] V. Spagnolo, G. Scamarcio, M. Troccoli, F. Capasso, C. Gmachl, A. M. Sergent, A. L. Hutchinson, D. L. Sivco, and A. Y. Cho. Nonequilibrium optical phonon generation by steady-state electron transport in quantum-cascade lasers. *Appl. Phys. Lett.*, 80:4303, 2002.
- [170] G. P. Srivastava. *The Physics of Phonons*. Adam Hilger, Bristol, 1990.

- [171] S. Stankovich, D. A. Dikin, G. H. B. Dommett, K. M. Kohlhaas, E. J. Zimney, E. A. Stach, R. D. Piner, S. T. Nguyen, and R. S. Ruoff. Graphene-based composite materials. *Nature*, 442:282–286, 2006.
- [172] J. C. Stephenson, R. E. Wood, and C. B. Moore. Temperature dependence of intramolecular vibration-vibration energy transfer in CO₂. *J. Chem. Phys.*, 54:3097–3102, 1971.
- [173] R. J. Stevens, L. V. Zhigilei, and P. M. Norris. Effects of temperature and disorder on thermal boundary conductance at solidsolid interfaces: Nonequilibrium molecular dynamics simulations. *Int. J. Heat Mass. Tran.*, 50:3977–3989, 2007.
- [174] F. H. Stillinger and T. A. Weber. Computer simulation of local order in condensed phases of silicon. *Phys. Rev. B*, 31:5262–5271, 1985.
- [175] A. Sugimurt and W. Vogenitzf. Monte carlo simulation of ion collection by rocket-borne mass spectrometer. *J. Geophys. Res.*, 80:673–684, 1975.
- [176] E. T. Swartz and R. O. Pohl. Thermal boundary resistance. *Rev. Mod. Phys.*, 61:605–668, 1989.
- [177] S. M. Sze. *Semiconductor Devices - Physics and Technology*. John Wiley & Sons Inc., 1985.
- [178] Z. T. Tian, B. E. White Jr., and Y. Sun. Phonon wave-packet interference and phonon tunneling based energy transport across nanostructured thin films. *Appl. Phys. Lett.*, 96:263113, 2010.

- [179] S. Tiwari. *Compound Semiconductor Device Physics*. Academic Press, 1992.
- [180] J. E. Turney, A. J. H. McGaughey, and C. H. Amon. Assessing the applicability of quantum corrections to classical thermal conductivity predictions. *Phys. Rev. B*, 79:224305–1–7, 2009.
- [181] N. B. Vargaftik. *Handbook of thermal conductivity of liquids and gases*. CRC Press, Boca Raton, 1994.
- [182] D. Vashaee and A. Shakouri. Improved thermoelectric power factor in metal-based superlattices. *Phys. Rev. Lett.*, 92:106103, 2004.
- [183] S. Volz. *Thermal Nanosystems and Nanomaterials (Series: Topics in Applied Physics, Vol. 118)*. Springer, 2009.
- [184] C. S. Wang, J. S. Chen, J. Shiomi, and S. Maruyama. A study on the thermal resistance over solidliquidvapor interfaces in a finite-space by a molecular dynamics method. *Int. J. Therm. Sci.*, 46:1203–1210, 2007.
- [185] C. Z. Wang, C. T. Chan, and K. M. Ho. Tight-binding molecular-dynamics study of phonon anharmonic effects in silicon and diamond. *Phys. Rev. B*, 42:11276–11283, 1990.
- [186] J.-S. Wang, X. Ni, and J.-W. Jiang. Molecular dynamics with quantum heat baths: Application to nanoribbons and nanotubes. *Phys. Rev. B*, 80:224302, 2009.

- [187] J.-S. Wang, J. Wang, and J. T. Lü. Quantum thermal transport in nanostructures. *Eur. Phys. J. B*, 62:381, 2008.
- [188] L.-H. Wang, S. L. Jacques, and L.-Q. Zheng. Monte carlo modeling of photon transport in multi-layered tissues. *Computer Methods and Programs in Biomedicine*, 47:131–146, 1995.
- [189] L.-H. Wang and H. I. Wu. *Biomedical Optics: Principles and Imaging*. Wiley, 2007.
- [190] R. Y. Wang, R. A. Segalman, and A. Majumdar. Room temperature thermal conductance of alkanedithiol self-assembled monolayers. *Appl. Phys. Lett.*, 89:173113, 2006.
- [191] X.-G. Wang and J. R. Smith. Si/Cu interface structure and adhesion. *Phys. Rev. Lett.*, 95:156102, 2005.
- [192] B. L. Whitten and N. F. Lane. Near-threshold vibrational excitation in electron-CO₂ collisions: A simple model. *Phys. Rev. A*, 26:3170–3176, 1982.
- [193] D. Wineland, R. E. Drullinger, and F. L. Walls. Radiation-pressure cooling of bound resonant absorbers. *Phys. Rev. Lett.*, 40:1639–1642, 1978.
- [194] B. T. Wong, M. Francoeur, and M. P. Mengüç. A monte carlo simulation for phonon transport within silicon structures at nanoscales with heat generation. *Int. J. Heat Mass. Tran.*, 54:1825–1838, 2011.

- [195] B. T. Wong and M. P. Mengüç. *Thermal Transport for Applications in Micro/Nanomachining*. Springer, 2008.
- [196] J. T. Yardley and C. B. Moore. Intramolecular vibration-to-vibration energy transfer in carbon dioxide. *J. Chem. Phys.*, 46:4491–4495, 1967.
- [197] M. Zebarjadi, A. Shakouri, and K. Esfarjani. Thermoelectric transport perpendicular to thin-film heterostructures calculated using the monte carlo technique. *Phys. Rev. B*, 74:195331, 2006.
- [198] W. Zhang, T. S. Fisher, and N. Mingo. The atomistic green’s function method: an efficient simulation approach for nanoscale phonon transport. *Numer. Heat Transfer, Part B*, 51:333, 2007.
- [199] W. Zhang, T. S. Fisher, and N. Mingo. Simulation of interfacial phonon transport in sige heterostructures using an atomistic greens function method. *J. Heat Transfer*, 129:483–491, 2007.
- [200] V. P. Zhdanov. Relaxation of internal vibrational excitation of a diatomic adsorbed molecule. *Theor. Exp. Chem.*, 16:188–190, 1980.
- [201] Q. S. Zhu, S. M. Mou, X. C. Zhou, and Z. T. Zhong. Determination of the conduction-band offset of a single AlGaAs barrier layer using deep level transient spectroscopy. *Appl. Phys. Lett.*, 62:2813, 1993.